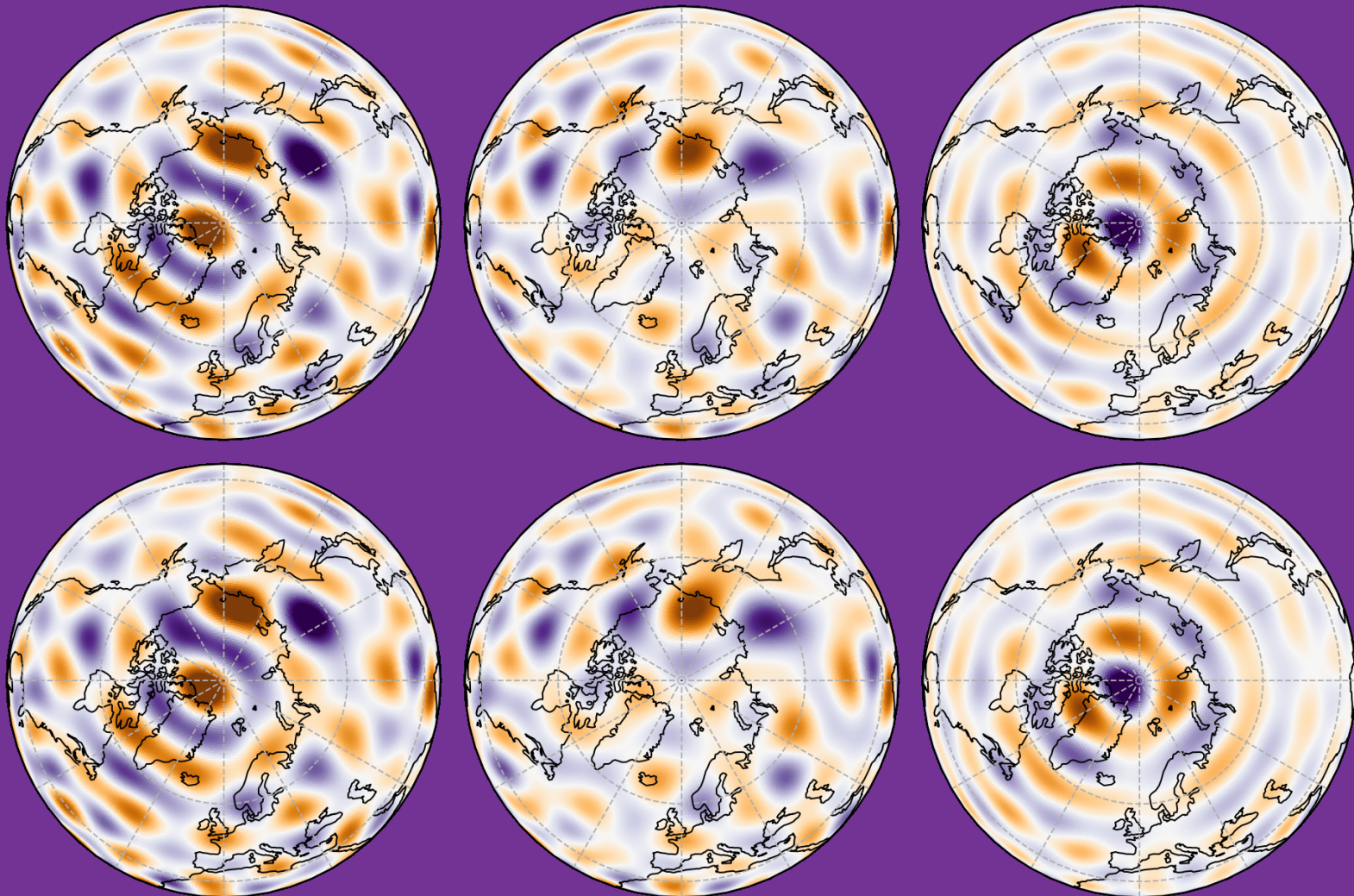


Geomagnetic field modelling and polar ionospheric currents



Clemens Kloss
April 2021

Geomagnetic field modelling and polar ionospheric currents

A thesis presented by

Clemens Kloss

to

DTU Space - National Space Institute
for the degree of Doctor of Philosophy

Technical University of Denmark

Copenhagen, Denmark

April 2021

Preface

This thesis entitled “Geomagnetic field modelling and polar ionospheric currents” is the outcome of a three-year PhD program at the Division of Geomagnetism and Geospace at the Technical University of Denmark.

Supervisors

The project supervisor were:

- (1) Prof. Christopher Charles Finlay at DTU Space, Technical University of Denmark
- (2) Prof. Nils Peter Olsen at DTU Space, Technical University of Denmark

Funding

This project was funded by the European Research Council (ERC) under the European Union’s Horizon 2020 research and innovation programme (grant agreement No. 772561), and by the Technical University of Denmark.

Location

DTU Space
Technical University of Denmark
Centrifugevej 356
2800 Kongens Lyngby
Denmark

ISBN: 978-87-91694-50-9

© 2021 – Clemens Kloss

Abstract

The Earth's magnetic field is the result of a wide range of geophysical processes both internal and external with respect to the Earth's surface. The strongest contribution originates in Earth's core, where it is generated by vast flows of liquid metal in a process known as the Geodynamo. By analyzing slow changes of the geomagnetic field, known as Secular Variation, it is possible to study this process. However, this requires that the core field signal can be accurately monitored over a sufficiently long period and separated from the other magnetic signals. The description and separation of field sources are the main goals of geomagnetic field modelling. Although difficult, field separation can be achieved given high-quality magnetic data with good spatial and temporal coverage and an understanding of the physical processes underlying the sources. Satellites in low-Earth orbit today provide a wealth of magnetic data. If this can be exploited by new field modelling techniques, it promises an improved understanding of the Earth's magnetic field.

The CHAMP and *Swarm* satellites, with their careful design and focus on magnetic field surveying, have been crucial to recent advances in geomagnetism. Unfortunately, the time series of data from these satellites is interrupted from 2010 to 2013, which limits how accurately the core field can be mapped during this gap period. Platform magnetometers provide an alternative source of data during this period with the required global coverage, although of lower quality. Such data are collected by many satellites in low-Earth orbit for navigational purposes but require careful processing and calibration in order to be useful. Here I show the necessary calibration can be achieved during field modelling through an approach that co-estimates magnetometer calibration parameters. Both internal and external fields are included during the model estimation procedure in contrast to earlier work where only the internal field and calibration parameters were co-estimated. Utilizing this new capability, a geomagnetic field model is derived with high-quality data from CHAMP and *Swarm* together with platform magnetometer data from the CryoSat-2 and GRACE satellites. I find evidence for strong correlations between the calibration parameters and some internal and external field parameters during the gap period, but I show these correlations can be avoided by modifying the model parameterization and estimation scheme. Including platform magnetometer data leads to small differences in the recovered core field during the gap period, particularly regarding the small-scale field acceleration in oceanic regions, but it has essentially no effect during the CHAMP and *Swarm* times.

Detailed study of the core field also requires that one can appropriately describe external fields produced by the electric current systems in the Earth's ionosphere and magnetosphere. The interaction of the solar wind and the magnetosphere drives particularly strong currents in the polar ionosphere, whose associated magnetic field may contaminate the core field model if not properly taken into consideration. Earlier studies have developed several techniques to include the ionospheric field in geomagnetic field modelling. However, these approaches have only been able to account for specific periodicities in the field or have used relatively little information on the underlying physi-

cal processes. Here I implement a new approach for representing the ionospheric field during field modelling, with a focus on the challenging polar regions. Magnetic apex coordinates are employed and the time-dependence of observed solar driving parameters is exploited. Test geomagnetic field models including the new ionospheric field parameterization are used to investigate the impact on the core field and to study the polar current system under geomagnetically quiet conditions. I find that the misfit in the polar regions is reduced, indicating success in accounting for previously unmodelled ionospheric signals. An ambiguity is however found between the zonal part of the ionospheric model and the internal field. This can be managed through model regularization. I find that the divergence-free part of the horizontal ionospheric currents is relatively weak under the geomagnetically quiet conditions used here for field modelling and dominated by a single cell structure in the polar regions. Co-estimating the ionospheric model results in an improvement in the high-degree and low-order components of the core field Secular Variation, this is easily visible at the core-mantle boundary and in the polar regions.

The results of my thesis highlight the possibility of improving geomagnetic field models through the use of platform magnetometer data in addition to data collected by dedicated magnetic survey satellites and by the inclusion of an ionospheric field model that is linked to solar wind driving and defined in a suitable magnetic coordinate system.

Dansk Resumé

Geomagnetisk feltmodellering og polare ionosfæriske strømme

Jordens magnetfelt er resultatet af en lang række af geofysiske processer, der findes både internt og eksternt i forhold til jordens overflade. Det største bidrag kommer fra jordens kerne, og genereres af vidtstrakte bevægelser af flydende metal i en proces kaldet geodynamoen. Ved at analysere langsomme ændringer i jordens magnetfelt, kaldet sekular variationen, er det muligt at studere denne proces. Dette kræver at signalet fra kernen kan monitoreres nøjagtigt over en tilstrækkelig lang periode, og separeres fra andre magnetiske signaler. Beskrivelsen og adskillelsen af kilderne til feltet, er de primære mål for geomagnetisk feltmodellering. Selvom dette er vanskeligt, kan separering af feltet opnås ved brug af magnetfeltsdata af høj kvalitet der har god rumlig og tidlig dækning, samt ved en forståelse af de underliggende fysiske årsager til kilderne. Satellitter i lave kredsløb bidrager med et væld af magnetisk data. Hvis disse kan udnyttes sammen med nye teknikker til feltmodellering, vil det forbedre forståelsen af jordens magnetfelt.

Inden for geomagnetisme har CHAMP og *Swarm* satellitterne, med deres omhyggelige design og fokus på magnetfeltsopmåling, været altafgørende de seneste store fremskridt. Desværre er tidsserier af data fra disse satellitter afbrudt fra 2010 til 2013, hvilket begrænser nøjagtigheden af kernefeltets kortlægning i denne mellempperiode. Platformsmagnetometre kan bidrage med data i den mellemliggende periode og yde globale opmålinger, selvom dette er af lavere kvalitet. Denne form for data er indsamlet til navigationsformål af flere satellitter i lavere kredsløb, men kræver en omhyggelig processering og kalibrering for at kunne bruges. Jeg viser her, at den nødvendige kalibrering kan gennemføres under feltmodelleringen, ved at medestimere magnetometrenes kalibreringsparametre. Under modelestimeringen inkluderes både interne og eksterne felter, hvilket står i modsætning til tidligere hvor kun det interne felt og kalibreringsparametrene blev estimeret samtidigt. Ved at anvende denne nye fremgangsmåde, bestemmes en geomagnetisk feltmodel ud fra CHAMP og *Swarm* data sammen med data fra platformsmagnetometre på satellitterne CryoSat-2 og GRACE. Jeg finder evidens for stærke korrelationer mellem kalibreringsparametrene og visse af de interne og eksterne feltparametre i den mellemliggende periode, men jeg viser at disse korrelationer kan undgås ved at ændre modelparametriseringen og estimeringsproceduren. Inkluderingen af data fra platformsmagnetometre fører til mindre forskelle i det estimerede kernefelt i den mellemliggende periode, og især i forhold til feltaccelerationen på mindre skala i oceanområder. Der er dog ingen væsentlig effekt i perioder, hvor CHAMP og *Swarm* data er tilgængeligt.

Detaljerede studier af kernefeltet kræver desuden en beskrivelse af de eksterne felter, der produceres af elektriske strømme i jordens ionosfære og magnetosfære. Solvindens interaktion med magnetosfæren driver stærke ionosfæriske strømme i polarområderne, der generer magnetfelter som kontaminere kernefeltmodellen hvis der ikke tages højde for disse. Tidligere studier har udviklet adskillige teknikker til at inkludere ionosfæriske felter i geomagnetisk feltmodellering. Dog har disse

fremgangsmåder kun været i stand til at tage højde for en specifik periodicitet af feltet eller udnyttet relativ lidt information om de underliggende fysiske processer. Jeg har implementeret en ny metode til at repræsentere det ionosfæriske felt i feltmodelleringen, med fokus på de udfordrende polarområder. Magnetiske apex koordinater bliver her anvendt, og der tages højde for observerede parametre, der drives af solen, og deres tidsafhængighed. Geomagnetiske feltmodeller, der inkluderer den nye parametrisering af ionosfæriske felter, testes og bruges til at undersøge påvirkningen af kernefeltet og til at studere det polare strømsystem under rolige geomagnetisk forhold. Jeg finder her, at misfit i de polare egne bliver reduceret, hvilket indikerer succes i forhold til umodelled ionosfæriske signaler, der ikke tidligere er blevet taget højde for. Der er dog fundet en tvetydighed i den længdeafhængige del af den ionosfæriske model og det interne felt. Dette kan håndteres ved at regularisere modellen. Jeg finder her, at den divergensfrie del af de horisontale ionosfæriske strømme er relativt svag under de rolige geomagnetisk forhold der her anvendes til feltmodelleringen, og den domineres af en enkelt cellestruktur i polarområderne. Den samtidige estimering af den ionosfæriske model, resulterer i en forbedring af de højere grader og lavere ordner af kernefeltets sekular variation, hvilket især er tydeligt ved kerne-kappe grænsen og i polarområderne.

Resultaterne af min afhandling, fremhæver muligheden for at forbedre geomagnetiske feltmodeller ved brug af data fra platformsmagnetometre sammen med data indsamlet af satellitter der har til formål at foretage magnetiske opmålinger, samt inkluderingen af en ionosfærisk feltmodel der er koblet til solvinden og defineret i et velegnet magnetiske koordinatsystem.

Acknowledgements

The last three years have been challenging but worth the effort. Above all, I want to express my sincerest gratitude to Chris Finlay for helping me navigate the obstacles of the PhD project. His support and encouragement, not to mention his vast knowledge of the geomagnetic field, have made this thesis possible. I also want to thank him for introducing me to Geomagnetism and for giving me the opportunity to work in this field of research.

I would like to thank Nils Olsen for sharing his profound understanding and knowledge of the geomagnetic field. I am also thankful for his support and all the advice.

I am grateful to Karl Magnus Laundal, who took good care of me when I was visiting the Birkeland Centre for Space Science in Bergen, Norway, for three months. I owe him my sincere gratitude for helping with the models of the ionospheric currents. I felt in particular very fortunate for the time we spent outside the office. The hiking, fishing, running and climbing trips around Bergen made it a truly enjoyable time.

I am also thankful to the entire group of the the Division of Geomagnetism and Geospace. The pleasant and joyful work atmosphere have made me feel fortunate to be part of this group. In particular, I am grateful to Magnus Hammer, Jonas Nielsen, Olivier Barrois, Tobias Bjerg, Mikkel Otzen, Thomas Edwards, Anna Joensen, Eduardo Simões da Silva, Lars William Pedersen, Anna Willer, Klaus Nielsen, Poul Erik Olsen and Lars Tøffner-Clausen for the interesting and enjoyable conversations during lunch and coffee breaks and in between. I would like to thank the European Research Council. The financial support for this PhD project is gratefully acknowledged.

Finally, I owe my deepest gratitude to my parents Andreas and Kathrin, and my brother Sebastian and his wife Michelle for their support and encouragement, especially during this trying time of writing a PhD thesis.

Clemens Kloss, April 2021, Copenhagen

Contents

1. Introduction	1
1.1. Aim of the thesis	3
1.2. Thesis outline	4
2. The Earth's magnetic field	5
2.1. Measuring Earth's magnetic field	5
2.1.1. Coordinate systems and vector components	5
2.1.2. Ground-based measurement	7
2.1.3. Satellite-based measurement	8
2.2. Electrodynamic theory and potentials	10
2.2.1. Maxwell's equations and quasi-static approximation	10
2.2.2. Magnetic scalar potential	11
2.2.3. Poloidal and toroidal potentials	13
2.3. Sources of Earth's magnetic field	15
2.3.1. Core field	15
2.3.2. Lithospheric and ocean-induced fields	19
2.3.3. Ionospheric and magnetospheric fields	21
2.4. Geomagnetic activity indices	23
2.4.1. Kp -index	23
2.4.2. Dst -index and RC -index	24
2.4.3. $F_{10.7}$ -index	25
3. Fundamentals of geomagnetic field modelling	27
3.1. Correcting and calibrating magnetic vector data	27
3.2. Data selection for internal field modelling	29
3.3. Model parameterization	29
3.3.1. Core and lithospheric fields	30
3.3.2. Magnetospheric and associated induced fields	31
3.3.3. Alignment parameters	34
3.4. Model parameter estimation: solving an inverse problem	35
3.4.1. Data error covariance matrix	37
3.4.2. Model regularization	37
3.5. State of the art of geomagnetic field modelling	39
4. Development of the modelling software	41
4.1. Motivation	41

4.2.	Multifit: software for modelling the geomagnetic field	42
4.2.1.	Example workflow for producing a CHAOS-type model	44
4.3.	ChaosMagPy: a python package to evaluate the CHAOS model	47
4.4.	Validation	49
4.5.	Concluding remarks	49
5.	Co-estimating calibration parameters in geomagnetic field modelling	51
5.1.	Introduction	51
5.2.	Data and data processing	52
5.2.1.	Absolute satellite data from scientific magnetometers	53
5.2.2.	Relative satellite data from platform magnetometers	53
5.2.3.	Ground observatory data	54
5.2.4.	Satellite data selection	54
5.3.	Model parameterization	55
5.3.1.	Internal field parameters	56
5.3.2.	External field parameters	57
5.3.3.	Alignment parameters	57
5.3.4.	Calibration parameters	57
5.4.	Model parameter estimation	58
5.4.1.	Data weighting	58
5.4.2.	Model regularization	60
5.5.	Results and discussion	61
5.5.1.	Fit to satellite data and ground observatory SV data	61
5.5.2.	Calibration parameters	66
5.5.3.	Results of the experiments	67
5.5.4.	Secular acceleration	70
5.6.	Conclusions	71
6.	Co-estimating models of polar ionospheric fields in geomagnetic field modelling	73
6.1.	Modelling of the ionospheric magnetic field	74
6.2.	Satellite and ground observatory data	78
6.3.	Model parameterization	79
6.3.1.	Internal field	81
6.3.2.	Magnetospheric and associated induced fields	81
6.3.3.	Ionospheric field	82
6.3.4.	Alignment parameters	82
6.4.	Model parameter estimation	82
6.5.	Initial tests based on synthetic data	83
6.6.	Experiments on the co-estimation of ionospheric and internal fields	85
6.6.1.	Comparisons with satellite data and ground observatory SV data	87
6.6.2.	Investigations of ambiguities related to modelling the zonal ionospheric field	95
6.6.3.	Tests with <i>SML</i> -index based data selection criteria	99

6.7. Results and discussion	106
6.7.1. Spatial and temporal characteristics of quiet-time, nightside polar currents	107
6.7.2. Extending the AMPS model parameterization to include indirectly driven polar currents	111
6.7.3. Effect of co-estimating ionospheric currents on the estimated high-latitude time-dependent internal field	112
6.8. Concluding remarks	122
7. Summary and conclusions	123
Bibliography	127
A. Publications	137

Symbols and notation

Symbol	Description
$A_n^{m,m'}$	Coefficients that multiply spherical harmonics in the primed coordinate system and accomplish a coordinate transformation to spherical harmonics in the unprimed coordinates.
B_C	Alternative notation of the geodetic component of the magnetic field vector pointing vertically down (identical to Z).
B_E	Alternative notation of the geodetic component of magnetic field vector pointing towards geographic East (identical to Y).
B_N	Alternative notation of the geodetic component of magnetic field vector pointing towards geographic North (identical to X).
B_r	Spherical geocentric component of the magnetic field vector pointing radially outward.
$B_{IMF,y}$	IMF component along the y -axis with respect to the GSM coordinate system.
$B_{IMF,z}$	IMF component along the z -axis with respect to the GSM coordinate system.
B_ϕ	Spherical geocentric component of the magnetic field vector pointing in the azimuthal direction.
B_θ	Spherical geocentric component of the magnetic field vector pointing in the co-latitudinal direction.
B_t	Magnitude of the IMF in the y - z plane of the GSM coordinate system.
D	Declination, angle between the horizontal and the northward components of the magnetic field vector.
$F_{10.7}$	Solar radio flux index measured in sfu.
F	Magnetic field strength or total intensity, total length of the magnetic field vector.
H	Horizontal component of the magnetic field vector.
I	Inclination, angle between the horizontal and the downward components of the magnetic field vector.
J_u	Vertical or upward current density.
L	Target convergence level for the iterative model estimation to terminate.
M	Truncation order of a spherical harmonic expansion of the ionospheric E-layer field and ionospheric toroidal field.
N^{far}	Truncation degree of the magnetic scalar potential associated with far-magnetospheric sources.
N^{int}	Truncation degree of the potential associated with Earth's internal magnetic field.
N^{ion}	Truncation degree of the magnetic scalar potential associated with the ionospheric E-layer field.

Symbol	Description
N^{near}	Truncation degree of the magnetic scalar potential associated with near-magnetospheric sources.
N^{tor}	Truncation degree of the ionospheric toroidal potential.
N_d	Number of data in \mathbf{d} .
N_m	Number of model parameters in \mathbf{m} .
N_p	Number of data in a partition of \mathbf{d} .
P_n^m	Coefficient of degree n and order m of the poloidal potential.
P	Poloidal potential of the magnetic field.
$R_{n,\text{GSM}}^m$	Modification of the solid spherical harmonics that take the GSM coordinate transformation and induction into account.
$R_{n,\text{SM}}^m$	Modification of the solid spherical harmonics that take the SM coordinate transformation and induction into account.
S	Spherical shell $S(r_1, r_2) \subset \mathbb{R}^3$ with $0 < r_1 \leq r \leq r_2 < \infty$. If $r = r_1 = r_2$ then $S(r)$ denotes a spherical surface of radius r .
T^{ion}	Scalar potential of the ionospheric toroidal field.
T_n^m	Coefficient of degree n and order m of a toroidal potential.
$T_{n,i}^{m,\text{ion}}$	Coefficient multiplying the i th base function of the ionospheric toroidal field coefficient $T_n^{m,\text{ion}}$.
$T_n^{m,\text{ion}}$	Coefficients associated with the ionospheric toroidal field.
T	Toroidal potential of the magnetic field.
W_n^e	Spatial power spectrum of the external magnetic field.
W^e	Squared magnitude of the external magnetic field averaged over the spherical surface.
W_n^i	Spatial power spectrum of the internal magnetic field.
W^i	Squared magnitude of the internal magnetic field averaged over the spherical surface.
W_n^{tor}	Spatial power spectrum of the toroidal magnetic field.
W^{tor}	Squared magnitude of the toroidal magnetic field averaged over the spherical surface.
X_i	i th basis function of the AMPS parameterization.
X	Geodetic component of magnetic field vector pointing towards geographic North.
Y_n^m	Spherical harmonics function of degree n and order m .
Y	Geodetic component of magnetic field vector pointing towards geographic East.
Z	Geodetic component of the magnetic field vector pointing vertically down.
Δq_1^m	RC-baseline corrections.
Φ	Cost function.
α	First Euler angle: angle to rotate vector about first axis.
β_{tilt}	Dipole tilt angle.
β	Second Euler angle: angle to rotate vector about second axis.
Λ_{cal}	Regularization matrix that penalizes the time variations of the calibration parameters.
Λ_{df}	Regularization matrix of the ionospheric E-layer field.
Λ_{mag}	Regularization matrix that penalizes the time variations of the RC-baseline corrections.
Λ_{tor}	Regularization matrix of the ionospheric toroidal field.

Symbol	Description
Λ_t	Regularization matrix that penalizes third time-derivative of the radial internal field averaged over the entire model time interval.
Λ_{t_e}	Regularization matrix that penalizes the second time-derivative of the radial internal field at the model end time.
Λ_{t_s}	Regularization matrix that penalizes the second time-derivative of the radial internal field at the model start time.
Λ	Model regularization matrix.
χ	Zenith angle of the Sun.
δ_{kl}	Kronecker delta.
δ	Delta function.
ϵ_0	Permittivity of free space ($\epsilon_0 = \frac{1}{\mu_0 c^2} = 8.8542 \times 10^{-12} \text{ F m}^{-1}$).
ϵ	Solar wind-magnetospheric coupling function.
γ	Third Euler angle: angle to rotate vector about third axis.
$\hat{q}_{1,SM}^m$	Degree-1 regression parameters of the RC-index.
κ	Angle between the magnetic field vector and the bore-sight direction \mathbf{n} of the star camera.
λ_0	Regularization parameter of the zonal coefficients of the internal time-dependent field model.
λ_{GD}	Geodetic latitude with respect to the reference ellipsoid defined by WGS84.
λ_{MA}	Modified-Apex latitude.
λ_{QD}	Quasi-Dipole latitude.
λ_{df}	Regularization parameter that multiplies Λ_{df} .
λ_{mag}	Regularization parameter that multiplies Λ_{mag} .
λ_{tor}	Regularization parameter that multiplies Λ_{tor} .
λ_b	Regularization parameter on the time variations of the offsets (b_1, b_2, b_3).
λ_m	Regularization parameter of the non-zonal coefficients of the internal time-dependent field model.
λ_s	Regularization parameter on the time variations of the sensitivities (s_1, s_2, s_3).
λ_t	Regularization parameter that multiplies Λ_t .
λ_u	Regularization parameter on the time variations of the non-orthogonalities (u_1, u_2, u_3).
λ_{t_e}	Regularization parameter that multiplies Λ_{t_e} .
λ_{t_s}	Regularization parameter that multiplies Λ_{t_s} .
\mathbb{R}	Space of real numbers.
\mathbf{B}^{ext}	External magnetic field associated with the sources in the ionosphere and magnetosphere.
\mathbf{B}^e	Magnetic field associated with the external part of the magnetic scalar potential.
\mathbf{B}^{int}	Internal magnetic field associated with the sources in the Earth's core and lithosphere.
\mathbf{B}^{ion}	Ionospheric magnetic field.
\mathbf{B}^i	Magnetic field associated with the internal part of the magnetic scalar potential.
\mathbf{B}^{mag}	Magnetospheric magnetic field.

Symbol	Description
$\mathbf{B}^{\text{pol,e}}$	Poloidal magnetic field produced by external sources.
$\mathbf{B}^{\text{pol,i}}$	Poloidal magnetic field produced by internal sources.
$\mathbf{B}^{\text{pol,sh}}$	Poloidal magnetic field inside a current-carrying spherical shell.
\mathbf{B}^{pol}	Poloidal magnetic field.
\mathbf{B}^{tor}	Toroidal magnetic field.
\mathbf{B}_{CRF}	Magnetic field vector with respect to the reference frame of the optical bench on the satellite (Common Reference Frame).
\mathbf{B}_{GEO}	Magnetic field vector expressed in terms of geocentric spherical components.
\mathbf{B}_{VFM}	Magnetic field vector in the orthogonal basis of the magnetometer.
\mathbf{B}_{raw}	Vector of raw sensor readings of the magnetometer.
\mathbf{B}	Magnetic field vector.
\mathbf{C}_d	Data error covariance matrix.
\mathbf{C}_m	Model covariance matrix.
\mathbf{D}_2	Second difference matrix.
\mathbf{D}	Forward difference matrix.
\mathbf{E}	Electric field vector.
\mathbf{F}_L	Lorentz force.
\mathbf{G}	Matrix of partial derivatives of the residuals with respect to the model parameters.
\mathbf{J}^{cf}	Curl-free part of the horizontal current density.
\mathbf{J}^{df}	Divergence-free part of the horizontal current density.
\mathbf{J}^{pol}	Poloidal electrical current.
\mathbf{J}^{sh}	Horizontal current density.
\mathbf{J}^{tor}	Toroidal electrical current.
\mathbf{J}	Current density vector.
\mathbf{P}	Matrix of non-orthogonality angles.
\mathbf{R}_1	Matrix that rotates vector about first axis.
\mathbf{R}_3	Matrix that rotates vector about second axis.
\mathbf{R}_3	Matrix that rotates vector about third axis.
$\mathbf{R}_{\text{CRF} \leftarrow \text{VFM}}$	Matrix that rotates a vector from the magnetometer frame to the common reference frame.
$\mathbf{R}_{\text{GEO} \leftarrow \text{CRF}}$	Matrix that rotates a vector from the common reference frame to the geocentric spherical basis.
\mathbf{S}	Matrix of sensitivities.
\mathbf{b}	Bias vector used in the vector calibration.
\mathbf{c}	Columns vector of calibration parameters.
\mathbf{d}_1	First basis vector of the Modified-Apex coordinate system.
\mathbf{d}_2	Second basis vector of the Modified-Apex coordinate system.
\mathbf{d}	Data vector (column vector).
\mathbf{e}	Column vector of residuals.
\mathbf{f}_1	First basis vector of the Quasi-dipole coordinate system.

Symbol	Description
\mathbf{f}_2	Second basis vector of the Quasi-dipole coordinate system.
\mathbf{g}	Column vector of the geomagnetic field model estimates.
\mathbf{k}	Unit vector that points vertically up as defined by the geodetic coordinate system.
\mathbf{m}_{LS}	Least-squares solution of the model parameter vector.
\mathbf{m}_{dip}	Unit vector that points in the direction of the geomagnetic dipole moment.
$\mathbf{m}_{\text{prior}}$	A-priori model parameter vector.
\mathbf{m}	Model parameter vector (column vector).
\mathbf{n}	Unit vector along the bore-sight direction of the star camera.
\mathbf{p}	Column vector of the geomagnetic field model parameters.
\mathbf{q}	Column vector of Euler angles.
\mathbf{r}	Position vector.
\mathbf{s}	Unit vector that points in the direction of the Sun.
\mathbf{v}_q	Velocity vector of charged particle.
$B_{k,i}$	i th B-spline basis function of order k .
\mathcal{P}_n^m	Schmidt semi-normalized associated Legendre polynomials of degree n and order m .
$\mathcal{P}_{n,m}$	Associated Legendre polynomials of degree n and order m .
AE	Auroral electrojet index, difference between lower and upper envelopes.
AL	Auroral electrojet index, lower envelope.
AO	Auroral electrojet index, mean value of the lower and upper envelopes.
AU	Auroral electrojet index, upper envelope.
Dst	Disturbance field index.
Kp	Global geomagnetic activity index.
RC_{ext}	External part of the ring current index RC .
RC_{int}	Internal part of the ring current index RC .
RC	Ring current index.
SML_{MLT}	SuperMAG version of the MLT-dependent AL index.
SML	SuperMAG version of the AL index.
μ_0	Permeability of free space ($\mu_0 = 4\pi \times 10^{-7} \text{ H m}^{-1}$).
μ	Arithmetic or weighted mean value.
∇	Triplet of partial derivatives, e.g. with respect to the three spatial coordinates (x, y, z) : $\nabla = (\partial_x, \partial_y, \partial_z)$. Often used as a vector to simplify the notation.
ν	Angular uncertainty in a rotation about an axis perpendicular to the bore-sight direction \mathbf{n} of the star camera.
ω	Angular frequency.
∂	Partial derivative operator with respect to the variable used as subscript, e.g. ∂_t is the partial derivative with respect to time.
ϕ_{GSM}	Longitude in the GSM coordinate system.
ϕ_{MLT}	Magnetic local time in degrees.
ϕ_{SM}	Longitude in the SM coordinate system.
ϕ	Azimuthal angle or longitude.

Symbol	Description
ψ^{cf}	Current potential of the curl-free part of the horizontal current density.
ψ^{df}	Current function of the divergence-free part of the horizontal current density.
ψ^{e}	External part of the magnetic scalar potential in a source-free shell.
$\psi^{\text{far,e}}$	Magnetic scalar potential associated with the external field produced by far-magnetospheric sources.
$\psi^{\text{far,i}}$	Magnetic scalar potential associated with the internal field produced by far-magnetospheric sources.
ψ^{far}	Magnetic scalar potential associated with the field produced by far-magnetospheric sources.
ψ^{int}	Magnetic scalar potential associated with Earth's internal magnetic field.
ψ^{ion}	Magnetic scalar potential associated with the ionospheric E-layer field.
ψ^{i}	Internal part of the magnetic scalar potential in a source-free shell.
ψ^{near}	Magnetic scalar potential associated with the field produced by near-magnetospheric sources.
ψ	Magnetic scalar potential.
ρ_{ij}	Model correlation matrix.
ρ	Electric charge density.
σ	Standard or weighted deviation.
τ	Based on the solar wind-magnetospheric coupling function but maximizes when the IMF is northward.
θ_{GSM}	Co-latitude in the GSM coordinate system.
θ_{MA}	Modified-Apex colatitude.
θ_{QD}	Quasi-Dipole colatitude.
θ_{SM}	Co-latitude in the SM coordinate system (dipole co-latitude).
θ_{c}	Clock angle of the IMF.
θ	Polar angle from the north polar axis (co-latitude).
\tilde{Q}_n	Q-response function in the frequency domain for a radial conductivity profile.
$\tilde{Q}_{nn'}^{mm'}$	Q-response function in the frequency domain.
ι	Imaginary unit.
ξ	Angular uncertainty in a rotation about the bore-sight direction \mathbf{n} of the star camera.
a	Earth's mean surface radius, $a = 6371.2$ km.
b_1	First component of the bias vector.
b_2	Second component of the bias vector.
b_3	Third component of the bias vector.
c	Radius of the core-mantle boundary, $c = 3485$ km.
g_n^m	Spherical harmonic coefficient of degree n and order m of the internal magnetic scalar potential.
$g_{n,i}^m$	Coefficient multiplying the i th B-spline basis function of the internal magnetic field coefficient g_n^m .

Symbol	Description
$g_{n,i}^{m,\text{ion}}$	Coefficient multiplying the i th base function of the ionospheric E-layer field coefficient $g_n^{m,\text{ion}}$.
$g_n^{m,\text{far}}$	Coefficients associated with the internal field produced by far-magnetospheric sources in GEO coordinates.
$g_n^{m,\text{ion}}$	Coefficients associated with the ionospheric E-layer field.
h_A	Geodetic height of the apex used in the definition of magnetic apex coordinates.
h_R	Geodetic reference height in the definition of Modified Apex coordinates.
h_n^m	Alternative notation of the spherical harmonic coefficient, i.e. g_n^{-m} for $m > 0$.
h	Geodetic height with respect to the reference ellipsoid defined by WGS84.
m	Spherical harmonic order.
n	Spherical harmonic degree.
q_{error}	Attitude uncertainty for CryoSat-2.
q_n^m	Spherical harmonic coefficient of degree n and order m of the external magnetic scalar potential.
$q_{n,\text{GSM}}^{m,\text{far}}$	Coefficients associated with the external field produced by far-magnetospheric sources in GSM coordinates.
$q_{n,\text{SM}}^{m,\text{near}}$	Coefficients associated with the external field produced by near-magnetospheric sources in SM coordinates.
$q_n^{m,\text{far}}$	Coefficients associated with the external field produced by far-magnetospheric sources in GEO coordinates.
q	Electric charge.
r	Radial distance from the origin.
s_1	First sensitivity.
s_2	Second sensitivity.
s_3	Third sensitivity.
s_n^m	Alternative notation of the external spherical harmonic coefficient, i.e. q_n^{-m} for $m > 0$.
t_e	Model end time.
t_s	Model start time.
t	Variable used to denote time.
u_1	First non-orthogonality angle.
u_2	Second non-orthogonality angle.
u_3	Third non-orthogonality angle.
v_x	Component of the solar wind velocity along the x-axis in GSM coordinates.
w_m	Order-dependent weighting function used for the regularization of the internal time-dependent field model.
w_n	Degree-dependent weighting function used for the regularization of the internal time-dependent field model.
w	Weighting function used for the regularization of the internal time-dependent field model.

Acronyms

Acronym	Description
AE	Auroral electrojet indices
AEJ	Auroral electrojet
AMPS	Average Magnetic field and Polar Current System
ASM	Absolute scalar magnetometer
CHAMP	CHAllenging Minisatellite Payload
CM4	Comprehensive Model 4
CM6	Comprehensive Model 6
CMB	Core-mantle boundary
CRF	Common reference frame
DMSP	Defense Meteorological Satellite Program
DTU	Technical University of Denmark
ECEF	Earth-centered Earth-fixed coordinate system
EEJ	Equatorial electrojet
ESA	European Space Agency
FGM	Platform fluxgate magnetometer
GD	Geodetic coordinate system
GEO	Geocentric spherical coordinate system (Earth-centered Earth-fixed coordinate system in spherical geometry)
GFZ	German Research Centre for Geosciences
GPS	Global Positioning System
GRACE	Gravity Recovery and Climate Experiment
GRIMM	GFZ Reference Internal Magnetic Model
GSM	Geocentric solar magnetic coordinate system
GUA	Guam (United States of America)
HEALPix	Hierarchical Equal Area isoLatitude Pixelization scheme
HER	Hermanus (South Africa)
HON	Honolulu (United States of America)
HRN	Hornsund (Norway)
ICRF	International celestial reference frame
IGRF	International Geomagnetic Reference Field
IHFAC	Inter-hemispheric field-aligned currents
IMF	Interplanetary magnetic field
INTERMAGNET	International Real-time Magnetic Observatory Network

Acronym	Description
ITRF	International terrestrial reference frame
KOU	Kourou (France)
LER	Lerwick (United Kingdom)
MA	Modified-Apex coordinate system
MAW	Mawson (Antarctica)
MCQ	Macquarie Island (Australia)
MLT	Magnetic local time
MPI	Messaging Passing Interface
NGK	Niemegk (Germany)
POGO	Polar Orbiting Geophysical Observatories
QD	Quasi-Dipole coordinate system
R1	Region 1 currents
R2	Region 2 currents
RMS	Root-mean-square value
SA	Secular Acceleration
SAA	South Atlantic Anomaly
SAC-C	Scientific Application Satellite-C
SHE	Saint Helena (United Kingdom)
SM	Solar magnetic coordinate system
Sq	Solar quiet daily variations
STR	Star tracker or star imager
SV	Secular Variation
VFM	Vector field magnetometer
WGS84	World Geodetic System 1984

1. Introduction

The existence of Earth's magnetic field has been known for centuries, but questions about its origin and evolution in time remain open and are today active subjects of research ([Hulot et al., 2010](#)). Answering these questions is a challenging task because Earth's magnetic field is produced by a wide variety of geophysical processes inside and around the Earth, which operate on a wide range of length and time-scales ([Olsen and Stolle, 2012](#)). The study of Earth's magnetic field greatly benefits from separating the magnetic signals into the contributing sources, which are then open to scientific investigations. However, this separation requires high-quality magnetic field observations on a global scale and powerful modelling techniques. The progress in the study of Earth's magnetic field is ongoing thanks to the continued acquisition of magnetic data and the development of new modelling techniques. Their combination leads to new insights and a better understanding of the underlying geophysical processes.

A major focus of interest in geomagnetism is the primary source of the field in the Earth's outer core, where a liquid metal is vigorously moving, largely as a result of the cooling and continued differentiation of the planet (e.g. [Olson, 2007](#)). The motions of the core fluid give rise to electric currents, which generate the strongest internal component of the observed magnetic field at the Earth's surface and above. This core field changes slowly on time-scales from years to decades, known as Secular Variation (SV) ([Jackson and Finlay, 2007](#)). The electric currents in the outer core are thought to be maintained by self-sustaining Geodynamo process, although the details of this are not fully understood. An accurate and detailed description of the core field and its time-dependence facilitate studies of the inner workings of the Geodynamo and core dynamics in general. An eventual outcome of this research could be to establish ways of predicting the evolution of the core field in the near future (e.g. [Fournier et al., 2010](#)).

Separating the various sources, and in particular isolating the core field, is the main goal of geomagnetic field modelling. The estimation of a geomagnetic field model requires a good coverage of high-quality magnetic data and a basic physical understanding of the major contributing sources. Magnetic ground observatories have played an important role in providing these data in the past and continue to do so. However, they are unevenly distributed on the Earth's surface, which limits the resolution of the estimated field models. In the last few decades, magnetic survey satellites in low-Earth orbits such as the Ørsted satellite, the CHALLENGING Minisatellite Payload (CHAMP) satellite and *Swarm* satellites have vastly enhanced the accuracy and resolution of geomagnetic field models ([Olsen and Stolle, 2012](#); [Hulot et al., 2015](#)). But these dedicated survey satellites are not always available and have limited local time coverage. Furthermore, apart from the sources in the Earth's core, geomagnetic field modelling involves the external sources in the near-Earth space, most notably the electric currents in the magnetosphere and the ionosphere. The electric current sources in the polar ionosphere are particularly challenging because they cause rapid time-varying and small-scale magnetic fields that are difficult to represent in field models and, thus, hard to separate from the

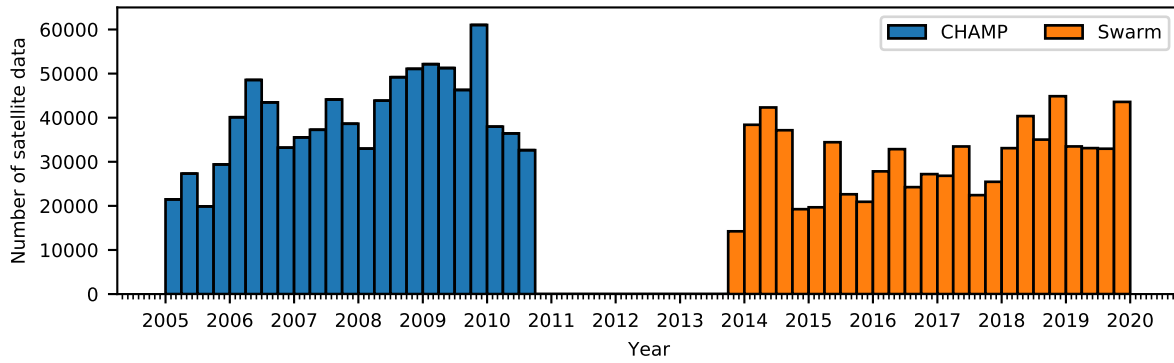


Figure 1.1.: Number of satellite data from the CHAMP and *Swarm* mission every 3 months from 2005.0 to 2020.0 satisfying selection conditions typically used for geomagnetic field modelling (e.g. [Finlay et al., 2016b](#)). The gap period between September 2010 and November 2013 without high quality magnetic survey data is clearly visible.

core field (e.g. [Finlay et al., 2016a](#)).

Satellites play a crucial role in monitoring the Earth's magnetic field on a global scale and they are beginning to provide time series that are long enough to become important for studies of the slow core field changes. Unfortunately, there was a gap in the time series of accurate magnetic survey satellite data between the CHAMP and *Swarm* missions between September 2010 and November 2013 (Fig. 1.1). However, a number of other low-Earth orbit satellites did collect magnetic data during this time, although primarily for navigational purposes. These measurements can in principle also be exploited in geomagnetic field modelling. Although platform magnetometer data are crude in quality, they may be utilized if properly calibrated ([Olsen et al., 2003](#)). The calibration can be done either by comparing the data to a reference model ([Olsen et al., 2020](#); [Olsen, 2020](#)) or through a co-estimation approach ([Alken et al., 2020](#)). The former is problematic because it requires a known field model for the calibration and, thus, there is a risk of biasing the calibrated data towards this model. The latter is an alternative approach whereby the calibration is directly integrated into the estimation of the geomagnetic field model. This co-estimation has the potential to improve both the field model and the calibration parameters.

Detailed knowledge about the current systems surrounding Earth is also crucial in determining the core field. Strong electric currents are driven in the polar ionosphere as a result of the interaction of the solar wind and the magnetosphere. These currents are organized by the Earth's magnetic field and stay mostly fixed with respect to the sun. The associated ionospheric magnetic field is internal as seen by low-Earth orbit satellites and may not average out due to the time-dependent driving processes. It could thus potentially contaminate the core field model if not properly accounted for ([Finlay et al., 2016a](#)). The presence of unmodelled ionospheric signals leads to residuals, i.e. differences between the model estimates of the field and the data used for the model estimation, which have a distinct spatial structure (Fig. 1.2). A number of techniques have been developed in order to represent the ionospheric field within geomagnetic field modelling, but so far these have been limited by a restriction to specific field periodicities (e.g. [Sabaka et al., 2002](#)), or have used relatively little information regarding the underlying physical processes (e.g. [Lesur et al., 2008](#); [Ropp et al., 2020](#); [Baerenzung et al., 2020](#)). Techniques recently developed in the space physics community, where the time-dependence of the ionospheric currents is linked to the measured solar driving and

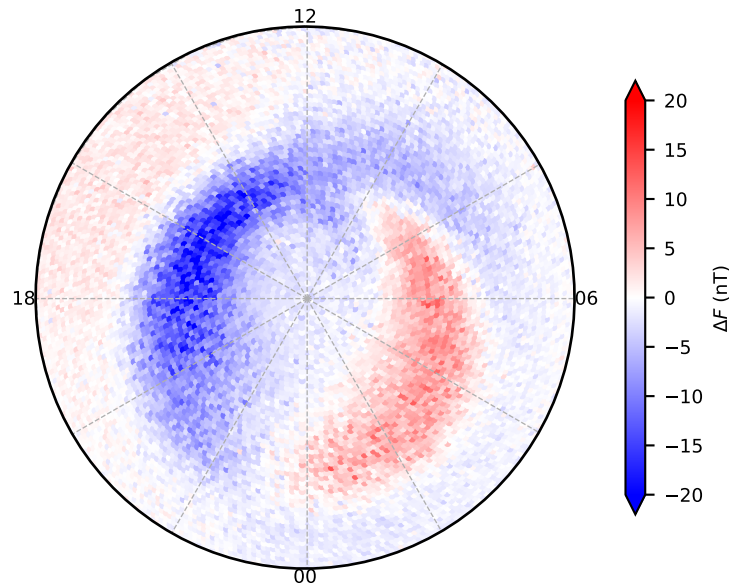


Figure 1.2.: Residuals ΔF between field magnitude observed and that predicted by a CHAOS-type geomagnetic field model over the north polar region (within 30° of the north pole) in a coordinate system that stays aligned with the sun. Noon is at the top (12), dawn on the right (06), midnight at the bottom (00) and dusk on the left (18). The residuals are the difference between a geomagnetic field model that did not account for the ionospheric field and the satellite data in Fig. 1.1, values were averaged over time in $0.5^\circ \times 0.5^\circ$ bins.

modelling is done in coordinate systems that are organized by both the near-Earth magnetic field and the sun position ([Laundal et al., 2017](#)), suggest a possible way to progress.

1.1. Aim of the thesis

The aim of this thesis is to provide new geomagnetic field modelling tools that can (i) exploit the improved satellite data coverage offered by platform magnetometer data and (ii) better account for the ionospheric field, especially within the polar region.

The work is carried out within the framework of the well-established CHAOS geomagnetic field model (e.g. [Olsen et al., 2006a, 2014](#); [Finlay et al., 2020](#)). The acronym CHAOS originally pointed to the CHAMP, Ørsted and Scientific Application Satellite-C (SAC-C) satellites whose data was initially used, but the model was later extended to also include ground observatory data and, most recently, data from the *Swarm* mission has become crucial. CHAOS is a time-dependent high-resolution model that parameterizes both internal and external fields along with data alignment parameters (more details in Chapter 3).

To address the first goal, I implement a scheme for co-estimating calibration parameters within the CHAOS framework. This new capability is used to derive a geomagnetic field model that includes high-quality data from CHAMP and *Swarm*, supplemented with multiple platform magnetometer datasets (from the Cryosat-2 and Gravity Recovery and Climate Experiment (GRACE) satellites) that are available during the gap period. I discuss trade-offs between the calibration parameters and the field model parameters, and investigate the effect of the co-estimation on the recovered magnetic field during the gap period. This part of the thesis has been published ([Kloss et al., 2021](#)).

To address the second goal, I further extend the CHAOS modelling framework to co-estimate

an ionospheric field model based on the approach used by the average magnetic field and polar current system (AMPS) model of [Laundal et al. \(2017\)](#). AMPS parameterizes ionospheric currents and the associated magnetic field in terms of a linear combination of solar wind driving parameters and other external inputs that correlate with solar wind-magnetospheric coupling (more details are given in Chapter 6). It furthermore describes the ionospheric fields in terms of appropriate magnetic apex coordinates ([Richmond, 1995](#)) and magnetic local time. These follow the geometry of the Earth's magnetic field and account for the apparent daily movement of the sun. I derive test models of the geomagnetic field to explore the effect of co-estimating an ionospheric field model on the estimated core field. And, by focusing on the polar regions, I study the polar current system under geomagnetically quiet conditions.

1.2. Thesis outline

The thesis is organized as follows. Chapter 2 introduces the Earth's magnetic field and the main contributing sources along with the basic physical concepts and the essential mathematical tools. Chapter 3 provides more detailed theoretical background to geomagnetic field modelling, giving special attention to the techniques used within the CHAOS modelling framework. Chapter 4 gives a brief introduction to the new modelling software that has been developed in the Python language during this PhD study. All the models and results presented in the thesis are based on this new software. Chapter 5 describes the scheme developed for co-estimating calibration parameters within the CHAOS modelling framework and results for a series of models derived from platform magnetometer data. Chapter 6 describes the co-estimation of an AMPS-type ionospheric field model together with a CHAOS-type field model. Resulting changes to the internal field are examined and the ionospheric current system in the polar region under geomagnetic quiet conditions is discussed. Chapter 7 summarizes the results and findings, and presents the conclusions. Finally, Appendix A includes a publication that has been made in connection with this thesis.

2. The Earth's magnetic field

For centuries the Earth's magnetic field (or the geomagnetic field) has been observed and studied. It is a superposition of the magnetic field produced by a range of electric current sources located inside the Earth, and in the region between the Earth's surface and the boundary of the magnetosphere ([Hulot et al., 2015](#)). Outside of the magnetosphere the interplanetary magnetic field (IMF) originating in the sun dominates. In the context of geomagnetic field modelling the focus of interest is naturally occurring phenomena that are static or relatively slowly changing in time, up to a few Hertz. High-frequency phenomena such as electromagnetic waves are thus neglected.

2.1. Measuring Earth's magnetic field

The magnetic field \mathbf{B} is a vector quantity, it has a magnitude and a direction. It is typically measured in units of $\text{nT} = 10^{-9} \text{ T}$ (nanoTesla) when Earth's magnetic field is considered. There are two primary observational systems in operation for monitoring the geomagnetic field: magnetic observatories at the Earth's surface and magnetic survey satellites in low-Earth orbit. Both systems have strengths and weaknesses but when combined, they are the best source of information currently available for modelling and studying the Earth's magnetic field. In the following, I briefly present both ground-based and satellite-based measurement systems. But first, I introduce coordinate systems and vector components commonly used for expressing the magnetic field vector.

2.1.1. Coordinate systems and vector components

A variety of coordinate systems are used to specify the place where \mathbf{B} is measured with respect to the Earth and to define basis vectors for resolving \mathbf{B} into components. Although any coordinate system can be chosen, some are more suitable than others in the sense that fewer parameters are needed to sufficiently describe the spatial and dynamical features of the magnetic signals of interest. The choice of the coordinate system is in particular of importance to geomagnetic field modelling since an appropriate representation may help with the separation of the magnetic signals of the different sources. For example, ionospheric and magnetospheric magnetic signals are strongly organized by the geometry of Earth's internal field, which motivates the usage of so-called magnetic coordinates.

Geodetic and geocentric coordinate systems

Measurements of Earth's magnetic field are typically expressed in coordinate systems that are fixed with respect to Earth's surface such as the geodetic (GD) coordinate system and the Earth-centered Earth-fixed (ECEF) coordinate system. Based on those coordinate systems, a set of right-handed orthogonal base vectors can be defined to resolve the magnetic field vector into components.

In the GD coordinate system, a point in space is given with respect to the reference ellipsoid of the World Geodetic System 1984 (WGS84) in terms of the geodetic coordinates (h, λ_{GD}, ϕ) , where h is the height above the ellipsoid approximating Earth's surface, λ_{GD} is the geodetic longitude, and ϕ is the geodetic latitude. Traditionally, magnetic measurements at ground observatories are resolved into the geodetic vector components (also called magnetic elements) X , Y , and Z , which point horizontally towards geographic north, horizontally towards geographic East and vertically down, respectively. The magnetic elements X , Y , and Z are also sometimes denoted as B_N , B_E , and B_C , which refer to the north component, east component, and center component, respectively. Other ways of representing the magnetic field on Earth's surface include the horizontal intensity $H = \sqrt{X^2 + Y^2}$, the field strength or total intensity $F = \sqrt{X^2 + Y^2 + Z^2}$, the magnetic declination $D = \arctan Y/X$ (angle between the horizontal and northward components), and the inclination $I = \arctan Z/H$ (angle between the horizontal and downward components).

The ECEF coordinate system is most useful in spherical geometry expressed in terms of a geocentric spherical (GEO) coordinate system defined by (r, θ, ϕ) , where r is the radial distance from the Earth's center, θ is the angular distance from the geographic north pole (colatitude), and ϕ the angular distance from the prime meridian in Greenwich (longitude). In contrast to the geodetic components for ground observations, satellite-based measurements of \mathbf{B} are typically resolved into geocentric spherical components B_r , B_ϕ , and B_θ along the radially outward direction, along the tangent of the colatitude coordinate line pointing south, and along the tangent of the azimuth coordinate line pointing East, respectively. The field intensity is computed with $F = \sqrt{B_r^2 + B_\theta^2 + B_\phi^2}$.

Orthogonal magnetic coordinate systems

Magnetic coordinate systems are based on the geometry of Earth's magnetic field and are, therefore, useful to describe phenomena which are organized by the geomagnetic field. Commonly used orthogonal magnetic coordinate systems are the dipole coordinate system, the solar magnetic (SM) coordinate system and the geocentric solar magnetic (GSM) coordinate system (for an overview, see [Laundal and Richmond, 2017](#)).

The dipole coordinate system is the simplest and most used orthogonal magnetic coordinate system. It is defined by cartesian coordinate axes so that the z-axis is aligned with the geomagnetic dipole moment as given by the International Geomagnetic Reference Field (IGRF), the y-axis is perpendicular to the plane spanned by the geomagnetic dipole moment and the geographic rotation axis, and the x-axis completes the right-handed system.

The SM coordinate system is based on cartesian coordinate axes so that the z-axis is along the geomagnetic dipole axis and the y-axis is perpendicular to the plane spanned by the geomagnetic dipole moment and the Earth-sun line. Again, the x-axis completes the right-handed system.

The GSM coordinate system is defined by cartesian coordinate axes so that the x-axis aligns with the Earth-sun line and the y-axis is perpendicular to both the Earth-sun line and the geomagnetic dipole moment. Here, the z-axis completes the right-handed coordinate system. Both the SM and GSM coordinate systems depend on time.

Non-orthogonal magnetic coordinate systems

There are also magnetic coordinate systems that take the non-dipolar geometry of Earth's magnetic field into account. In this case, the coordinate lines are not straight but curved, unlike the coordinate axes in the case of the dipole, SM, and GSM coordinate systems.

The magnetic apex coordinate systems ([VanZandt et al., 1972](#); [Richmond, 1995](#)) fall into this category. They are defined by the location of the apex which is the highest point on a particular magnetic field line of the IGRF with respect to the reference ellipsoid that approximates Earth's surface. Hence, any point in the space close to Earth can be traced to the apex of the IGRF field line that intersects this point. In magnetic apex coordinates, the point's longitude then is given by the dipole longitude of the apex, whereas its latitude is determined by a mapping of the apex height onto a reference height along the IGRF field line. [Richmond \(1995\)](#) defined two types of mapping of the apex height. In Quasi-Dipole (QD) coordinates, the latitude is calculated with

$$\lambda_{\text{QD}} = \pm \cos^{-1} \sqrt{\frac{a+h}{a+h_A}}, \quad (2.1)$$

where a is the mean Earth radius, h is the geodetic height of the point in question and h_A is the geodetic height of the apex. The latitude in Modified-Apex (MA) coordinates is given by

$$\lambda_{\text{MA}} = \pm \cos^{-1} \sqrt{\frac{a+h_R}{a+h_A}}, \quad (2.2)$$

where h_R is a chosen reference height of the mapping. The sign of the QD and MA latitudes is positive for points on the northern magnetic hemisphere and negative for points on the southern magnetic hemisphere. From the definitions in Eqs. (2.1) and (2.2), it follows that points on the same IGRF field line have the same MA latitude but differ in QD latitude as the latter depends on the height of the points. The longitude of the points on the IGRF field line, however, are always equal to the dipole longitude of the apex irrespective of the type of magnetic apex coordinates.

2.1.2. Ground-based measurement

Ground-based magnetic observatories are indispensable for geomagnetic field modelling as they provide long time-series of high-quality absolute measurements of the Earth's magnetic field dating back to as early as the 19th century. Since 1991 the International Real-time Magnetic Observatory Network (INTERMAGNET) has been overseeing operations of a global network of geomagnetic observatories (e.g. [Love, 2008](#); [Chulliat et al., 2016](#); [Matzka et al., 2010](#)). [Fig. 2.1](#) shows the geographic locations of the 127 observatories which are part of the INTERMAGNET system in 2020. The majority of the observatories are located in the northern Hemisphere and there is a particularly dense network in Europe. However, most of the Earth's surface is covered with oceans where no ground observatories can be set up except for a few isolated locations on islands. The uneven spatial distribution of the observatories allows for the retrieval of only the largest spatial scales of the geomagnetic field, which already points to the importance of measurements from low Earth orbit satellites in providing data with global coverage. Nonetheless, the significance of ground observatory data is evident for the following reasons. First, thanks to the continuous monitoring and the high quality of the magnetic

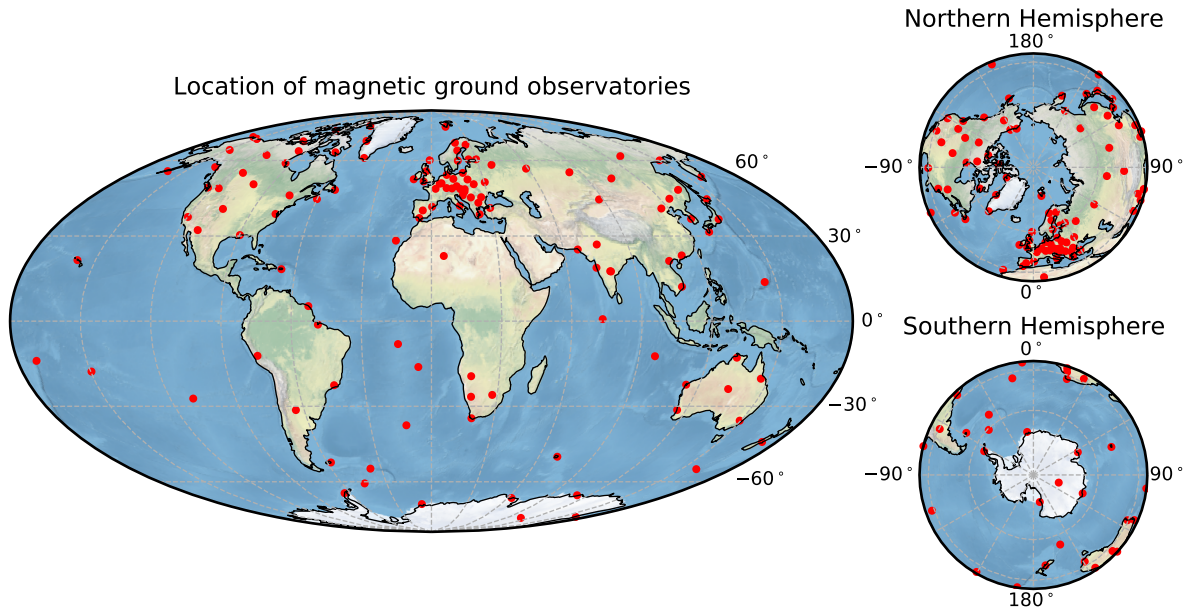


Figure 2.1.: Locations of 127 ground observatories that are currently part of the INTERMAGNET system.

data, ground observatories allow the study of past ([Jackson and Finlay, 2015](#)) and present ([Hulot et al., 2015](#)) changes in the geomagnetic field. Second, their measurements are the basis for deriving magnetic activity indices such as K_p , Dst , RC from low to mid-latitude stations and the auroral electrojet indices AL and AU from stations in the auroral zone in the northern polar region (Sec. 2.4). Those activity indices are important in the design of selection criteria, which are used to identify magnetically quiet data for geomagnetic field modelling. Finally, ground observatories are located between the magnetic sources inside the Earth and those in the ionosphere, which could, in principle, prove important for the separation of the two contributions.

In this thesis, instead of the standard ground-based hourly mean observations of the magnetic field vector, I used annual differences of revised monthly mean values ([Olsen et al., 2014](#)) that are designed to follow the slow time-dependence of the Earth's internal field. A robust method based on Huber-weights was used to compute the revised monthly mean values from ground observatory hourly means from all local times, following the method described by [Macmillan and Olsen \(2013\)](#), who removed trends, large spikes and discontinuities. Prior to computing the monthly values, hourly estimates of the ionospheric field given by the Comprehensive Model 4 (CM4) ([Sabaka et al., 2004](#)) and the magnetospheric field given by CHAOS-6-x9 ([Finlay et al., 2016b](#)), including their induced counterparts, were removed from the hourly ground observatory data. As annual differences, the ground observatories give additional information primarily on the core field secular variation over the entire time interval considered here. Importantly for this thesis, they also provide valuable information during the gap period of satellite vector data between September 2010 and the end of November 2013.

2.1.3. Satellite-based measurement

Recent decades have seen considerable advances in the quality and resolution of geomagnetic field models thanks to the growing availability of global magnetic data taken by satellites in low-Earth orbit ([Olsen et al., 2010a](#)). Today, satellite-based magnetic survey missions are, together with the ground

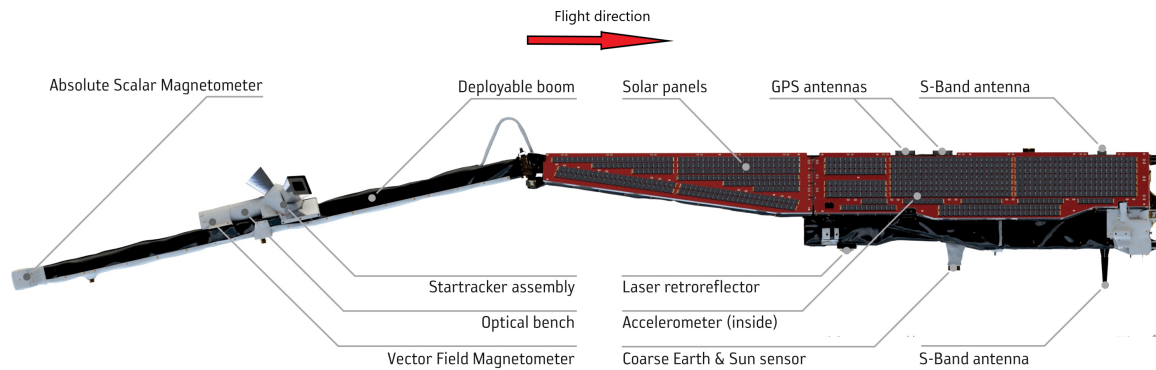


Figure 2.2.: Side view of the instruments onboard *Swarm* (reprinted from ESA/AOES Medialab¹).

observatory network, an important source of high-quality, global observations of Earth's magnetic field.

The first successful survey missions to monitor the global magnetic field from space was the Polar Orbiting Geophysical Observatories (POGO) satellite series (1965–1971), which collected field intensity (scalar) data. However, it was soon realized and later shown by [Backus \(1970\)](#) that scalar data alone is not enough to build robust global models of the geomagnetic field, even if the data is perfectly known. The ambiguity can be resolved by using the whole vector information of the magnetic field, which is, however, more challenging to measure than the field intensity. The first satellite mission to achieve vector measurements was Magsat (1979–1980). Since then, the satellite missions Ørsted (1999–2013), CHAMP (2000–2010) and presently the *Swarm* satellites (2013–today) have provided reliable magnetic vector data for the past 20 years, except for a 3-year gap period between the CHAMP and *Swarm* missions when only a small amount of intermittent Ørsted scalar data was available.

Swarm is a mini-satellite constellation mission within the Earth Explorer Opportunity Program of European Space Agency (ESA) and aims at mapping the geomagnetic field and its temporal evolution with unprecedented accuracy ([Olsen et al., 2006b](#); [Friis-Christensen et al., 2008](#)). It was launched in November 2013 and consists of the three satellites Swarm-A (Alpha), Swarm-B (Bravo) and Swarm-C (Charlie), which fly on two different orbital planes. Swarm-A and Swarm-C fly side-by-side in an orbital plane of 87.4° at a mean altitude of 450 km, whereas Swarm-B flies in a higher inclination orbit of 88° at a mean altitude of 530 km. This orbital configuration is a great advantage of *Swarm* because it allows simultaneous measurements of the geomagnetic field at different points in space, which improves the separation of the different sources contributing to Earth's magnetic field. In addition, differences between the measurements of close-by satellites can be utilized in a field gradient approach within geomagnetic field modelling ([Olsen et al., 2010a](#)). For example, east-west gradients of the field can be estimated with magnetic data from Swarm-A and Swarm-C, which fly with an east-west separation of about 1.4° .

All three *Swarm* satellites carry the same instrumentation onboard. Relevant for measuring the magnetic field are the absolute scalar magnetometer (ASM), the vector field magnetometer (VFM), the three-head star tracker (STR) assembly ([Jørgensen et al., 2003](#)). Fig. 2.2 shows the different instruments as a side view on one of the *Swarm* spacecrafts. The ASM takes absolute measurements

of the scalar field intensity, which are important for the correction and calibration of the vector field measurements taken by the VFM (*Tøffner-Clausen et al., 2016*). The STR assembly allows an accurate attitude determination, which is essential for determining correct vector components from the VFM observations. The ASM, VFM and STR assembly are mounted on a 5.1 m long, deployable boom, which places these instruments at sufficient distance from the spacecraft body. This is designed to minimize any magnetic disturbances due to the spacecraft with the aim of very high magnetic cleanliness.

Using satellites to map the global magnetic field has a number of advantages (*Olsen et al., 2010b*). Chief amongst them is that satellites in a near polar orbit allow a dense spatial sampling, which is important for studying the small length-scales in the geomagnetic field, in particular the lithospheric field. Another advantage is the fact that a single high quality instrument carries out the measurement globally, which avoids issues related to there being a multitude of measurement systems in ground observatories. At the same time, use of satellite-based observations is complicated by the mixing of spatial and temporal variations in the field measurements onboard the moving satellite along its orbit. And, it requires not only precise field measurements but also accurate knowledge of the rapidly changing magnetometer orientation.

In this thesis, I use magnetic satellite data from dedicated survey missions CHAMP and *Swarm*, as well as platform magnetometer data from the CryoSat-2 and GRACE satellites. Further details about the specific selections of data used and the processing applied prior to field modelling are given in Secs. 5.2 and 6.2.

2.2. Electrodynamic theory and potentials

In this section I introduce the theoretical framework for describing Earth's magnetic field.

2.2.1. Maxwell's equations and quasi-static approximation

The electric field \mathbf{E} and the magnetic field \mathbf{B} in a vacuum are described by Maxwell's equations (e.g. *Griffiths, 2014*, p. 342)

$$\nabla \cdot \mathbf{E} = \frac{\rho}{\epsilon_0} \quad (\text{Gauss's law}) \quad (2.3a)$$

$$\nabla \cdot \mathbf{B} = 0 \quad (\text{no name}) \quad (2.3b)$$

$$\nabla \times \mathbf{E} + \partial_t \mathbf{B} = \mathbf{0} \quad (\text{Faraday's law}) \quad (2.3c)$$

$$\nabla \times \mathbf{B} - \mu_0 \epsilon_0 \partial_t \mathbf{E} = \mu_0 \mathbf{J}, \quad (\text{Ampère's law with Maxwell's correction}) \quad (2.3d)$$

where ρ is the electric charge density and \mathbf{J} is the total electric current density, the sum of free and bounded currents. Further, ϵ_0 is the permittivity and μ_0 is the permeability of vacuum—both fundamental constants of nature. The arrangement of the terms differs from the traditional way of writing the Maxwell's equations to emphasize that the sources of the electric and magnetic field, shown on the left side, are ultimately charges and electric currents, shown on the right side. Maxwell's equations alone are not enough to uniquely determine the fields: they must be supplemented with

¹https://www.esa.int/ESA_Multimedia/Images/2012/11/Swarm_instruments_side_view

appropriate boundary conditions. For example, a suitable condition is to require that the fields vanish at large distance from localized charge and current distributions. In the theoretical case of charged planes or current lines that extend to infinity, one needs to invoke symmetry arguments to determine the fields. Together with the Lorentz force \mathbf{F}_L , according to which a particle with charge q and velocity \mathbf{v}_q experiences the force (e.g. [Schwartz, 2012](#), p. 131)

$$\mathbf{F}_L = q(\mathbf{E} + \mathbf{v}_q \times \mathbf{B}), \quad (2.4)$$

one can, in principle, solve any dynamics problem involving the interaction of electric charges and their motions.

When studying the geomagnetic field, the time-scales involved are sufficiently long that Eq. (2.3d) can be written in the quasi-static approximation as

$$\nabla \times \mathbf{B} = \mu_0 \mathbf{J}, \quad (\text{Ampère's law}) \quad (2.5)$$

where the displacement current $\mu_0 \epsilon_0 \partial_t \mathbf{E}$ is neglected ([Backus, 1986](#); [Sabaka et al., 2010](#)). In this approximation, the description of the magnetic field only depends on the distribution of electric currents, in particular whether or not $\mathbf{J} = \mathbf{0}$ in the region of interest. In the case of vanishing currents, the region is said to be source-free and the magnetic field can be represented by a scalar potential. Such is the case when considering measurements at ground observatories, which measure the magnetic field within the neutral atmosphere. If, on the other hand, electric currents exist in the region of interest, a more elaborate description involving toroidal and poloidal potentials is needed. This is the case for satellite-based measurements of the field in the F-layer of Earth's ionosphere ([Olsen, 1997](#)). The different ways of representing the magnetic field along these lines are described in the following.

2.2.2. Magnetic scalar potential

Consider a spherical shell $S(r_1, r_2) \subset \mathbb{R}^3$ with $0 < r_1 \leq r \leq r_2 < \infty$ bounded below and above by closed spherical surfaces at $r = r_1$ and $r = r_2$, respectively. Following the quasi-static approximation of the magnetic field and assuming that $S(r_1, r_2)$ is free of electric currents and magnetized material ($\mathbf{J} = \mathbf{0}$), all sources of the magnetic field must lie outside of $S(r_1, r_2)$. Under those conditions, Ampère's law in Eq. (2.5) states that the magnetic field is curl-free and can be expressed as the negative gradient of a scalar function ψ , the magnetic scalar potential (e.g. [Backus et al., 1996](#); [Jackson, 1999](#); [Griffiths, 2014](#); [Sabaka et al., 2010](#)), for a point $\mathbf{r} \in S(r_1, r_2)$

$$\mathbf{B} = -\nabla\psi. \quad (2.6)$$

Due to $\nabla \cdot \mathbf{B} = 0$ in Eq. (2.3b), ψ satisfies Laplace's equation

$$\nabla^2 \psi = 0 \quad (2.7)$$

subject to boundary conditions compatible with the magnetic field produced by the sources outside of $S(r_1, r_2)$. The solution of Laplace's equation are known as harmonic functions.

Note that the magnetic scalar potential can only exist in finite domains within which $\mathbf{J} = \mathbf{0}$ since

the magnetic field written in terms of a gradient field in all of space is incompatible with Eq. (2.5) and would require currents to vanish everywhere. Also note that a spherical shell is not only convenient for describing the space around Earth but is also suitable in the context of simply-connected regions, i.e. any closed curve in $S(r_1, r_2)$ can be contracted to a single point without leaving $S(r_1, r_2)$. This ensures that ψ is single-valued and well-behaved. In spherical coordinates Laplace's equation reads

$$\nabla^2\psi = \frac{1}{r^2}\partial_r(r^2\partial_r\psi) + \frac{1}{r^2\sin\theta}\partial_\theta(\sin\theta\partial_\theta\psi) + \frac{1}{r^2\sin^2\theta}\partial_\phi^2\psi = 0 \quad (2.8)$$

and has two linearly independent solutions

$$\psi = \psi^i + \psi^e, \quad (2.9)$$

where ψ^i is the internal part and ψ^e is the external part of the magnetic scalar potential. The two parts are infinite power series in r and r^{-1} scaled with a chosen reference radius a , typically the Earth's mean surface radius $a = 6371.2$ km, (e.g. [Backus et al., 1996](#); [Sabaka et al., 2010](#))

$$\psi^i(r, \theta, \phi, t) = a \sum_{n=1}^{\infty} \sum_{m=-n}^n \left(\frac{a}{r}\right)^{n+1} g_n^m(t) Y_n^m(\theta, \phi) \quad (2.10a)$$

$$\psi^e(r, \theta, \phi, t) = a \sum_{n=1}^{\infty} \sum_{m=-n}^n \left(\frac{r}{a}\right)^n q_n^m(t) Y_n^m(\theta, \phi). \quad (2.10b)$$

The internal part is due to sources within $r < r_1$, while the external part is due to sources confined to $r > r_2$. The expressions of the magnetic scalar potential involve the spherical harmonic functions

$$Y_n^m(\theta, \phi) \equiv \begin{cases} \cos(m\phi) \mathcal{P}_n^m(\cos\theta), & m \geq 0 \\ \sin(|m|\phi) \mathcal{P}_n^{|m|}(\cos\theta), & m < 0, \end{cases} \quad (2.11)$$

where the integers n and m are respectively the spherical harmonic degree and spherical harmonic order, g_n^m and q_n^m are the spherical harmonic coefficients of the internal and external parts, respectively, and \mathcal{P}_n^m are the associated Legendre polynomials defined by

$$\mathcal{P}_{n,m}(x = \cos\theta) = \frac{1}{2^n n!} (1-x^2)^{\frac{m}{2}} \frac{d^{n+m}}{dx^{n+m}} (x^2-1)^n \quad (2.12)$$

for $0 \leq m \leq n$ using the Schmidt semi-normalization given by

$$\mathcal{P}_n^m(\cos\theta) = \begin{cases} \mathcal{P}_{n,m}(\cos\theta), & m = 0 \\ \sqrt{\frac{2(n-m)!}{(n+m)!}} \mathcal{P}_{n,m}(\cos\theta), & m > 0, \end{cases} \quad (2.13)$$

which has been adopted by the Geomagnetism community as the conventional norm ([Winch et al., 2005](#)). When the spherical harmonics are combined with the radial dependence, they are referred to as solid harmonics. The spherical harmonic coefficients are also known as Gauss coefficients.

The spherical harmonics form a complete and orthogonal set of functions on the surface of a sphere. This formally includes the terms with $n = 0$, but in the case of Geomagnetism they can be

omitted from Eq. (2.10) since these terms vanish for the internal potential due to the divergence-free nature of the magnetic field or are constant for the external potential, thus, contributing nothing to the field. The spherical harmonic coefficients g_n^m and q_n^m follow from the boundary conditions. The orthogonality of the spherical harmonics can be expressed as

$$\langle Y_n^m, Y_{n'}^{m'} \rangle \equiv \frac{1}{4\pi} \int_0^\pi \int_0^{2\pi} Y_n^m(\theta, \phi) Y_{n'}^{m'}(\theta, \phi) \sin \theta d\theta d\phi = \frac{1}{2n+1} \delta_{nn'} \delta_{mm'}, \quad (2.14)$$

where $\langle \cdot, \cdot \rangle$ denotes the integral over the surface of a unit sphere and δ_{kl} is the Kronecker delta of the two indexes k and l defined by

$$\delta_{kl} = \begin{cases} 0, & k \neq l \\ 1, & k = l. \end{cases} \quad (2.15)$$

The total magnetic field in the source-free shell $S(r_1, r_2)$ can now be written, in correspondence to the two solutions of the potential, as the sum of internal and external parts

$$\mathbf{B} = -\nabla\psi^i - \nabla\psi^e = \mathbf{B}^i + \mathbf{B}^e. \quad (2.16)$$

After computing the gradients in spherical coordinates and introducing the more traditional notation of $h_n^m \equiv g_n^{-m}$ and $s_n^m \equiv q_n^{-m}$ for $m \geq 0$, the components of the internal magnetic field can be written as

$$\begin{aligned} B_r^i &= (n+1) \sum_{n=1}^{\infty} \sum_{m=0}^n \left(\frac{a}{r}\right)^{n+2} [g_n^m \cos(m\phi) + h_n^m \sin(m\phi)] \mathcal{P}_n^m(\cos \theta) \\ B_\theta^i &= - \sum_{n=1}^{\infty} \sum_{m=0}^n \left(\frac{a}{r}\right)^{n+2} [g_n^m \cos(m\phi) + h_n^m \sin(m\phi)] \frac{d\mathcal{P}_n^m(\cos \theta)}{d\theta} \\ B_\phi^i &= \sum_{n=1}^{\infty} \sum_{m=0}^n \left(\frac{a}{r}\right)^{n+2} m [g_n^m \sin(m\phi) - h_n^m \cos(m\phi)] \frac{\mathcal{P}_n^m(\cos \theta)}{\sin \theta} \end{aligned} \quad (2.17)$$

and the components of the external magnetic field as

$$\begin{aligned} B_r^e &= -n \sum_{n=1}^{\infty} \sum_{m=0}^n \left(\frac{r}{a}\right)^{n-1} [q_n^m \cos(m\phi) + s_n^m \sin(m\phi)] \mathcal{P}_n^m(\cos \theta) \\ B_\theta^e &= - \sum_{n=1}^{\infty} \sum_{m=0}^n \left(\frac{r}{a}\right)^{n-1} [q_n^m \cos(m\phi) + s_n^m \sin(m\phi)] \frac{d\mathcal{P}_n^m(\cos \theta)}{d\theta} \\ B_\phi^e &= \sum_{n=1}^{\infty} \sum_{m=0}^n \left(\frac{r}{a}\right)^{n-1} m [q_n^m \sin(m\phi) - s_n^m \cos(m\phi)] \frac{\mathcal{P}_n^m(\cos \theta)}{\sin \theta}. \end{aligned} \quad (2.18)$$

2.2.3. Poloidal and toroidal potentials

Instead of the source-free region described above, the spherical shell $S(r_1, r_2) \subset \mathbb{R}^3$ with $0 < r_1 \leq r \leq r_2 < \infty$ is allowed to carry electric currents such that the curl of \mathbf{B} is non-zero. Irrespective of the local currents, the divergence of \mathbf{B} is zero everywhere in space thanks to Eq. (2.3b). Any solenoidal vector field, i.e. with vanishing divergence such as \mathbf{B} , can be decomposed into poloidal

and toroidal scalar potentials, T and P , written as (e.g. [Backus, 1986](#); [Sabaka et al., 2010](#))

$$\mathbf{B} = \nabla \times \nabla \times P \mathbf{r} + \nabla \times T \mathbf{r} = \mathbf{B}^{\text{pol}} + \mathbf{B}^{\text{tor}} \quad (2.19)$$

where \mathbf{B}^{pol} and \mathbf{B}^{tor} are the poloidal and toroidal components, respectively. This decomposition, also known as the Mie representation, is unique provided the average value of the potentials over any spherical surface in the region of interest is zero. Note that the toroidal field can also be written as

$$\mathbf{B}^{\text{tor}} = \nabla \times T \mathbf{r} = -\mathbf{r} \times \nabla T, \quad (2.20)$$

and the minus sign in the last expression is sometimes absorbed into the toroidal potential. As with the scalar magnetic potential ψ , the poloidal and toroidal scalar potentials can be decomposed into spherical harmonics

$$P(r, \theta, \phi, t) = \sum_{n=1}^{\infty} \sum_{m=-n}^n P_n^m(r, t) Y_n^m(\theta, \phi) \quad (2.21a)$$

$$T(r, \theta, \phi, t) = \sum_{n=1}^{\infty} \sum_{m=-n}^n T_n^m(r, t) Y_n^m(\theta, \phi), \quad (2.21b)$$

where P_n^m and T_n^m are the poloidal and toroidal coefficients of the expansion, respectively.

In the quasi-static approximation, the electric current is also a solenoidal vector field since $\nabla \cdot \mathbf{J} = \nabla \cdot \left(\frac{1}{\mu_0} \nabla \times \mathbf{B} \right) = 0$ everywhere in space. Hence, \mathbf{J} has its own poloidal-toroidal decomposition, $\mathbf{J} = \mathbf{J}^{\text{tor}} + \mathbf{J}^{\text{pol}}$, which offers a useful way of interpreting \mathbf{B}^{pol} and \mathbf{B}^{tor} in terms of their sources. It can be shown that the toroidal currents \mathbf{J}^{tor} produce a poloidal magnetic field everywhere in space whereas the poloidal currents \mathbf{J}^{pol} give only rise to a local toroidal magnetic field ([Sabaka et al., 2010](#)). Therefore, \mathbf{B}^{tor} is always confined to the conductor carrying the electric current. Conversely, the local magnetic field is sensitive to all toroidal currents and the local poloidal currents but not to the remote poloidal currents. In the context of the magnetic field inside the current-carrying shell $S(r_1, r_2)$, the poloidal component in Eq. (2.19) may be further subdivided such that

$$\mathbf{B} = \mathbf{B}^{\text{pol},i} + \mathbf{B}^{\text{pol},e} + \mathbf{B}^{\text{pol},sh} + \mathbf{B}^{\text{tor}}, \quad (2.22)$$

where $\mathbf{B}^{\text{pol},i}$ is the poloidal field produced by the internal electric currents ($r < r_1$), $\mathbf{B}^{\text{pol},e}$ is the poloidal field produced by the external electric currents ($r > r_2$), $\mathbf{B}^{\text{pol},sh}$ is the poloidal field of the toroidal currents in $S(r_1, r_2)$, and \mathbf{B}^{tor} is the toroidal magnetic field due to the local poloidal electric currents at the point of interest ($\mathbf{r} \in S(r_1, r_2)$). If the electric currents in the shell are zero, $\mathbf{B}^{\text{pol},sh}$ and \mathbf{B}^{tor} disappear while $\mathbf{B}^{\text{pol},i}$ and $\mathbf{B}^{\text{pol},e}$ are the only non-zero terms since they are produced by sources outside of the shell. This situation is identical with the one discussed in Sec. 2.2.2 regarding the magnetic scalar potential. Therefore, the terms $\mathbf{B}^{\text{pol},i}$ and $\mathbf{B}^{\text{pol},e}$ can be identified as

$$\mathbf{B}^{\text{pol},i} = -\nabla \psi^i, \quad \mathbf{B}^{\text{pol},e} = -\nabla \psi^e, \quad (2.23)$$

whereas $\mathbf{B}^{\text{pol},sh}$ and \mathbf{B}^{tor} are represented by poloidal and toroidal potentials (Eq. 2.19), respectively.

Finally, a unique decomposition of the magnetic field on a specific spherical surface $S(r_0)$ of radius

$r = r_0$ surrounded by sources can be introduced in the form of ([Sabaka et al., 2010](#))

$$\mathbf{B} = \mathbf{B}^{\text{pol},i} + \mathbf{B}^{\text{pol},e} + \mathbf{B}^{\text{tor}} = -\nabla\psi^i - \nabla\psi^e + \nabla \times T\mathbf{r}, \quad (2.24)$$

where $\mathbf{B}^{\text{pol},i}$ and $\mathbf{B}^{\text{pol},e}$ are due to all sources below and above $r = r_0$, respectively. In contrast to Eq. (2.22), $\mathbf{B}^{\text{pol},\text{sh}}$ disappears here since the toroidal currents in the current-carrying shell are now accounted for by $\mathbf{B}^{\text{pol},i}$ and $\mathbf{B}^{\text{pol},e}$.

Spatial power spectra are a convenient tool for looking at the different components that contribute to Earth's magnetic field. Thanks to the orthogonality of the spherical harmonics, the average squared magnitude of the magnetic field on $S(r_0)$ can be written as (e.g. [Sabaka et al., 2010](#))

$$\begin{aligned} \langle |\mathbf{B}|^2 \rangle_{S(r_0)} &= \frac{1}{4\pi} \int_0^\pi \int_0^{2\pi} |\mathbf{B}(r_0, \theta, \phi)|^2 dS \\ &= W^i(r_0) + W^e(r_0) + W^{\text{tor}}(r_0), \end{aligned} \quad (2.25)$$

where $dS = \sin\theta d\theta d\phi$ and

$$W^i(r_0) = \sum_{n=1}^{\infty} W_n^i(r_0), \quad W^e(r_0) = \sum_{n=1}^{\infty} W_n^e(r_0), \quad W^{\text{tor}}(r_0) = \sum_{n=1}^{\infty} W_n^{\text{tor}}(r_0) \quad (2.26)$$

with

$$\begin{aligned} W_n^i(r_0) &= (n+1) \left(\frac{a}{r_0}\right)^{2n+4} \sum_{m=-n}^n (g_n^m)^2 \\ W_n^e(r_0) &= n \left(\frac{r_0}{a}\right)^{2n-2} \sum_{m=-n}^n (q_n^m)^2 \\ W_n^{\text{tor}}(r_0) &= \frac{n(n+1)}{2n+1} \sum_{m=-n}^n (T_n^m(r_0))^2. \end{aligned} \quad (2.27)$$

2.3. Sources of Earth's magnetic field

The sources of Earth's magnetic field vary in their location within the Earth system, in the physical processes that give rise to a magnetic field, and in the strength and spatiotemporal behavior of the produced magnetic field. Singling out the different contributions contained in a magnetic field measurement is known as source separation and represents an important goal of geomagnetic field modelling. Fig. 2.3 summarizes the most important sources and their location in space. Traditionally, the sources below Earth's surface are referred to as internal sources and those above as external sources. Internal sources include the electric currents in the metallic core, the mantle and crust, and the magnetized rock in the uppermost layer of the solid Earth. Among the external sources are electric currents located above the neutral atmosphere in the ionosphere (90–1000 km) and in the magnetosphere (above 10,000 km). A brief overview of the different sources is given in the following.

2.3.1. Core field

The Earth's core is a metallic sphere located at more than 2900 km below Earth's surface. It consists of the solid inner core and the liquid outer core. It is believed that the outer core is rapidly moving

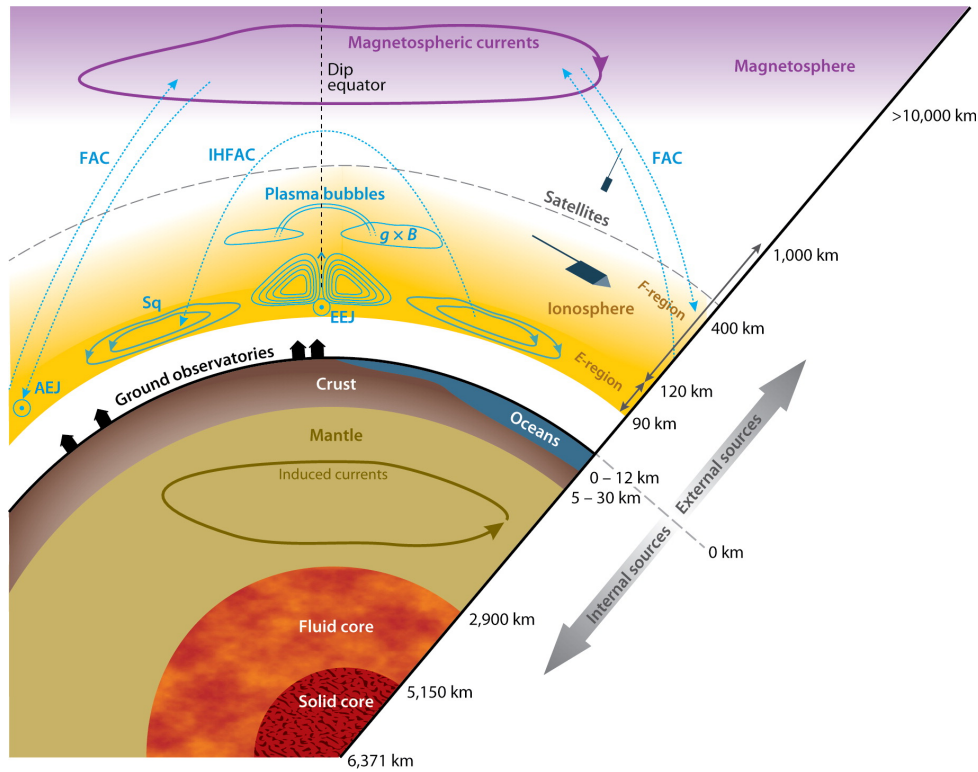


Figure 2.3.: Schematic illustration of the sources that contribute to Earth's magnetic field. Abbreviations stand for field-aligned currents (FAC), auroral electrojet (AEJ), equatorial electrojet (EEJ), Solar quiet (Sq), and inter-hemispheric field-aligned currents (IHFAC) (reprinted from [Olsen and Stolle, 2012](#)).

due to convection driven by the cooling of the planet and chemical differentiation at the inner core boundary ([Finlay et al., 2010](#)). At the same time, the Earth's rotation creates strong Coriolis forces, which constrain and organize the flow. The motion of the core fluid in the local magnetic field induces an electromotive force, which drives electric currents and reinforces the magnetic field. Motional induction in this way constantly converts the kinetic energy of the fluid motion into electromagnetic energy and, thus, maintains the magnetic field against dissipation. It is a self-sustaining dynamo, called the Geodynamo.

The strong electric currents that circulate in the Earth's core give rise to the core field, which is the most intense component of the Earth's magnetic field. The dominant role of the core field is evident in the spatial power spectrum of the internal field at the Earth's surface as given by the CHAOS model ([Fig. 2.4](#)). The large-scale portion of the spectrum, say $n \leq 15$, can be attributed to the core field, whereas the small-scale portion ($n > 15$) is due to the lithospheric field. However, one should be keep in mind that a crude distinction between the two sources based on the spatial power spectrum alone is an approximation, especially around degrees 12 to 18. In reality, the core field merely dominates the internal field on the largest length-scales, masking the large-scale lithospheric field, whereas the lithospheric field dominates the internal field at small length-scales, masking the small-scale core field.

At the Earth's surface the core field has mostly a dipolar configuration that is slightly tilted away from Earth's rotational axis. [Fig. 2.5](#) shows the estimates of the radial component of the internal field up to spherical harmonic degree 13 at the Earth's surface based on the CHAOS model. The field strength ranges from 30,000 nT at the Equator to 60,000 nT at the poles in the Northern

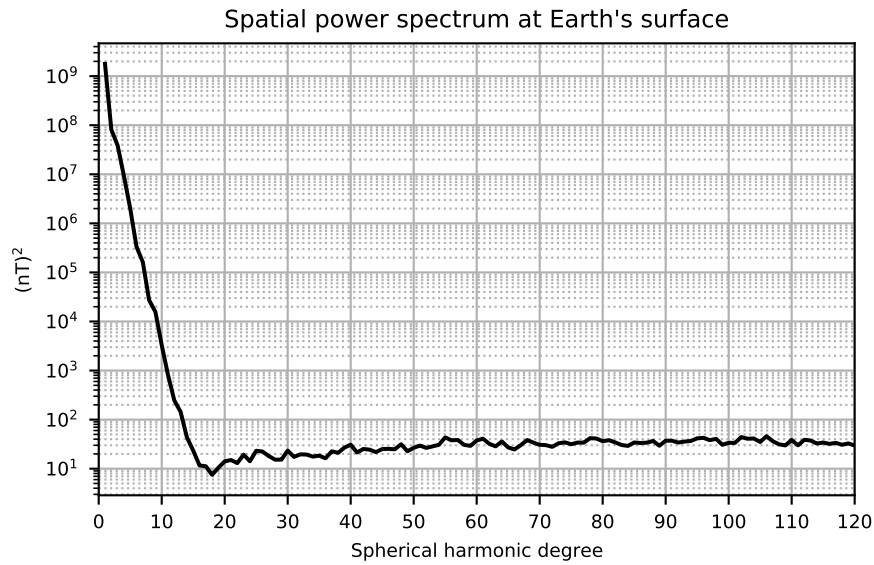


Figure 2.4.: Spatial power spectrum of the internal magnetic field at Earth's surface in 2019.0 as given by CHAOS-7.4.

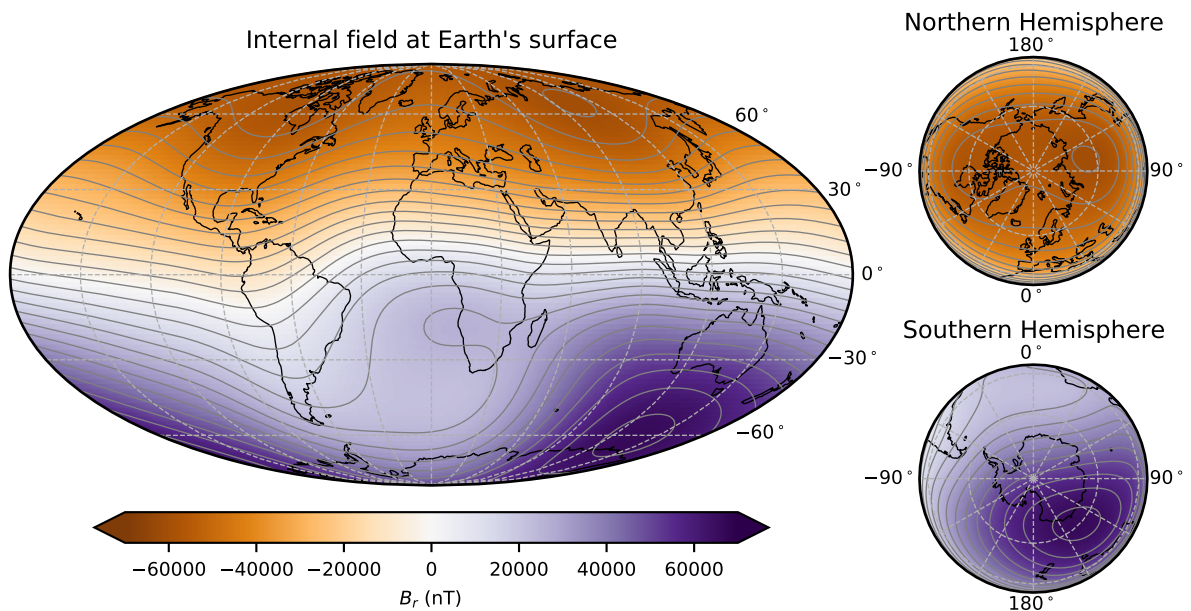


Figure 2.5.: Radial component of the internal field for spherical harmonic degrees $n \leq 13$ at Earth's surface in 2019.0 as given by CHAOS-7.4. The solid grey lines are the contours of the radial field strength every 5000 nT.

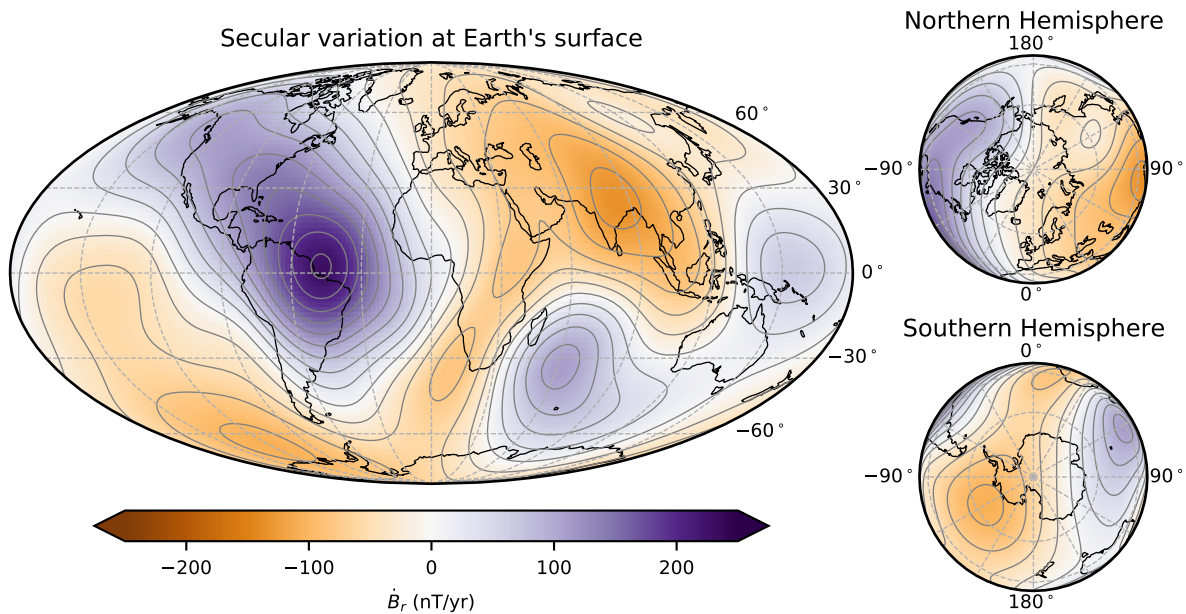


Figure 2.6.: Radial component of the SV for spherical harmonic degree $n \leq 16$ at Earth's surface in 2019.0 as given by CHAOS-7.4. The solid grey lines are the contours of the radial SV every 25 nT/yr.

and Southern hemispheres. In addition to the dipole, the core field contains significant non-dipolar components. For example, when looking at the South Atlantic region, the field is found to be relatively weak. This feature is therefore known as the South Atlantic Anomaly (SAA). However, at and above Earth's surface, such non-dipolar components that originate in the core decrease rapidly in strength as the considered length-scales becomes smaller.

When snapshots of the large-scale internal field are compared in time, it becomes clear that it is slowly evolving. The change is small but appreciable over decades and centuries and is, therefore, referred to as Secular Variation (SV). Only slow changes are observable at the Earth's surface since signals with periods shorter than a few months originating in the core are screened by the weakly conducting mantle. Fig. 2.6 shows a map of the estimates of the radial SV in 2019.0 at Earth's surface as given by the CHAOS model. The SV pattern of positive and negative patches reflects the observed changes in the position and amplitude of the features in the core field and are associated with phenomenon such as the westward expansion of the SAA (e.g. [Finlay et al., 2020](#)) and the movement of the north magnetic pole towards Siberia ([Livermore et al., 2020](#)).

At 3485 km from Earth's center at the core-mantle boundary (CMB), the SV has features that are much smaller in length-scale than at the Earth's surface. This can be seen in Fig. 2.7, which shows a map of the estimates of the radial SV in 2019.0 at the CMB as given by the CHAOS model. Noteworthy are the non-zonal SV patches that can be found in the northern polar region. For studies of the outer core dynamics (e.g. [Livermore et al., 2017](#)), it is important to establish that these patches in the polar region are robust. This question is revisited in Chapter 6.

Taking the second derivative of the core field in time gives the Secular Acceleration (SA). The fact that it changes on shorter time-scales than the SV is most prominently reflected in the occurrence of geomagnetic jerks, which are abrupt changes in linear trends in the SV due to a jump and sign change in the SA (e.g. [Olsen and Manda, 2007](#); [Manda et al., 2010](#)). Geomagnetic jerks are thought to be related to the fast changes of the liquid outer core and present an opportunity to study the core

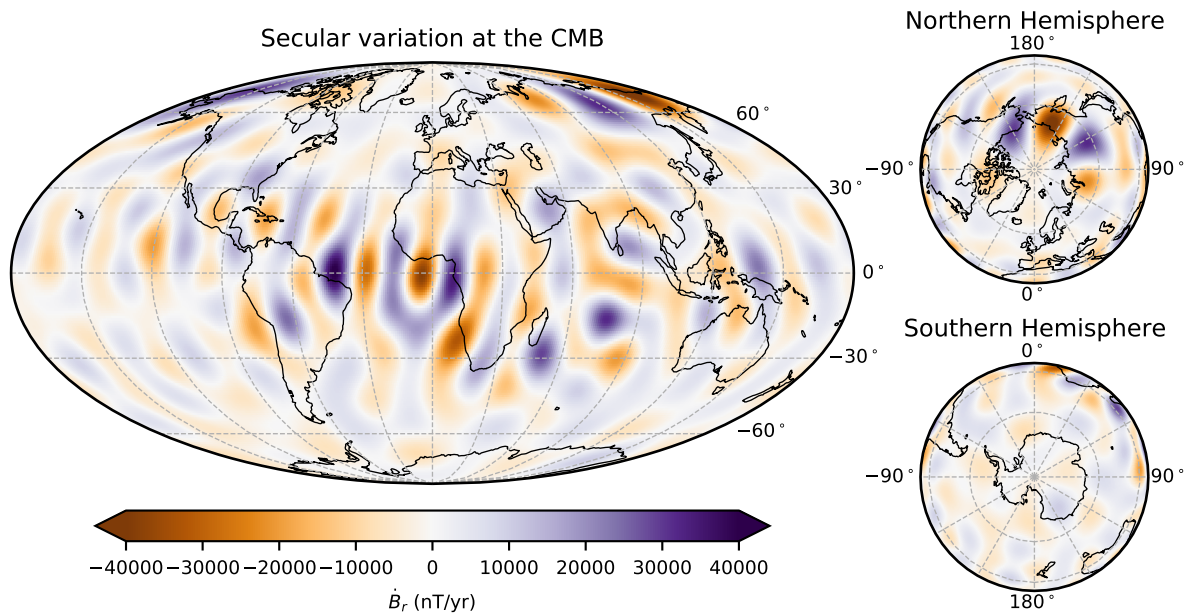


Figure 2.7.: Radial component of the SV for spherical harmonic degree $n \leq 16$ at the CMB in 2019.0 as given by CHAOS-7.4.

dynamics with magnetic observations.

Fig. 2.8 shows the spatial power spectrum of the core field, SV, and the SA at the Earth's surface (left) and the CMB (right) in 2019.0 as given by the CHAOS model. The spectra of all components are mostly decreasing with larger spherical harmonic degree at the Earth's surface, whereas considerable power is contained in the small length-scales closer to the source at the CMB. This behaviour is a geometric effect; small length-scale contributions are attenuated with increasing distance from the source region, here the outer core. However, the fact that the internal field spectrum plateaus above $n = 16$ at the Earth's surface and sharply increases above $n = 14$ at the CMB indicates a clear contamination with lithospheric field contributions at and above this degree.

2.3.2. Lithospheric and ocean-induced fields

The Earth's lithosphere contains significant amounts of ferromagnetic minerals. Rocks rich in such minerals can carry both a remanent and an induced magnetization. While the induced magnetization is proportional to the surrounding magnetic field, the remanent magnetization is fixed and is a record of the local magnetic field at the time the minerals were formed.

The lithospheric field is notably different from the core field in terms of the spatial scales involved at Earth's surface. While the core field is the most intense part of the internal field at large length-scales, the lithospheric field contributes to all length-scales and dominates when spatial scales below approximately 2000 km are considered. This is evident when looking at an example of a lithospheric field model, LCS-1 ([Olsen et al., 2017](#)), in Fig. 2.9. At the Earth's surface, the field strength ranges from a few tens of nT to several thousand nT. However, at satellite altitude (400–1000 km) the lithospheric field strength is much weaker, which limits the resolution of the small-scale contributions that can be reliably retrieved from satellite data. Since the temporal changes of the remanent part of the lithospheric field happen on geological time-scales, which are much longer than the time period that are of interest to the modelling of Earth's magnetic field, it is often regarded as static. Although

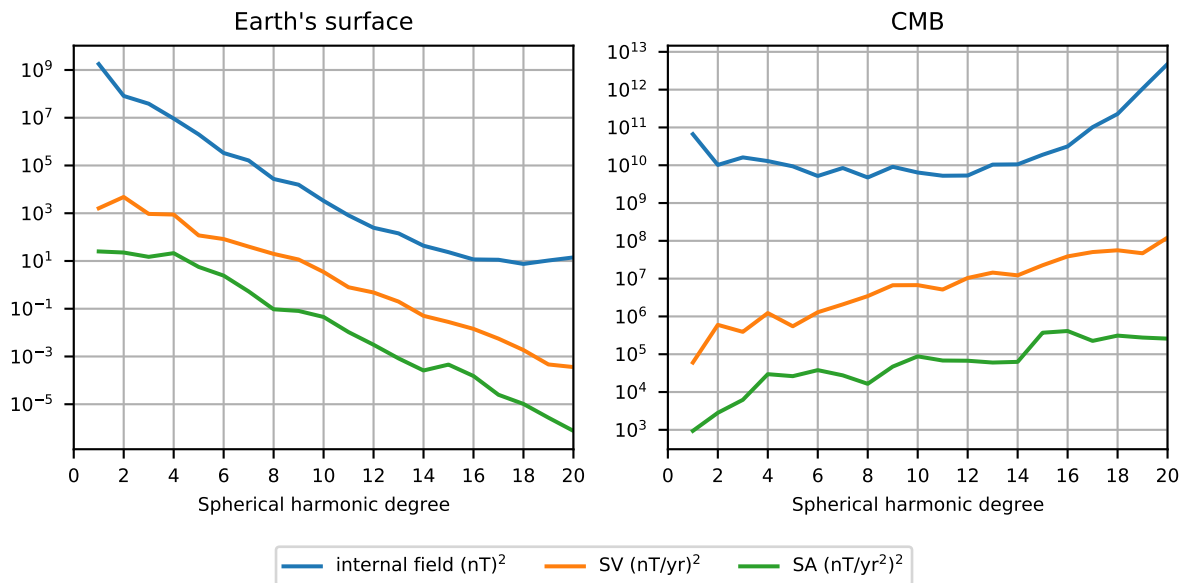


Figure 2.8.: Spatial power spectrum of the internal field (blue), SV (orange) and SA (green) at Earth's surface (left) and the CMB (right) in 2019.0 as given by CHAOS-7.4.

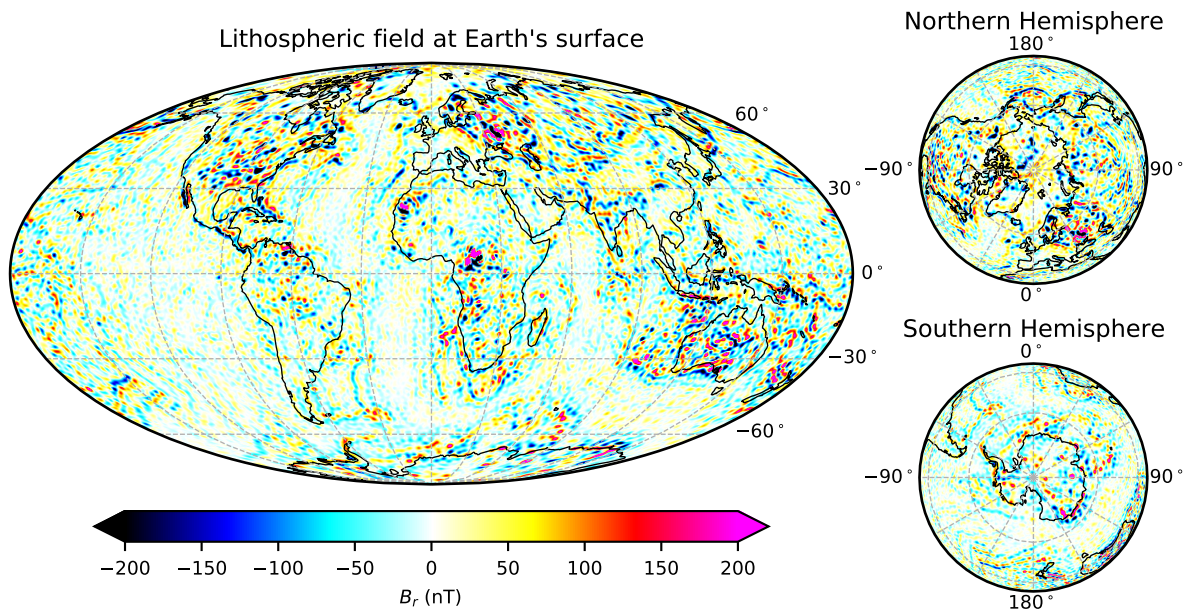


Figure 2.9.: Radial component of the lithospheric field at Earth's surface as is given by the LCS-1 model for spherical harmonic degrees $n \leq 185$ (Olsen *et al.*, 2017).

the induced lithospheric field changes along with the magnetizing core field, such changes are smaller than can presently be observed ([Thébault et al., 2009](#)).

Apart from the magnetized rocks, the oceans also contribute to the magnetic field through motional induction since the electrically conducting water of the oceans is moving within the Earth's magnetic field. In addition, electric currents are produced in the conducting mantle by the fast variations of the external magnetic field, which is observable as the internally induced counterpart (e.g. [Manoj et al., 2006](#); [Maus, 2007](#); [Kuvshinov, 2008](#)).

2.3.3. Ionospheric and magnetospheric fields

The Earth's ionosphere and magnetosphere are regions where strong electric currents circulate primarily due to the interaction between the Earth's internal magnetic field in space and the solar wind. Those electric currents are very sensitive to changes in the magnetosphere-solar wind coupling and, thus, produce a complex and dynamic magnetic field, which is commonly referred to as the Earth's external magnetic field.

The solar wind is a stream of charged particles emitted from the sun, which carries with it the solar magnetic field that constitutes the IMF. Under the frozen-flux approximation, which is relevant for good electrical conductors such as plasmas, the solar wind plasma cannot pass through the plasma frozen onto the Earth's magnetic field in the near-Earth space but, instead, flows around it thus defining the outer edge of the magnetosphere, the magnetopause. The antisunward directed solar wind gives the magnetosphere its shape, pushing the magnetopause closer to Earth on the side facing the sun while dragging it out into a tail-like shape, the magnetotail, on the opposite side. The deformation of the magnetosphere is associated with electric currents, the Chapman-Ferraro currents, which flow from dawn to dusk along the sunward portion of the magnetopause and from dusk to dawn along the magnetotail magnetopause ([Chapman and Ferraro, 1931](#)). In addition, there are cross-tail currents flowing from dawn to dusk in the equatorial plane of the magnetotail, where the magnetic field reverses its direction from sunward in the northern part to antisunward in the southern part. Moreover, the magnetosphere closer to the Earth is composed of hot plasma, which due to the dipolar configuration of the internal magnetic field is associated with a westward flowing ring current ([Chapman and Ferraro, 1931, 1941](#)). The magnetopause currents, the cross-tail currents and the ring currents are assumed to be the main sources of magnetospheric origin that contribute to the Earth's magnetic field.

The conditions of the frozen-flux approximation do not always hold. In particular, at the sun-facing side of the magnetopause during southward IMF conditions, magnetic reconnection ([Treumann and Baumjohann, 1997](#)) can occur and create open magnetic field lines, i.e. field lines with one end connected to the Earth and the other to the IMF. The open field lines are moved along with the solar wind past the poles towards the magnetotail. In the equatorial plane of the magnetotail, the open field lines are merged through magnetic reconnection and carried sunward back to the dayside of the magnetosphere, completing a full cycle—the Dungey cycle ([Dungey, 1961](#)). In the course of the cycle, the footprints of the field lines undergo a similar circulation in the ionosphere. Here, the open field lines drift across the polar cap from the dayside to the nightside, followed by a sunward drift of the closed field lines at auroral latitudes (between 65–70° dipole latitude) back to the dayside. The ionospheric plasma primarily follows this convection pattern but is slowed down due to collisions

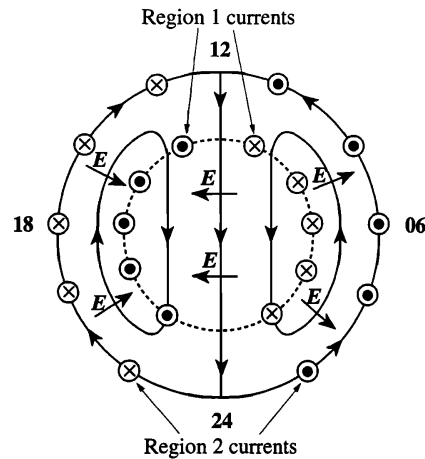


Figure 2.10.: Schematic of the Dungey cycle flow in the northern polar ionosphere. Noon is at the top (12), midnight at the bottom (24), dawn on the right (06) and dusk on the left (18). The directed solid lines indicate the plasma flow, the dashed circle marks the polar cap boundary. The Pedersen currents flow in the direction of \mathbf{E} , while the Hall currents circulate similar to the plasma flow but in opposite direction. The poleward region of the upward (\odot) and downward (\otimes) field-aligned currents are the R1 currents, whereas the equatorward region of field-aligned currents are the R2 currents (reprinted from [Cowley, 2000](#)).

with the background population of neutrals in the ionosphere.

Considerations of charged particle motions in a collisional plasma shows that the drag on the ionospheric plasma is different for ions and electrons, leading to a differential drift and associated electric currents (e.g. [Cowley, 2000](#)). The strength of the currents is a function of the plasma density and the collision frequency with neutral particles, which in turn depends on the density of the neutral particles. Since appreciable plasma densities are found in the ionosphere (above 90 km) and the density of neutral particles quickly decreases with height, the currents maximize in the lower ionosphere, within the ionospheric E-layer. The currents have a component in the direction of the electric field ($\parallel \mathbf{E}$), called Pedersen currents, and another directed antiparallel to the plasma flow ($\parallel -\mathbf{E} \times \mathbf{B}$), called Hall currents. The Hall currents flow antisunward in the polar cap and compose the auroral electrojet (AEJ) in the auroral oval, which consists of the westward auroral electrojet on the dawn side and the eastward auroral electrojet on the dusk side. While the Hall currents, assuming uniform conductance, circulate in closed loops similar to the plasma flow, the Pedersen currents diverge and converge within the ionosphere. This implies that field-aligned currents must exist to close the Pedersen currents and, during times of non-uniform conductance, ensure closure of the Hall currents.

The field-aligned currents, also known as Birkeland currents ([Birkeland, 1908](#)), couple the polar ionosphere with the magnetopause and inner magnetosphere. At the polar cap boundary, the converging and diverging Pedersen currents, due to the shear in the plasma flow, produce field-aligned currents, which are upward at dusk and downward at dawn. These currents are referred to as region 1 (R1) currents ([Iijima and Potemra, 1976](#)). A similar system of field-aligned currents, termed region 2 (R2) currents, can be found at the equatorward edge of the convection pattern but opposite in polarity to the R1 currents (Fig. 2.10). In the ionospheric F-layer (120–1000 km), the field-aligned currents produce a magnetic field that take the form of toroidal-poloidal contributions in satellite-based measurements of Earth's magnetic field.

Moreover, the currents in the midnight sector on the nightside of the aural oval are found to undergo intermittent enhancements in the westward direction, known as substorms ([Akasofu and Chapman, 1961](#); [Akasofu, 1964](#)). This intensified westward current couples to the magnetotail through a pair of field-aligned currents on either side of the local midnight, forming a pattern that is referred to as the substorm current wedge ([Kepko et al., 2015](#), and references therein).

Turning to non-polar latitudes, ionospheric electric currents driven by the difference in solar heating on the day and nightside produce daily variations of the Earth's magnetic field, known as solar quiet daily variation (Sq) ([Yamazaki and Maute, 2016](#)). The Sq current system is large-scale, approximately the size of the Earth's dayside but confined to the ionospheric E-layer. It consists of a counter-clockwise vortex on the Northern Hemisphere and a clockwise vortex on the Southern Hemisphere. The currents have a strong eastward component along the dayside dip equator within a $\pm 4^\circ$ dipole latitude, which is typically referred to as the equatorial electrojet (EEJ). Furthermore, the asymmetry in the driving processes and ionospheric conductivities between the two vortices leads to inter-hemispheric field-aligned currents (IHFAC) (Fig. 2.3). Although the Sq is primarily located on the dayside, the Earth-induced counterpart may also lead to significant magnetic contributions on the nightside, which has implications for internal field modelling when using dark-time selection criteria for the magnetic data ([Olsen et al., 2005a](#)).

2.4. Geomagnetic activity indices

Geomagnetic activity indices are frequently employed to quantify and to empirically study the variations of the magnetic field associated with the ionosphere-magnetosphere system in response to the solar wind driving. The indices are usually derived from magnetic data collected by the global network of ground observatories but differ in the steps involved in the processing of these data. As a result, the different current systems in the near-Earth space are reflected by different indices. However, inasmuch as the observed magnetic field is a superposition of all sources, a single index also contains contributions from current systems it was not designed to monitor, making the interpretation sometimes difficult ([Lockwood, 2013](#)). There are also indices that are not based on magnetic observations but are useful proxies of geomagnetic activity. Such is the case for the $F_{10.7}$ -index, which is often used to follow long-term variations in the solar activity level and, therefore, the driving behind the geomagnetic activity.

Geomagnetic activity indices play an important role in geomagnetic field modelling, providing data selection criteria and a temporal parameterization of external magnetic field variations. The most important indices are summarized below.

2.4.1. K_p -index

The K_p -index is a widely used 3-hourly index, which provides a global measure of the geomagnetic disturbance level (e.g. [Kauristie et al., 2017](#); [Matzka et al., 2021](#)). It is derived by the German Research Centre for Geosciences (GFZ) using the horizontal magnetic components from, presently, 13 ground observatories at sub-auroral latitudes. The details of the derivation of the index are described in [Matzka et al. \(2021\)](#). The index measures the disturbance level on a quasi-logarithmic scale ranging in steps of one third from 0 (most quiet) to 9 (most disturbed) every 3-hour UT interval

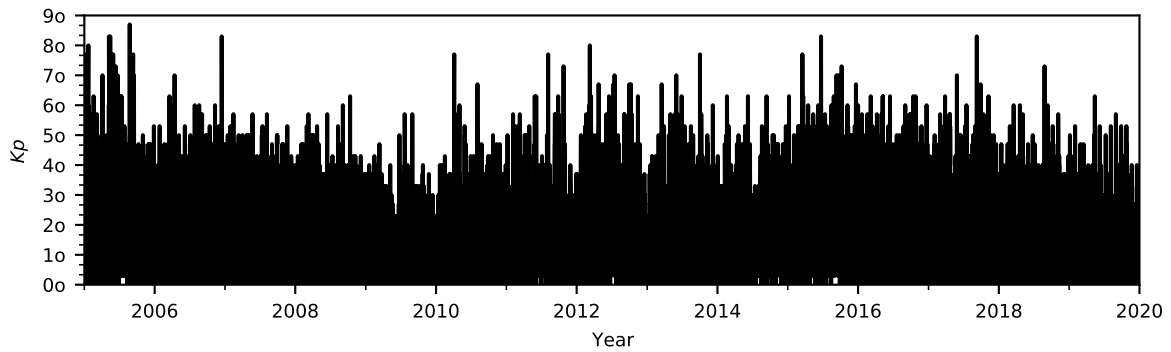


Figure 2.11.: Time series of the Kp -index from 2005.0 to 2020.0.

of a day (00–03, 03–06, . . . , 21–24 UT). The scale is often written in a symbolic notation using 0o, 0+, 1-, . . . , 9-, 9o, where the symbol "o" stands for using the integer value as is, "+" for adding one third to the integer value, and "-" for subtracting one third from the integer value. In geomagnetic field modelling, the Kp -index is used to select magnetically quiet-time data by allowing only data that are below a limit, say $Kp \leq 2o$. Fig. 2.11 presents a time series of the Kp -index from 2005.0 to 2020.0. The Kp -index and other parameters regarding the solar wind and interplanetary magnetic field can be obtained from the NASA/GSFC's OMNI dataset (King and Papitashvili, 2005) through OMNIWeb².

2.4.2. Dst -index and RC -index

The Dst -index (Sugiura and Kamei, 1991) and related indices, in particular the RC -index (Olsen et al., 2014), provide a quantitative measure of the disturbance in the horizontal component of the geomagnetic field at equatorial and mid latitudes. During magnetic storms, the horizontal component is found to undergo strong variations in time, most notably a sharp decrease associated with the main phase of the storm. This can be crudely represented, neglecting departures from axisymmetry that can in reality be considerable during storms, by a disturbance field that is axially symmetric with respect to Earth's dipole axis but opposite in sign. It is assumed that the disturbance field is mostly produced by the ring currents but also contains small contributions from the magnetopause currents and the cross-tail currents in the magnetotail.

The construction of the Dst -index involves the removal of a time-dependent baseline, which in the original version of the index can have discontinuities since it consists of fitting piecewise polynomials. Those discontinuities are small and can be neglected for studies of magnetically disturbed times. But they make the Dst -index less suitable to parameterize the quiet-time magnetospheric field for internal field modelling. This led Olsen et al. (2014) to derive a new hourly index, called RC -index, giving special attention to the stability of the baseline. The RC -index is currently constructed using 14 ground observatories globally distributed at mid and low latitudes. Only the data of the observatories on the nightside during the hour under consideration contribute to the index value of that hour. Details of the derivation are given by Olsen et al. (2014) and Kauristie et al. (2017). In a final step, the RC -index is separated into an internal (induced) and external (inducing) component, $RC(t) = RC_{\text{int}}(t) + RC_{\text{ext}}(t)$, using the Q -response function (e.g. Olsen, 1999) of an electrical

²<https://omniweb.gsfc.nasa.gov/ow.html>

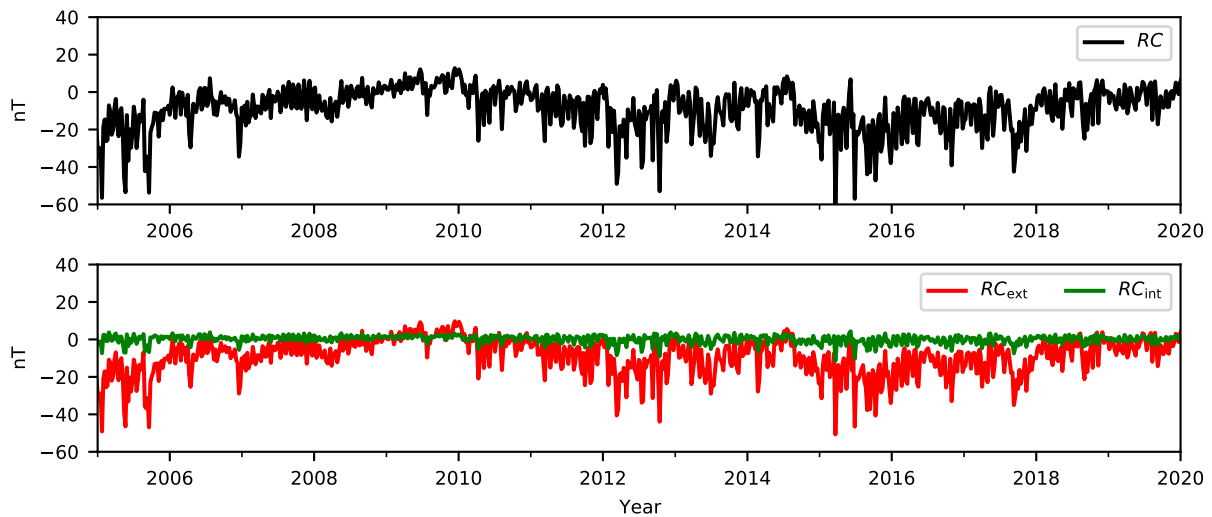


Figure 2.12.: Time series of one-week averages of the hourly RC -index (black) and the separated parts RC_{ext} (red) and RC_{int} (green) from 2005.0 to 2020.0.

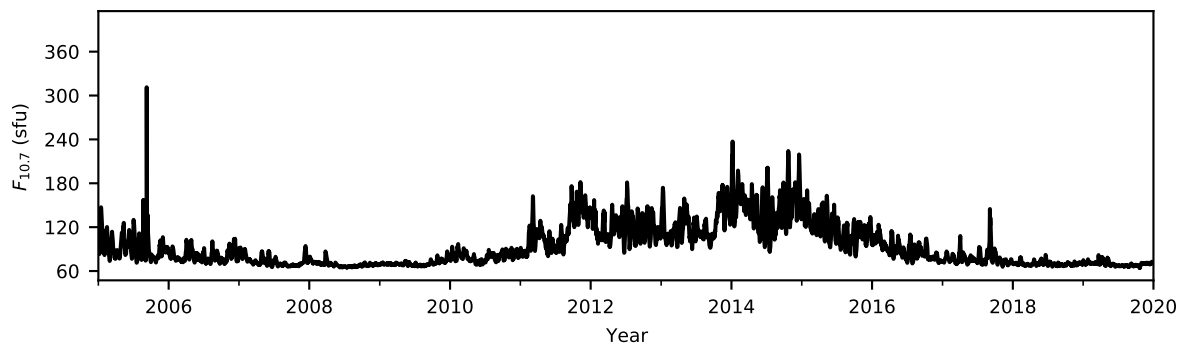


Figure 2.13.: Time series of the daily $F_{10.7}$ -index from 2005.0 to 2020.0, which corresponds to roughly 1.5 solar cycles. Solar minimum was reached around 2009 and the solar maximum around 2014.

conductivity model of the Earth. This step is important for modelling the magnetospheric signal at satellite altitude. Fig. 2.12 shows one-week averages of the RC -index, RC_{ext} and RC_{int} from 2005.0 to 2020.0. The hourly RC -index is available at Technical University of Denmark (DTU) Space³.

2.4.3. $F_{10.7}$ -index

The sun has a profound influence on the near-Earth magnetic environment. It is not only the driver of the solar wind but also controls the ionization level in the Earth's ionosphere and with it the strength of the ionospheric-magnetospheric coupling. The solar activity level changes in time and can be monitored in various ways. The $F_{10.7}$ -index is a widely used measure of the solar activity, which correlates well with the daily sunspot number (*Tapping and Charrois, 1994*). The index consists of daily averages of measurements of the solar flux at 10.7 cm wavelength or 2800 MHz. The units are $\text{sfu} = 10^{-22} \text{ W m}^{-2} \text{ Hz}^{-1}$. Fig. 2.13 shows a time series of the $F_{10.7}$ -index from 2005.0 to 2020.0, covering approximately 1.5 solar cycles.

³<http://www.spacecenter.dk/files/magnetic-models/RC/>

The $F_{10.7}$ -index is available at daily resolution from the Canadian Solar Radio Monitoring Program⁴ and accessible through LISIRD⁵.

⁴<https://www.spaceweather.gc.ca/solarflux/sx-en.php>

⁵https://lasp.colorado.edu/lisird/data/penticton_radio_flux/

3. Fundamentals of geomagnetic field modelling

In this chapter I describe the basic field modelling framework that is extended in the Chapters 5 and 6. I primarily present the approach of the CHAOS modelling framework, which puts emphasis on the accurate determination of the slow changes of the internal field.

Geomagnetic field modelling is concerned with finding a mathematical function, the geomagnetic field model, which can accurately reproduce the spatiotemporal behavior of the Earth's magnetic field and allows for a separation of the contributing sources. The goal is not an interpolation but rather a physics-based representation of the magnetic data that can be further analysed. This is a challenging task because the magnetic signals of the sources overlap in both space and time. It is therefore essential to have a good understanding of the underlying physical processes.

Given a geomagnetic field model, it is straight-forward to compute model estimates of the magnetic field. A good model provides estimates that agree with the corresponding magnetic observations to within the observational error. However, in reality the model is not known, but it may be specified so that only a finite number of parameters remain, which become the unknowns. The goal is then to infer the values of those model parameters from actual magnetic observations.

The problem of predicting the observations using the model is called the forward problem, whereas the problem of determining the model parameters from observations is referred to as the inverse problem. The solution of the inverse problem is not unique since multiple models can lead to the same predictions. However, the non-uniqueness can be reduced and eventually resolved by using a-priori information on the model parameters, i.e. knowledge that is independent of the observations. Unfortunately, prior information is often not available, instead it must be given in the form of assumptions.

The most general formulation of inverse problems is a probabilistic theory, where model parameters and prior information are random variables and represented by probability distributions ([Tarantola, 2005](#)). However, the theory can be greatly simplified to a least-squares criterion in the case of problems that involve linear or mildly non-linear forward equations and whose initial uncertainties can be modelled through Gaussian distributions. Such is the case for geomagnetic field modelling.

3.1. Correcting and calibrating magnetic vector data

Magnetic field observations taken by satellites in low-Earth orbit such as the *Swarm* satellite constellation are the main source of data used in geomagnetic field modelling today. The key to deriving accurate models is global availability of magnetic vector data of absolute accuracy ([Finlay, 2019](#)).

Measuring the full vector quantity is important because scalar intensity data alone cannot uniquely determine a model of the geomagnetic field, even if the data are perfect, owing to a fundamental

ambiguity known as the Backus effect ([Backus, 1970](#)). However, the measurement of vector quantities onboard satellites is challenging since it requires knowledge about the orientation of the satellite. On the *Swarm* satellites, this is accomplished with non-magnetic, high-precision STRs, which are mounted in close proximity to the vector magnetometer ([Jørgensen et al., 2003](#)).

Absolute accuracy is achieved in magnetic survey missions thanks to the high standards of magnetic cleanliness during construction of the spacecraft, the care that goes into the design of the magnetometers and the characterization of magnetic stray fields of the spacecraft prior to launch ([Merayo et al., 2008](#)). It is also important to perform an in-flight calibration and correction of the magnetometer sensor output using independent measurements of the scalar intensity taken by an ASM onboard the satellite (e.g. [Olsen et al., 2003](#); [Yin and Lühr, 2011](#)). The corrections involve the removal of temperature effects, non-linearities, and magnetic disturbances caused by solar array, battery, and magneto-torquer coil currents, whereas the calibration removes biases in the sensor output, non-orthogonalities between the component directions and sensitivity differences.

The calibration step can be formulated by assuming a linear VFM, which provides a vector measurement of the surrounding magnetic field in the form of a raw sensor output. Let \mathbf{B}_{VFM} be the magnetic field at the VFM resolved into orthogonal components and \mathbf{B}_{raw} be the raw sensor output of the VFM expressed in terms of non-orthogonal components (in units of quasi nanoTesla, will be referred to as engineering units eu). Following [Olsen et al. \(2003\)](#), \mathbf{B}_{raw} can be related to \mathbf{B}_{VFM} through the matrix equation

$$\mathbf{B}_{\text{VFM}} = \mathbf{P}^{-1} \mathbf{S}^{-1} (\mathbf{B}_{\text{raw}} - \mathbf{b}), \quad (3.1)$$

where \mathbf{B}_{VFM} and \mathbf{B}_{raw} are used as column vectors. \mathbf{P}^{-1} is the inverse matrix of

$$\mathbf{P}(u_1, u_2, u_3) = \begin{bmatrix} 1 & 0 & 0 \\ -\sin u_1 & \cos u_1 & 0 \\ \sin u_2 & \sin u_3 & \sqrt{1 - \sin^2 u_2 - \sin^2 u_3} \end{bmatrix} \quad (3.2)$$

based on the three non-orthogonality angles u_1 , u_2 , and u_3 (radians) measuring the angular deviation of the non-orthogonal VFM axes from orthogonality. \mathbf{S}^{-1} is the inverse matrix of

$$\mathbf{S}(s_1, s_2, s_3) = \begin{bmatrix} s_1 & 0 & 0 \\ 0 & s_2 & 0 \\ 0 & 0 & s_3 \end{bmatrix}, \quad (3.3)$$

with the three sensitivities s_1 , s_2 , and s_3 (in units of eu nT⁻¹) on its diagonal. Finally, \mathbf{b} is a vector of the three biases b_1 , b_2 , b_3 (in units of eu), which can be written as a column vector

$$\mathbf{b}(b_1, b_2, b_3) = \begin{bmatrix} b_1 \\ b_2 \\ b_3 \end{bmatrix} \quad (3.4)$$

Taken together, Eq. 3.1 removes the bias from the sensor output, rescales it with the sensitivities and projects it onto an orthogonal basis. The 9 calibration parameters of the VFM are found by minimizing the difference between $|\mathbf{B}_{\text{VFM}}|$, the magnitude of \mathbf{B}_{VFM} , and the field intensity measurements of the independent ASM.

Many satellites whose main objective is not directly related to magnetic field mapping still carry magnetometers onboard for navigational purposes. Although the data of such platform magnetometers are of lesser quality, they can be used in geomagnetic field modelling, provided they are carefully calibrated. Unfortunately, those satellites usually lack an ASM with which to perform the calibration. In this case, an alternative approach can be applied, which consists of estimating the calibration parameters along with the geomagnetic field model as part of a co-estimation scheme (Alken *et al.*, 2020). Now, the calibration parameters become part of the model parameter vector and are determined through the estimation procedure. An example application of this method using satellite data from CryoSat-2 and the GRACE satellite pair is presented in Chapter 5.

3.2. Data selection for internal field modelling

Earth's magnetic field involves a sum of the contributions from many sources on different length and time-scales. Ideally, every contributing source is taken into account in geomagnetic field modelling. In practice, however, it is necessary to focus on the magnetic signals that contribute most to the observed magnetic measurements. Data selection is a common approach to limit the multitude of magnetic signals in the data (e.g. Finlay, 2019).

For internal field modelling, the focus is on the slow changes of the magnetic field generated in the Earth's outer core. The signals from the current systems in the ionosphere (internal from the satellites point of view) and the magnetosphere are reduced as much as possible, especially during geomagnetic disturbed times since those signals, if not properly accounted for, will contaminate the internal field model. Therefore, one seeks to give more weight to geomagnetic quiet conditions. The characterization of the near-Earth environment is typically based on solar wind and interplanetary magnetic field parameters, and geomagnetic activity indices. For example, Olsen *et al.* (2006a) defined geomagnetically quiet conditions as the rate of change of Dst or similar indices measuring the strength of the ring current is smaller than 2 nT/h, the geomagnetic activity index Kp is lower than 2o for data low-latitude data (equatorward of $\pm 60^\circ$ QD-latitude), and the merging electric field (Kan and Lee, 1979) at the magnetopause is less than 0.8 mV/m for data in the polar regions.

3.3. Model parameterization

Following the description of the main sources (Sec. 2.3), Earth's magnetic field can be decomposed in terms of sources internal and external to the Earth's surface as

$$\begin{aligned} \mathbf{B} &= \mathbf{B}^{\text{int}} + \mathbf{B}^{\text{ext}} \\ &= \mathbf{B}^{\text{int}} + \mathbf{B}^{\text{mag}} + \mathbf{B}^{\text{ion}}, \end{aligned} \tag{3.5}$$

where \mathbf{B}^{int} is the internal magnetic field produced by the sources in the Earth's core and lithosphere, \mathbf{B}^{ext} is the external magnetic field produced by the sources in the ionosphere and magnetosphere. \mathbf{B}^{ext} is thus further divided into the magnetospheric magnetic field, \mathbf{B}^{mag} , and the ionospheric magnetic field, \mathbf{B}^{ion} . The model parameterization of the \mathbf{B}^{int} and \mathbf{B}^{mag} is presented in the following. An approach to parameterizing \mathbf{B}^{ion} will be discussed in more detail in Chapter 6.

3.3.1. Core and lithospheric fields

The Earth's internal magnetic field, consisting of the core and lithospheric field, is expressed in terms of

$$\mathbf{B}^{\text{int}} = -\nabla\psi^{\text{int}}, \quad (3.6)$$

where ψ^{int} is the scalar potential of internal magnetic field. ψ^{int} is written as a truncated spherical harmonic expansion based on Eq. (2.10a) such that

$$\psi^{\text{int}}(r, \theta, \phi, t) = a \sum_{n=1}^{N^{\text{int}}} \sum_{m=-n}^n \left(\frac{a}{r}\right)^{n+1} g_n^m(t) Y_n^m(\theta, \phi). \quad (3.7)$$

where N^{int} is the truncation degree and g_n^m are the coefficients of Earth's internal magnetic field. N^{int} is chosen for practical reasons to restrict the expansion to length-scales which are large enough to be reliably retrieved from the data. Moreover, the low-degree coefficients, say up to 16 or 20, are allowed to be time-dependent to account for the SV of the core field. The high-degree coefficients are assumed static and mostly represent the small-scale lithospheric field. The time-dependence of the coefficients can be implemented in various ways. For example, the widely used IGRF ([Alken et al., 2021](#)) provides coefficients as a time series at reference epochs every five years. The estimate of the internal field at a time between the reference epochs is then computed by linearly interpolating the time series of coefficients

$$g_n^m(t) = g_n^m(t_i) + \frac{g_n^m(t_{i+1}) - g_n^m(t_i)}{t_{i+1} - t_i} (t - t_i), \quad t \in [t_i, t_{i+1}], \quad (3.8)$$

where t_i with $i = 1, 2, \dots, l$ are the reference epochs. As this approach only allows for a constant SV between the reference epochs. Higher-order Taylor expansions that include quadratic terms have also been used to represent the field around a specific reference epoch t_0 ([Maus et al., 2006](#); [Chulliat and Maus, 2014](#))

$$g_n^m(t) = g_n^m|_{t_0} + \dot{g}_n^m|_{t_0}(t - t_0) + \frac{1}{2} \ddot{g}_n^m|_{t_0}(t - t_0)^2, \quad (3.9)$$

where \dot{g}_n^m and \ddot{g}_n^m are the first and second time-derivative of the coefficients, respectively. In field models that span longer time periods, the internal coefficients are typically parameterized in terms of B-splines. In particular, the B-spline basis ([De Boor, 1978](#)) is a convenient way of expressing the coefficients in time

$$g_n^m(t) = \sum_{i=1}^l g_{n,i}^m \mathcal{B}_{k,i}(t), \quad (3.10)$$

where $\{\mathcal{B}_{k,i}(t)\}$ for $i = 1, \dots, l$ are pre-defined order- k B-splines and $g_{n,i}^m$ are the B-spline coefficients. B-splines are defined by specifying a sequence of knots on the time interval of interest. The knot sequence determines the amount of smoothness of the B-splines in time and there can be several knots at the same site (knot multiplicity). Between knots the B-spline is a k th order polynomial with known continuity properties. However, at a site with multiple knots the continuity of the B-spline is reduced by a number equal to the multiplicity at that site. In the extreme case of a k -fold knot, the B-spline will not have a single continuity condition enforced at that site. A dense knot sequence allows to represent fast time variations in the coefficients but may also lead to artificial oscillations

in the presence of noise or insufficient data, unless additional smoothing constraints are imposed. The latest versions of CHAOS model series employ order-6 B-splines with a 6 month knot sequence and 6-fold knots at the model endpoints, which allow for a smooth secular acceleration in the form of cubic polynomials (second derivative of 6-order B-splines are cubic polynomials).

3.3.2. Magnetospheric and associated induced fields

The electric currents in the magnetosphere are a major source of the external magnetic field that is measured both by magnetometers on ground and onboard satellites. The most important current systems are the magnetopause currents, the tail currents in the neutral sheet of the magnetotail and the ring currents around the Earth in the plane perpendicular to the Earth's dipole axis. Since the Earth's internal field and the position of the sun play an important role in organizing those current systems, it is common to use magnetic coordinates to describe the spatial and temporal features of the magnetic field contributions of those currents (*Maus and Lühr, 2005; Olsen et al., 2005b*). In particular, SM coordinates are used for the ring currents, which are mostly organized by the Earth's internal field due to the proximity to Earth, whereas GSM coordinates are suitable for the magnetopause and magnetotail currents, which are strongly influenced by the sun and the solar wind (Sec. 2.1.1). Moreover, the magnetospheric magnetic field varies in time and, therefore, induces a magnetic field in the conducting Earth. The induced field must be properly taken into account for an accurate separation of sources since it could be misinterpreted as an internal field signal coming from the Earth's core, in particular, if it varies on annual and longer time-scales similar to those expected core field changes.

The magnetospheric magnetic field can be written as

$$\mathbf{B}^{\text{mag}} = -\nabla\psi^{\text{near}} - \nabla\psi^{\text{far}}, \quad (3.11)$$

where ψ^{near} and ψ^{far} are the potentials associated with the magnetic field produced by the near-magnetospheric sources (i.e. the magnetospheric ring current and associated induced currents) and the far-magnetospheric sources (i.e. magnetopause and magnetotail currents and associated induced currents), respectively. Those potentials can be further decomposed into

$$\psi^{\text{far}} = \psi^{\text{far},i} + \psi^{\text{far},e}, \quad (3.12)$$

where $\psi^{\text{far},i}$ and $\psi^{\text{far},e}$ are associated with the internal (induced) field and the external (inducing) field of the far-magnetospheric sources, respectively (similarly for ψ^{near}).

The external field produced by the far-magnetospheric sources is often modelled as a static axisymmetric field in GSM coordinates. The associated potential is then given by (*Olsen et al., 2005b*)

$$\psi^{\text{far},e}(r, \theta_{\text{GSM}}, \phi_{\text{GSM}}, t) = a \sum_{n=1}^{N^{\text{far}}} \left(\frac{r}{a}\right)^n q_{n,\text{GSM}}^{0,\text{far}} Y_n^0(\theta_{\text{GSM}}, \phi_{\text{GSM}}), \quad (3.13)$$

where N^{far} is the chosen truncation degree to limit the spatial resolution of the spherical harmonic expansion, $q_{n,\text{GSM}}^{m,\text{far}}$ (here only $m = 0$) are the spherical harmonic coefficients with respect to the GSM coordinate system. Because spherical harmonics form a complete set of orthogonal functions,

they can be used to express any function defined on the surface of a sphere. Therefore, Eq. (3.13) must also have a spherical harmonic expansion in geocentric coordinates. In fact, since the time-dependent transformation from geocentric to GSM coordinates merely involves a rotation around the Earth's center, $Y_n^m(\theta_{\text{GSM}}, \phi_{\text{GSM}})$ can be written as a linear combination of degree- n spherical surface harmonics with respect to the geocentric spherical coordinate system (Maus and Lühr, 2005)

$$Y_n^m(\theta_{\text{GSM}}, \phi_{\text{GSM}}) = \sum_{m'=-n}^n A_n^{m,m'}(t) Y_n^{m'}(\theta, \phi), \quad (3.14)$$

where $A_n^{m,m'}$ are time-dependent coefficients. The $A_n^{m,m'}$ can be determined efficiently by numerically evaluating the orthogonality conditions in Eq. (2.14) using a Gauss-Legendre quadrature. Inserting Eq. (3.14) into Eq. (3.13) results in

$$\begin{aligned} \psi^{\text{far,e}}(r, \theta, \phi, t) &= a \sum_{n=1}^{N^{\text{far}}} \sum_{m=-n}^n \left(\frac{r}{a}\right)^n A_n^{0,m}(t) q_{n,\text{GSM}}^{0,\text{far}} Y_n^m(\theta, \phi) \\ &= a \sum_{n=1}^{N^{\text{far}}} \sum_{m=-n}^n \left(\frac{r}{a}\right)^n q_n^{m,\text{far}}(t) Y_n^m(\theta, \phi), \end{aligned} \quad (3.15)$$

where $q_n^{m,\text{far}}(t) = A_n^{0,m}(t) q_{n,\text{GSM}}^{0,\text{far}}$ can be identified as time-dependent spherical harmonic coefficients with respect to the geocentric spherical coordinate system. Adding $\psi^{\text{far,i}}$ with the same truncation degree to $\psi^{\text{far,e}}$ gives

$$\psi^{\text{far}}(r, \theta, \phi, t) = a \sum_{n=1}^{N^{\text{far}}} \sum_{m=-n}^n \left[q_n^{m,\text{far}}(t) \left(\frac{r}{a}\right)^n + g_n^{m,\text{far}}(t) \left(\frac{a}{r}\right)^{n+1} \right] Y_n^m(\theta, \phi), \quad (3.16)$$

where $g_n^{m,\text{far}}(t)$ are the spherical harmonic coefficients of the induced magnetic field. The spherical harmonic coefficients of the induced and inducing field produced by the far-magnetospheric sources can be coupled through the so-called Q -response (Olsen, 1999), which depends on the conductivity distribution in the Earth. In the frequency domain, indicated by the tilde, the relationship is algebraic and in its most general form given by

$$\tilde{g}_n^{m,\text{far}}(\omega) = \sum_{n'=1}^{N^{\text{far}}} \sum_{m'=-n'}^{n'} \tilde{Q}_{nn'}^{mm'}(\omega) \tilde{q}_{n'}^{m',\text{far}}(\omega), \quad (3.17)$$

which shows that an external excitation (a single nonzero coefficient $\tilde{q}_{n'}^{m',\text{far}}$) can induce contributions over the whole spherical harmonic spectrum. If the conductivity is only allowed to vary in r , i.e. shells of constant conductivity, as it is assumed to be an appropriate first approximation for the Earth (Kuvshinov, 2008), the equation can be simplified to

$$\tilde{g}_n^{m,\text{far}}(\omega) = \tilde{Q}_n(\omega) \tilde{q}_n^{m,\text{far}}(\omega). \quad (3.18)$$

Inserting this expression into Eq. (3.16) in the frequency-domain yields

$$\begin{aligned}\tilde{\psi}^{\text{far}}(r, \theta, \phi, \omega) &= a \sum_{n=1}^{N^{\text{far}}} \sum_{m=-n}^n \left[\tilde{q}_n^{m, \text{far}}(\omega) \left(\frac{r}{a}\right)^n + \tilde{g}_n^{m, \text{far}}(\omega) \left(\frac{a}{r}\right)^{n+1} \right] Y_n^m(\theta, \phi) \\ &= a \sum_{n=1}^{N^{\text{far}}} \sum_{m=-n}^n \left[\tilde{q}_n^{m, \text{far}}(\omega) \left(\frac{r}{a}\right)^n + \tilde{q}_n^{m, \text{far}}(\omega) \tilde{Q}_n(\omega) \left(\frac{a}{r}\right)^{n+1} \right] Y_n^m(\theta, \phi).\end{aligned}\quad (3.19)$$

Moving $q_{1, \text{GSM}}^0$ out of the inner sum gives

$$\begin{aligned}\tilde{\psi}^{\text{far}}(r, \theta, \phi, \omega) &= a \sum_{n=1}^{N^{\text{far}}} q_{n, \text{GSM}}^{0, \text{far}} \sum_{m=-n}^n \left[\tilde{A}_n^{0, m}(\omega) \left(\frac{r}{a}\right)^n + \tilde{A}_n^{0, m}(\omega) \tilde{Q}_n(\omega) \left(\frac{a}{r}\right)^{n+1} \right] Y_n^m(\theta, \phi) \\ &= a \sum_{n=1}^{N^{\text{far}}} q_{n, \text{GSM}}^{0, \text{far}} \tilde{R}_{n, \text{GSM}}^0(r, \theta, \phi, \omega),\end{aligned}\quad (3.20)$$

where $\tilde{R}_{n, \text{GSM}}^0$ collects terms and is the frequency-domain version of $R_{n, \text{GSM}}^m$ (here only $m = 0$). $R_{n, \text{GSM}}^m$ can be considered a modification of the solid spherical harmonics which includes the coordinate transformation and the internally induced counterparts. It only remains to transform Eq. (3.20) from the frequency-domain back into the time-domain. Since a constant axisymmetric external field in GSM coordinates mostly varies with daily and annual frequencies (and weak multiples) relative to Earth's surface, it is sufficient to consider only the K frequencies containing most power $\omega_k \geq 0$

$$\tilde{A}_n^{0, m}(\omega) \approx \sum_{k=1}^K \tilde{A}_n^{0, m}(\omega_k) \delta(\omega - \omega_k), \quad (3.21)$$

where δ is the delta function. Through this assumption, the transformation can be written as a finite sum of the spectral contributions

$$R_{n, \text{GSM}}^0(r, \theta, \phi, t) = \sum_{k=1}^K \Re \left\{ \tilde{R}_{n, \text{GSM}}^0(r, \theta, \phi, \omega_k) \exp(i\omega_k t) \right\}, \quad (3.22)$$

where i is the imaginary unit and \Re denotes the real part of the complex-valued expression. Finally, the potential associated with the sources in the remote magnetosphere is written as

$$\psi^{\text{far}}(r, \theta, \phi, t) = a \sum_{n=1}^{N^{\text{far}}} q_{n, \text{GSM}}^{0, \text{far}} R_{n, \text{GSM}}^0(r, \theta, \phi, t). \quad (3.23)$$

In the CHAOS model framework the truncation degree is usually set to $N^{\text{far}} = 2$.

The potential associated with the magnetic field produced by the near-magnetospheric sources is almost identical to Eq. (3.23) except that SM coordinates are used instead of GSM coordinates and that an additional dipole term with time-dependence based on the hourly RC -index, derived from ground observatory data (see Sec. 2.4.2), is added to account for the fast variations of the ring

currents

$$\begin{aligned} \psi^{\text{near}}(r, \theta, \phi, t) = & a \sum_{n=1}^{N^{\text{near}}} \sum_{m=-n}^n q_{n,\text{SM}}^{m,\text{near}} R_{n,\text{SM}}^m(r, \theta, \phi, t) \\ & + a \sum_{m=-1}^1 \hat{q}_{1,\text{SM}}^m \left[RC_{\text{int}}(t) \left(\frac{a}{r}\right)^2 + RC_{\text{ext}}(t) \left(\frac{r}{a}\right) \right] Y_n^m(\theta_{\text{SM}}, \phi_{\text{SM}}) \end{aligned} \quad (3.24)$$

where N^{near} is the truncation degree ($N^{\text{near}} = 2$ in CHAOS), $R_{n,\text{SM}}^m$ are modifications of the solid harmonics similar to Eq. (3.22) but in SM coordinates, $\hat{q}_{1,\text{SM}}^m$ are constant regression parameters for the RC -index decomposed into the internal RC_{int} and external RC_{ext} parts with $RC = RC_{\text{int}} + RC_{\text{ext}}$. The degree-1 coefficients $\Delta q_1^m \equiv q_{1,\text{SM}}^{m,\text{near}}$ are corrections to the baseline of the RC -index and are typically estimated in monthly bins. In contrast, the degree-2 coefficients $q_{2,\text{SM}}^{m,\text{near}}$ are assumed static over the entire model time interval.

3.3.3. Alignment parameters

The measurements of the magnetic field vector taken by the VFM on-board a satellite can be expressed in terms of orthogonal components \mathbf{B}_{VFM} after an appropriate calibration, whereas the estimates of the geomagnetic field models are computed in terms of GEO components $\mathbf{B}_{\text{GEO}} = [B_r \ B_\theta \ B_\phi]^\top$, here compactly written in terms of a column vector. Determining the magnetometer attitude to relate the magnetic field components in the two systems is an important aspect of using satellite data for geomagnetic field modelling known as data alignment ([Finlay, 2019](#)).

The relationship between \mathbf{B}_{VFM} and \mathbf{B}_{GEO} involves a series of rotations which follow from the position and orientation of the satellite in space ([Olsen et al., 2007](#), pp. 40–42). While the satellite's position is known from the Global Positioning System (GPS) signal, its orientation is determined by STRs, which are carried together with the magnetometer onboard the satellite. On *Swarm*, the VFM and STRs are mounted on an optical bench at the center of a boom further away from the satellite body to minimize contaminating signals from the satellite's operation. The optical bench defines a system of three orthogonal axes, the common reference frame (CRF). The magnetic field \mathbf{B}_{CRF} expressed in terms of components in the CRF is then computed from \mathbf{B}_{VFM} in matrix notation with

$$\mathbf{B}_{\text{CRF}} = \mathbf{R}_{\text{CRF} \leftarrow \text{VFM}} \mathbf{B}_{\text{VFM}}, \quad (3.25)$$

where $\mathbf{R}_{\text{CRF} \leftarrow \text{VFM}}$ is a rotation matrix which is typically defined using Euler angles α , β and γ . In the 1-2-3 convention of the Euler angles, the rotation matrix is written as

$$\mathbf{R}_{\text{CRF} \leftarrow \text{VFM}}(\alpha, \beta, \gamma) = \mathbf{R}_3(\gamma) \mathbf{R}_2(\beta) \mathbf{R}_1(\alpha) \quad (3.26)$$

involving three separate rotation matrices

$$\mathbf{R}_1 = \begin{bmatrix} 1 & 0 & 0 \\ 0 & \cos \alpha & -\sin \alpha \\ 0 & \sin \alpha & \cos \alpha \end{bmatrix}, \quad \mathbf{R}_2 = \begin{bmatrix} \cos \beta & 0 & \sin \beta \\ 0 & 1 & 0 \\ -\sin \beta & 0 & \cos \beta \end{bmatrix}, \quad \mathbf{R}_3 = \begin{bmatrix} \cos \gamma & -\sin \gamma & 0 \\ \sin \gamma & \cos \gamma & 0 \\ 0 & 0 & 1 \end{bmatrix}. \quad (3.27)$$

\mathbf{B}_{CRF} then undergoes a series of rotations which transform the vector components from the CRF,

first, to components in the International Celestial Reference Frame (ICRF) as determined with STR observations, then, to components in the International Terrestrial Reference Frame (ITRF) based on the time of the field measurement, next, to components in the ECEF system and, finally, to the GEO components based on the satellite position. Taken together, the transformation can be written as

$$\mathbf{B}_{\text{GEO}} = \mathbf{R}_{\text{GEO} \leftarrow \text{CRF}} \mathbf{B}_{\text{CRF}}, \quad (3.28)$$

where $\mathbf{R}_{\text{GEO} \leftarrow \text{CRF}}$ is the matrix that combines the individual rotations. The complete data alignment can finally be written as

$$\mathbf{B}_{\text{GEO}} = \mathbf{R}_{\text{GEO} \leftarrow \text{CRF}} \mathbf{R}_{\text{CRF} \leftarrow \text{VFM}} \mathbf{B}_{\text{VFM}}. \quad (3.29)$$

Typically, $\mathbf{R}_{\text{GEO} \leftarrow \text{CRF}}$ is well-known and $\mathbf{R}_{\text{CRF} \leftarrow \text{VFM}}$ can be assumed fixed although the defining Euler angles may on some satellites slightly vary in time due to thermomechanical instabilities. In advanced models such as CHAOS, possible time-dependence of these Euler angles is permitted, e.g. in the form of a piecewise constant, and the resulting parameters co-estimated together with the field model parameters. In this case, the model parameter estimation is a non-linear problem and requires the use of iterative methods.

With the rotation matrices in place, one can choose to determine the model parameters (see next Section) from vector residuals computed either in the VFM system or from the GEO components. If the Euler angles are fixed, there is no difference. But if the Euler angles are co-estimated, it turns out that the numerically superior method is to form the vector residuals based on the GEO components (*Olsen et al., 2007*, pp.43–45).

3.4. Model parameter estimation: solving an inverse problem

Having specified the basic parts of the model parameterization, the values of the initially unknown model parameters are estimated by solving a least-squares inverse problem.

Let $\mathbf{m} = [\mathbf{p}^T \mathbf{q}^T]^T$ be a column vector of length N_m , which consists of the parameters of the geomagnetic field model in the column vector \mathbf{p} (internal and magnetospheric sources) and the Euler angles of each satellite dataset in the column vector \mathbf{q} . Moreover, let there be N observations of the magnetic field vector $\{\mathbf{B}_1(\mathbf{r}_1, t_1), \dots, \mathbf{B}_N(\mathbf{r}_N, t_N)\}$ expressed in terms of components in GEO. The vector components can be arranged in a single column vector $\mathbf{d} = \mathbf{d}(\mathbf{q})$ containing the $N_d = 3N$ components one after another. Here, N_d refers to the number of data in \mathbf{d} and the dependence of \mathbf{d} on \mathbf{q} merely expresses the fact that the vector components are rotated from VFM to GEO by means of the Euler angles in \mathbf{q} . In addition to the vector components, the field intensity can be used as data and appended to \mathbf{d} , in which case the dependence on \mathbf{q} disappears for these specific elements.

The relationship between the model parameter vector \mathbf{m} and the observed data \mathbf{d} is given by N_d equations and can be written in matrix notation as

$$\mathbf{d}(\mathbf{q}) = \mathbf{g}(\mathbf{p}) + \mathbf{e}, \quad (3.30)$$

where \mathbf{g} solves the forward problem, i.e. it provides the predictions of the geomagnetic field model that correspond to the data. The column vector \mathbf{e} contains the residuals, which are the differences between the observed data and the predictions of the geomagnetic field model. The residuals based

on vector components are referred to as vector residuals, whereas the residuals based on the field intensity data are referred to as scalar residuals. In the case that the model describes all relevant field sources, the residuals would contain only observational errors which, for now, could be assumed Gaussian distributed. In the least-squares estimation approach, the values of the model parameters can then be estimated by minimizing a quadratic cost function in the residuals, and in the deviations of the parameters from a-priori parameters $\mathbf{m}_{\text{prior}}$ if these are known, ([Tarantola, 2005](#), pp. 68–69)

$$\mathbf{m}_{\text{LS}} = \underset{\mathbf{m}}{\text{argmin}} \Phi(\mathbf{m}) \quad (3.31)$$

with

$$\Phi(\mathbf{m}) = \frac{1}{2} [\mathbf{g}(\mathbf{p}) - \mathbf{d}(\mathbf{q})]^T \mathbf{C}_d^{-1} [\mathbf{g}(\mathbf{p}) - \mathbf{d}(\mathbf{q})] + \frac{1}{2} (\mathbf{m} - \mathbf{m}_{\text{prior}})^T \mathbf{\Lambda} (\mathbf{m} - \mathbf{m}_{\text{prior}}), \quad (3.32)$$

where $\mathbf{C}_d^{-1} \in \mathbb{R}^{N_d \times N_d}$ is the inverse of the data error covariance matrix and $\mathbf{\Lambda} \in \mathbb{R}^{N_m \times N_m}$ is the inverse of the a-priori model covariance matrix (also sometimes called the regularization matrix) which specifies prior information on the model parameters in the form of a Gaussian process defined by its mean and covariances. A widely used minimization algorithm in geomagnetism is the iterative quasi-Newton method, which requires both the gradient and the Hessian matrix of Φ , that is

$$\frac{\partial \Phi}{\partial \mathbf{m}} = \mathbf{G}^T \mathbf{C}_d^{-1} [\mathbf{g}(\mathbf{p}) - \mathbf{d}(\mathbf{q})] + \mathbf{\Lambda} (\mathbf{m} - \mathbf{m}_{\text{prior}}), \quad \text{and} \quad \left(\frac{\partial^2 \Phi}{\partial m_i \partial m_j} \right) \approx \mathbf{G}^T \mathbf{C}_d^{-1} \mathbf{G} + \mathbf{\Lambda}, \quad (3.33)$$

where $\mathbf{G} \in \mathbb{R}^{N_d \times N_m}$ is known as the Jacobian matrix (or sometimes called design matrix) with elements that are the partial derivatives of the residuals with respect to the model parameters,

$$(\mathbf{G})_{ij} = \frac{\partial [\mathbf{g}(\mathbf{p}) - \mathbf{d}(\mathbf{q})]_i}{\partial (\mathbf{m})_j}. \quad (3.34)$$

Starting from an initial model \mathbf{m}_0 , a local minimum of Φ can then be iteratively approached with

$$\mathbf{m}_{k+1} = \mathbf{m}_k - (\mathbf{G}_k^T \mathbf{C}_d^{-1} \mathbf{G}_k + \mathbf{\Lambda})^{-1} \left\{ \mathbf{G}_k^T \mathbf{C}_d^{-1} [\mathbf{g}(\mathbf{p}_k) - \mathbf{d}(\mathbf{q}_k)] + \mathbf{\Lambda} (\mathbf{m}_k - \mathbf{m}_{\text{prior}}) \right\}, \quad (3.35)$$

where k denotes the iteration number and $\mathbf{G}_k = \mathbf{G}(\mathbf{m}_k)$ is re-evaluated each iteration. If Φ has a single minimum, then the iterative method converges to it. If, on the other hand, there are several minima, then \mathbf{m}_0 must be chosen close to the global minimum. The iterative method is terminated once a chosen convergence criterion is satisfied, and the final iterate is taken to be the least-squares solution. A possible convergence criterion can be, for example, that the relative change of the cost function value or a norm of the model parameter vector is below a chosen threshold from one iteration to the next. The latter choice has the advantage that it relates to the values of the model parameters, which are the quantities of geophysical significance.

In this thesis I use the ratio between the norm of the model update $\|\mathbf{m}_{k+1} - \mathbf{m}_k\|_2$ and the model norm $\|\mathbf{m}_k\|_2$ at iteration k as the convergence measure, where $\|\cdot\|_2$ is the Euclidean norm. The model is considered converged when this measure falls below the target level L

$$\frac{\|\mathbf{m}_{k+1} - \mathbf{m}_k\|_2}{\|\mathbf{m}_k\|_2} < L. \quad (3.36)$$

The target level should be chosen to give a good compromise between having stable model parameter values and the computation time needed for the model estimation to terminate. This convergence measure allows one to monitor the progress of the estimation and, most usefully, to detect diverging model parameters.

3.4.1. Data error covariance matrix

In the CHAOS field modelling framework the data error covariance is specified in a co-ordinate system related to field direction and the STR boresight. This allows the specification of appropriate anisotropic errors when only a single STR is available, for example in the early Ørsted mission or in the case that additional STRs are blinded by the sun or moon.

For a single vector measurement the error covariance matrix is diagonal if \mathbf{B} is resolved into components along unit vectors in the direction of \mathbf{B} , $\mathbf{n} \times \mathbf{B}$, and $\mathbf{n} \times (\mathbf{n} \times \mathbf{B})$, where \mathbf{n} is the boresight direction of the STR assumed not parallel to \mathbf{B} (Holme and Bloxham, 1996; Holme, 2000). In this frame of reference, called B23, the data error covariance becomes

$$\mathbf{C}_d = \begin{bmatrix} \sigma^2 & 0 & 0 \\ 0 & \sigma^2 + B^2(\xi^2 \sin^2 \kappa + \nu^2 \cos^2 \kappa) & 0 \\ 0 & 0 & \sigma^2 + B^2\nu^2 \end{bmatrix}, \quad (3.37)$$

where σ is an isotropic (scalar) uncertainty in the vector measurement, ξ is the angular uncertainty in the rotation about \mathbf{n} (rotational error), ν is the angular uncertainty in the rotation about any axis perpendicular to \mathbf{n} (pointing error), and κ is the angle between \mathbf{B} and \mathbf{n} . The treatment of multiple vector measurements, assuming no correlation between the vector errors, is identical except that the full matrix \mathbf{C}_d is block-diagonal with the 3×3 blocks of Eq. (3.37) on the diagonal in correspondence to the residuals arranged in \mathbf{e} .

In order to account for observed long-tailed error distributions each entry on the diagonal of \mathbf{C}_d is also multiplied with a corresponding Huber-weight (Constable, 1988; Huber, 2004)

$$w_i = \min \left(1.5 \left| \frac{\sqrt{(\mathbf{C}_d)_{ii}}}{e_i} \right|, 1 \right), \quad (3.38)$$

where e_i is an element of the vector of residuals \mathbf{e} . In addition, due to the dense spatial sampling in the polar regions if data are sampled at a constant rate along-track, satellite data is often weighted by the inverse of the area density of the measurements to achieve a uniform global sampling. A simple approach in this regard is to multiply the diagonal of \mathbf{C}_d with $\sin \theta_i$, where θ_i is the colatitude of the measurement location. Finally, \mathbf{C}_d is transformed from B23 to GEO and inverted as required in Eq. (3.32).

3.4.2. Model regularization

Model regularization ensures the convergence of the model estimation procedure by providing prior information on the model parameters. In principle it involves specifying an a-priori model vector $\mathbf{m}_{\text{prior}}$ and the inverse of the a-priori model covariance matrix (also known as the regularization matrix) $\mathbf{\Lambda}$. In constructing satellite geomagnetic field models such as CHAOS, $\mathbf{m}_{\text{prior}}$ is typically set to zero and

$\mathbf{\Lambda}$ is crudely designed in order to reduce spurious temporal variations of the internal time-dependent field and the magnetospheric field. The complete regularization matrix can then be written as

$$\mathbf{\Lambda} = \lambda_t \mathbf{\Lambda}_t + \lambda_{t_s} \mathbf{\Lambda}_{t_s} + \lambda_{t_e} \mathbf{\Lambda}_{t_e} + \lambda_{\text{mag}} \mathbf{\Lambda}_{\text{mag}}, \quad (3.39)$$

where the regularization parameters effectively λ_t , λ_{t_s} , λ_{t_e} and λ_{mag} control the regularization strength and are chosen by experimentation prior to estimating the model parameters. The various regularization matrices are introduced in the following.

The regularization of the time-dependent internal field is based on the third time-derivative of the radial magnetic field averaged over the CMB and the model time interval (*Finlay et al., 2020*)

$$\langle \langle \ddot{\mathbf{B}}_r^2 \rangle_{S(c)} \rangle_t = \frac{1}{(t_e - t_s)} \int_{t_s}^{t_e} \frac{1}{4\pi} \int_{S(c)} \left(\frac{\partial^3 B_r}{\partial t^3} \right)^2 dS dt \quad (3.40)$$

where $\langle \cdot \rangle_t = \frac{1}{t_e - t_s} \int_{t_s}^{t_e} dt$ denotes the time average over the entire model time interval, $c = 3485.0$ km is the chosen radius of the CMB, and t_s and t_e are the model start and end time, respectively. Evaluating the spatial integral with the help of Eq. (2.14) and using the fact that the time-dependent internal field is expressed in terms of order-6 B-splines, results in

$$\begin{aligned} \langle \langle \ddot{\mathbf{B}}_r^2 \rangle_{S(c)} \rangle_t &= \sum_{n=1}^{N_{\text{int}}} \sum_{m=-n}^n \frac{(n+1)^2}{2n+1} \left(\frac{a}{c} \right)^{2n+4} \langle \langle \ddot{g}_n^m \rangle^2 \rangle_t \\ &= \sum_{n=1}^{N_{\text{int}}} \sum_{m=-n}^n \frac{(n+1)^2}{2n+1} \left(\frac{a}{c} \right)^{2n+4} \sum_{i,i'} g_{n,i}^m g_{n,i'}^m \langle \ddot{\mathbf{B}}_{6,i} \ddot{\mathbf{B}}_{6,i'} \rangle_t, \end{aligned} \quad (3.41)$$

which is a quadratic form in the B-spline coefficients $g_{n,i}^m$ of the internal field model. The time-derivatives of the B-spline functions are known analytically and the time averaging can be evaluated through numerical integration methods such as a sum of rectangles. In matrix notation Eq. (3.41) becomes

$$\langle \langle \ddot{\mathbf{B}}_r^2 \rangle_{S(c)} \rangle_t = \mathbf{m}^T \mathbf{\Lambda}_t \mathbf{m}, \quad (3.42)$$

where $\mathbf{\Lambda}_t$ is a block-diagonal matrix whose non-zero entries only act on the internal field coefficients $g_{n,i}^m$ in \mathbf{m} .

Similar expressions are used to regularize the second time-derivative of the radial magnetic field at the CMB at the model start time

$$\begin{aligned} \langle \ddot{\mathbf{B}}_r^2(t_s) \rangle_{S(c)} &= \frac{1}{4\pi} \int_{S(c)} \left(\frac{\partial^2 B_r}{\partial t^2} \Big|_{t=t_s} \right)^2 dS \\ &= \sum_{n=1}^{N_{\text{int}}} \sum_{m=-n}^n \frac{(n+1)^2}{2n+1} \left(\frac{a}{c} \right)^{2n+4} \sum_{i,i'} g_{n,i}^m g_{n,i'}^m \ddot{\mathbf{B}}_{6,i}(t_s) \ddot{\mathbf{B}}_{6,i'}(t_s) \\ &= \mathbf{m}^T \mathbf{\Lambda}_{t_s} \mathbf{m}, \end{aligned} \quad (3.43)$$

and at the model end time by replacing t_s with t_e

$$\langle \ddot{\mathbf{B}}_r^2(t_e) \rangle_{S(c)} = \mathbf{m}^T \mathbf{\Lambda}_{t_e} \mathbf{m}. \quad (3.44)$$

Regarding the magnetospheric field model, only the bin-to-bin variability of the three *RC*-baseline corrections is regularized using a quadratic form in the first forward difference of neighboring bins. The forward difference operator is applied to the coefficients of each correction

$$\mathbf{D} = \frac{1}{t_e - t_s} \begin{bmatrix} -1 & 1 & & \\ & \ddots & \ddots & \\ & & -1 & 1 \end{bmatrix}, \quad (3.45)$$

where the number of columns is equal to the number of bins that are used to parameterize each *RC*-baseline correction Δq_1^m in time. The resulting regularization matrix is block-diagonal and given by

$$\mathbf{\Lambda}_{\text{mag}} = \text{diag}(0, \dots, 0, \mathbf{D}_2, \mathbf{D}_2, \mathbf{D}_2, 0, \dots, 0), \quad (3.46)$$

where $\mathbf{D}_2 = \mathbf{D}^T \mathbf{D}$ appears three times in correspondence to the three *RC*-baseline corrections. The additional zeros on the diagonal of $\mathbf{\Lambda}_{\text{mag}}$ indicate that model parameters unrelated to the *RC*-baseline corrections are not acted upon.

3.5. State of the art of geomagnetic field modelling

The above sections have focused on the CHAOS field modelling framework, which has been developed at DTU. A number of other modelling approaches do however exist. The variety of approaches has recently been showcased in the candidates models submitted to the 13th generation of the IGRF ([Alken et al., 2021](#)). Here I illustrate the diversity in the adopted approaches by presenting a brief overview of some prominent models that take a rather different approach to that of CHAOS.

The comprehensive inversion approach (e.g. [Sabaka et al., 2002, 2004, 2015, 2018](#)) aims at co-estimating models of the majority of dominant magnetic signals measured in the near-Earth space to achieve the best separation of sources. The latest geomagnetic field model based on this approach is the Comprehensive Model 6 (CM6) ([Sabaka et al., 2020](#)), which parameterizes the magnetic contributions produced by current systems in the core, lithosphere, ionosphere and magnetosphere and their associated internally-induced fields, as well as some constituents of the oceanic tidal field. In addition, alignment parameters for the satellite vector datasets are co-estimated. CM6 is derived from both scalar and vector measurements from the Ørsted, SAC-C, CHAMP and the *Swarm* satellites, and hourly mean vector measurements from ground-based observatories. One of the main differences to CHAOS is that CM6 partly accounts for the ionospheric field (more details of this are discussed in Chapter 6).

Limitations of the strong temporal regularization of the internal field that is typically applied, and a wish to provide better error estimates for field models, have led to the development of alternative ways to provide a-priori information on the internal field coefficients. The COV-OBS models ([Gillet et al., 2013, 2015](#); [Huder et al., 2020](#)) use stochastic prior information in the form of temporal cross-covariances of the time-dependent internal coefficients to obtain estimates for posterior probability density functions of the internal and slowly varying external field. This approach assumes that the evolution of the internal coefficients in time is governed by mean-free auto-regressive processes of order-2, for which only two parameters per spherical harmonic degree need to be specified. Those

parameters are inferred from spatial power spectra of field models determined from satellite data. This approach leads to more realistic prior covariances, which in turn allows improved error estimates of the resulting field model. However, COV-OBS uses a relatively simple magnetospheric model and ionospheric signals in the data are either ignored or corrected for using the CM model prior to the model estimation.

Estimating a high-resolution geomagnetic field model requires large amounts of magnetic data and many model parameter to capture the major contributing sources. This can be computationally expensive, which has recently motivated the development of an alternative sequential modelling approach ([Ropp et al., 2020](#); [Baerenzung et al., 2020](#)). This approach consists of estimating a time series of snapshot models using a Kalman filter. The Kalman filter progresses through the time series one step at a time. At each step it (i) updates the a-priori information on a given snapshot model (which can include a prediction from the previous snapshot) with the magnetic data in the corresponding interval and (ii) makes a prediction with this updated information for the snapshot model at the next step. When the whole time series has been processed, a backward smoothing filter is applied. The sequential estimation is initiated with simple a-priori information at the first snapshot model. [Ropp et al. \(2020\)](#) used a time step of 3 months, whereas [Baerenzung et al. \(2020\)](#) used a much shorter step size of 30 min, allowing to represent fast external field variations. Strong and reliable prior information on the modelled sources is also required for this approach.

4. Development of the modelling software

An important operational aspect of geomagnetic field modelling is the software tools actually used to perform the modelling. Field modelling typically involves the processing of a large number of magnetic data, which consumes a considerable amount of memory and computer processing power. Therefore, much effort goes into the development of specialized computer programs and algorithms that can handle these requirements and estimate a field model in a timely fashion.

In the following, I briefly report on a new field modelling software package developed during this PhD thesis that can be used to evaluate and derive geomagnetic field models within a CHAOS-type modelling framework. This software was written in Python and was based on and tested against existing MATLAB software that has traditionally been used to derive the CHAOS model series. Porting the MATLAB software over to Python has been an extensive task that has consumed time during this PhD project. The goal is to provide a flexible and efficient new framework for developing future versions of the CHAOS model, including the extensions reported later in this thesis.

4.1. Motivation

The CHAOS modelling framework has been developed by Nils Olsen, who released the first CHAOS model in 2006 with inputs from Terence Sabaka and Herman Lühr (*Olsen et al., 2006a*). Since then, the CHAOS model has become a whole series of models, the latest being CHAOS-7.6 (as of March 2021), which are regularly extended thanks to the continuing release of high-quality satellite magnetic data, most recently from the *Swarm* satellites.

Over the years, the modelling framework and the actual modelling software written in MATLAB have seen numerous improvements, e.g. with the inclusion of gradient data. While the software has grown in complexity, its structure and organization, which is essentially that of a single script and a collection of helper functions, has mostly stayed the same. Therefore, adding a new functionality to the software has become increasingly difficult to implement. In addition, the modelling software is parallelized using an open-source MATLAB toolkit of an older version of the Messaging Passing Interface (MPI) standard, which cannot be easily updated. These limitations of the existing modelling software motivated the development of a new implementation designed to facilitate future developments of the CHAOS modelling framework.

Although this new modelling software could have again been written in MATLAB, it was decided to completely redesign the software using the Python programming language. The advantage of Python is that it is easy to learn and open source¹, i.e. freely usable and distributable, and it can be used in combination with compiled languages such as Fortran and C. In addition, due to its open source licensing, there is an increasing number of Python users, among them many researchers, who develop and share software useful for science.

¹<https://opensource.org/>

The following list describes a number of key features, ordered from high to low priority, of the new modelling software. They are not to be understood as strict requirements but rather as guiding principles for the software development:

Packaged: The software should be organized in a package, i.e., it should consist of multiple Python files which each have a specific purpose and are as self-contained as possible. The only dependency can be among the Python files within the package or in the form of an external dependency on other packages. As a package, it can be distributed and installed. Moreover, there should be a unique identifier to label different versions of the software (i.e. version number).

Version-controlled: The software should be version-controlled, e.g. via git, so that all changes made to the software in the past and future are recorded. This allows to trace back which change was made by whom and when the change took place. Furthermore, the version-control system facilitates the collaboration between multiple developers since it permits to safely merge the recorded changes made independently by each developer without compromising the consistency of the software.

Documented: The functionality of each component of the software should be documented. In particular, special attention should be given to documenting the inputs and outputs of functions. This allows new users to quickly get familiar with the software's capabilities, and it helps with fixing error in the code.

Modular: The software's functionality should be separated into relatively small, independent units with well-defined interfaces. Moreover, the units should be interchangeable to ease a modification of the existing functionality and the development of new capabilities.

Testable: The software should include a test suite to verify that all components are working as intended. This also helps to avoid erroneous software changes that may be caused inadvertently during software development.

Maintainable: The software should be maintainable, i.e. the developers make sure to add meaningful comments that explain key points of the implementation to every other line of code. Furthermore, it is important for the readability of the code that the developers follow good coding practices such as having a consistent notation and using a generous code layout (line breaks and empty lines).

4.2. Multifit: software for modelling the geomagnetic field

The implementation of the CHAOS modelling software in Python is called Multifit. Although the Python implementation heavily borrows from the original MATLAB software and is primarily intended for deriving new CHAOS models, it is more general and fits into the broader scope of geomagnetic field modelling. The idea has been to develop a software package that contains all the tools necessary for field modelling. And, to write a top-level script that combines all these tools in order to derive the CHAOS model.

The left of Fig. 4.1 presents a simplified directory structure of the Multifit software package, while the right depicts the dependency graph of the principal components of Multifit. The directory structure shows that there are a number of txt-files at the top level of the package. Here, `changelog.txt`

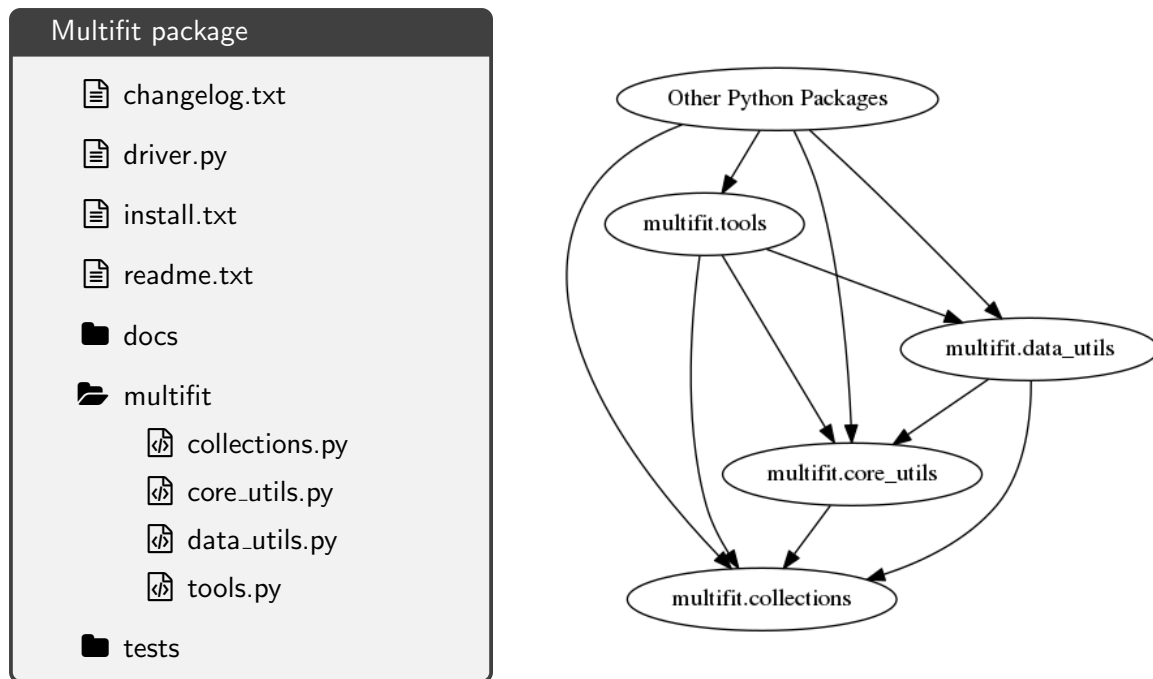


Figure 4.1.: Simplified directory structure of the Multifit software (left) and dependency graph of the key components (right).

lists the changes from one version to the next (in addition to the version control system), `driver.py` is the top-level script to derive the CHAOS model, `install.txt` provides instructions on how to install the package, and `readme.txt` gives general comments. The `docs` directory contains the source files needed to compile the documentation, the `multifit` directory contains the actual Python files needed for performing the functionality of the package, and `tests` directory is the test suite. Turning to the dependency graph, the arrows point away from the dependency and toward the target component so that the most dependent one is placed at the bottom of the graph. At the top are several Python packages such as Numpy², Pandas³, Matplotlib⁴, and ChaosMagPy (Kloss, 2020). They are external dependencies and form the basis of the Multifit software by providing the fundamental tools for scientific computing, data analysis and manipulation, and visualization. ChaosMagPy plays a special role here. It is a Python package that was developed during the early stages of the thesis in order to efficiently evaluate and visualize the CHAOS model. It contains basic field modelling functions to compute spherical harmonics and Legendre polynomials. More details about ChaosMagPy are given in Sec. 4.3. Aside from the external packages, the other components shown on the right side of Fig. 4.1 are actual Python files. The first of those is `multifit.tools`, which provides many general-purpose functions that are useful for geomagnetic field modelling. For example, it contains functions to compute Huber weights, rotation matrices for Euler angles, and helper functions to label and mask a sequence of spherical harmonic coefficients. Further down in the dependency graph is `multifit.data_utils`, which collects everything related to reading, writing and processing magnetic data. In `multifit.core_utils` are tools related to setting up the different parts of a geomagnetic field model such as the spherical harmonic representation of the internal field and the

²<https://numpy.org/>

³<https://pandas.pydata.org/>

⁴<https://matplotlib.org/>

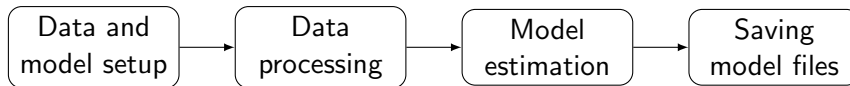


Figure 4.2.: Schematic illustration of the different parts in the driver file.

time-dependence of the Euler angle parameterization. Hence, it provides the most important or *core* functionality of the Multifit software and should not only be associated with the core field. Finally, `multifit.collections` contains several functions specifically intended to be used in connection with the CHAOS model. These functions require only a minimum of inputs and are, therefore, highly specialized. For example, there are functions for producing the CHAOS model files, which are distributed to the end users every time a new extension is released.

4.2.1. Example workflow for producing a CHAOS-type model

Not shown in Fig. 4.1 is the so-called driver script, which puts into action the functionality of the Multifit package to derive from magnetic data a geomagnetic field model, in this case, CHAOS. The driver consists of several parts, which are depicted in Fig. 4.2. The first part of the driver is concerned with the data and model setup. Here, the paths to the data files are given, the parameters for the data selection are specified, and the different parts of the geomagnetic field model are defined. This part is lazy, i.e. there are only definitions and nothing gets executed that is computationally expensive. In the second and third part, the driver executes the actual data processing and model estimation, respectively. After a specified number of iterations have finished or the chosen convergence criteria are met, the driver saves the estimated parameters to a file for later evaluation and plotting. The following lines reproduce a simplified version of the driver script:

```

1  from chaosmagpy.data_utils import mjd2000, dyear_to_mjd, mjd_to_dyear
2  import multifit.core_utils as mco
3  import multifit.data_utils as mda
4
5  # Data and model setup
6  setup = {
7      'Kp.max': 20, # selection criterion: remove data with Kp > 20
8      'dRC.max': 2, # selection criterion: remove data with |dRC/dt| > 2 nT/hr
9      'external.Kp-index': mda.KpIndex('/Kp_index.dat'), # where to find Kp-index
10     'external.RC-index': mda.RCIndex('/RC_index.dat'), # where to find RC-index
11 }
12
13 mda.register_worker(mda.ScalarWorker( # ScalarWorker to process scalar data
14     mda.ScalarData( # special reader for Oersted data
15         datafile=('/oersted_scalar.dat'), # path to Oersted data
16         name='Oersted'
17     ),
18     config=setup # supply parameters for data selection
19 ))
20
21 mda.register_worker(mda.VectorWorker( # VectorWorker to process vector data

```

```
22     mda.VectorData( # special reader for Swarm data
23         datafile='/swarm_a_vector.dat', # path to Swarm-A data
24         name='Swarm-A'
25     ),
26     config=setup # supply parameters for data selection
27 ))
28
29 models = [] # create empty list and append different field model parts
30
31 models.append(mco.CoreModel( # add internal spherical harmonic model
32     name='Core', # alias for large-scale, time-dependent internal field
33     params=0., # initialize model parameters with zeros
34     breaks=dyear_to_mjd([2019.0, 2019.5, 2020.0]), # breaks every 0.5 yr
35     order=6, # use 6-order B-splines
36     nmax=20, # set maximum spherical harmonic degree to 20
37     nmin=1, # set minimum spherical harmonic degree to 1
38     config={'lambda': 1.0} # set a regularization parameter
39 ))
40
41 models.append(mco.CrustModel( # add another internal spherical harmonic model
42     name='Crust', # alias for small-scale, static internal field
43     params=0., # initialize model parameters with zeros
44     order=1, # use a piecewise constant in time
45     breaks=dyear_to_mjd((2019.0, 2020.0)), # single bin in mjd2000
46     nmax=60, # set maximum spherical harmonic degree to 60
47     nmin=21, # set minimum spherical harmonic degree to 21
48 ))
49
50 models.append(mco.GSMModel( # add external spherical harmonic model in GSM
51     name='GSM', # alias for far-magnetospheric sources
52     params=0., # initialize model parameters with zeros
53     order=1, # use a piecewise constant in time
54     breaks=dyear_to_mjd((2019.0, 2020.0)), # single bin in mjd2000
55     nmax=2, # set maximum spherical harmonic degree to 2
56     mmax=0 # use only zonal terms
57 ))
58
59 models.append(mco.EulerModel( # add Euler angles for Swarm-A vector data
60     name='Swarm-A', # name for convenience
61     params=[11.8, -76.2, -12.6], # initialize angles with non-zero values
62     order=1, # use a piecewise constant in time
63     breaks=[5070., 5080., 5090.], # mjd2000, two 10 day bins
64     source='Swarm-A'
65 ))
66
67 mult = mco.Multifit( # create the iterator
68     models, # supply the list of model parts
69     iter_max=15, # maximum number of iterations
70     robust='Huber', # choose Huber weights for data weighting
```

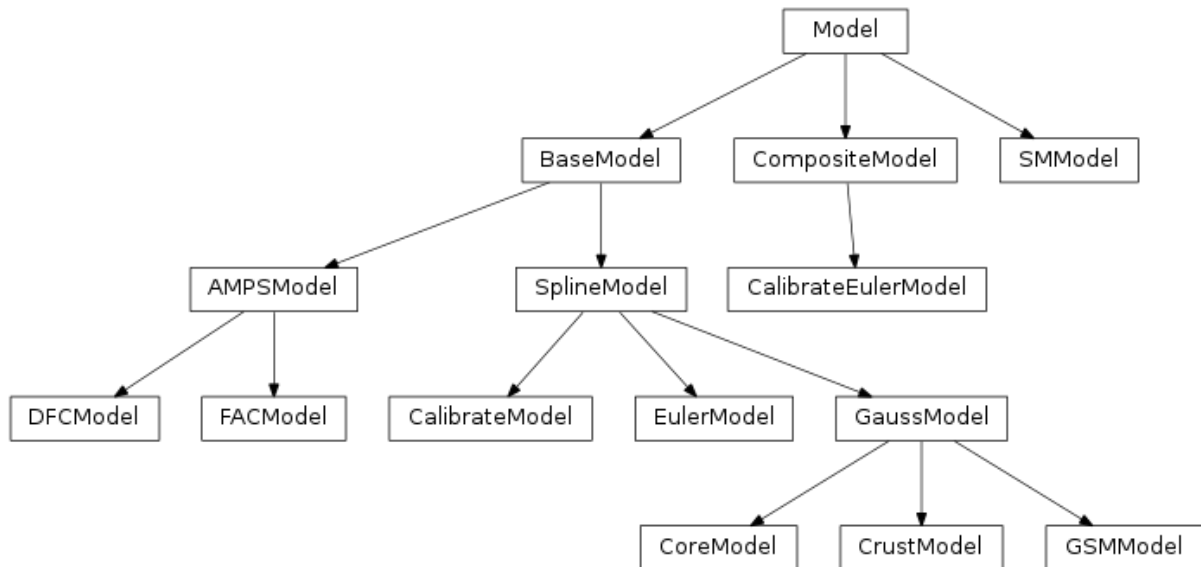


Figure 4.3.: Inheritance tree of the model parts implemented in Multifit. The most generic model part is situated at the top, called Model. The parts become increasingly specialized when going down the tree as indicated by the arrow direction.

```

71     chunksize=10000, # partition data into chunks of 10000
72     nthreads=16 # parallelize with 16 threads
73 )
74
75 # Data processing
76 mda.process() # execute data processing and write selected data to a file
77
78 # Model estimation
79 mult.fit() # iterate: compute the design matrix and solve linear equations
80
81 # Saving model files
82 mult.save() # save model parameters to a file

```

The crucial point to notice is that the driver consists of several blocks or units. For example, defining the Ørsted scalar data occupies the lines 13–19, the Swarm-A vector data is on lines 21–27, and the definition of the model part representing the time-dependent internal field is on lines 31–39. By removing or adding similar blocks, this kind of modularization makes it simple to change the magnetic datasets and the composition of the geomagnetic field model. Furthermore, each block can be easily modified if necessary. For example, the data worker `mda.VectorWorker` (line 21), which implements the selection criteria specifically for vector data, can be replaced with `mda.ScalarWorker` to convert the vector data to scalar data and apply the appropriate selection criteria.

Apart from the field models and the model for Euler angles shown in the example driver, there is an entire family of models implemented in Multifit. Each member of the model family represents a specific part of the geomagnetic field model, but all of them inherit their basic functionality from a generic model. This establishes a well-defined interface so that the model parts can be combined. Fig. 4.3 depicts the inheritance tree of the implemented model parts in Multifit. Some notable members are `SMMModel` and `GSMMModel` used for the magnetospheric sources, `CalibrateModel` for

the calibration of platform magnetometer data, and DFCModel and FACModel for the ionospheric sources.

Returning to the example driver, the model estimation algorithm is called on line 70. In this step, the values of the model parameters are iteratively updated according to Eq. (3.35). The most expensive components of the algorithm in terms of memory and processing power are the computation of the design matrix \mathbf{G}_k and the matrix operation $\mathbf{G}_k^T \mathbf{C}_d^{-1} \mathbf{G}_k$, which are repeated every iteration k . Recall that \mathbf{G}_k is of size $N_d \times N_m$ (number of data times number of model parameters), leading to a memory requirement that is prohibitively large given the millions of data and thousands of model parameters that are typically involved in geomagnetic field modelling. However, the block-diagonal structure of \mathbf{C}_d^{-1} makes it possible to subdivide the data into smaller partitions $\{[1, N_p], [N_p+1, 2N_p], \dots, [(P-1)N_p+1, N_d]\}$, where $p = 1, \dots, P$ counts the partitions and $N_p < N_d$ is the partition length. Each data partition can be processed independently and the results are added together at a later stage according to

$$\mathbf{G}_k^T \mathbf{C}_d^{-1} \mathbf{G}_k = \sum_{p=1}^P \mathbf{G}_{k,p}^T (\mathbf{C}_d^{-1})_p \mathbf{G}_{k,p}, \quad (4.1)$$

where $(\mathbf{C}_d^{-1})_p$ is the p th block on the diagonal of \mathbf{C}_d^{-1} and $\mathbf{G}_{k,p}$ is the submatrix of \mathbf{G}_k that corresponds to the data in the p th partition. This approach reduces the memory footprint and opens up the possibility of parallelization.

Multifit uses Dask⁵, a flexible library in Python, for parallel computing. The Dask workflow can be briefly summarized as follows. Eq. (4.1) is translated into a task graph, where each term and each pairwise sum of terms represents a task. To perform the computation in parallel, the task graph is submitted through a central scheduler to a network of several worker processes, possibly spread across multiple machines, which form a cluster. The scheduler coordinates the action between the worker processes in the cluster, assigning tasks to the workers while balancing the load on each worker to maximize efficiency. Once, the computation is finished, the result (left side of Eq. 4.1) is sent back to the main process, where the linear system of equations for the model update is solved. Since Dask comes with a powerful scheduler, the parallelization of a Python software package is easier to implement than in MPI, which does not have a ready-made scheduler.

4.3. ChaosMagPy: a python package to evaluate the CHAOS model

ChaosMagPy (Kloss, 2020) is an independent software package in Python to evaluate the CHAOS model based on the official model files⁶. The package was developed before the full Multifit inversion software described above and is already freely available for download on GitHub⁷ and PyPI⁸.

ChaosMagPy allows the evaluation of all parts in the CHAOS model. Furthermore, it offers simple tools for coordinate and time format transformations and for model visualization. The following lines show an example of how to use it:

⁵<https://dask.org/>

⁶CHAOS-7 model files: <http://www.spacecenter.dk/files/magnetic-models/CHAOS-7/>

⁷GitHub repository of ChaosMagPy: <https://github.com/ancklo/ChaosMagPy>

⁸PyPI repository of ChaosMagPy: <https://pypi.org/project/chaosmagpy/>

Figure 4.4.: Front page of the ChaosMagPy documentation.

```

1 import chaosmagpy as cp
2
3 radius = 3485. # km, core-mantle boundary
4 theta = 30. # colatitude in degrees
5 phi = 80. # longitude in degrees
6
7 time = cp.data_utils.mjd2000(2000, 3, 2) # March 2, 2000
8
9 # load the CHAOS model from CHAOS-7.5.mat
10 model = cp.load_CHAOS_matfile('CHAOS-7.5.mat')
11
12 # compute Gauss coefficients of the time-dependent internal field
13 coeffs = model.synth_coeffs_tdep(time)
14
15 # compute spherical geocentric components of the time-dependent internal field
16 B_r, B_t, B_p = model.synth_values_tdep(time, radius, theta, phi)

```

On line 10, the model file is loaded and used to compute the Gauss coefficients (line 13) and the components (line 16) of the time-dependent internal field. Similar code can be used for the external field represented in CHAOS.

In addition, there is an comprehensive documentation available on Read the Docs⁹, which explains every component of the software package and gives several usage examples (Fig. 4.4).

⁹ChaosMagPy documentation: <https://chaosmagpy.readthedocs.io/en/stable/readme.html>

4.4. Validation

Both Multifit and ChaosMagPy come with an extensive test suite to benchmark the validity and performance of the Python implementation against the original MATLAB software.

The test suite contains not only short sanity checks of regularly used functions but also thorough test scripts to verify the correct interaction of different parts of the software. In addition, there are several tests where the computed results are directly compared to the output of the MATLAB software, requiring them to be identical, in the case of integers and strings, or equal to within a relative error tolerance of 10^{-7} , in the case of floats. Those tests are regularly executed to ensure that the code is working correctly and that no errors are inadvertently introduced during development.

In a larger test case, I derived a geomagnetic field model identical to CHAOS-7.4 ([Finlay et al., 2020](#)), which was built with the MATLAB software, using the same magnetic data sets, model parameterization and type of regularization. A comparison between the model parameter values as determined with Multifit and those of CHAOS-7.4 showed that both models were in good agreement. For example, regarding the time-dependent internal field model, the squared magnitude of the field difference averaged over the Earth's surface and the model time interval was 0.3 nT , the same quantity for the SV was 0.1 nT yr^{-1} , and for the SA 0.2 nT yr^{-2} . These small differences can be attributed to minor variations in the implementation of the data selection and rounding errors in the computation of regularization matrices. The same conclusions were drawn from a similar benchmark test against the SIFMplus model ([Olsen et al., 2016](#)). Performance tests comparing computation times suggest that Multifit is faster than the MATLAB software, likely due to the outdated MPI implementation used in the latter. In summary, a number of validation tests have been carried out, which confirm that Multifit is equivalent to the MATLAB software and is, thus, suitable for future research and development in field modelling.

4.5. Concluding remarks

The Multifit package is still being developed but has essentially the same functionality as the MATLAB software traditionally used to derive the CHAOS model. Recent improvements to the CHAOS modelling framework have been developed within Multifit, which gradually replaces the MATLAB software. Nonetheless, the current implementation of Multifit has limitations, in particular, concerning the memory requirement. At present, Multifit cannot determine models that have more than, say 60000 parameters, due to an excessive memory demand of each worker. In the future, this limitation is bound to cause an issue since the time series of high-resolution magnetic data are continuously being extended. However, this limitation can be addressed through, for example, more sophisticated parallelization strategies, which Multifit can readily support thanks to its flexible architecture.

5. Co-estimating calibration parameters in geomagnetic field modelling

In this chapter I implement and test a scheme for co-estimating calibration parameters within the CHAOS framework of geomagnetic field modelling. The chapter is an excerpt from the publication: “Co-estimating geomagnetic field and calibration parameters: modeling Earth’s magnetic field with platform magnetometer data” ([Kloss et al., 2021](#)), which has been made during this PhD study. The full paper can be found in Appendix A. The presentation of the results has been shortened here, but the conclusions are identical to the original publication. Unlike the rest of the thesis, I use “we” to reflect the input from the co-authors in this chapter.

5.1. Introduction

The study of processes in Earth’s outer core on decadal or longer time-scales requires long time-series of magnetic vector data with high spatial and temporal resolution. Along with ground-based magnetic observatories, low-earth orbit satellites from dedicated magnetic survey missions such as CHAMP (2000–2010) and the *Swarm* trio (since 2013) provide such data. However, other than scalar data from Ørsted, no high-quality calibrated magnetic vector data from satellites are available between the end of the CHAMP mission in September 2010 and the launch of the *Swarm* satellites in November 2013. This data gap not only cuts in two an otherwise uninterrupted time-series of high-quality magnetic satellite data since the year 2000, but also limits our ability to derive accurate core field models that resolve temporal changes of the magnetic field on timescales of a few years and less in the gap period. To address the issue, one can utilize the crude magnetometers that are carried by most satellites for navigational purposes, the so-called platform magnetometers. Although not a substitute for dedicated high-quality magnetic survey satellites, platform magnetometers can supplement ground observatory data in gaps between dedicated missions and help improve the local time data coverage of simultaneously flying high-quality magnetic survey satellites.

Satellite-based magnetic vector data need to be calibrated to remove magnetometer biases, scale factors, and non-orthogonalities between the three vector component axes ([Olsen et al., 2003](#)). Comparing the vector magnetometer output with a magnetic reference field allows the estimation of these calibration parameters. On dedicated survey mission satellites, the reference is a second, absolute scalar, magnetometer mounted in close proximity to the vector magnetometer and measuring the magnetic field intensity. However, non-dedicated satellites carrying platform magnetometers are typically not equipped with such scalar reference magnetometers. In this case, it is possible to use a-priori geomagnetic field models like CHAOS ([Olsen et al., 2006a](#); [Finlay et al., 2020](#)) or the IGRF ([Thébault et al., 2015](#)) as reference. Such an approach has been successfully used, e.g., by [Olsen et al. \(2020\)](#) for calibrating data from the CryoSat-2 magnetometer, but use of a fixed reference field

model is not without risks and could lead to biased calibration parameters.

An alternative venue has been explored by [Alken et al. \(2020\)](#), who combined high-quality magnetic data from CHAMP and *Swarm* with platform magnetometer data from CryoSat-2 and several satellites of the Defense Meteorological Satellite Program (DMSP) to estimate a model of the internal field and the required calibration parameters for each satellite simultaneously. Ideally, such a co-estimation scheme eliminates the need for a-priori geomagnetic field models, but [Alken et al. \(2020\)](#) fall short by co-estimating only the internal field while still relying on a fixed model of the external field. Nevertheless, their study convincingly demonstrated that platform magnetometer data provide valuable information about the time-dependence of Earth's magnetic field.

In this study, we followed [Alken et al. \(2020\)](#) and developed a co-estimation strategy but within the framework of the CHAOS field model series. Our implementation differs in three important aspects. First, we estimated both the internal (core and crust) and external (magnetospheric) geomagnetic field contributions in contrast to only the internal field. This way, we avoided having to remove a fixed external field model from the satellite data prior to the model parameter estimation. Following the methodology of the CHAOS model, we did use a prior external field model for processing the ground observatory data which we used in addition to the satellite data. Second, we used the platform magnetometer data from CryoSat-2 and, instead of DMSP, data from the GRACE satellite pair. Finally, to reduce the significant correlation between the internal axial dipole and the calibration parameters during periods of poor coverage of high-quality magnetic data, we excluded platform magnetometer data from determining the internal axial dipole (its time variation is well resolved with ground observatory data during the gap period, while its absolute value is constrained by *Swarm* and CHAMP data on both sides of the gap) rather than controlling the temporal variability of the internal axial dipole through an additional regularization as done by [Alken et al. \(2020\)](#).

The chapter is organized as follows. In the first part, we present the datasets and the data processing. Next, we describe the model parameterization and define the calibration parameters, which are similar to those used for the Ørsted satellite ([Olsen et al., 2003](#)). We go on by presenting a geomagnetic field model derived from high-quality calibrated data from the CHAMP and the *Swarm* satellites as well as ground observatory secular variation data and supplemented this with previously uncalibrated platform magnetometer data from CryoSat-2 and GRACE, spanning a 10 year period from 2008 to 2018. Finally, we explore in a series of experiments the effect of co-estimating an external field, the trade-off between the internal dipole and the calibration parameters, and the importance of including dayside platform magnetometer data when estimating calibration parameters. We conclude the chapter by looking at the secular acceleration of our model, paying particular attention to the data gap between 2010 and 2013.

5.2. Data and data processing

We used calibrated magnetic data from the *Swarm* satellites Alpha (*Swarm*-A) and Bravo (*Swarm*-B), and from the CHAMP satellite from January 2008 to the end of December 2017, supplemented with five datasets of uncalibrated magnetic data from the three platform fluxgate magnetometers (FGMs) on-board the CryoSat-2 satellite (CryoSat-2 FGM1, CryoSat-2 FGM2 and CryoSat-2 FGM3), the one on-board the first GRACE satellite (GRACE-A), and the other one on-board the second GRACE

satellite (GRACE-B). In addition to the satellite data, we included revised monthly mean values of the SV from ground observatories to contribute to the Earth's internal time-dependent field. Details of the datasets are given in the following.

5.2.1. Absolute satellite data from scientific magnetometers

The satellite data from scientific magnetometers are in general of high quality in terms of accuracy, precision and magnetic cleanliness. The high standard of the data is achieved by low noise instruments that are mounted together with star cameras on an optical bench further away from the spacecraft body at the center of a several meter long boom. The data are regularly calibrated in-flight with a second absolute scalar magnetometer placed at the end of the boom and carefully cleaned from magnetic disturbance fields originating from the spacecraft body.

From the CHAMP mission, we used the Level 3 1 Hz magnetic data, version CH-ME-3-MAG ([Rother and Michaelis, 2019](#)), between January 2008 and August 2010, downsampled to 15 s, and only when attitude information from both star cameras was available. From the *Swarm* mission, we used the Level 1b 1 Hz magnetic data product, baseline 0505/0506, from the Swarm-A and Swarm-B satellites between November 2013 and December 2018, also downsampled to 15 s. Here, we worked with vector data from CHAMP and *Swarm* in the magnetometer frame.

5.2.2. Relative satellite data from platform magnetometers

Relative satellite data refer to the raw sensor output from platform magnetometers. The data have to be corrected and calibrated before they can be used in geomagnetic field modelling. The correction of the data accounts for temperature effects, magnetic disturbances due to solar array and battery currents, magnetorquer activity, as well as non-linear sensor effects, whereas the calibration removes magnetometer biases, scale differences, and non-orthogonalities between the three vector component axes.

From CryoSat-2, we took magnetic data, baseline 0103, from the three platform magnetometers as described in [Olsen et al. \(2020\)](#) from August 2010 to December 2018 and only when the attitude uncertainty q_{error} was below $40''$. Since the purpose of this chapter is the co-estimation of calibration parameters for the platform magnetometers, we processed the dataset using the original calibration parameters to undo the calibration step that has been performed by [Olsen et al. \(2020\)](#) but keeping the applied correction for magnetic disturbances from the spacecraft and its payload. This way, we obtained essentially uncalibrated data while still retaining the corrections for magnetic disturbances, temperature effects and non-linearities. In a pre-whitening and data reduction step, we computed residuals to the CHAOS-6-x9 model in the uncalibrated magnetometer frame, removed those larger than 1000 eu in absolute value to discard gross outliers, computed component-wise robust mean values of the residuals in 1 min bins to reduce the original 4 s sampled data to 1 min values, and added the CHAOS-6-x9 model values back. Fig. 5.1 shows an example of the raw vector residuals $\Delta\mathbf{B}_{\text{raw}}$ of CryoSat-2 FGM1 in the uncalibrated magnetometer frame over 3 h on March 24, 2016. In a similar way, we processed the 1 Hz data from the GRACE satellites, baseline 0101, to obtain 1 min uncalibrated but corrected vector data between January 2008 and October 2017 (GRACE-A) and August 2017 (GRACE-B) ([Olsen, 2020](#)).

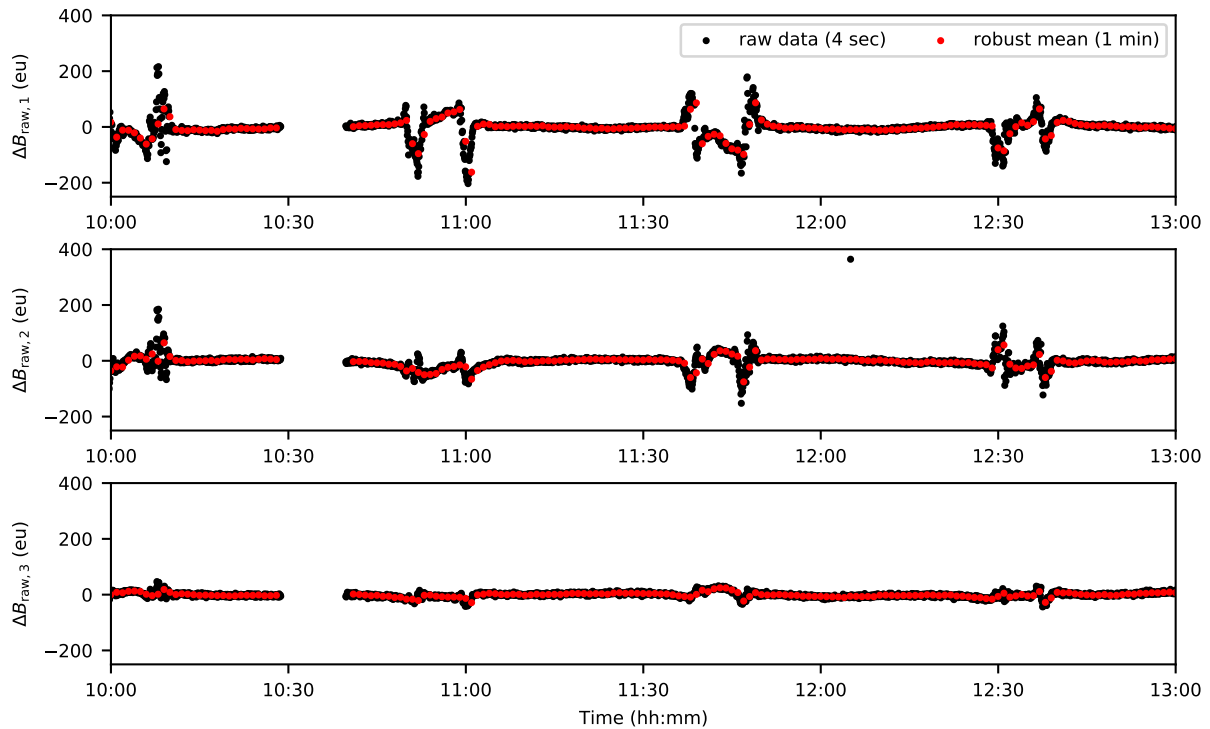


Figure 5.1.: Residuals of raw vector data from CryoSat-2 FGM1 with respect to the CHAOS-6-x9 model values in the uncalibrated magnetometer frame for an example period of 3 h on March 24, 2016. The gap in the raw data between 10:30 and 10:40 is due to the rejection of data with poor attitude information ($q_{\text{error}} > 40''$).

The computation of 1 min values served two purposes. First, to reduce the random noise of the magnetometers by taking the average of successive values and, second, to decrease the number of platform magnetometer data, so that a fair amount of absolute satellite data was able to guide the co-estimation of the calibration parameters.

5.2.3. Ground observatory data

In addition to satellite data, we added annual differences of monthly mean values from 162 ground observatories to help determine the time changes of the core field (secular variation). Following [Olsen et al. \(2014\)](#), we computed revised monthly means as Huber-weighted averages of the hourly observatory mean values from the AUX OBS database ([Macmillan and Olsen, 2013](#)) at all local times after removing estimates of the ionospheric field of the CM4 ([Sabaka et al., 2004](#)) and the large-scale magnetospheric field of CHAOS-6-x9, including their internally induced parts.

5.2.4. Satellite data selection

We organized the satellite data according to QD latitude ([Richmond, 1995](#)) into a non-polar (equal to and equatorward of $\pm 55^\circ$) and a polar (poleward of $\pm 55^\circ$) data subset. From each subset, we selected data under quiet geomagnetic conditions. Specifically, we selected data from the non-polar subset that satisfied the following criteria:

- Low geomagnetic activity as indicated by the planetary activity index Kp smaller than or equal to 2σ ;

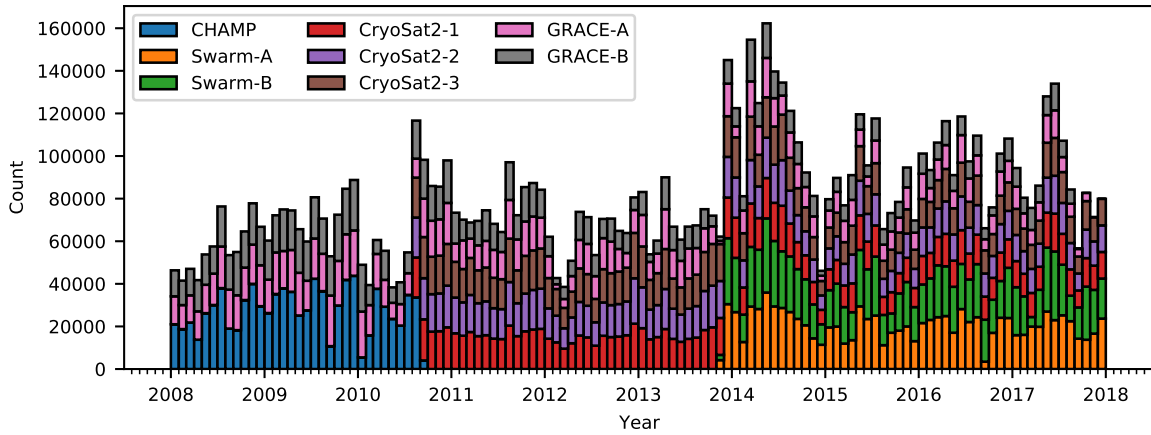


Figure 5.2.: Number of selected scalar and vector satellite data per month as stacked histogram. Ground observatories contribute with approximately 130 vector measurements of the SV per month.

- Dark condition as indicated by a solar zenith angle greater than 100° for the *Swarm* and CHAMP satellites (i.e., sun at least 10° below the horizon). From CryoSat-2 and GRACE, we used data from dark and sunlit regions, since we found that this leads to better determined calibration parameters;
- Slow change of the magnetospheric ring current as indicated by the *RC*-index ([Olsen et al., 2014](#)) rate of change in absolute terms being smaller than 2 nT h^{-1} .

From the polar subset, we kept data according to the following criteria:

- Dark condition except in the case of platform magnetometers on-board CryoSat-2 and GRACE, where we also used sunlit data;
- *RC*-index rate of change in absolute terms smaller than or equal to 2 nT h^{-1} ;
- The merging electric field at the magnetopause in mV m^{-1} $\epsilon = 10^{-3} |v_x|^{4/3} B_t^{2/3} \sin^{8/3} |\theta_c| / 2$, where v_x is the solar wind speed, $B_t = \sqrt{B_{\text{IMF},y}^2 + B_{\text{IMF},z}^2}$ is the interplanetary magnetic field in the y - z -plane in GSM coordinates, and $\theta_c = \arctan 2(B_{\text{IMF},y}/B_{\text{IMF},z})$, was on average smaller than 2.4 mV m^{-1} over the previous 2 h;
- The interplanetary magnetic field component $B_{\text{IMF},z}$ in GSM coordinates was on average positive over the previous 2 h.

Fig. 5.2 shows a stacked histogram of the number of data for each satellite after the data selection. It can be clearly seen that platform magnetometer data are the main contributor to the number of data in the gap period, whereas it is comparable to the number of data from CHAMP and the *Swarm* satellites in the time before and after the gap. The ground observatories contribute approximately 130 monthly mean values of the SV each month throughout the entire model time interval, which is much less than the monthly average number of satellite data.

5.3. Model parameterization

Our modeling approach follows that of earlier models of the CHAOS model series ([Olsen et al., 2006a, 2014](#); [Finlay et al., 2016b, 2020](#)) and consists of describing the geomagnetic field with the

Table 5.1.: Summary of the model parameterization. All parts of the model have both a spatial (S) and temporal (T) parameterization except for the Euler angles and calibration parameters.

	Number of parameters	Spatial and temporal parameterization
Internal field		
Time-dependent field	6375	S: Spherical harmonics in GEO, $n \leq 15$ T: Order-6 B-splines with knots every 0.5 year and 6-fold knots at model endpoints
Static field	2345	S: Spherical harmonics in GEO, $16 \leq n \leq 50$ T: All terms are static in GEO
Magnetospheric field*		
Near-magnetospheric field	248	S: Spherical harmonics in SM, $n \leq 2$ T: Degree-1 terms are scaled by hourly <i>RC</i> -index, degree-2 terms are static in SM, and <i>RC</i> -baseline corrections are estimated in 30 day bins and a single 3 year bin during the gap period
Far-magnetospheric field	2	S: Spherical harmonics in GSM, $n \leq 2, m = 0$ T: All terms are static in GSM
Alignment		
CHAMP	99	Euler angles (1-2-3 convention), 30 day bins
Swarm-A	150	Euler angles (1-2-3 convention), 30 day bins
Swarm-B	150	Euler angles (1-2-3 convention), 30 day bins
Alignment/calibration		
CryoSat-2 FGM1	1092	Euler angles and calibration parameters, 30 day bins
CryoSat-2 FGM2	1092	Euler angles and calibration parameters, 30 day bins
CryoSat-2 FGM3	1092	Euler angles and calibration parameters, 30 day bins
GRACE-A	1440	Euler angles and calibration parameters, 30 day bins
GRACE-B	1416	Euler angles and calibration parameters, 30 day bins
Total	15501	

*includes the internally induced response based on an electrical conductivity model of the Earth.

help of scalar potentials whose exact form depends on a set of coefficients that multiply the solid harmonics. The coefficients are estimated by minimizing a quadratic cost function in the residuals. We used two kinds of residuals: the components of vector differences expressed in terms of spherical geocentric components (vector residuals) and the difference of vector magnitudes (scalar residuals). More specifically, we computed vector residuals of the non-polar satellite data, scalar residuals of the polar satellite data, and vector residuals of the ground observatory SV data at all QD latitudes. Tab. 5.1 summarizes the different parts of the model and the corresponding number of parameters.

5.3.1. Internal field parameters

The expressions of the scalar potential used for modelling the magnetic field produced by internal sources are given in Sec. 3.3.1. We truncated the formally infinite sum of solid harmonics at $N^{\text{int}} = 50$ (Eq. 3.7) and expanded the spherical harmonic coefficients of degree $n \leq 15$ in time using order-6 B-splines (Eq. 3.10), while we kept the higher degree coefficients ($n > 15$) constant in time. The B-spline basis is defined on knots at 6-month intervals and six-fold multiplicity at the model endpoints

in $t_s = 2008.0$ and $t_e = 2018.0$ in years. For the purposes of testing the co-estimation of calibration parameters here, it was deemed sufficient to only allow the internal coefficients of degrees $n \leq 15$ to be time-dependent.

5.3.2. External field parameters

We account for the magnetospheric field and the associated induced fields as described in Sec. 3.3.2. The scalar potentials associated with the near-magnetospheric sources (Eq. 3.24) and far-magnetospheric sources (Eq. 3.23) are truncated at $N^{\text{near}} = 2$ and $N^{\text{far}} = 2$, respectively. Those potentials include internally induced contributions based on the diagonal part of the Q -response matrix (Eq. 3.17) that has been derived from a 3D conductivity model of Earth (Finlay *et al.*, 2020). The RC-baseline corrections Δq_1^m were estimated in bins of 30 days except in the gap period, where we used a single bin from August 2010 to January 2014 to reduce the strong co-linearity between the calibration parameters and the baseline corrections that earlier tests had revealed. We did not include the ionospheric field in the models of this chapter.

5.3.3. Alignment parameters

We performed the data alignment as described in Sec. 3.1 for the satellite datasets from CHAMP, Swarm-A, Swarm-B, CryoSat-2, and GRACE. For each dataset, we parameterized the Euler angles in time as a piecewise constant function using a sequence of 30 day bins.

5.3.4. Calibration parameters

The calibration can be viewed as an extension of the data alignment which makes it possible to use platform magnetometer data in geomagnetic field modelling. We performed the calibration for CryoSat-2 and the GRACE satellites using Eqs. (3.1)–(3.4).

Combining the calibration step in Eq. (3.1) and the data alignment step in Eq. (3.29), yields an equation that transforms the raw sensor output \mathbf{B}_{raw} into calibrated and aligned vector components

$$\mathbf{B}_{\text{GEO}} = \mathbf{R}_{\text{GEO} \leftarrow \text{CRF}}(r, \theta, \phi) \mathbf{R}_{\text{CRF} \leftarrow \text{VFM}}(\alpha, \beta, \gamma) \mathbf{P}^{-1} \mathbf{S}^{-1} (\mathbf{B}_{\text{raw}} - \mathbf{b}). \quad (5.1)$$

We estimated the nine basic calibration parameters and the three Euler angles in bins of 30 days. For data equatorward of $\pm 55^\circ$ QD latitude, we performed a vector calibration using the component residuals of \mathbf{B}_{GEO} for estimating the model parameters. In contrast, for data poleward of $\pm 55^\circ$ QD latitude, we performed a scalar calibration by using the residuals of the vector magnitude, in which case the rotation matrices $\mathbf{R}_{\text{GEO} \leftarrow \text{CRF}}$ and $\mathbf{R}_{\text{CRF} \leftarrow \text{VFM}}$ disappear

$$\begin{aligned} |\mathbf{B}_{\text{GEO}}| &= \sqrt{\mathbf{B}_{\text{GEO}}^T \mathbf{B}_{\text{GEO}}} \\ &= \sqrt{(\mathbf{B}_{\text{raw}} - \mathbf{b})^T \mathbf{S}^{-1} (\mathbf{P}^{-1})^T \mathbf{P}^{-1} \mathbf{S}^{-1} (\mathbf{B}_{\text{raw}} - \mathbf{b})} \end{aligned} \quad (5.2)$$

at the expense of losing the ability to estimate the Euler angles.

5.4. Model parameter estimation

The geomagnetic field model parameters in \mathbf{p} , the Euler angles in \mathbf{q} , and the calibration parameters in \mathbf{c} were determined by minimizing a cost function in the model parameter vector $\mathbf{m} = [\mathbf{p}^T \mathbf{q}^T \mathbf{c}^T]^T$ identical to Eq. (3.32) but for which the data was a function of the Euler angles and the calibration parameters, $\mathbf{d}(\mathbf{q}, \mathbf{c})$. Hence, the treatment of the calibration parameters in the cost function was similar to the Euler angles.

We used the iterative quasi-Newton method in Eq. (3.35) to find the minimum of the cost function. However, we modified the design matrix \mathbf{G}_k (Eq. (3.34)) used in that algorithm to prevent some data subsets from constraining certain parts of the internal field model. In particular, we set entries of \mathbf{G}_k to zero for the following criteria:

1. The row index of the matrix entry corresponded to dayside data from a platform magnetometer, on-board CryoSat-2 or GRACE, and the column index corresponded to model parameters that describe the internal and external magnetic field. Therefore, the dayside data were only used to determine the Euler angles and calibration parameters of the respective platform magnetometer.
2. The row index of the matrix entry corresponded to data from a platform magnetometer, on-board CryoSat-2 or GRACE, and the column index corresponded to the B-spline parameters that parameterize the g_1^0 coefficients of the internal field in time. Therefore, no platform magnetometer data were used to constrain the B-spline coefficients of the axial dipole which we believe are well determined using ground observatory data.

Tab. 5.2 gives an overview of whether or not certain datasets constrained specific parts of the model. Nevertheless, we used the full model description in the forward evaluation to compute the residuals.

The iterative procedure described in Eq. (3.35) requires a starting model \mathbf{m}_0 to initialize the model parameter estimation. We initialized the internal field model parameters using the corresponding part of CHAOS-6-x9, while we set the external field model parameters to zero. To initialize the Euler angles, we used the values from CHAOS-6-x9 in case of *Swarm* and CHAMP satellites, or set the angles to zero in case of CryoSat-2 and the GRACE satellite duo. For the calibration parameters, we simply set the offsets and non-orthogonalities to zero and the sensitivities to one over the whole model time interval. The parameter estimation usually converged after 10–15 iterations to a level of $L = 10^{-6}$ (Eq. 3.36). We also tested other starting models, e.g. random calibration parameters, but found that our choice had little impact on the converged model parameters other than increasing the number of necessary iterations.

5.4.1. Data weighting

The data error covariance matrix \mathbf{C}_d was built according to Sec. 3.4.1. Tab. 5.3 summarizes the values of σ and the attitude errors, setting ξ equal to ν , for the different satellite datasets. We scaled the diagonal entries of the covariance matrix with Huber weights (Constable, 1988; Sabaka et al., 2004) that we calculated for each component in the B23 reference frame to downweight data points that greatly deviated from the model evaluated at the previous iteration. After inverting and rotating the Huber-weighted covariance matrix of the individual data point into the RTP frame, we arranged them into a block-diagonal matrix completing the desired inverse data covariance matrix \mathbf{C}_d^{-1} . In

Table 5.2.: Overview of which data subset constrained which part of the model. The cross refers to non-zero entries in the design matrix, whereas the circle refers to zeros. The SV data refer to the annual difference of the revised monthly means.

	Non-polar satellite data		Polar satellite data		SV data
	Day	Night	Day	Night	
Internal field					
Time-dependent field	○	X*	○	X*	X
Static field	○	X	○	X	○
Magnetospheric field					
Near-magnetospheric field	○	X	○	X	○
Far-magnetospheric field	○	X	○	X	○
Alignment					
CHAMP	○	X	○	○	○
Swarm-A	○	X	○	○	○
Swarm-B	○	X	○	○	○
CryoSat-2 FGM1	X	X	○	○	○
CryoSat-2 FGM2	X	X	○	○	○
CryoSat-2 FGM3	X	X	○	○	○
GRACE-A	X	X	○	○	○
GRACE-B	X	X	○	○	○
Calibration					
CryoSat-2 FGM1	X	X	X	X	○
CryoSat-2 FGM2	X	X	X	X	○
CryoSat-2 FGM3	X	X	X	X	○
GRACE-A	X	X	X	X	○
GRACE-B	X	X	X	X	○

*Entries related to g_1^0 B-spline coefficients and platform magnetometer data are zero.

Table 5.3.: Chosen values of σ and ξ (set equal to ν) for the different satellite datasets. The values under Swarm apply to the data from the two *Swarm* satellites in this study (Swarm-A and Swarm-B), the values under CryoSat-2 to the data of the three magnetometers (FGM1, FGM2 and FGM3), and the values under GRACE to the data from both GRACE satellites (GRACE-A and GRACE-B).

	CHAMP	Swarm	CryoSat-2	GRACE
σ (nT)	2.5	2.2	6	10
ξ (arcsec)	10	5	30	100

case of the vector magnitude of the polar satellite data, we simply used σ^2 scaled with Huber weights as variance. The covariance of the ground observatory SV vector data was derived from detrended residuals to the CHAOS-6-x9 model, including the covariance between vector components at a given location.

5.4.2. Model regularization

The regularization matrix follows closely the form presented in Eq. (3.39) except that the matrix $\mathbf{\Lambda}_{\text{cal}}$ is added in order to also regularize the time variations of the calibration parameters.

Turning to the internal part of the model, following the example of earlier models in the CHAOS series, we designed a regularization over the entire model time interval (Eq. 3.40) and at the model start and end (Eqs. 3.43–3.44). However, in those expressions we multiplied the factor $\frac{(n+1)^2}{2n+1} \left(\frac{a}{c}\right)^{2n+4}$ with a weighting function

$$w(n, m) = w_n(n)w_m(m), \quad (5.3)$$

which gives additional control over the regularization strength based on the degree and order of the internal field coefficients. Following [Finlay et al. \(2020\)](#), in order to relax the regularization at higher spherical harmonic degree, we defined w_n as a tapered window which gradually reduces from one to 0.005

$$w_n(n) = \begin{cases} 1, & n < n_{\min} \\ \frac{0.995}{2} \left[1 + \cos \left(\pi \frac{n - n_{\min}}{n_{\max} - n_{\min}} \right) \right] + 0.005, & n_{\min} \leq n \leq n_{\max} \\ 0.005, & n > n_{\max} \end{cases} \quad (5.4)$$

where $n_{\min} = 3$ and $n_{\max} = 6$ are the chosen limits of a half-cosine taper. In contrast to [Finlay et al. \(2020\)](#), who used $n_{\max} = 11$ to achieve stable power spectra with more power in the time-dependence of the high-degree coefficients without causing instabilities, we were able to further decrease the upper limit of the taper. The magnetospheric and ionospheric field and their induced counterparts may also cause the estimation of the internal field parameters to become unstable. Our experience shows that the zonal harmonics are typically the first to become unstable if the regularization is not sufficiently strong. Therefore, in addition to the degree-dependent temporal regularization, there is a special treatment of zonal and non-zonal coefficients based on

$$w_m(m) = \begin{cases} \lambda_0, & m = 0 \\ \lambda_m, & m \neq 0. \end{cases} \quad (5.5)$$

Turning to the external part of the model, we regularized only the bin-to-bin variability of the three RC baseline corrections using the regularization matrix in Eq. (3.46).

Finally, we regularized a quadratic form in the bin-to-bin variability of each calibration parameter for the five platform magnetometers (three on CryoSat-2 and one on each of the two GRACE satellites). The regularization matrix $\mathbf{\Lambda}_{\text{cal}}$ is block-diagonal with blocks $\mathbf{\Lambda}_{\text{cal},i}$, $i = 1, \dots, 5$, each corresponding to the calibration parameters of one of the five platform magnetometers. The regularization matrix can be written as

$$\begin{aligned} \mathbf{\Lambda}_{\text{cal}} &= \text{diag}(0, \dots, 0, \mathbf{\Lambda}_{\text{cal},1}, \dots, \mathbf{\Lambda}_{\text{cal},5}, 0, \dots, 0) \\ \mathbf{\Lambda}_{\text{cal},i} &= \text{diag}(\lambda_{b,i}, \lambda_{s,i}, \lambda_{b,i}) \otimes \text{diag}(\mathbf{D}_2, \mathbf{D}_2, \mathbf{D}_2), \end{aligned} \quad (5.6)$$

where \otimes is the Kronecker product, and $\lambda_{b,i}$, $\lambda_{s,i}$, and $\lambda_{u,i}$ are regularization parameters for each platform magnetometer to control the temporal smoothness of the offsets, sensitivities, and non-orthogonalities, respectively.

5.5. Results and discussion

We built two geomagnetic field models which span 10 years from the 1st of January 2008 to the 31st of December 2018, but differ in the use of platform magnetometer data to constrain the field model parameters.

The first model, Model-A, was derived with data from the Swarm-A, Swarm-B, and CHAMP satellites, and the monthly SV data from ground observatories. It served as a reference model, which allowed us to identify differences to models which were derived using platform magnetometer data in addition. Considering the model parameterization, regularization, and estimation, Model-A is very similar to the CHAOS model series. In fact, the parameterization of the geomagnetic field and the alignment parameters of the satellite data are identical, except for the lower truncation degree of the internal field and the longer bins of the alignment parameters and *RC*-baseline corrections in Model-A. A notable difference is the use of gradient data in the CHAOS model. The strong temporal regularization of the high-degree Gauss coefficients of the time-dependent internal field has been relaxed in the newly released CHAOS-7 model through a taper, which we also used here. For Model-A, we tuned the regularization, such that the model parameters matched the ones of the CHAOS-6-x9 model as close as possible. Tab. 5.4 shows the numerical values of the regularization parameters.

The second model, Model-B, is our preferred model and was derived with data from Swarm-A, Swarm-B, CHAMP, monthly ground observatory SV data, and, as opposed to Model-A, platform magnetometer data from CryoSat-2 FGM1, CryoSat-2 FGM2, CryoSat-2 FGM3, GRACE-A, and GRACE-B. In addition to Model-A and Model-B, we built test models (Model-C, Model-D, and Model-E) in a series of experiments to investigate the effect of platform magnetometer data on the estimation of the geomagnetic field model. Details of these test models are given below. The regularization parameters are the same for all the presented models.

5.5.1. Fit to satellite data and ground observatory SV data

We begin with reporting on the fit of Model-B to the satellite data and ground observatory SV data. The histograms of the scalar and vector residuals for each dataset are shown in Fig. 5.3. The residuals of Swarm-A, Swarm-B, CHAMP and the ground observatories show narrow and near-zero centered peaks, which demonstrate the high-quality and low-noise level of these datasets. In contrast, the peaks are broader for CryoSat-2 and even more in the case of GRACE, which is, as expected, due to the higher data noise level. By separating the residuals poleward of $\pm 55^\circ$ QD latitude from the ones equatorward, we find that peaks are broader at polar QD latitudes for all datasets, which is a result of unmodelled magnetic signal of the polar ionospheric current system. Also, the histograms of the GRACE residuals are biased toward negative values. Upon further investigation, we found a local time-dependence especially visible in the scalar residuals, which could indicate that signals from solar array and battery currents have not been fully removed from the GRACE datasets used here.

Table 5.4.: Chosen numerical values of the regularization parameters. In the table CryoSat-2 refers to the three magnetometers FGM1, FM2 and FGM3, and GRACE refers to GRACE-A and GRACE-B. The values are valid for all the models built in this chapter insofar as the regularization terms are applicable to the specific model.

Regularization parameters	
Internal field	
Time-dependent field	$\lambda_t = 1.0 \left(\frac{\text{nT}}{\text{yr}^3}\right)^{-2}$, $\lambda_{t_s} = \lambda_{t_e} = 0.03 \left(\frac{\text{nT}}{\text{yr}^2}\right)^{-2}$, $\lambda_0 = 60$, $\lambda_m = 0.65$
Static field	None
Magnetospheric field	
Near-magnetospheric field	$\lambda_{\text{mag}} = 4 \times 10^5 \left(\frac{\text{nT}}{\text{yr}}\right)^{-2}$
Far-magnetospheric field	None
Alignment	
CHAMP	None
Swarm-A	None
Swarm-B	None
CryoSat-2	None
GRACE	None
Calibration*	
CryoSat-2	$\lambda_b = 9.1 \times 10^2 \left(\frac{\text{eu}}{\text{yr}}\right)^{-2}$, $\lambda_s = 9.1 \times 10^{10} \left(\frac{\text{eu}}{\text{nTyr}}\right)^{-2}$, $\lambda_u = 2.8 \times 10^2 \left(\frac{1^\circ}{\text{yr}}\right)^{-2}$
GRACE	$\lambda_b = 1.2 \times 10^3 \left(\frac{\text{eu}}{\text{yr}}\right)^{-2}$, $\lambda_s = 1.2 \times 10^{13} \left(\frac{\text{eu}}{\text{nTyr}}\right)^{-2}$, $\lambda_u = 3.7 \times 10^8 \left(\frac{1^\circ}{\text{yr}}\right)^{-2}$

*Not applicable to Model-A, which was not derived from platform magnetometer data.

The residual statistics are summarized in Tab. 5.5 for the satellite data and Tab. 5.6 for the ground observatory SV data.

Fig. 5.4 shows the time-series of the SV components at six chosen ground observatories together with the computed values from Model-A and Model-B. Overall, the fit of Model-A and Model-B to the ground observatory SV data is good, as expected, for the first five observatory SV shown since these data were used in the model parameter estimation. The computed values of Model-A and Model-B differ especially during the gap from 2010 to 2014, where Model-B can make use of platform magnetometer data in addition to the ground observatory SV data, while Model-A only relies on the ground observatories. That shows that platform magnetometer data contribute to the internal field model especially when there is a lack of calibrated satellite data from CHAMP and *Swarm*. Perhaps even more convincing is the performance of both models when compared to a dataset not used in the inversion. With the SV data from Saint Helena, we show such an independent dataset in the last row of Fig. 5.4. Although both models fit Saint Helena well, Model-B performs slightly better in the radial SV in 2013 and the azimuthal SV at least in the first half of the gap period, until 2012.

To summarize, with Model-B we built a model that fits both the satellite and ground observatory SV data to a satisfactory level, which shows that platform magnetometer data can be successfully used in geomagnetic field modelling.

Table 5.5.: Number N , Huber-weighted mean μ , and standard deviation σ computed from the residuals of the satellite data for each vector component and split into polar (poleward $\pm 55^\circ$) and non-polar (equatorward $\pm 55^\circ$) QD latitudes. Note that non-polar scalar data were not used in the model parameter estimation—statistics are only shown for completeness.

Dataset	QD latitude	Component	N	μ (nT)	σ (nT)
CHAMP	Non-polar	B_r	707131	0.02	1.93
		B_θ	707131	-0.11	2.84
		B_ϕ	707131	0.03	2.32
		F	707131	0.01	1.93
	Polar	F	200084	-0.02	5.10
CryoSat-2 FGM1	Non-polar	B_r	958362	-0.06	4.39
		B_θ	958362	-0.31	5.76
		B_ϕ	958362	0.06	6.49
		F	958362	0.06	4.18
	Polar	F	331097	-0.28	7.56
CryoSat-2 FGM2	Non-polar	B_r	958362	-0.03	6.42
		B_θ	958362	-0.29	6.01
		B_ϕ	958362	0.07	6.55
		F	958362	0.18	4.86
	Polar	F	331097	-1.70	8.21
CryoSat-2 FGM3	Non-polar	B_r	958362	-0.07	4.76
		B_θ	958362	-0.23	5.71
		B_ϕ	958362	0.04	6.80
		F	958362	0.12	4.35
	Polar	F	331097	-1.01	7.86
GRACE-A	Non-polar	B_r	1082071	-0.12	11.40
		B_θ	1082071	-0.24	10.48
		B_ϕ	1082071	-0.79	13.57
		F	1082071	-0.16	10.59
	Polar	F	356988	0.32	15.56
GRACE-B	Non-polar	B_r	997802	-0.30	11.77
		B_θ	997802	-0.69	11.09
		B_ϕ	997802	-0.68	12.35
		F	997802	0.02	11.53
	Polar	F	331516	-0.24	15.56
Swarm-A	Non-polar	B_r	817400	-0.03	1.65
		B_θ	817400	-0.06	2.97
		B_ϕ	817400	-0.02	2.59
		F	817400	-0.03	2.06
	Polar	F	218776	0.22	4.66
Swarm-B	Non-polar	B_r	809720	-0.09	1.63
		B_θ	809720	-0.05	3.02
		B_ϕ	809720	-0.04	2.61
		F	809720	-0.01	2.03
	Polar	F	218106	0.30	4.29

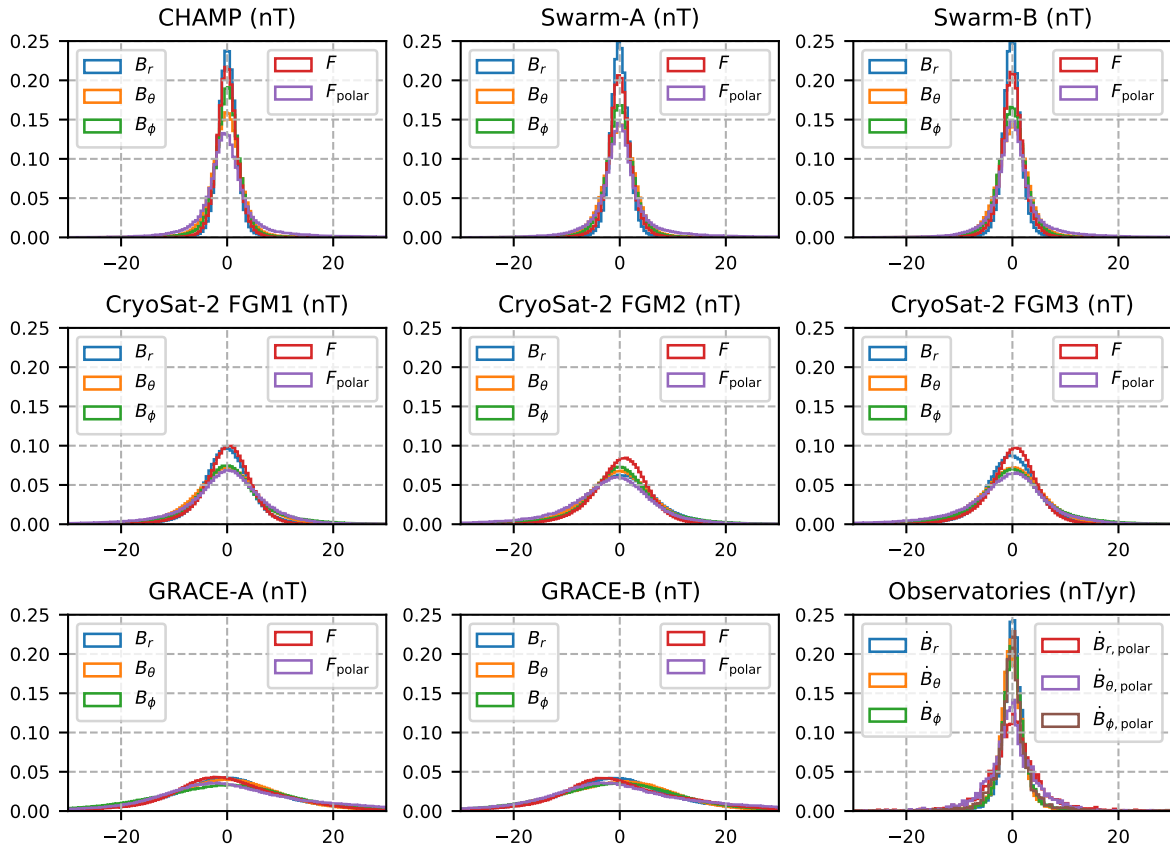


Figure 5.3.: Histograms of the residuals of each satellite and ground observatory SV data using Model-B. The histograms have been normalized to have unit area. Computed statistics are shown in Tab. 5.5 for the satellite data and Tab. 5.6 for the ground observatory SV data.

Table 5.6.: Number N , Huber-weighted mean μ , and standard deviation σ computed from the residuals of the monthly ground observatory SV data for each component and split into polar (poleward $\pm 55^\circ$) and non-polar (equatorward $\pm 55^\circ$) QD latitudes.

Dataset	QD latitude	Component	N	μ (nT/yr)	σ (nT/yr)
Observatories	Non-polar	\dot{B}_r	11348	0.20	2.09
		\dot{B}_θ	11348	-0.18	2.26
		\dot{B}_ϕ	11348	0.06	2.43
Observatories	Polar	\dot{B}_r	3609	0.22	4.43
		\dot{B}_θ	3609	-0.19	4.21
		\dot{B}_ϕ	3609	-0.08	2.85

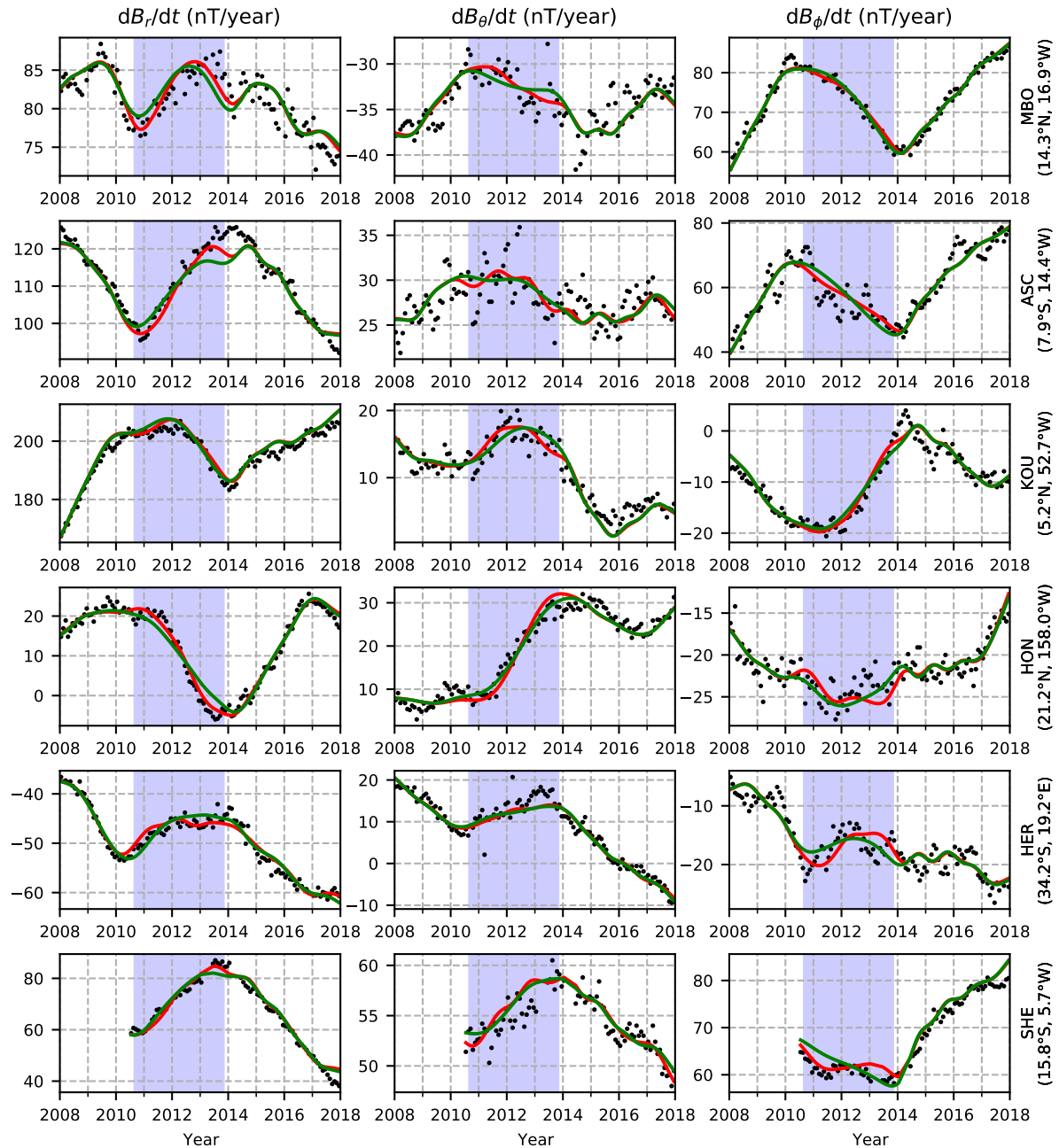


Figure 5.4.: Examples of time-series of monthly ground observatory SV data (black dots) and modelled SV using Model-A (green lines) and Model-B (red lines). The observatory names are MBour (MBO), Ascension (ASC), Kourou (KOU), Honolulu (HON), Hermanus (HER), and Saint Helena (SHE). The SV data of SHE are an independent dataset not used in the inversion. The gap period between CHAMP and *Swarm* is indicated as a blue shaded region (Sep 2010 to Nov 2013).

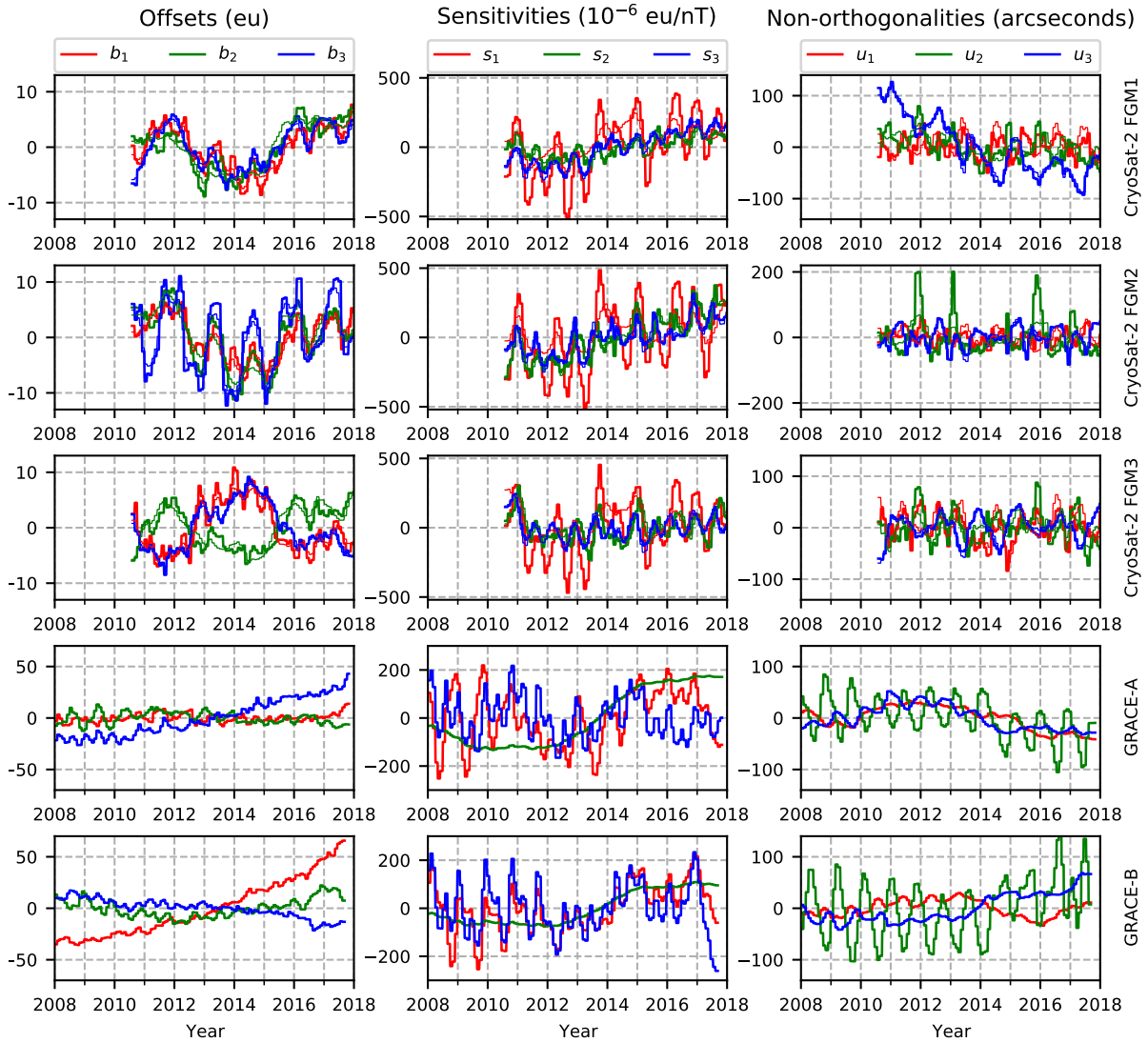


Figure 5.5.: Time series of the calibration parameters of Model-B for each platform magnetometer dataset (thick lines) and calibration parameters of *Olsen et al. (2020)* for CryoSat-2 (thin lines). The respective mean values in time were removed and are listed in Tab. 5.7.

5.5.2. Calibration parameters

We document the estimated calibration parameters of each platform magnetometer dataset by showing the time-series in Fig. 5.5 and the respective mean values in Tab. 5.7. In Fig. 5.5, the rows of panels correspond to the CryoSat-2 (top three) and GRACE (bottom two) platform magnetometer datasets, and the columns of panels show the offsets (left), sensitivities (middle), and non-orthogonality angles (right). Since *Alken et al. (2020)* also used magnetic data from the three platform magnetometers on-board CryoSat-2, it is possible to compare the estimated calibration parameters. First, comparing the time-averaged values of the calibration parameters (Tab. 5.7 here and Tab. 4 in *Alken et al. (2020)*), we find that the non-orthogonalities are equal to within 0.01° and the offsets to within 1 eu. The averaged values of sensitivities are equal to within 1×10^{-4} eu/nT (notice that *Alken et al. (2020)* use the reciprocal of the sensitivity). In terms of the temporal variability, we find that our estimated calibration parameters have amplitudes that are smaller, or equal in case of the offsets, which is likely due to a difference in the regularization strength. In Fig. 5.5, we also show

Table 5.7.: Mean values of the calibration parameters for each platform magnetometer dataset (CS refers to CryoSat-2). The time-series are shown in Fig. 5.5.

Dataset	b_1 (eu)	b_2 (eu)	b_3 (eu)	s_1 (eu/nT)	s_2 (eu/nT)	s_3 (eu/nT)	u_1 (°)	u_2 (°)	u_3 (°)
CS-2 FGM1	5.0	165.6	-10.7	1.005178	1.004851	1.004479	0.453	0.191	-0.336
CS-2 FGM2	77.6	-16.6	61.8	1.004697	1.003993	1.003427	-0.288	0.050	0.502
CS-2 FGM3	-115.2	-29.4	-44.6	1.000863	1.005424	1.002168	0.745	-0.045	-0.000
GRACE-A	746.4	-2632.1	-2310.0	1.034238	1.032041	1.018168	-0.251	-0.161	0.048
GRACE-B	406.0	-2622.0	-2005.6	1.029785	1.026781	1.017845	-0.056	-0.209	0.106

the CryoSat-2 calibration parameters of [Olsen et al. \(2020\)](#) for comparison. Again, the calibration parameters are very similar and differ only in the time variations (e.g., s_1) due to the choice of the regularization parameters of this study and [Olsen et al. \(2020\)](#). Given the acceptable fit to the platform magnetometer data and the reasonable temporal variability of the calibration parameters, we conclude that the calibration of the CryoSat-2 and GRACE platform magnetometers was successful.

5.5.3. Results of the experiments

We conducted a series of experiments in which we changed the model estimation, parameterization, and data selection with the goal to investigate and document difficulties when dealing with platform magnetometer data in a co-estimation scheme. This section also justifies the modelling strategies that went into the construction of our preferred geomagnetic field model, Model-B.

In a first experiment, we allowed the nightside platform magnetometer data to participate in the estimation of the axial dipole coefficient of the time-dependent internal field. That is, we derived a test model, Model-C, identical to Model-B but left the design matrix \mathbf{G} unchanged so that the entries corresponding to the B-spline coefficients $g_{1,i}^0$ were non-zero and, thus, the satellite data contributed to the estimation of the internal dipole coefficients. On the left of Fig. 5.6, we show the time-derivative of g_1^0 as a function of time computed with Model-B and Model-C, while, on the right, we show s_1 of GRACE-A as an example of the calibration parameters. In contrast to Model-B, Model-C features a conspicuous detour of the time-derivative of the g_1^0 coefficient in the gap between CHAMP and *Swarm* data (blue-shaded region). Although we only show s_1 of GRACE-A in Fig. 5.6, we find that all three sensitivities of each platform magnetometer differ in the gap period between Model-C and Model-B. The other internal Gauss coefficients also deviate but to a lesser extent. Interestingly, other model parameters such as the offsets, non-orthogonality angles, Euler angles and external field parameters seem qualitatively unaffected. The same correlation between the internal axial dipole coefficient and the sensitivities has been reported by [Alken et al. \(2020\)](#) who show that this effect can be mitigated either by including large amounts of previously calibrated data or through the use of a regularization that favors a linear time-dependence of the internal dipole during the gap period. Due to the lack of additional calibrated data and our interest in the high-degree SA during the gap that such a regularization affects by redistributing power to higher degrees, we chose to set the dependence of g_1^0 , the most affected internal Gauss coefficient, on the satellite platform magnetometer data to zero. In other words, we completely relied on the ground observatory SV data

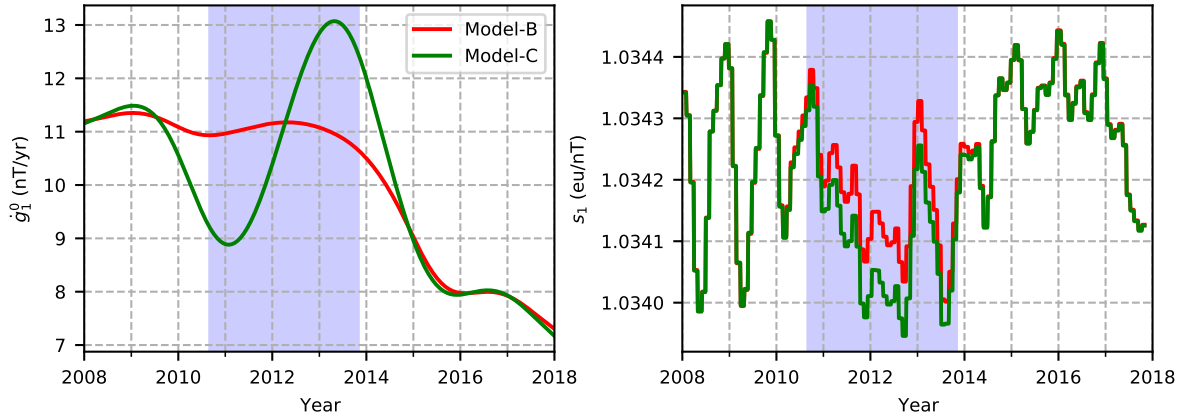


Figure 5.6.: Time-derivative of g_1^0 (left) and sensitivity s_1 for GRACE-A as computed from Model-B and Model-C (right). For Model-C, we allowed nightside platform magnetometer data to contribute to the estimation of the internal g_1^0 Gauss coefficient. The gap period between CHAMP and *Swarm* is indicated as a blue-shaded region (Sep 2010 to Nov 2013).

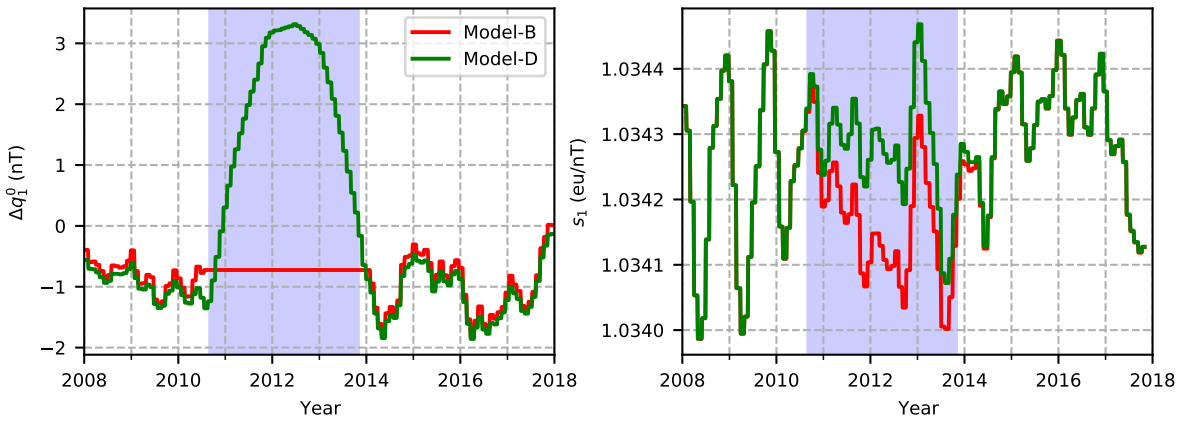


Figure 5.7.: Time series of the RC-baseline correction Δq_1^0 (left) and sensitivity s_1 for GRACE-A as computed from Model-B and Model-D (right). The gap period between CHAMP and *Swarm* is indicated as a blue shaded region (Sep 2010 to Nov 2013). For Model-D, the bins of the RC-baseline corrections are 30 days over the entire model time interval, while they were merged to a single bin in the gap period for Model-B.

and the temporal regularization to estimate the time-dependence of g_1^0 in the gap period.

In a second experiment, we built a test model, Model-D, which uses 30 day bins of the RC-baseline corrections consistently over the whole model time interval in contrast to Model-A and Model-B, which use a single bin spanning the entire gap period. As an example, Fig. 5.7 shows the RC-baseline correction Δq_1^0 on the left and the calibration parameter s_1 of GRACE-A on the right, computed with Model-D and Model-B. In Model-D, Δq_1^0 has a noticeable peak during the gap period that is much larger in value than the variation during CHAMP or *Swarm* times while the sensitivity is slightly offset to higher values. We find the same behavior for all RC-baseline corrections and calibration parameters, although most prominently for the sensitivities. Again, other model parameters seem unchanged, which indicates that there is a significant correlation between the RC-baseline corrections and the calibration parameters of the platform magnetometers. Using a single bin for the RC-baseline corrections in the gap period helps to reduce that effect. As a final comment regarding Model-C and Model-D, we performed a simulation combining both experiments; that is, we determined g_1^0 with

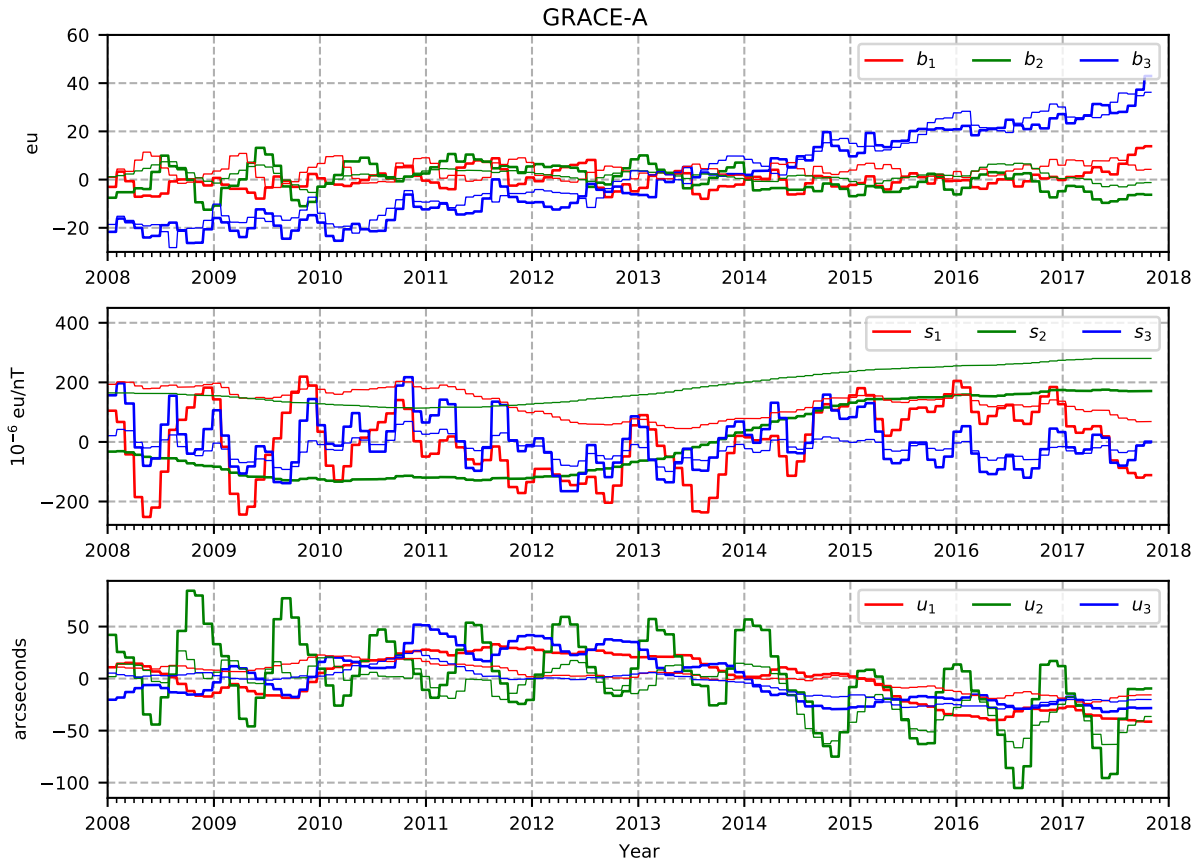


Figure 5.8.: Calibration parameters of GRACE-A computed with Model-B (thick lines) and Model-E (thin lines). We removed the mean values from the calibration parameters as given in Tab. 5.7.

the platform magnetometer data and estimated the *RC*-baseline corrections in 30 day bin over the entire model time interval. In this case, we observed deviations from Model-B which were identical to those shown in Figs. 5.6 and 5.7 but, now, affected the internal axial dipole, the *RC*-baseline corrections, and the sensitivities all at the same time.

In an effort to analyze the relationship between the calibration and the other model parameters in a quantitative manner, we also investigated the model correlations $\rho_{ij} = (\mathbf{C}_m)_{ij} / \sqrt{(\mathbf{C}_m)_{ii}(\mathbf{C}_m)_{jj}}$ based on the entries of the model covariance matrix

$$\mathbf{C}_m = (\mathbf{G}^T \mathbf{C}_d^{-1} \mathbf{G} + \mathbf{\Lambda})^{-1} \quad (5.7)$$

evaluated with the converged model parameters (*Tarantola, 2005*, p. 71). Unfortunately, the analysis revealed a large number of small correlations, which are difficult to interpret. Therefore, we did not make significant use of it in the modelling and preferred to rely on experiments to guide our modelling strategy.

In a final experiment, we derived a test model, Model-E, by only using nightside platform magnetometer data as opposed to Model-B, where the calibration parameters were determined from dayside and nightside platform magnetometer data. Fig. 5.8 shows the calibration parameters for GRACE-A computed with Model-B (thick lines) and Model-E (thin lines). In the case of GRACE-A, using dayside data to determine the calibration parameters considerably changes the sensitivities and

non-orthogonalities as can be seen, for example, when looking at s_1 , s_2 or u_3 . In particular for s_2 , there is a vertical shift of approximately 200×10^{-6} eu/nT, which translates to 10 nT in a magnetic field of 50,000 nT. Irrespective of the platform magnetometer, the experiment shows that the local time coverage of the data plays an important role in determining the calibration parameters. The importance of using both day and nightside data becomes clear when appreciating that the orbital plane of the satellites is slowly drifting in local time. Under a possible nightside data selection criteria, the drift leads to the selection of data from either the ascending or descending parts of the orbit at a time. For example, if the ascending node of the orbit is on the nightside, then the platform magnetometer collects data of the magnetic field that mostly points along the direction of flight, in agreement with the predominant dipolar field configuration, until the ascending node crosses over to the dayside placing the descending part of the orbit on the nightside. Now, the observed magnetic field mostly points against the direction of flight. In the case of CryoSat-2, it takes the ascending node 8 months and GRACE around 11 months to traverse the nightside, which is longer than the monthly bins used for estimating the calibration parameters. Hence, the data of each bin will be collected either from the ascending or descending nodes with the respective bias of the field direction. Instead, by using both nightside and dayside, we ensured that the data within each bin covered a broad range of local times to excite the platform magnetometer from various directions, which we believe improves the estimation of the calibration parameters. Nevertheless, we did not use any dayside data to constrain the geomagnetic field model since we do not account for the strong ionospheric sources on the dayside. Those ionospheric sources, however, may contaminate the calibration parameters.

5.5.4. Secular acceleration

One motivation for using platform magnetometer data has been the growing interest in SA pulses, enhancements of the SA that occur on sub-decadal time-scales and are seen most prominently at low latitudes. These pulses have been reported by several studies ([Olsen and Manda, 2007](#); [Chulliat et al., 2010](#); [Chulliat and Maus, 2014](#)) and are thought to reflect the dynamical processes in the Earth's outer core. To further study SA pulses and the SA in general, accurate internal field models are needed, which rely on long and continuous time-series of satellite data to give a global picture. When supplemented with high quality satellite data, platform magnetometer data may play an important role in providing those models.

To investigate the effect of platform magnetometer data on the recovered SA, we show in Fig. 5.9 time-longitude maps of the radial SA on the Equator at the CMB computed with Model-B (left) and Model-A (center) alongside the difference map (right). Recall that Model-B is partly based on platform magnetometer data in contrast to Model-A, so that the difference of the two reflects the use of these data. Both models show the SA pulses in 2009, 2013 and most recently in 2017 as enhancement of the radial SA on the Equator. Of special interest is the pulse in 2013, right in between periods of high-quality magnetic data from the CHAMP and *Swarm* missions. In the difference map, the SA during CHAMP and *Swarm* period is largely unchanged, which suggests that the effect of the CryoSat-2 and GRACE data is rather minimal during these times. In contrast, the SA in the gap period is distinctly different for the two models. Differences that are large in absolute value seem to be concentrated around 0° and 180° longitude on the Equator which coincides with the

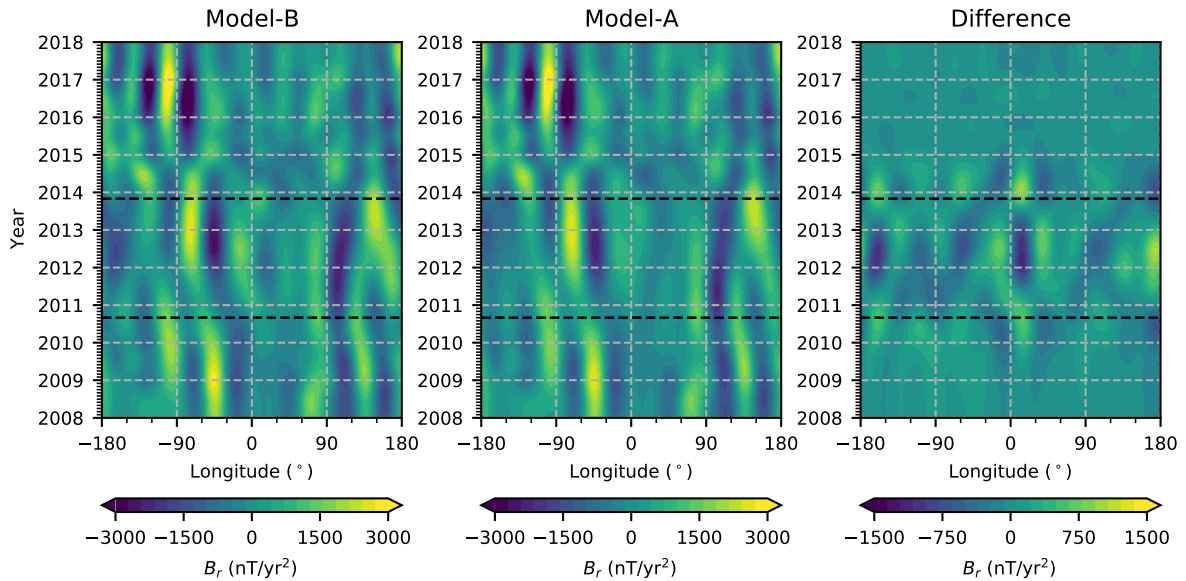


Figure 5.9.: Time-longitude maps of the radial SA up to degree 10 on the Equator at the CMB as computed with Model-B (left), Model-A (center) and their difference, Model-B minus Model-A (right). The gap period between CHAMP and *Swarm* is in between the black dashed lines (Sep 2010–Nov 2013).

Pacific and the region in the South Atlantic close to Central Africa. The geographical location of the differences is more clearly seen in Fig. 5.10, which shows global maps of the radial SA at the CMB during the SA pulses in 2009, 2013 and 2017. Again, the difference between Model-B and Model-A is small in 2009 and 2017, i.e. during CHAMP and *Swarm* times, but large in 2013 in the middle of the gap period. The regions with the largest differences are located in the Southern hemisphere and the Equatorial region with prominent examples in the West and South Pacific Ocean, and Central Africa. Our findings seem to indicate that the platform magnetometers have the desired effect of balancing the uneven spatial distribution of the ground observatory network in the gap period.

5.6. Conclusions

In this study, we present a co-estimation scheme within the framework of the CHAOS field model series that is capable of estimating both a geomagnetic field model and, at the same time, calibration parameters for platform magnetometers. This approach enables us to use platform magnetometer data to supplement high-quality magnetic data from magnetic survey satellites and removes the requirement for utilizing a-priori geomagnetic field models to calibrate platform magnetometer data.

We followed [Alken et al. \(2020\)](#) but went further in that we co-estimated a model of not only the internal field but also the external field. The co-estimation scheme relies on absolute magnetic data which we took from CHAMP, *Swarm*-A, *Swarm*-B and the monthly SV data from ground observatories between 2008 and 2018. Magnetic data from five platform magnetometers were used: three on-board *CryoSat*-2 and one on-board each of the *GRACE* satellite pair. This allowed us to considerably improve the geographical and temporal coverage of satellite data after CHAMP and before the launch of the *Swarm* satellites.

We successfully co-estimated a geomagnetic field model along with calibration parameters of the five platform magnetometers. The misfit to the high-quality satellite data and ground observatory

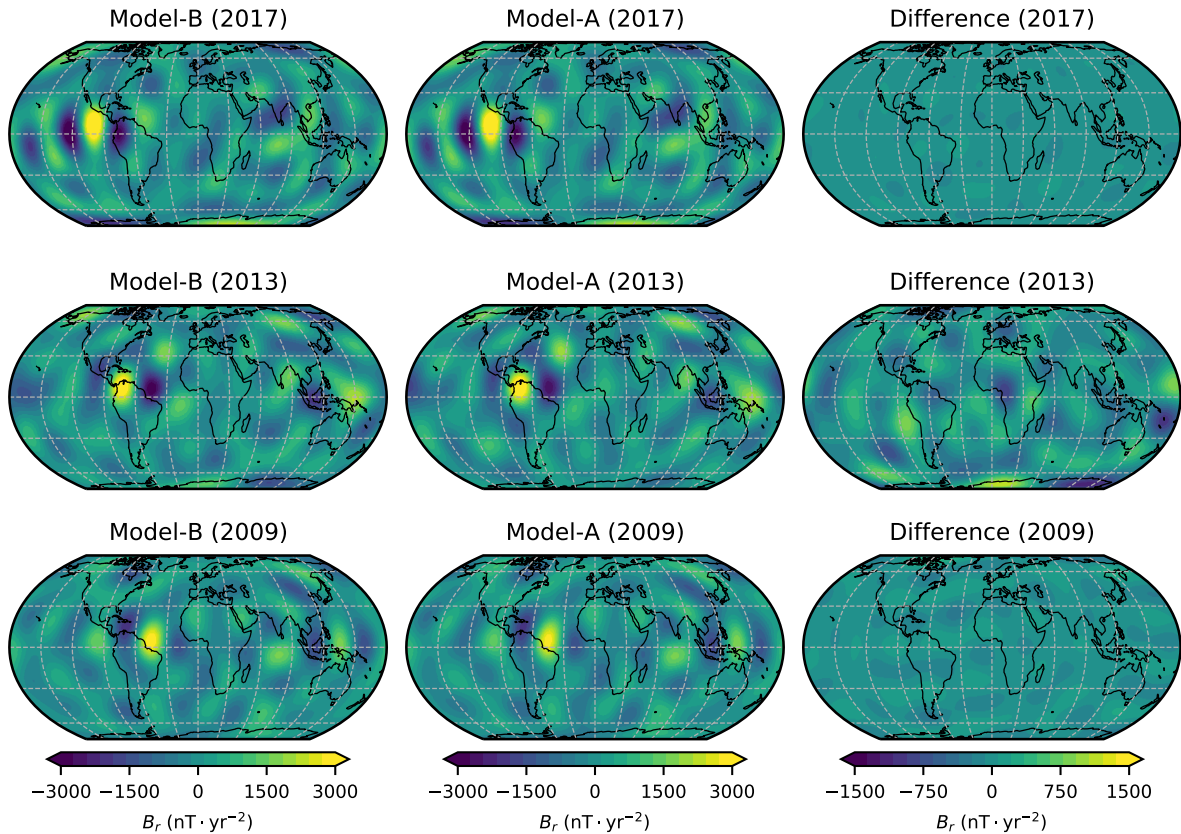


Figure 5.10.: Global maps of the radial SA up to degree 10 at the CMB for Model-B (left column), Model-A (center column) and the difference (right column). The maps are computed in 2009 (bottom row), 2013 (center row) and 2017 (top row). The projection is Equal Earth ([Šavrič et al., 2018](#)).

SV data was similar to that for models derived without including platform magnetometer data, and the good fit to an independent ground observatory dataset from Saint Helena provide evidence that our modelling approach performs well.

In a series of experiments we investigated the trade-offs when co-estimating calibration and geomagnetic field model parameters. We found that the calibration parameters strongly correlate with the internal axial dipole and the *RC*-baseline corrections of the external field during the gap period, when there is less high-quality data available. By preventing platform magnetometer data from contributing to the internal axial dipole and using constant *RC*-baseline corrections throughout the entire gap period, we successfully avoided those complications.

Our experiments showed that including platform magnetometer data leaves the SA signal practically unchanged during the CHAMP and *Swarm* period but leads to differences in the gap period. The difference in the recovered SA signal is stronger in the West and South Pacific, where only a few observatories are located, which suggests that platform magnetometer data help to improve the global picture of the SA. Based on our investigations, we find that it is worthwhile to include platform magnetometer data in internal field modelling, in particular from CryoSat-2 given the relative low noise level.

6. Co-estimating models of polar ionospheric fields in geomagnetic field modelling

In this chapter, I report on a series of field models that account for the currents in the polar ionosphere based on a parameterization previously used in the the AMPS model of [Laundal et al. \(2017\)](#). By examining those test models, which essentially vary in the way they are parameterized, I explore how best to optimize the setup for geomagnetic field modelling. I then go on to study the resulting field model in more detail focusing on two aspects. First, considering the ionospheric part of the model, I investigate the climatological nightside polar current system under quiet conditions. Second, I examine the effect of co-estimating an ionospheric model on the high-latitude core field and the SV. The results are finally discussed in the context of whether such a co-estimation can help improve our knowledge of the quiet-time ionospheric current system and, thus, contribute to the development of improved geomagnetic field models.

Earlier studies have tried to account for the ionospheric field within geomagnetic field modelling. The first generation GFZ Reference Internal Magnetic Model (GRIMM) ([Lesur et al., 2008](#)) includes a model of the magnetic field produced by the currents in the polar ionosphere. This polar ionospheric field is modelled through a scalar magnetic potential, associated with the currents in the ionospheric E-layer, and a toroidal potential, associated with radial field-aligned currents in the ionospheric F-layer. Each potential is expanded into a basis of localized functions in spherical geocentric coordinates confined to the polar regions, poleward of $\pm 55^\circ$ dipole latitude. The expansion coefficients have a time-dependence that consists of a constant term and an annual variation. [Lesur et al. \(2008\)](#) used the full vector satellite data from all local times to allow the separation between the internal field and the ionospheric field during the model estimation. However, they did not co-estimate the internal and ionospheric fields but had to use a sequential estimation procedure whereby the ionospheric field model was estimated with the residuals obtained by first fitting the data to the non-ionospheric part of GRIMM, i.e. the model of the internal field, the large-scale external field and associated internally-induced counterparts. They concluded that the internal and ionospheric field models cannot be separated unless better ways of parameterizing the ionospheric current systems are available. Consequently, for the second generation of GRIMM, [Lesur et al. \(2010\)](#) decided to remove the ionospheric field model altogether, also because, as they argue, its estimation only resulted in a marginal improvement of the fit to the data.

In the CM6 model ([Sabaka et al., 2020](#)) the ionospheric field produced by the currents confined to the ionospheric E-layer is represented by a magnetic scalar potential. This potential is spatially parameterized in terms of a basis of QD symmetric functions, which are linear combinations of spherical harmonics in magnetic dipole coordinates and follow the overall geometry of Earth's magnetic field. The coefficients of this ionospheric E-layer potential are periodic in time with daily and sub-daily periods of 24 h, 12 h, 8 h and 6 h, which are further modulated by annual and semi-annual period-

icities and scaled by a 3-month running average of the $F_{10.7}$ -index. [Sabaka et al. \(2020\)](#) applied a regularization to smooth the nightside currents in the ionospheric E-layer at 110 km. The CM5 and earlier models ([Sabaka et al., 2015](#)) also included a parameterization of the toroidal field in the ionospheric F-layer. In CM5, there are two toroidal potentials, one centered on the Ørsted sampling shell at 750 km and one centered on the CHAMP sampling shell at 400 km above Earth's surface. These potentials are expanded into the QD symmetric basis similar to the ionospheric E-layer potential. The CM6 approach is able to represent the ionospheric field and internally-induced part but is restricted to specific periodicities. However, the solar wind driving of the ionospheric currents also leads to signals with different frequencies, which are, therefore, not well represented in CM6. This stresses the need for a parameterization that takes the underlying driving processes properly into account.

6.1. Modelling of the ionospheric magnetic field

Satellites in low-Earth orbit measure the magnetic field at an altitude between 160–1000 km (e.g. around 450 km for *Swarm*) in the F-region of the ionosphere. Here the satellites fly above the mostly horizontal currents, which form a thin sheet around 110 km above the Earth's surface in the E-layer of the ionosphere, but pass through intermittent field-aligned electric currents that connect the E-layer below the satellites with the magnetospheric current system above. At polar latitudes it is appropriate to assume that the field-aligned currents are purely radial. Therefore, the ionospheric magnetic field can be written as ([Laundal et al., 2016](#))

$$\mathbf{B}^{\text{ion}} = -\nabla\psi^{\text{ion}} + \mathbf{r} \times \nabla T^{\text{ion}}, \quad (6.1)$$

where ψ^{ion} is associated with the divergence-free part of the horizontal currents in the E-layer, which are internal with respect to low-Earth orbit satellites, and T^{ion} is associated with the in-situ field-aligned currents at the height of the satellite in the polar F-layer. The first term $-\nabla\psi^{\text{ion}}$ is a gradient field, which I refer to as the ionospheric E-layer field, while the second term $\mathbf{r} \times \nabla T^{\text{ion}}$ is a toroidal magnetic field.

Following [Laundal et al. \(2016\)](#), the potentials are expanded into spherical harmonics using the non-orthogonal magnetic apex coordinate systems ([Richmond, 1995](#))

$$\psi^{\text{ion}}(h, \theta_{\text{QD}}, \phi_{\text{MLT}}, t) = a \sum_{n=1}^{N^{\text{ion}}} \sum_{\substack{m=-n \\ |m| \leq M}}^n \left(\frac{a}{a+h} \right)^{n+1} g_n^{m,\text{ion}}(t) Y_n^m(\theta_{\text{QD}}, \phi_{\text{MLT}}) \quad (6.2a)$$

$$T^{\text{ion}}(\theta_{\text{MA}}, \phi_{\text{MLT}}, t) = \sum_{n=1}^{N^{\text{tor}}} \sum_{\substack{m=-n \\ |m| \leq M}}^n T_n^{m,\text{ion}}(t) Y_n^m(\theta_{\text{MA}}, \phi_{\text{MLT}}), \quad (6.2b)$$

where N^{ion} is the truncation degree of ψ^{ion} , N^{tor} is the truncation degree of T^{ion} , M is the truncation order, h is the geodetic height, $\theta_{\text{QD}} = 90^\circ - \lambda_{\text{QD}}$ is the QD colatitude, $\theta_{\text{MA}} = 90^\circ - \lambda_{\text{MA}}$ is the MA colatitude, and ϕ_{MLT} is the magnetic local time (MLT) in degrees defined as

$$\phi_{\text{MLT}} = \phi - \phi_{\text{noon}} + 180^\circ, \quad (6.3)$$

where ϕ and ϕ_{noon} are the dipole longitudes of the apex and the subsolar point, respectively (see Sec. 2.1.1 for definitions of magnetic apex coordinates).

The advantage of magnetic apex coordinates is that they are based on the geometry of Earth's magnetic field as given by the IGRF model. And, since the ionospheric currents are strongly organized by the Earth's magnetic field, the magnetic apex coordinates are well suited to describe the produced ionospheric magnetic field and may potentially allow for mathematical expressions that have fewer parameters (*Sabaka et al., 2002*). In Eq. (6.2) both types of magnetic apex coordinates are used. The height-independent MA latitude is appropriate for T^{ion} , which is approximately constant along field lines (*Matsuo et al., 2015*), whereas the height-dependent QD latitude is used for ψ^{ion} to account for the radial dependence of the magnetic field produced by the remote currents in the E-layer of the ionosphere. Moreover, magnetic apex longitude has been replaced with magnetic local time since the ionospheric magnetic field structure follows the position of the sun. Finally, Eq. (6.2) includes a truncation order which allows for a lower resolution in longitude than latitude. This is possible because the structure of the large-scale average of the ionospheric currents has been found to have a similar asymmetry in the spatial resolution (*Weimer, 2001, 2013*).

Differentiating the potentials in Eq. (6.2) according to Eq. (6.1) with respect to the magnetic apex coordinates produces the ionospheric magnetic field components

$$\begin{aligned} \mathbf{B}^{\text{ion}} = & -\frac{1}{a+h} \left(\frac{1}{\sin \theta_{\text{QD}}} \frac{\partial \psi^{\text{ion}}}{\partial \phi_{\text{MLT}}} \mathbf{f}_2 \times \mathbf{k} + \frac{\partial \psi^{\text{ion}}}{\partial \theta_{\text{QD}}} \mathbf{f}_1 \times \mathbf{k} \right) - \sqrt{|\mathbf{f}_1 \times \mathbf{f}_2|} \frac{\partial \psi^{\text{ion}}}{\partial h} \mathbf{k} \\ & + \left(\frac{1}{\sin \theta_{\text{MA}}} \frac{\partial T^{\text{ion}}}{\partial \phi_{\text{MLT}}} \mathbf{k} \times \mathbf{d}_1 + \frac{\sqrt{4 - 3 \sin^2 \theta_{\text{MA}}}}{2 \cos \theta_{\text{MA}}} \frac{\partial T^{\text{ion}}}{\partial \theta_{\text{MA}}} \mathbf{k} \times \mathbf{d}_2 \right) \end{aligned} \quad (6.4)$$

where \mathbf{k} is the upward pointing unit vector (or vertical) relative to GD coordinates, $\{\mathbf{d}_1, \mathbf{d}_2, \mathbf{f}_1, \mathbf{f}_2\}$ are the non-orthogonal base vectors of the magnetic apex coordinate systems expressed in terms of geodetic components (*Richmond, 1995*). The base vectors can be computed with a software published by *Emmert et al. (2010)*, for which a Python wrapper is also available (*Meeren et al., 2018*). As the reference height, which is part of the definition of the apex coordinates, I chose $h_{\text{R}} = 110$ km in accordance with *Laundal et al. (2017)*, which is approximately the height of the most conductive sheet in the E-layer of the ionosphere.

The ionospheric currents associated with the ionospheric magnetic field can be calculated with $\mathbf{J} = \frac{1}{\mu_0} \nabla \times \mathbf{B}$. According to *Richmond (1995)*, the magnetic field components in Eq. (6.4) can be approximately related to currents in the apex coordinate system by treating the apex and MLT coordinates as orthogonal spherical coordinates with $a+h$ as the geocentric radius. Hence, the ionospheric currents follow directly from the potentials in Eq. (6.2) with the ∇ -operator in spherical coordinates. The ionospheric currents are typically decomposed into an height-integrated horizontal current density \mathbf{J}^{sh} (sheet current density) and a vertical current density consisting of the single component J_{\parallel} along the upward direction. J_{\parallel} can be interpreted as the field-aligned currents (Birkeland currents) in the polar regions, where the magnetic field lines are assumed radial and, thus, almost parallel to the upward direction. Furthermore, \mathbf{J}^{sh} can be written as

$$\mathbf{J}^{\text{sh}} = \mathbf{J}^{\text{df}} + \mathbf{J}^{\text{cf}} = \mathbf{k} \times \nabla \psi^{\text{df}} + \nabla \psi^{\text{cf}}, \quad (6.5)$$

where the divergence-free part \mathbf{J}^{df} is expressed in terms of the current function ψ^{df} and the curl-free

part \mathbf{J}^{cf} in terms of the current potential ψ^{cf} . In contrast to the representation of the ionospheric magnetic field in terms of the potentials in Eq. (6.2), there is an ambiguity in the height at which to calculate \mathbf{J}^{sh} . In agreement with [Laundal et al. \(2017\)](#), I chose the height to be equal to the reference height h_{R} of the apex coordinates so that the current function and current potential (both in units of μA) are given by

$$\psi^{\text{df}} = -\frac{a}{\mu_0} \sum_{n=1}^{N^{\text{ion}}} \sum_{\substack{m=-n \\ |m| \leq M}}^n \frac{2n+1}{n} \left(\frac{a}{a+h_{\text{R}}} \right)^{n+1} g_n^{m,\text{ion}} Y_n^m(\theta_{\text{QD}}, \phi_{\text{MLT}}) \quad (6.6a)$$

$$\psi^{\text{cf}} = -\frac{a+h_{\text{R}}}{\mu_0} \sum_{n=1}^{N^{\text{tor}}} \sum_{\substack{m=-n \\ |m| \leq M}}^n T_n^{m,\text{ion}} Y_n^m(\theta_{\text{MA}}, \phi_{\text{MLT}}), \quad (6.6b)$$

where the units are $[a] = [h_{\text{R}}] = \text{km}$, $[g_n^{m,\text{ion}}] = [T_n^{m,\text{ion}}] = \text{nT}$ and $[\mu_0] = \text{H m}^{-1} = \text{T m A}^{-1}$. The magnetic eastward and northward components of \mathbf{J}^{df} (units of mA m^{-1}) are then written as

$$J_{\text{e}}^{\text{df}} = -\frac{10^6}{\mu_0} \sum_{n=1}^{N^{\text{ion}}} \sum_{m=0}^{\min(n,M)} \left\{ \frac{2n+1}{n} \left(\frac{a}{a+h_{\text{R}}} \right)^{n+2} \cdot [g_n^{m,\text{ion}} \cos(m\phi_{\text{MLT}}) + g_n^{-m,\text{ion}} \sin(m\phi_{\text{MLT}})] \frac{d\mathcal{P}_n^m(\cos\theta_{\text{QD}})}{d\theta_{\text{QD}}} \right\} \quad (6.7a)$$

$$J_{\text{n}}^{\text{df}} = \frac{10^6}{\mu_0} \sum_{n=1}^{N^{\text{ion}}} \sum_{m=0}^{\min(n,M)} \left\{ \frac{2n+1}{n} \left(\frac{a}{a+h_{\text{R}}} \right)^{n+2} \cdot m [g_n^{m,\text{ion}} \sin(m\phi_{\text{MLT}}) - g_n^{-m,\text{ion}} \cos(m\phi_{\text{MLT}})] \frac{\mathcal{P}_n^m(\cos\theta_{\text{QD}})}{\sin\theta_{\text{QD}}} \right\} \quad (6.7b)$$

and the horizontal magnetic components of \mathbf{J}^{cf} (units of mA m^{-1}) as

$$J_{\text{e}}^{\text{cf}} = \frac{10^6}{\mu_0} \sum_{n=1}^{N^{\text{tor}}} \sum_{m=0}^{\min(n,M)} m [T_n^{m,\text{ion}} \sin(m\phi_{\text{MLT}}) - T_n^{-m,\text{ion}} \cos(m\phi_{\text{MLT}})] \frac{\mathcal{P}_n^m(\cos\theta_{\text{MA}})}{\sin\theta_{\text{MA}}} \quad (6.8a)$$

$$J_{\text{n}}^{\text{cf}} = \frac{10^6}{\mu_0} \sum_{n=1}^{N^{\text{tor}}} \sum_{m=0}^{\min(n,M)} [T_n^{m,\text{ion}} \cos(m\phi_{\text{MLT}}) + T_n^{-m,\text{ion}} \sin(m\phi_{\text{MLT}})] \frac{d\mathcal{P}_n^m(\cos\theta_{\text{MA}})}{d\theta_{\text{MA}}}. \quad (6.8b)$$

Finally, the vertical current density (units of $\mu\text{A m}^{-2}$) can be computed from the current continuity condition $J_u = -\nabla \cdot \mathbf{J}^{\text{cf}}$ and is given by

$$J_u = -\frac{10^6}{\mu_0(a+h)} \sum_{n=1}^{N^{\text{tor}}} \sum_{\substack{m=-n \\ |m| \leq M}}^n n(n+1) T_n^{m,\text{ion}} Y_n^m(\theta_{\text{MA}}, \phi_{\text{MLT}}). \quad (6.9)$$

Following the parameterization of the AMPS model ([Laundal et al., 2017](#)), the spherical harmonic coefficients of the scalar and toroidal potentials in Eq. (6.2) are expanded in time

$$g_n^{m,\text{ion}}(t) = g_{n,0}^{m,\text{ion}} + \sum_{i=1}^{18} g_{n,i}^{m,\text{ion}} X_i(t), \quad (6.10)$$

where the X_i , $i = 1, \dots, 18$ are base functions which contain different combinations of external parameters to describe the response of the ionosphere driven by the time-varying solar wind and the IMF

$$\begin{aligned}
X_1 &= \sin \theta_c & X_2 &= \cos \theta_c \\
X_3 &= \epsilon & X_4 &= \epsilon \sin \theta_c & X_5 &= \epsilon \cos \theta_c \\
X_6 &= \beta_{\text{tilt}} & X_7 &= \beta_{\text{tilt}} \sin \theta_c & X_8 &= \beta_{\text{tilt}} \cos \theta_c \\
X_9 &= \epsilon \beta_{\text{tilt}} & X_{10} &= \epsilon \beta_{\text{tilt}} \sin \theta_c & X_{11} &= \epsilon \beta_{\text{tilt}} \cos \theta_c \\
X_{12} &= \tau & X_{13} &= \tau \sin \theta_c & X_{14} &= \tau \cos \theta_c \\
X_{15} &= \tau \beta_{\text{tilt}} & X_{16} &= \tau \beta_{\text{tilt}} \sin \theta_c & X_{17} &= \tau \beta_{\text{tilt}} \cos \theta_c \\
X_{18} &= F_{10.7}.
\end{aligned} \tag{6.11}$$

The coefficients $g_{n,0}^{m,\text{ion}}, \dots, g_{n,18}^{m,\text{ion}}$ (similarly for $T_n^{m,\text{ion}}$) are 19 unknowns for each spherical harmonic coefficient that need to be determined by the model estimation procedure. The external parameters in Eq. (6.11) are mostly derived from solar wind parameters and include the IMF clock angle

$$\theta_c = \arctan2(B_{\text{IMF},y}, B_{\text{IMF},z}), \tag{6.12}$$

where $B_{\text{IMF},y}$ and $B_{\text{IMF},z}$ are the cartesian components of the IMF in GSM coordinates; the dipole tilt angle

$$\beta_{\text{tilt}} = \arcsin(\mathbf{s} \cdot \mathbf{m}_{\text{dip}}), \tag{6.13}$$

where \mathbf{s} is the unit vector in the direction of the sun and \mathbf{m}_{dip} is the unit vector along the geomagnetic dipole axis; the solar wind-magnetospheric coupling function ([Newell et al., 2007](#)) in mV m^{-1}

$$\epsilon = 10^{-3} |v_x|^{4/3} B_t^{2/3} \sin^{8/3} \frac{|\theta_c|}{2}, \tag{6.14}$$

where v_x is the solar wind speed in km s^{-1} along the x-axis of the GSM coordinate system and $B_t = \sqrt{B_{\text{IMF},y}^2 + B_{\text{IMF},z}^2}$; a similar coupling function that maximizes for northward IMF conditions ($B_{\text{IMF},z} > 0$) in mV m^{-1}

$$\tau = 10^{-3} |v_x|^{4/3} B_t^{2/3} \cos^{8/3} \frac{\theta_c}{2} \tag{6.15}$$

and the solar radio (10.7 cm) flux index, $F_{10.7}$, which is used as a measure of the solar irradiation level on the ionosphere. Except for β_{tilt} and the $F_{10.7}$ index, the external parameters are derived from measured solar wind parameters $B_{\text{IMF},y}$, $B_{\text{IMF},z}$, and v_x . The tilt angle undergoes a yearly variation between $\pm 23.3^\circ$ with zero crossings at equinoxes and has a superimposed daily variation of approximately $\pm 10^\circ$.

Eqs. (6.10) and (6.11) are taken from [Laundal et al. \(2017\)](#), who modified the temporal parameterization that [Weimer \(2013\)](#) used in a spherical harmonics model of the ground magnetic field perturbations. Through an empirical approach, [Weimer \(2013\)](#) found the best performing model parameterization by defining each expansion coefficient as a linear combination of the IMF magnitude in the GSM y-z plane, dipole tilt angle, solar wind speed, $F_{10.7}$ index, and a second order Fourier series in the clock angle. The latter was chosen since it reproduces the non-linear response of the ionosphere well. [Laundal et al. \(2017\)](#) made then two adjustments by combining the magnitude

of the IMF in the GSM y - z and solar wind speed in the coupling functions ϵ and τ , and adding pairwise products of the external parameters with the exception of the $F_{10.7}$ index, which remained a single term. Using these multiplicative cross terms prevented large values of one external parameter from completely dictating the parameterization. However, as this increased the number of model parameters, [Laundal et al. \(2017\)](#) limited the Fourier series to first order terms.

6.2. Satellite and ground observatory data

For the models reported in this chapter, I used satellite data from CHAMP and the three *Swarm* satellites (Swarm-A, Swarm-B, and Swarm-C) supplemented with annual differences of revised monthly mean values from ground observatories (Sec. 2.1.2) in the time interval between January 2005 and the end of December 2019.

From the CHAMP mission, I used vector data of the Level 3 1 Hz magnetic data product, version CH-ME-3-MAG ([Rother and Michaelis, 2019](#)), between January 2005 and the end of August 2010 with a 45 s sampling period. I did not reject any vector data if only one of the two STRs was in operation since a rejection caused data gaps around the equatorial region during dusk and dawn which impacted the determination of the ionospheric field. From the *Swarm* mission, I worked with vector data from the Level 1b 1 Hz magnetic data product, baseline 0505/0506, from November 2013 to the end of December 2019 with 135 s sampling. The sampling period of the *Swarm* data is three times the one of the CHAMP data to have approximately the same amount of satellite data per time interval during the CHAMP and *Swarm* periods.

I selected satellite data according to the geomagnetically quiet conditions laid out by [Finlay et al. \(2020\)](#), which are favorable for estimating a model of the internal field. In particular, I kept satellite data if they satisfied the following criteria at the time of measurement:

- $Kp \leq 2\sigma$ at the observation time
- hourly RC -index changed at most 2 nT h^{-1} ,
- $\epsilon < 2.4 \text{ mV m}^{-1}$ at the magnetopause when averaged over the previous 2 h,
- $B_{\text{IMF},z} > 0$ at the magnetopause when averaged over the previous 2 h,
- $B_{\text{IMF},y} < 3 \text{ nT}$ at the magnetopause when averaged over the previous 2 h for satellite data on the northern QD hemisphere and $B_{\text{IMF},y} > -3 \text{ nT}$ on the southern QD hemisphere.

The IMF components and other solar wind parameters needed for computing ϵ at the magnetopause are available at 1 min time resolution from NASA/GSFC's OMNI dataset ([King and Papitashvili, 2005](#)) through OMNIWeb¹. In contrast to [Finlay et al. \(2020\)](#), I did not select the satellite data depending on the zenith angle of the sun since magnetic data from all local times is needed to estimate a model of the ionospheric magnetic field. However, I modified the model estimation procedure (Sec. 6.4) in an effort to reduce the impact of solar driven ionospheric currents on the estimation of the internal and magnetospheric parts of the geomagnetic field model. More specifically, I only allowed data in darkness as indicated by the sun's zenith angle χ with

¹<https://omniweb.gsfc.nasa.gov/ow.html>

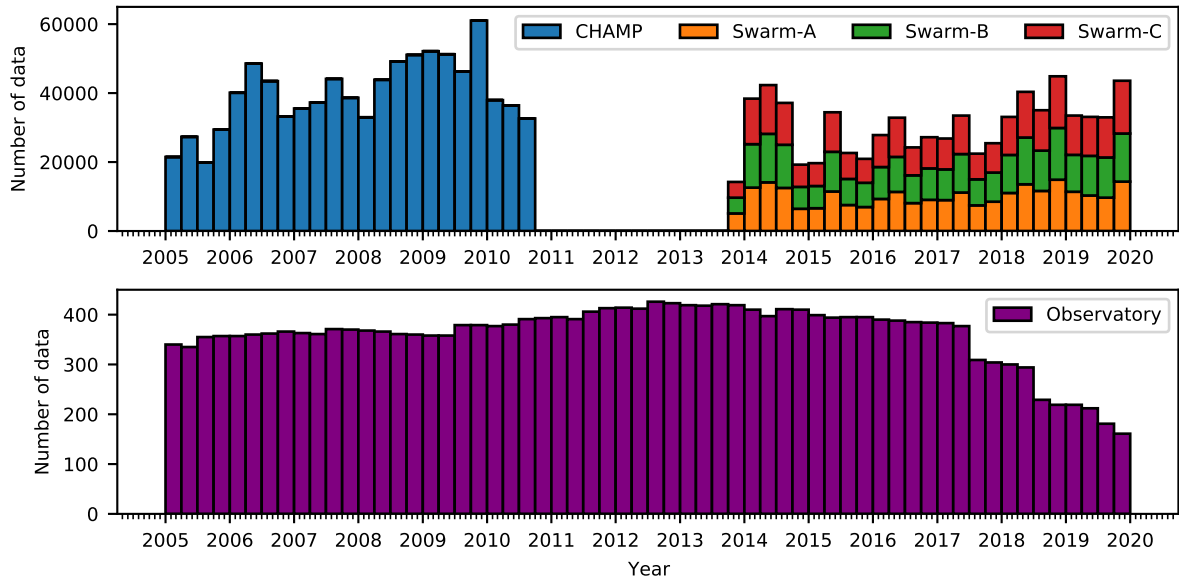


Figure 6.1.: Amount of selected satellite data as stacked histogram (upper panel) and the amount of ground observatory data (lower panel) every 3 months.

- $\chi \geq 100^\circ$ at the time of measurement

to determine the internal and magnetospheric part of the model. Fig. 6.1 shows the amount of data every 3 months as stacked histograms over the entire model time period.

To include a model of the ionospheric magnetic field of the form described in Eq. (6.10), I adopted the approach of [Laundal et al. \(2017\)](#) and derived the solar wind driving parameters θ_c , τ and ϵ , based on 1 min parameters mapped to the magnetopause, followed by averaging over the previous 20 min. This choice of temporal averaging is motivated by the 10–20 min it takes the global current system to directly react to changes in the solar wind driving ([Snekvik et al., 2017](#)). Some amount of averaging is desirable since averaged values may better represent the large-scale structure of the solar wind at the magnetopause in contrast to the actual measurements of the solar wind, which are taken in-situ at the location of the solar wind monitor at $\approx 240a$ ahead of the Earth on the Earth-sun line and then propagated to the magnetopause. Furthermore, I used daily values of the $F_{10.7}$ -index (Sec. 2.4.3). Finally, I linearly interpolated the solar wind driving parameters and the $F_{10.7}$ -index onto the time of the satellite data. To get a better understanding of the conditions that are represented in the selected data, I show in Fig. 6.2 the distribution of satellite data after data selection and in dependence of the external parameters and magnetic apex coordinates.

6.3. Model parameterization

The model parameterization adopted in this chapter closely follows that of the CHAOS model series ([Olsen et al., 2006a, 2009, 2010c, 2014](#); [Finlay et al., 2015, 2016b, 2020](#)) except for additional terms that represent the contribution of the ionospheric current system. In correspondence with the selected magnetic data, the model is defined between 2005.0 and 2020.0 in decimal years. Tab. 6.1 summarizes the different parts of the model and more details are given in the following paragraphs.

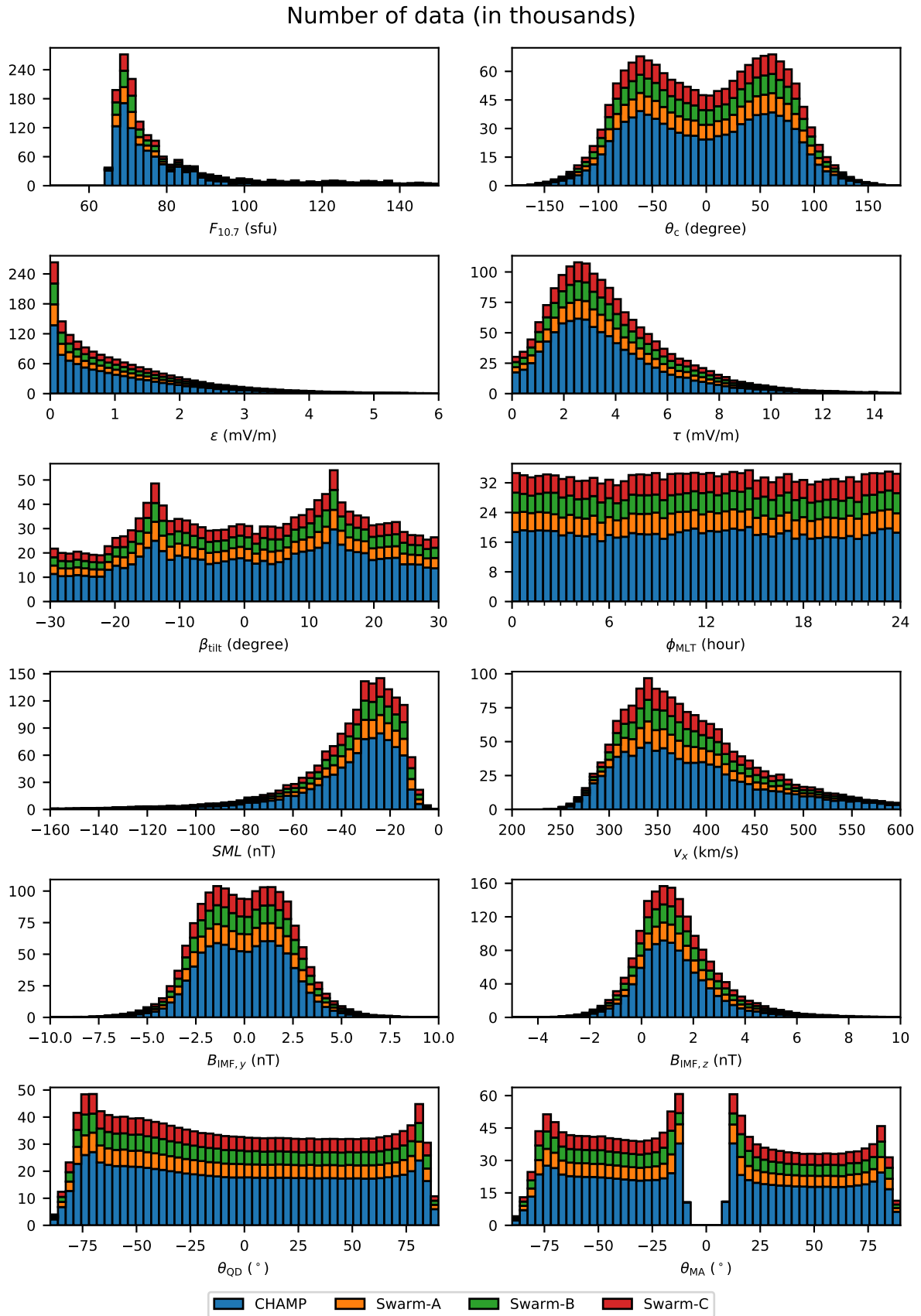


Figure 6.2.: Distribution of the satellite data in dependence of external parameters and magnetic apex coordinates. The distribution is shown as stacked histograms for each satellite dataset after data selection.

Table 6.1.: Summary of the model parameterization. All parts of the model except for the Euler angles have both a spatial (S) and temporal (T) parameterization.

	Number of parameters	Spatial and temporal parameterization
Internal field		
Time-dependent field	15400	S: Spherical harmonics in GEO, $n \leq 20$ T: Order-6 B-splines with knots every 0.5 year and 6-fold knots at model endpoints
Static field	3280	S: Spherical harmonics in GEO, $21 \leq n \leq 60$ T: All terms are static in GEO
Magnetospheric field*		
Near-magnetospheric field	413	S: Spherical harmonics in SM, $n \leq 2$ T: Degree-1 terms are scaled by hourly <i>RC</i> -index, degree-2 terms are static in SM, and <i>RC</i> -baseline corrections are estimated in 30 day bins and a single 3 year bin during the gap period
Far-magnetospheric field	2	S: Spherical harmonics in GSM, $n \leq 2, m = 0$ T: All terms are static in GSM
Ionospheric field		
E-layer field	4541	S: Spherical harmonics in QD/MLT, $n \leq 35, m \leq 3$ T: 18 terms based on solar wind parameters + const.
Toroidal field	8531	S: Spherical harmonics in MA/MLT, $n \leq 65, m \leq 3$ T: 18 terms based on solar wind parameters + const.
Alignment		
CHAMP	603	Euler angles (1-2-3 convention), 10 day bins
Swarm-A	663	Euler angles (1-2-3 convention), 10 day bins
Swarm-B	657	Euler angles (1-2-3 convention), 10 day bins
Swarm-C	660	Euler angles (1-2-3 convention), 10 day bins
Total	34750	

*includes the internally induced response based on an electrical conductivity model of the Earth.

6.3.1. Internal field

The internal magnetic field, consisting of the core field and lithospheric field, is written as the negative gradient of the internal part of the scalar magnetic potential expressed in terms of the truncated solid harmonics expansion in geocentric spherical coordinates (Eq. 3.7). The truncation level is set to $N^{\text{int}} = 60$ and the terms up to spherical harmonic degree $n = 20$ are allowed to be time-dependent while higher-degree terms are kept constant. The time-dependent internal field, which corresponds to the large-scale core and lithospheric field, is represented in time by a linear combination of order-6 B-splines defined on knots every 0.5 decimal years and 6-fold knots at the model endpoints (Eq. 3.10).

6.3.2. Magnetospheric and associated induced fields

The magnetic field produced in the magnetosphere is represented by the negative gradient of the external part of the scalar magnetic potential and includes contributions induced in the conducting Earth (Sec. 3.3.2). The potential associated with sources in the remote magnetosphere (Eq. 3.23)

is truncated at $N^{\text{far}} = 2$ and restricted to zonal terms, whereas the potential associated with the near-magnetospheric sources (Eq. 3.24) is truncated at spherical harmonic degree $N^{\text{near}} = 2$. The RC-baseline corrections are estimated in bins of 30 days except between May 2010 and end of March 2014, when a single bin is used to cover the gap period. The induced response is coupled to the external field parameterization using the diagonal part of a Q-matrix which is based on a 3D electrical conductivity model of the Earth (Grayver et al., 2017; Finlay et al., 2020).

6.3.3. Ionospheric field

The model parameterization of the ionospheric magnetic field is described in Sec. 6.6. The truncation level of the magnetic scalar potential representing the ionospheric E-layer field is set to $N^{\text{ion}} = 35$ for the spherical harmonic degree and $M = 3$ for the spherical harmonic order. The scalar potential of the ionospheric toroidal field is truncated at $N^{\text{tor}} = 65$ and $M = 3$.

6.3.4. Alignment parameters

The alignment rotations are estimated for each satellite dataset provided by CHAMP, Swarm-A, Swarm-B, and Swarm-C from all local times in the form of the three Euler angles α , β and γ in the 1-2-3 convention (Sec. 3.1). The Euler angles are treated as static in 10 day bins spanning the time interval of each dataset. The difference in the number of bins for the three *Swarm* satellites is due to small variations in the number of selected data, which resulted in some bins having no data. Each of those bins was combined with the next bin to form a 20 day bin.

6.4. Model parameter estimation

The model parameters, consisting of the coefficients of the internal field, the external field, the Euler angles, and the ionospheric field, were estimated by iteratively minimizing the quadratic cost function in Eq. (3.32) using the model update in Eq. (3.35). The design matrix (Eq. 3.34) used in the model parameter estimation procedure was modified, so that sunlit satellite data ($\chi < 100^\circ$) only contributed to the estimation of the ionospheric field model and the Euler angles but not to the internal and external parts of the field model. This was done by setting to zero the design matrix elements which relate the sunlit data to the model parts other than the ionospheric field model and the Euler angles. As starting values for the model parameters, I set the internal field model parameters to the CHAOS-6-x9 internal field estimates in 2015.0, the Euler angles to the values determined in pre-flight tests, the external field parameters as well as the ionospheric field parameters to zero. The cost function was then minimized by computing 15 iterations which was usually sufficient to ensure convergence to a level of $L = 5 \times 10^{-6}$ (Eq. 3.36).

The data error covariance matrix in the cost function was built from data error estimates based on data residual analysis of previous models. A treatment of the attitude error in the satellite vector was taken into account as described in Sec. 3.4.1. For the vector data of the three *Swarm* satellites, an isotropic component error of $\sigma = 2.2$ nT together with an isotropic attitude error of $\xi = \nu = 5''$ was assigned. For the CHAMP vector data, an isotropic component error of $\sigma = 2.5$ nT and an isotropic attitude error of $\xi = \nu = 10''$ was used. The effect of anisotropic attitude errors for data collected with only one STR in operation was neglected for simplicity. Furthermore, the boresight direction

Table 6.2.: Chosen regularization parameters.

Regularization parameters	
Internal field	
Time-dependent field	$\lambda_t = 1.0 \left(\frac{\text{nT}}{\text{yr}^3}\right)^{-2}$, $\lambda_{t_s} = \lambda_{t_e} = 0.01 \left(\frac{\text{nT}}{\text{yr}^2}\right)^{-2}$
Static field	None
Magnetospheric field	
Near-magnetospheric field	$\lambda_{\text{mag}} = 2.7 \times 10^5 \left(\frac{\text{nT}}{\text{yr}}\right)^{-2}$
Far-magnetospheric field	None
Ionospheric field	
E-layer field	None, unless stated
Toroidal field	$\lambda_{\text{tor}} = 10^5 (\text{nT})^{-2}$
Alignment	
CHAMP	None
Swarm-A	None
Swarm-B	None
Swarm-C	None

\mathbf{n} was simply set equal to the z-axis of the CRF system since the assumption of isotropic attitude errors allows \mathbf{n} to be arbitrary but not parallel to the vector measurement ([Holme and Bloxham, 1996](#)). All satellite data were weighted by $\sin \theta$ to counterbalance the dense spatial sampling in the polar regions. For each ground observatory, a data covariance matrix of the SV components was constructed from de-trended vector residuals with respect to CHAOS-7.2. Finally, Huber-weights (Eq. 3.38) were computed after each iteration and applied to down-weight data that falls in the tails of the data residual distribution.

The internal field model is regularized in time according to Eqs. (3.40) and (3.43). The temporal regularization of the internal field is degree-dependent and also includes an increase in the level of regularization for the zonal spherical harmonics by a factor of 10 relative to the non-zonal terms. This modification prevents strong oscillations in the zonal SV that are otherwise observed (see Sec. 6.7.3). The time variations of the *RC*-baseline corrections are regularized through a quadratic form in the difference between neighbouring bin values (Eq. 3.46). There was no regularization applied to the other external field parameters nor the Euler angles. The ionospheric E-layer field is not regularized unless stated. The ionospheric toroidal field is regularized by imposing a flat spatial power spectrum to prevent large amplitudes near the dip equator where the MA latitude is not well defined at satellite height. I initially chose the level of regularization of the internal time-dependent Gauss coefficients and the *RC*-baseline corrections such that the time variations were similar to CHAOS-7.4. The regularization parameter of the ionospheric toroidal field is taken from [Laundal et al. \(2017\)](#) and ensures a converged model. The chosen regularization parameters are summarized in Tab. 6.2.

6.5. Initial tests based on synthetic data

In this section I report on a simple experiment, based on synthetic data, which demonstrates it is possible to co-estimate and separate a model of the ionospheric field along with a model of Earth's

internal field.

For the experiment, I created synthetic vector data based on the times and locations of the satellite data and the ground observatory SV data as described in Sec. 6.2, but I replaced the real vector field measurements with calculated data resolved into GEO components using a known reference field model. For simplicity, I did not include any data of a magnetospheric field model nor account for Euler angles. Moreover, I did not add any noise so that the data were perfect in this regard. For the satellite data, I forward modelled the sum of both internal and ionospheric field estimates as given by the reference model, while, for the ground observatory data, I only used the calculated SV of the internal field part of the reference model. I omitted the ionospheric contributions from the synthetic SV to be consistent with the preprocessing step of the ground-based SV data, which involves the removal of magnetospheric and ionospheric field estimates using prior field models (Sec. 2.1.2).

For the known reference model I used CHAOS-7.4 (Finlay et al., 2020) to compute the estimates of the internal magnetic field and chose the AMPS parameterization with coefficients set to

$$\begin{aligned} g_{n,i}^{m,\text{ion}} &= \frac{1}{19} \left(\frac{a + h_R}{a} \right)^{n+2} \sqrt{\frac{1}{(n+1)(2 \min(n, M) + 1)}} \\ T_{n,i}^{m,\text{ion}} &= \frac{1}{19} \sqrt{\frac{(2n+1)}{n(n+1)(2 \min(n, M) + 1)}} \end{aligned} \quad (6.16)$$

for $i = 0, \dots, 18$ to provide the synthetic estimates for the ionospheric magnetic field. With this choice of ionospheric model coefficients, which are based on Eqs. (2.27), I imposed flat spatial power spectra on the ionospheric E-layer field at the reference height and on the toroidal magnetic field.

Based on the parameterization presented in Sec. 6.3 and the AMPS model, I designed a model of the internal and ionospheric field covering the time interval of the synthetic data and derived the model parameters through a least-squares approach neither using Huber-weights nor applying any regularization. To initialize the model estimation, I set all model parameters to zero.

For the converged model, the achieved misfit as measured by the root-mean-square (RMS) value of the difference between the model estimates and the synthetic data was essentially zero. The determined internal field model parameters agreed well with the input parameters, except during the gap period between CHAMP and *Swarm* where I only used ground observatory SV data. The internal coefficient differences, in terms of RMS vector field at the Earth's surface and at a given spherical harmonic degree, was less than 10^{-8} nT, except during the gap when they rose to 0.5 nT. On plotting the difference between estimates of the reference model and the derived model on the Earth's surface, the largest difference in the magnetic field appeared during the gap period in the Pacific. The ground observatories are the only source of information in the gap period. Since they are located on the continents and on a few islands, they provided an inadequate spatial sampling of the internal field especially over the oceans. This prevented an accurate retrieval of the time-dependent internal coefficients. The known problem in determining the internal field using ground data alone is in practise dealt with using temporal regularization or by the inclusion of platform magnetometer data (Chapter 5). I find that when satellite data is available it is possible to determine well the internal coefficients, even when the data contains ionospheric field signals, provided that the ionospheric field is co-estimated.

Turning to the ionospheric part of the estimated field model, the difference to the reference

model was small, which shows that these parts were well recovered. For the ionospheric E-layer, the difference in the coefficients expressed in terms of the RMS vector field at a given spherical harmonic degree was less than 10^{-8} nT at the reference height h_R and example values of external parameters $B_{IMF,y} = 0$ nT, $B_{IMF,z} = 3$ nT, $v_x = -350$ km s $^{-1}$, and $F_{10.7} = 70$ sfu. For the ionospheric toroidal field, the same quantity was less than 10^{-7} nT.

The results of the experiment suggest that it is possible to co-estimate an ionospheric field model together with a model of the internal field provided the spatiotemporal resolution of the data is appropriate. This was the case during the CHAMP and *Swarm* time thanks to the globally distributed satellite data but less so during the gap period with the ground observatory SV data. An appropriate spatiotemporal sampling of the magnetic field is important for retrieving not only the internal part but also the ionospheric part of the Earth's magnetic field. However, in the case of the ionospheric magnetic field the sampling in magnetic coordinates and MLT is crucial, which was ensured by the inclusion of sunlit conditions in this experiment. The test also demonstrated that it is important to state the range of the ionospheric field driving parameter values for which the model is valid. This simple proof-of-concept test provides a simple benchmark of my co-estimation code (Chapter 4). Of course, in reality the data is noisy and the source separation will be much more challenging.

6.6. Experiments on the co-estimation of ionospheric and internal fields

In the following I report on a series of geomagnetic field models derived from real data which, in addition to the usual modelling of internal and magnetospheric fields, include an AMPS-type parameterization of the ionospheric E-layer field and the toroidal field produced by the field-aligned currents. I also report results from models built without including the field-aligned currents. For the estimation of the latter models, I converted the vector data at QD latitudes poleward of 55° to scalar intensity data while keeping the vector data equatorward. Scalar data are less affected by polar field-aligned currents, which primarily cause perturbations in the magnetic field direction and relatively minor changes in the field intensity. For models that also account for the field-aligned currents, I used vector data at all latitudes.

As a first step, I built a CHAOS-type reference field model, referred to in the following as *Reference*. This involved inverting for the internal field (time-dependent and static), the magnetospheric field (inducing and induced), and the Euler angles for each satellite dataset using vector data at non-polar and scalar data at polar latitudes. I set the regularization parameters of the internal and external field model by comparison with CHAOS-7.4 and did not change these in any of the models reported in this sub-section.

Next, I derived a first test model, Model-A, which is identical to the reference case except that I additionally used the original AMPS parameterization of $g_n^{m,\text{ion}}(t)$ in Eq. (6.10) to co-estimate a model of the ionospheric E-layer field. The next experimental model, Model-B, is identical to Model-A except that I removed the constant zonal terms $g_{n,0}^{0,\text{ion}}$ from the AMPS parameterization. After that follows Model-C, which I set up as for Model-B, without the constant zonal terms, but

Table 6.3.: Summary of the ionospheric model parts of the test models.

Model	Satellite data	Ionospheric field regularization	Ionospheric field parameterization
Model-A*	Non-polar vector, polar scalar data	None	$g_n^{m,\text{ion}}(t) = g_{n,0}^{m,\text{ion}} + \sum_{i=1}^{18} g_{n,i}^{m,\text{ion}} X_i(t)$
Model-B	Non-polar vector, polar scalar data	None	$g_{n,i}^{m,\text{ion}}(t) = \sum_{i=1}^{18} g_{n,i}^{m,\text{ion}} X_i(t)$
Model-C	Non-polar vector, polar scalar data	None	$g_{n,i}^{m,\text{ion}}(t) = \sum_{i=1}^{18} g_{n,i}^{m,\text{ion}} (X_i(t) - \bar{X}_i)$
Model-D	Non-polar vector, polar scalar data	$g_{n,0}^{m,\text{ion}}$ terms	$g_{n,i}^{m,\text{ion}}(t) = g_{n,0}^{m,\text{ion}} + \sum_{i=1}^{18} g_{n,i}^{m,\text{ion}} (X_i(t) - \bar{X}_i)$
Model-E	Vector data at all latitudes	$g_{n,0}^{m,\text{ion}}$ terms, $T_n^{m,\text{ion}}$ terms	$g_{n,i}^{m,\text{ion}}(t) = g_{n,0}^{m,\text{ion}} + \sum_{i=1}^{18} g_{n,i}^{m,\text{ion}} (X_i(t) - \bar{X}_i)$ $T_n^{m,\text{ion}}(t) = T_{n,0}^{m,\text{ion}} + \sum_{i=1}^{18} T_{n,i}^{m,\text{ion}} X_i(t)$

*Model did not converge.

removed the following median values from the AMPS input parameters X_i , denoted \bar{X}_i

$$\begin{aligned}
& \bar{X}_1 = 0.008,19 & \bar{X}_2 = 0.588 \\
& \bar{X}_3 = 0.766 \text{ mV m}^{-1} & \bar{X}_4 = 0.000,022,2 \text{ mV m}^{-1} & \bar{X}_5 = 0.229 \text{ mV m}^{-1} \\
& \bar{X}_6 = 3.07^\circ & \bar{X}_7 = 0.944^\circ & \bar{X}_8 = 0.506^\circ \\
& \bar{X}_9 = 0.351^\circ \text{ mV m}^{-1} & \bar{X}_{10} = 0.0690^\circ \text{ mV m}^{-1} & \bar{X}_{11} = 0.152^\circ \text{ mV m}^{-1} \\
& \bar{X}_{12} = 3.25 \text{ mV m}^{-1} & \bar{X}_{13} = 0.0150 \text{ mV m}^{-1} & \bar{X}_{14} = 1.86 \text{ mV m}^{-1} \\
& \bar{X}_{15} = 6.10^\circ \text{ mV m}^{-1} & \bar{X}_{16} = 2.51^\circ \text{ mV m}^{-1} & \bar{X}_{17} = 0.879^\circ \text{ mV m}^{-1} \\
& \bar{X}_{18} = 73.0 \text{ sfu}.
\end{aligned} \tag{6.17}$$

In Model-D, I modified the original AMPS parameterization by removing the median values of the X_i but kept the constant zonal terms. For Model-D, I also designed a diagonal regularization matrix to force only the $g_{n,0}^{0,\text{ion}}$ towards zero with weights proportional to the values of the zonal coefficients $g_{n,i}^{0,\text{AMPS}}$ from AMPS ([Toresen and Laundal, 2018](#), updated version 1.4.0)

$$\mathbf{\Lambda}_{\text{df}} = \lambda_{\text{df}} \cdot \text{diag}_n \left(g_{n,0}^{0,\text{AMPS}} + \sum_{i=1}^{18} g_{n,i}^{0,\text{AMPS}} \bar{X}_i \right)^{-2} \tag{6.18}$$

where λ_{df} is a dimensionless regularization parameter, which was set to $\lambda_{\text{df}} = 5 \times 10^3$. In other words, the prior variances of the constant zonal coefficients were proportional to the zonal coefficients of AMPS. The sum in Eq. (6.18) is necessary to rescale the AMPS coefficient values in accordance with the modified parameterization using the median values of the basis functions. Finally, Model-E is based on Model-D but also accounts for the toroidal field produced by the field-aligned currents using the original AMPS parameterization (Eq. 6.10 replacing $g_n^{m,\text{ion}}$ with $T_n^{m,\text{ion}}$). For Model-E, I also needed to increase the regularization parameter of the ionospheric E-layer field by a factor of 2 to $\lambda_{\text{df}} = 1 \times 10^4$ to ensure convergence of the model. Tab. 6.3 summarizes how the ionospheric field was accounted for in each test model. Note that for Model-A the norm of the model update did not decrease below the target convergence level of $L = 5 \times 10^{-6}$ but stayed constant at around

2×10^{-5} after 15 iterations, which means that the model did not converge.

The purpose of the test models, Model-A through Model-E, is to explore various issues regarding the separation of the ionospheric E-layer field and the internal field, and the impact of co-estimating the toroidal field and including vector field data. Both the internal field and the ionospheric E-layer field are produced by electric currents which circulate below the satellites and never cross the satellite orbits. Hence, these two parts of the geomagnetic field can both be represented as the negative gradient of an internal potential expanded into spherical harmonics. The only way to distinguish them is through their distinctive variations with time, or if we have prior information regarding their structure and amplitude. The dependence of $m > 0$ terms on magnetic local time in the AMPS parameterization enables this part of the ionospheric E-layer field to be effectively separated from the geocentric internal field. However the AMPS parameterization of the ionospheric E-layer field also includes terms $g_{n,0}^{0,\text{ion}}$, which lack the a dependence on magnetic local time and are, therefore, inseparable from the static part of the internal magnetic field, unless additional assumptions concerning their amplitude are made. These issues are explored in Sec. 6.6.2

6.6.1. Comparisons with satellite data and ground observatory SV data

The effect of including a model of the ionospheric field on the fit to satellite data is illustrated in Fig. 6.3 in terms of both global and polar views of the satellite scalar residuals with respect to the reference model (using the full dataset) and to each of the test models. The maps were created by accumulating the scalar residuals of the satellite data in equal-area pixels using the Hierarchical Equal Area isoLatitude Pixelization (HEALPix) scheme² (Zonca et al., 2019; Gorski et al., 2005) in QD/MLT coordinates prior to computing the median value. When looking at the center of the global scalar residual maps, which corresponds to the region around the dip-equator on the nightside, both the reference model and the test models achieve very low median values. The absence of any discernible structure in the residuals suggest that all models perform well in that region. However, at polar latitudes for all MLT and at low latitudes on the dayside the maps of the reference model, which includes no modelling of the ionospheric field, are markedly different from similar maps for the test models.

For the reference model, the scalar residuals in each polar region exhibit characteristic patterns caused by the polar ionospheric current system in the form of two patches or cells that are approximately located on either side of the noon-midnight meridian and are opposite in sign. Moreover, comparing the two cells between the magnetic hemispheres shows a remarkable symmetry with respect to the magnetic equatorial plane. The scalar residuals at low QD latitudes on the dayside, however, are roughly organized in a single, negative-valued patch centered at noon, which is caused by the non-polar currents in the ionospheric E-layer on the dayside.

Turning to the test models, the organized patterns found in the scalar residual maps for the reference model are largely absent, which suggests that the parameterization of the ionospheric field successfully removes the time-averaged ionospheric signal. In the polar regions, the two cell pattern seen in the case of the reference model disappeared, leaving only weak, approximately circular patterns in the residuals around the magnetic poles. Model-A through Model-D show an arc-shaped pattern in the residuals at -60° QD latitude in the afternoon sector in the southern magnetic hemisphere,

²<http://healpix.sourceforge.net>

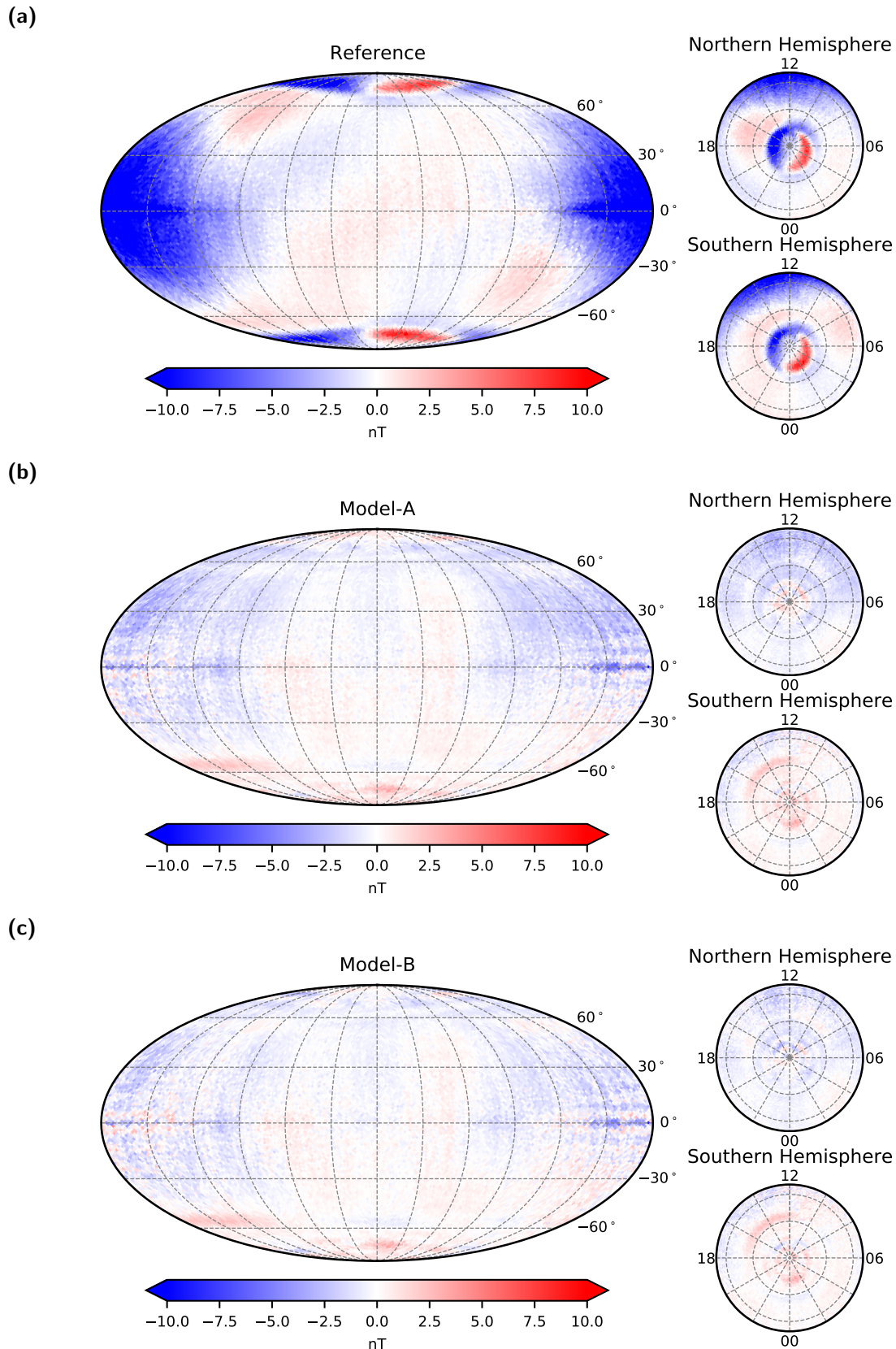


Figure 6.3.: Median value of the scalar residuals in QD/MLT coordinates as both global (left) and polar views (right) for the reference model (a) and each test model (b-f). The median values were computed from the scalar residuals in equal-area pixels using the HEALPix pixelation. The vertical line in the center of the global view is $\phi_{\text{MLT}} = 0^\circ$, while the horizontal line in the center is the dip-equator. The polar views extend to the dip-equator and indicate MLT in hours with magnetic noon (12 h), midnight (0 h), dawn (6 h), and dusk (18 h). See also next page.

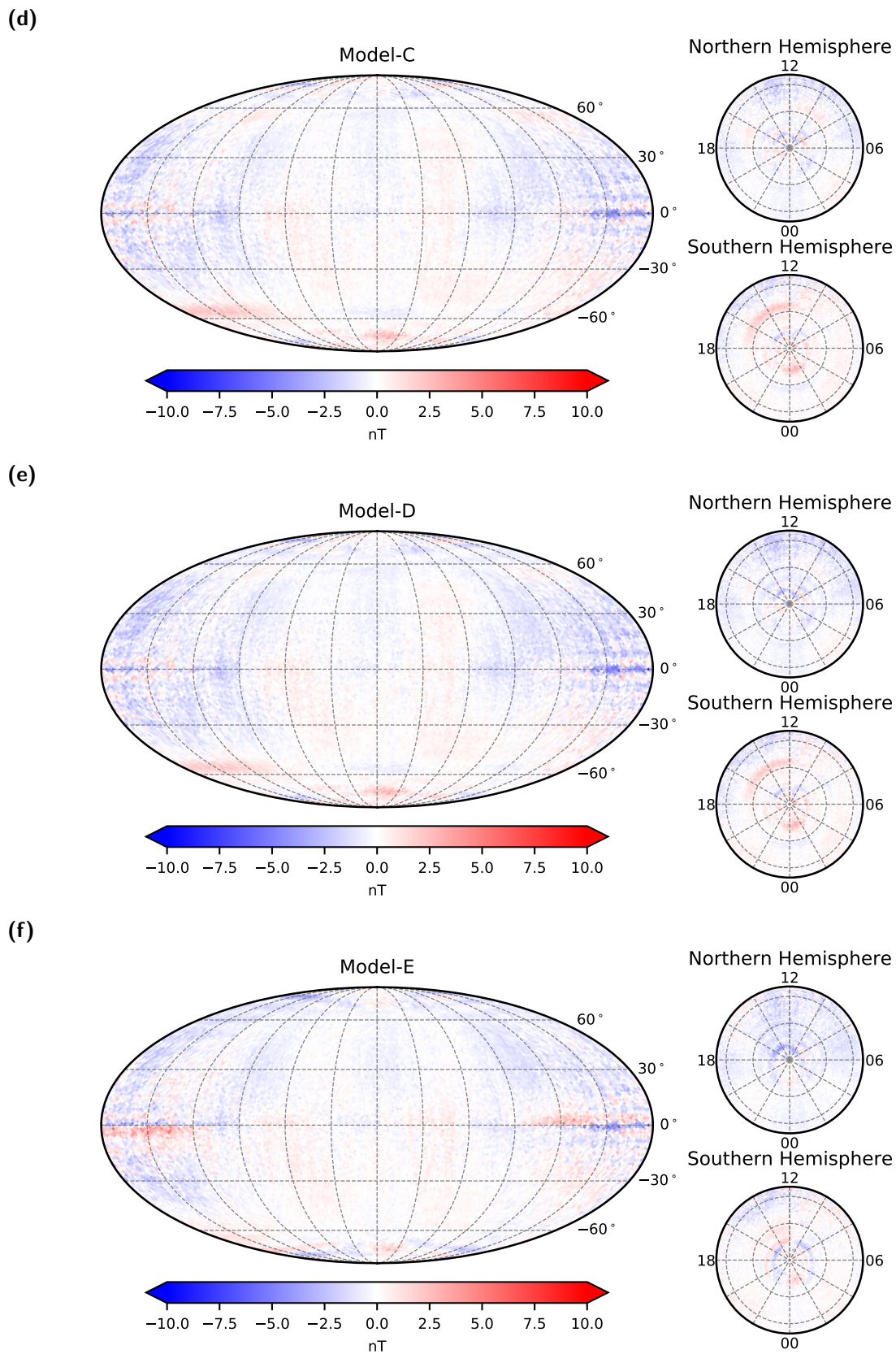


Figure 6.3.: Continued.

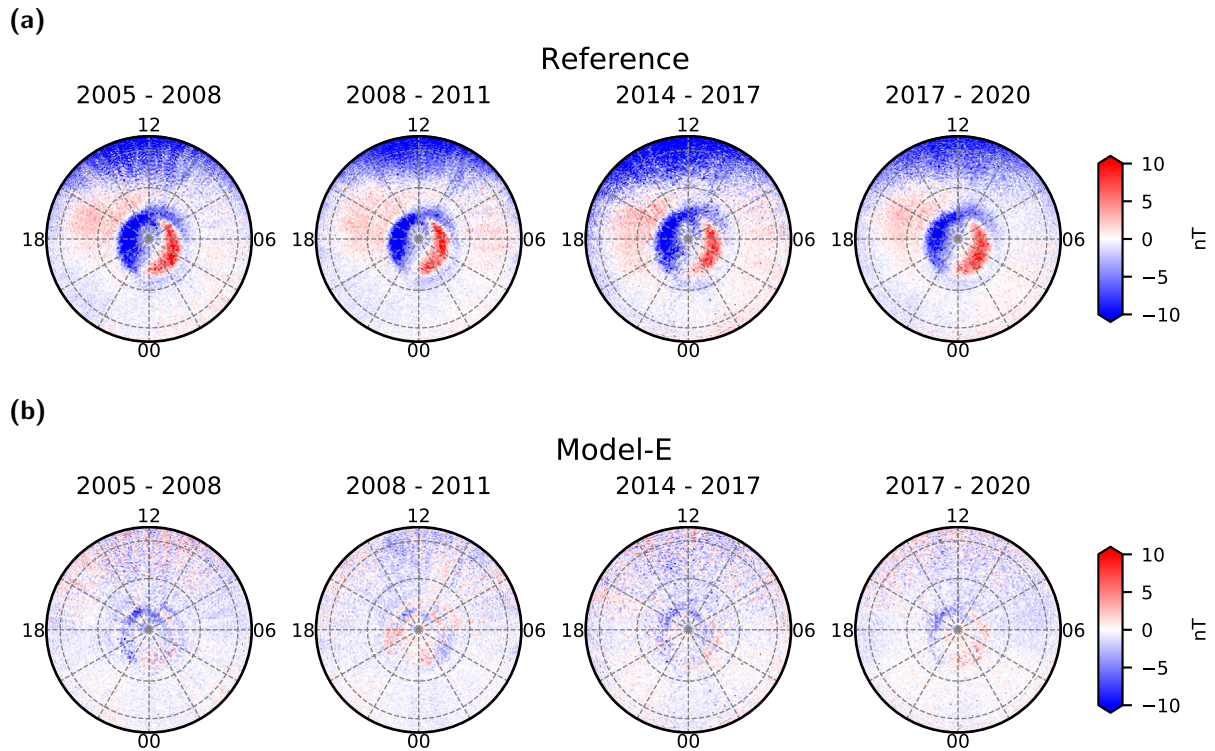


Figure 6.4.: Median values of scalar residuals (a) with respect to the reference model and (b) with respect to Model-E in the northern hemisphere in 3 year intervals which cover the entire model period from 2005.0 to 2020.0 except for the gap period. The maps are shown in QD/MLT coordinates and extend to the dip-equator. MLT is given in hours with noon at the top.

while, for Model-E, this pattern is also removed. At non-polar latitudes, the scalar residuals are small for the test models at all MLT, but the residuals on the dayside are not as small as on the nightside. In particular, the residuals on the sunlit part of the dip-equator remain slightly elevated in value, perhaps because the implemented ionospheric field models lack the spatial resolution to fully capture this feature.

Instead of considering scalar residuals averaged over the entire model interval, it is also important, especially with possible leakage of the ionospheric field into secular variation in mind, to investigate whether or not the residual pattern is time-dependent. To simplify the presentation, I present here only the scalar residuals of the reference model and Model-E in the northern polar hemisphere. Fig. 6.4 shows a sequence of 3 year intervals which cover the entire model period outside the gap period, i.e. from 2005 to the end of 2007 (2005-2008), from 2008 to the end of 2010 (2008-2011), from 2014 to the end of 2016 (2011-2016) and from 2017 to the end of 2019 (2017-2020). The intervals sample different stages of the solar cycle. For the data selection criteria considered here, the pattern in the scalar residuals remains mostly unchanged in time for the reference model. There is a slight difference when comparing the maps during CHAMP times with those during *Swarm*. The two cell pattern and in particular its dusk cell is clearer and has sharper edges during the CHAMP period. Also, the residuals are larger in amplitude during CHAMP since they saturate the color scale used in the maps more strongly than during *Swarm*. The reason for these differences is probably related to the altitude at which the data was collected. CHAMP was 50–150 km lower than the *Swarm* satellites and, therefore, closer to the currents in the ionospheric E-layer. The large negative patch

centered at noon for the residuals to the reference model seems to be more extended in MLT during the interval 2014-2017, when the sun was at solar maximum, compared to the other intervals. This could be an effect of the increased EUV flux during solar maximum, which enhances the ionospheric conductivity and the currents in the ionosphere on the dayside. Turning to Model-E, the median scalar residual maps show thin arcs of remaining increased residuals associated with the field-aligned R1 and R2 currents, which are not fully captured by the ionospheric model. Again, the maps during CHAMP time have a sharper appearance. Although there are time variations in the remaining residual patterns from epoch to epoch for Model-E there is no organized structure to this variation. This demonstrates that Model-E represents well the scalar field at all latitudes during the analyzed time intervals, when averaging over windows of three years or longer.

Misfit statistics are also useful when evaluating model performance. Regarding the satellite data, Tab. 6.4 collects misfit statistics in terms of Huber-weighted mean values and deviations of the residuals with respect to the reference model and each test model. Some of the statistics relate to components which were not used for the model estimation. They are included merely for completeness. Such is the case for the non-polar scalar and polar vector residuals of the reference model and also Model-A through Model-D, and, likewise, for the scalar residuals at all latitudes of Model-E. I find that the Huber-weighted deviations σ are generally larger at polar latitudes compared to non-polar latitudes, which is a signature of the highly dynamic activity of auroral current systems in the polar regions. This is especially apparent in the horizontal components, B_θ and B_ϕ . For example, $\sigma = 4.15$ nT for non-polar F from CHAMP with respect to the reference model compared to $\sigma = 8.08$ nT at polar latitudes, and, likewise, $\sigma = 5.96$ nT for non-polar B_θ from CHAMP with respect to the reference model compared to $\sigma = 20.56$ nT at polar latitudes. For F and B_r , the test models always provide significantly smaller σ than the reference model irrespective of latitude. For example in case of polar B_r from Swarm-A, $\sigma = 7.85$ nT relative to the reference model and $\sigma = 5.98$ nT relative to Model-A. However, this is not the case in the other two components, B_θ and B_ϕ , for which the test models only give smaller σ at non-polar latitudes with the notable exception of Model-E, which provides smaller σ of B_θ and B_ϕ at all latitudes, due to its modelling of field aligned currents.

Turning to a comparison of the models to annual differences of revised monthly mean ground observatory data, Huber-weighted mean values and deviations are shown in Tab. 6.5. Similar to the satellite data, σ is larger at polar latitudes than non-polar latitudes. But instead of the horizontal components for the satellite data, \dot{B}_r and \dot{B}_θ have considerably larger σ at polar latitudes on ground. The test model misfits are essentially unchanged from the reference model. Fig. 6.5 further illustrates this by showing, as an example, the SV data (black dots) from 8 ground observatories together with the SV estimates of the reference model (red lines), Model-A (blue lines) and Model-E (green lines). The observatories are shown in decreasing order of geographic latitude, which makes it easy to see that the SV data are more scattered in the polar regions. Furthermore, it can be seen that the three models fit the SV data equally well, in agreement with the very similar misfit statistics. This shows that including the ionospheric field, and with the relatively strong core field regularization adopted in these tests, has only a minor impact on the SV predicted at ground observatories.

The misfit statistics indicate that all models fit the data to a reasonable level and that there is no negative effect on the misfit when co-estimating a model of the ionospheric field. In fact, the

Table 6.4.: Number of data N , Huber-weighted mean μ and deviation σ of the vector and scalar residuals with respect to the reference model and the five test models for each satellite dataset. The non-polar dataset refers to the data equatorward of $\pm 55^\circ$ QD latitude and the polar dataset to the data poleward of this latitude. Note that the non-polar scalar and polar vector residuals of the reference model, and Model-A through Model-D are only shown for completeness since they were not minimized during the model parameter estimation. This is also the case for the scalar residuals at all latitudes of Model-E. See also next page.

Dataset	QD latitude	Comp.	N	Reference		Model-A		Model-B	
				μ (nT)	σ (nT)	μ (nT)	σ (nT)	μ (nT)	σ (nT)
CHAMP	Non-polar	B_r	564833	0.47	5.58	0.70	4.76	0.60	4.78
		B_θ	564833	1.09	5.96	0.36	5.52	0.31	5.52
		B_ϕ	564833	-0.13	9.18	-0.10	8.94	-0.10	8.94
		F	564833	-1.42	4.15	-0.36	2.95	-0.16	2.91
	Polar	B_r	349028	0.40	8.55	0.47	6.43	0.37	6.46
		B_θ	349028	0.58	20.56	-0.73	20.89	-0.53	20.86
		B_ϕ	349028	0.06	22.91	-0.09	23.04	-0.10	23.00
		F	349028	-1.35	8.08	0.23	5.63	0.14	5.65
Swarm-A	Non-polar	B_r	156455	0.01	4.24	0.19	3.17	0.11	3.19
		B_θ	156455	0.99	4.43	0.29	3.93	0.23	3.93
		B_ϕ	156455	0.03	6.20	0.03	5.91	0.03	5.91
		F	156455	-1.61	4.23	-0.43	2.87	-0.20	2.86
	Polar	B_r	97447	-0.05	7.85	0.15	5.98	0.10	6.06
		B_θ	97447	1.14	20.18	-0.06	20.48	0.26	20.46
		B_ϕ	97447	0.05	24.02	-0.09	24.10	-0.10	24.07
		F	97447	-1.66	7.49	-0.31	5.29	-0.51	5.36
Swarm-B	Non-polar	B_r	157271	-0.07	4.14	0.15	3.05	0.07	3.07
		B_θ	157271	0.99	4.33	0.28	3.81	0.23	3.81
		B_ϕ	157271	-0.00	6.12	0.01	5.86	0.01	5.85
		F	157271	-1.59	4.12	-0.41	2.75	-0.19	2.75
	Polar	B_r	97104	-0.08	7.32	0.12	5.61	0.07	5.69
		B_θ	97104	1.14	20.19	0.00	20.53	0.30	20.51
		B_ϕ	97104	0.11	23.97	0.05	24.09	0.04	24.06
		F	97104	-1.44	6.91	-0.11	4.88	-0.30	4.95
Swarm-C	Non-polar	B_r	158803	-0.03	4.20	0.15	3.18	0.07	3.19
		B_θ	158803	0.94	4.44	0.24	3.94	0.18	3.94
		B_ϕ	158803	0.06	6.18	0.05	5.90	0.06	5.89
		F	158803	-1.51	4.21	-0.36	2.87	-0.12	2.86
	Polar	B_r	98767	-0.03	7.84	0.17	5.98	0.12	6.05
		B_θ	98767	1.01	20.21	-0.20	20.53	0.12	20.51
		B_ϕ	98767	0.02	23.93	-0.11	24.03	-0.12	24.00
		F	98767	-1.50	7.48	-0.14	5.29	-0.34	5.36

Table 6.4.: Continued.

Dataset	QD latitude	Comp.	N	Model-C		Model-D		Model-E	
				μ (nT)	σ (nT)	μ (nT)	σ (nT)	μ (nT)	σ (nT)
CHAMP	Non-polar	B_r	564833	0.54	4.77	0.59	4.76	0.53	4.69
		B_θ	564833	0.28	5.51	0.32	5.51	-0.08	5.45
		B_ϕ	564833	-0.09	8.93	-0.10	8.94	-0.03	8.57
		F	564833	-0.10	2.88	-0.18	2.89	-0.10	2.89
	Polar	B_r	349028	0.20	6.41	0.28	6.40	0.25	6.28
		B_θ	349028	-0.50	20.85	-0.48	20.83	-0.28	17.53
		B_ϕ	349028	-0.10	23.00	-0.09	22.99	-0.02	19.11
		F	349028	0.22	5.56	0.08	5.57	-0.33	5.65
Swarm-A	Non-polar	B_r	156455	0.05	3.16	0.10	3.15	0.07	3.08
		B_θ	156455	0.22	3.91	0.26	3.91	-0.23	3.79
		B_ϕ	156455	0.03	5.91	0.02	5.91	-0.00	5.67
		F	156455	-0.18	2.81	-0.25	2.82	-0.15	2.82
	Polar	B_r	97447	-0.12	5.97	-0.03	5.97	-0.11	5.87
		B_θ	97447	0.17	20.44	0.19	20.43	0.30	16.97
		B_ϕ	97447	-0.10	24.07	-0.09	24.06	-0.08	20.04
		F	97447	-0.32	5.27	-0.46	5.27	-0.65	5.42
Swarm-B	Non-polar	B_r	157271	0.01	3.03	0.06	3.03	0.03	2.98
		B_θ	157271	0.22	3.79	0.25	3.79	-0.26	3.69
		B_ϕ	157271	0.02	5.85	0.01	5.85	-0.01	5.58
		F	157271	-0.17	2.71	-0.24	2.71	-0.13	2.71
	Polar	B_r	97104	-0.14	5.61	-0.05	5.61	-0.14	5.50
		B_θ	97104	0.21	20.50	0.23	20.49	0.28	16.94
		B_ϕ	97104	0.04	24.05	0.05	24.04	0.01	19.95
		F	97104	-0.12	4.85	-0.26	4.86	-0.47	5.03
Swarm-C	Non-polar	B_r	158803	0.01	3.16	0.06	3.15	0.03	3.07
		B_θ	158803	0.17	3.92	0.20	3.92	-0.29	3.79
		B_ϕ	158803	0.06	5.88	0.05	5.89	0.03	5.59
		F	158803	-0.10	2.81	-0.18	2.82	-0.07	2.80
	Polar	B_r	98767	-0.10	5.97	-0.01	5.97	-0.08	5.85
		B_θ	98767	0.02	20.49	0.04	20.48	0.19	16.97
		B_ϕ	98767	-0.13	23.99	-0.11	23.98	-0.08	20.05
		F	98767	-0.15	5.26	-0.29	5.27	-0.49	5.43

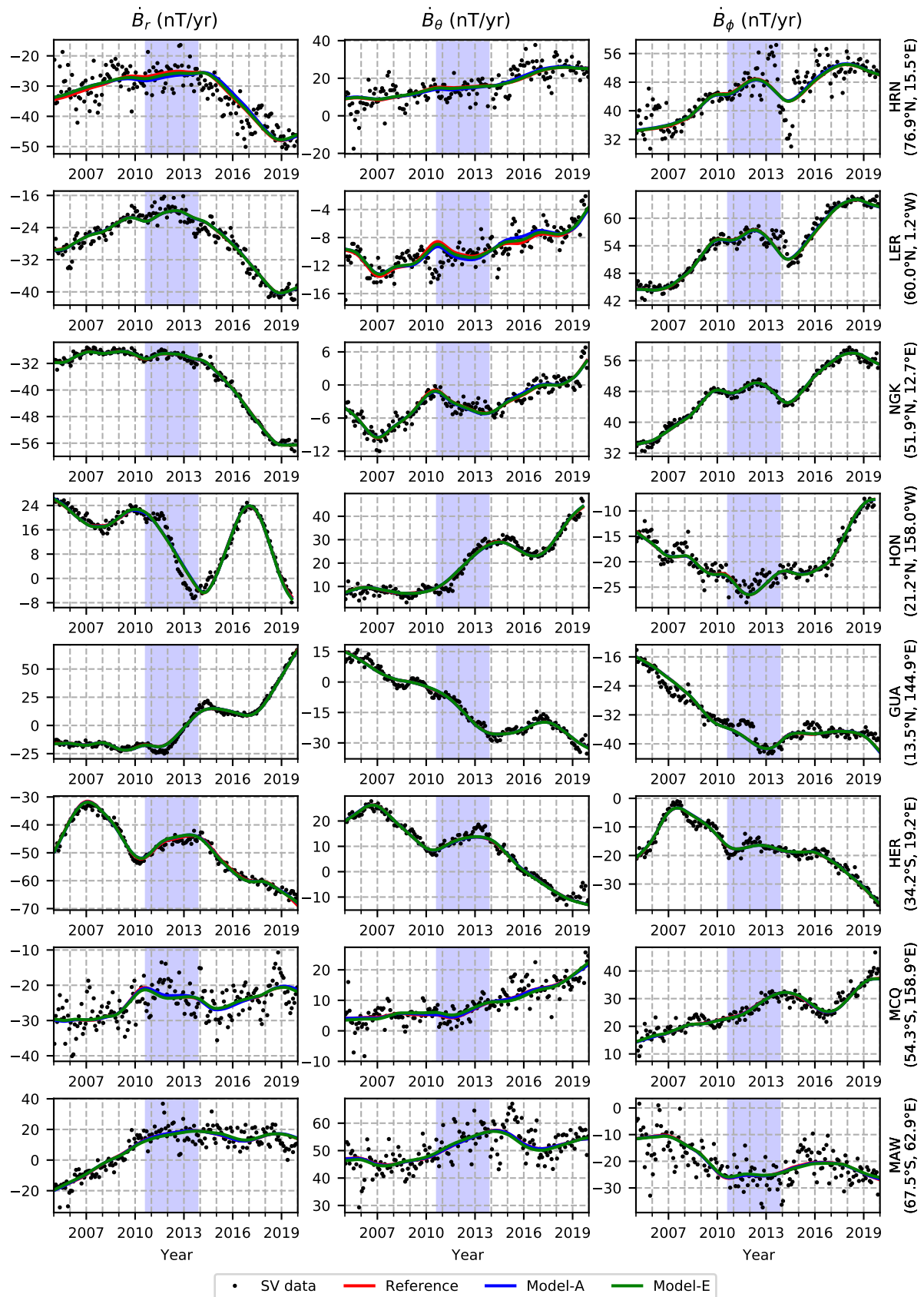


Figure 6.5.: Time series of the SV estimates computed with the reference model (red lines), Model-A (blue lines) and Model-E (green lines) along with the monthly SV data (black dots) from 8 ground observatories arranged in decreasing order of geographic latitude. The gap period is shown as blue shaded area. The observatories are located in Hornsund (HRN), Lerwick (LER), Niemegek (NGK), Honolulu (HON), Guam (GUA), Hermanus (HER), Macquarie Island (MCQ) and Mawson (MAW).

Table 6.5.: Number of data N , Huber-weighted mean μ and deviation σ of the SV vector residuals with respect to the reference model and the five test models for the ground observatory data. The non-polar dataset refers to data equatorward of $\pm 55^\circ$ QD latitude and the polar dataset to data poleward of this latitude.

Dataset	QD latitude	Comp.	N	Reference		Model-A		Model-B	
				$\mu \left(\frac{n\text{T}}{\text{yr}} \right)$	$\sigma \left(\frac{n\text{T}}{\text{yr}} \right)$	$\mu \left(\frac{n\text{T}}{\text{yr}} \right)$	$\sigma \left(\frac{n\text{T}}{\text{yr}} \right)$	$\mu \left(\frac{n\text{T}}{\text{yr}} \right)$	$\sigma \left(\frac{n\text{T}}{\text{yr}} \right)$
Observatory	Non-polar	\dot{B}_r	16485	0.15	2.04	0.16	2.04	0.15	2.07
		\dot{B}_θ	16485	-0.16	2.29	-0.16	2.29	-0.17	2.27
		\dot{B}_ϕ	16485	0.02	2.31	0.01	2.31	0.02	2.31
	Polar	\dot{B}_r	5185	0.16	4.42	0.15	4.49	0.12	4.48
		\dot{B}_θ	5185	-0.22	4.08	-0.25	4.07	-0.22	4.08
		\dot{B}_ϕ	5185	-0.03	2.81	-0.03	2.80	-0.02	2.80

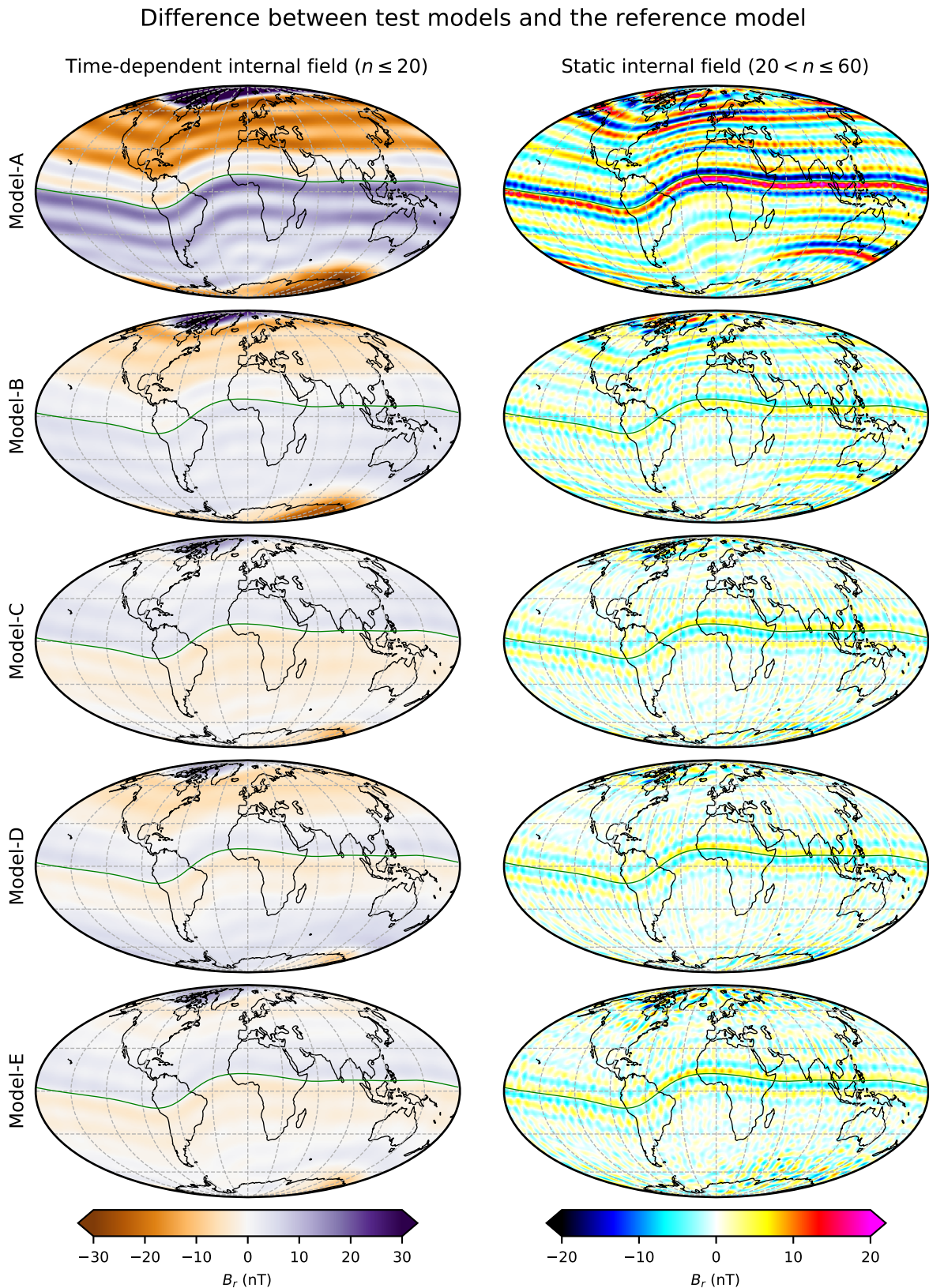
Dataset	QD latitude	Comp.	N	Model-C		Model-D		Model-E	
				$\mu \left(\frac{n\text{T}}{\text{yr}} \right)$	$\sigma \left(\frac{n\text{T}}{\text{yr}} \right)$	$\mu \left(\frac{n\text{T}}{\text{yr}} \right)$	$\sigma \left(\frac{n\text{T}}{\text{yr}} \right)$	$\mu \left(\frac{n\text{T}}{\text{yr}} \right)$	$\sigma \left(\frac{n\text{T}}{\text{yr}} \right)$
Observatory	Non-polar	\dot{B}_r	16485	0.16	2.04	0.16	2.04	0.17	2.04
		\dot{B}_θ	16485	-0.16	2.28	-0.16	2.28	-0.15	2.29
		\dot{B}_ϕ	16485	0.02	2.31	0.02	2.31	0.01	2.31
	Polar	\dot{B}_r	5185	0.13	4.50	0.14	4.48	0.13	4.43
		\dot{B}_θ	5185	-0.25	4.07	-0.24	4.07	-0.26	4.08
		\dot{B}_ϕ	5185	-0.03	2.80	-0.03	2.80	-0.03	2.80

co-estimation reduces σ of the vector components and F at non-polar latitudes, and B_r and F at polar latitudes. If the toroidal part of the ionospheric field is added to the field model, as in Model-E, σ of the polar horizontal components is significantly reduced. The reduction in σ of the horizontal components could also be due to the model parameter estimation, which was designed to minimize the vector misfit at polar latitudes for Model-E but only the scalar misfit for the reference model and the other test models.

6.6.2. Investigations of ambiguities related to modelling the zonal ionospheric field

In Fig. 6.6 I explore issues related to the separation of the zonal ionospheric field by first presenting global maps of the difference in the internal field estimated in the test models, which include a parameterization of the ionospheric E-layer field making various assumptions regarding the $g_{n,0}^{0,\text{ion}}$ terms, and the reference model, which ignores the ionospheric E-layer field. The maps show several parallel bands which are essentially constant along lines of constant QD latitude but vary in amplitude, or even alternate in sign with QD latitude. These bands form patterns which are clearly related to the zonal spherical harmonics in QD coordinates of different degrees.

When looking at the difference maps of the time-dependent internal field, there is a large-scale pattern which, based on the number of zero-crossings, seems dominated by spherical harmonics Y_3^0 (Model-A, Model-B, and Model-C) or Y_5^0 (Model-D, Model-E) in QD/MLT coordinates. In the case of Model-A, the large-scale pattern is overlaid with parallel narrow bands creating a pattern of stripes



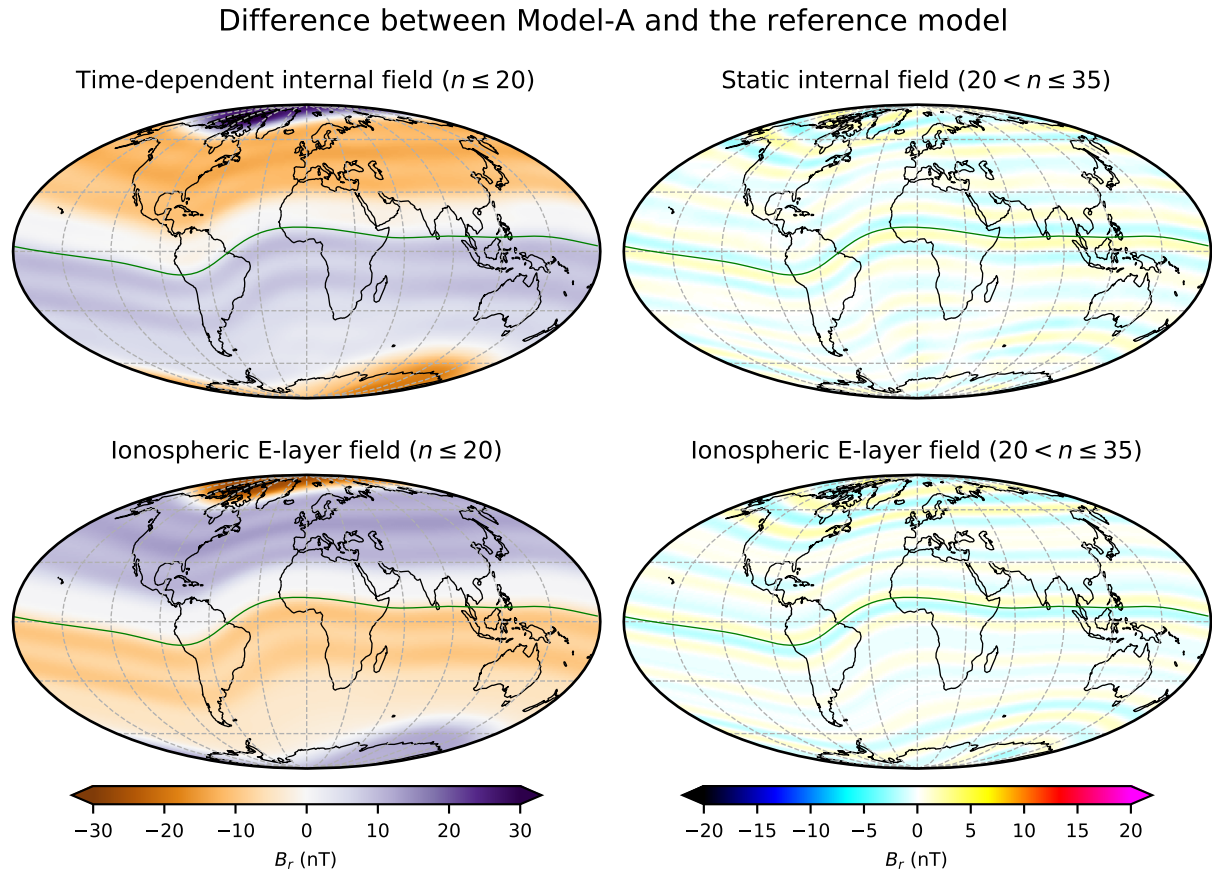


Figure 6.7.: Difference between Model-A and the reference model for the estimated radial component of the time-dependent internal field in 2019.0 (top left) and the static internal field (top right); and radial estimates of the ionospheric E-layer field using only the constant zonal term for $n \leq 20$ (bottom left) and $20 < n \leq 35$ (bottom right) of Model-A. The estimates are computed at 450 km above the Earth's surface. The green line indicates the dip-equator ($\lambda_{\text{QD}} = 0^\circ$).

along QD latitude. The stripes are also visible in Model-B, Model-C, Model-D and Model-E but are less strong compared to Model-A. The largest difference in value is found in the polar regions near the magnetic poles for all models. The difference is largest for Model-A, up to 40 nT, of order 20 nT in Model-B and up to 5 nT in models C to E.

Turning to the static internal field, similar stripes appear as for the time-dependent part, but they are narrower in latitude due to the high-degree spherical harmonics used to parameterize this part of the internal field. The amplitude of the stripes is large at the dip-equator ($\lambda_{\text{QD}} = 0^\circ$) and in the northern polar region, but largest for Model-A where the differences are up to 20 nT. For Model-A, there is also a smaller area below Australia where the difference is large.

To confirm that the difference pattern results from the constant zonal terms of the ionospheric part of the test models, I plot in Fig. 6.7 the radial estimates of the constant zonal terms of the co-estimated ionospheric field taken from Model-A along with the internal field differences between Model-A and the reference model at a height of 450 km, which is a typical height of magnetic survey satellites. The pattern of internal field difference and the constant zonal part of the ionospheric E-layer field are essentially identical except for a change in sign. Moreover, the strong zonal pattern that is visible in the static part of the internal field around the dip equator at the Earth's surface (Fig. 6.6)

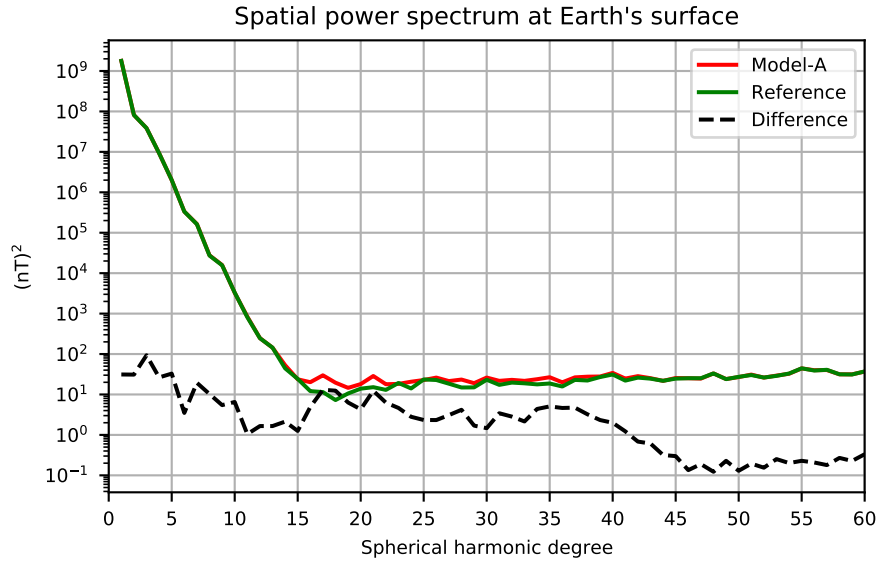


Figure 6.8.: Spatial power spectrum of the internal field estimates of Model-A, the reference model and the difference between both at the Earth's surface in 2019.0. The RMS value of the difference field is 14.8 nT.

has largely disappeared at 450 km above ground. This latter observation suggests a contamination of the internal field model by signals from sources which are internal at satellite height but external at the Earth's surface. When the internal field model is downward continued from the satellite height, where the data misfit is minimized, and evaluated at the Earth's surface, those contributions cause large distortions.

Fig. 6.8 compares the spatial power spectrum of the internal field in 2019.0 between Model-A and the reference model. It shows that the power in the difference field is almost evenly distributed over spherical harmonic degrees below $n = 35$ except for a small dip in power for $n \in [10, 15]$ and slightly increased levels for low degrees with a peak at $n = 3$. The power above $n = 35$ gradually decreases until it reaches a plateau after $n = 45$. Although the power is small when compared to the time-dependent part of the internal field, it becomes appreciable at higher degrees as the power spectrum of the internal field below $n = 15$ quickly decreases. The drop in the difference field power above $n = 35$ can be explained by the truncation level of the ionospheric E-layer field, which is set to that value. The reason for the gradual decrease above degree 35 may be related to the use of QD latitudes in the spherical harmonics expansion of the ionospheric E-layer field.

So far, I have presented only differences between the test models and the reference model. Looking only at such differences it is not easy to decide whether the difference pattern reflects a real improvement of the internal field model or whether it is an artifact introduced by field separation problems. In order to address this I next examine the internal field and the ionospheric field estimates independently for evidence that features they contain are unrealistic. Here, I examine only the ionospheric E-layer field and postpone a detailed investigation of the internal field and its time-dependence to Sec. 6.7.3.

In Fig. 6.9 I compare the radial estimates of the ionospheric E-layer field given by the test models with those given by CM6 ([Sabaka et al., 2020](#)), including the induced field, on 20 March 2018 during spring equinox, when the polar ionospheric currents are approximately equal in strength in both

hemispheres. I used $F_{10.7} = 70$ sfu and set the remaining external parameters needed for the test models equal to the actual values at 12:00 UTC on 20 March 2018 to have comparable estimates of CM6 and the test models. Note that setting the IMF in this way is to some extent arbitrary because the IMF changes all the time. The radial estimates of CM6 show the well-known MLT-dependent pattern at low latitudes created by the Sq current system, which involves a positive patch in the northern magnetic hemisphere and a negative patch in the southern magnetic hemisphere. The patches have an amplitude of up to 20 nT and are slightly elongated eastward due to the effect of induction, which delays the disappearance of the Sq signal on the eastern edge as the whole pattern follows the westward movement of the subsolar point. In contrast, the Sq signal of Model-A has only a weak MLT-dependence and is almost zonal in QD latitude. This is a clear indication of a problem in the ionospheric field in Model-A due to the ambiguity between the ionospheric E-layer field and the internal field. The situation is much improved for Model-B, which is less dominated by large-scale zonal structures seen for Model-A. However, there are still relatively strong but narrow zonal patterns in QD latitude in Model-B, these are further reduced for Model-C, Model-D and Model-E. Among those three models there is not much difference except for the slightly larger amplitude given by Model-D compared to Model-C and Model-E. It is interesting that the estimates of those three models in the polar regions are much more pronounced and better delineated than in CM6. Yet, they provide estimates of the ionospheric E-layer field at the low latitude dayside that are similar to CM6.

6.6.3. Tests with SML-index based data selection criteria

The magnetic field in the polar regions is known to undergo large and highly dynamic variations associated with ionospheric currents whose activity is controlled by the solar wind-magnetosphere coupling, but where the response to solar forcing may be delayed or indirect. Taking those variations into account for internal field modelling is difficult so that modelers are dependent on various criteria used in an attempt to select quiet-time data. Those criteria are typically based on the Kp -index, Dst -index, IMF components, solar wind speed and derived quantities such as coupling functions (e.g. summarized by [Kauristie et al., 2017](#)). The auroral electrojet (AE) indices ([Davis and Sugiura, 1966](#)) are however rarely used for designing quiet-time selection criteria although they aim to characterize the strength of the auroral currents in the polar regions and to capture the intensification linked to substorm activity.

The AE indices consist of AE , AL , AU and AO , and are based on the data from 10–13 magnetic observatories located between 65° – 75° dipole latitude under the average location of the auroral oval in the northern hemisphere. The lower and upper envelopes of the perturbations in the horizontal component, H , of 1 min measurements (quiet-time baseline removed) from those observatories defines the AL and AU indices, respectively. AL is designed to measure the strength of the westward electrojet and AU the eastward electrojet. The difference $AU - AL$ then gives the AE index and the mean value $(AL + AU)/2$ the AO index. Here, the AL index is of interest because, in principle, it can be used to identify indirectly substorm activity, which appears as a negative excursion in the AL index due to an intensification of the westward electrojet. Such indirectly driven substorm activity is not well captured by the AMPS ionospheric field parameterization, which works best in describing the climatology of directly driven polar currents ([Laundal et al., 2017](#)), so it is of considerable interest here if this part of the ionospheric currents can be minimized by an additional data selection criteria.

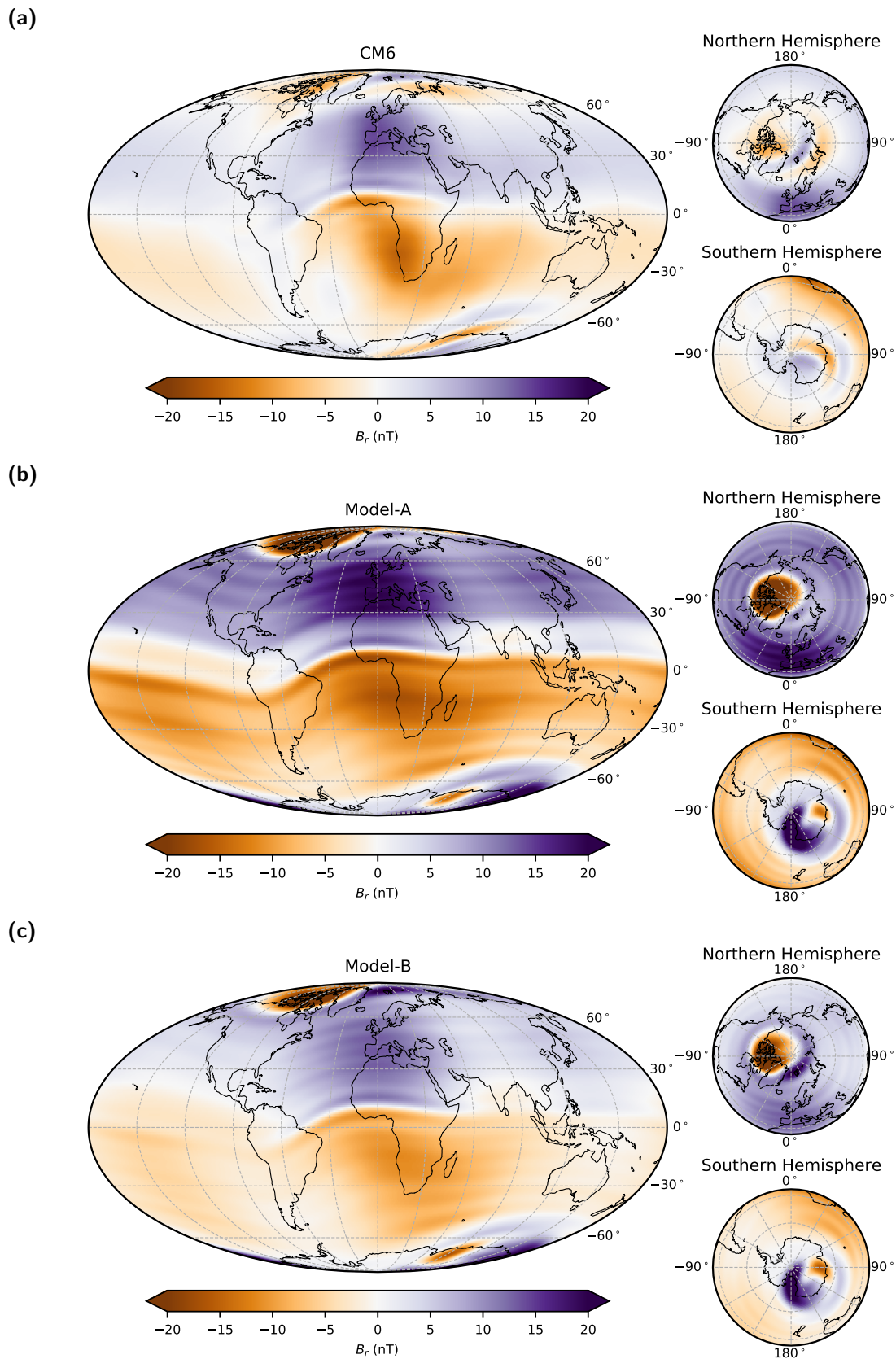
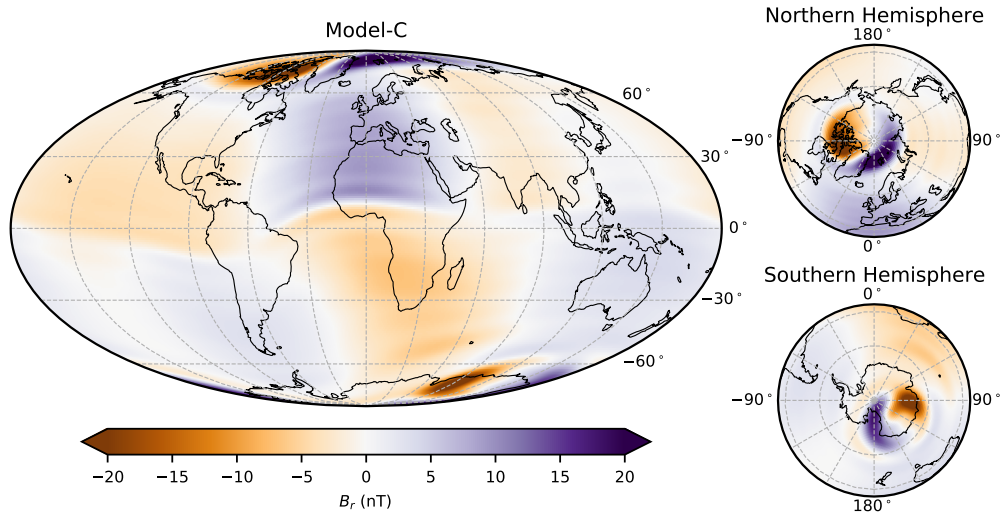
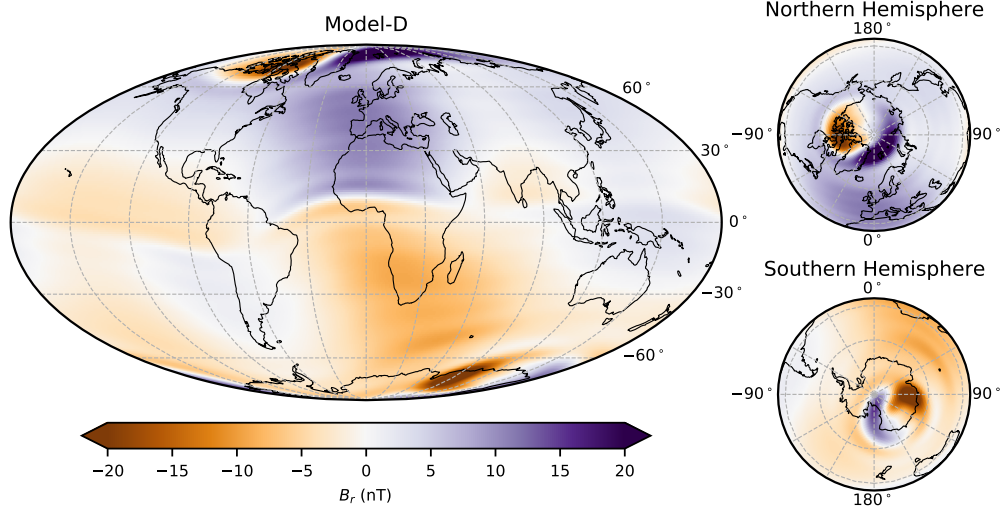


Figure 6.9.: Radial estimates of the ionospheric E-layer field computed with (a) CM6 and (b–f) the test models at 450 km height on 20 March 2018, noon in Greenwich (spring equinox). The external parameters were $B_t = 2.25$ nT, $\theta_c = -134^\circ$, $v_x = 440$ km s $^{-1}$, $F_{10.7} = 70$ sfu, and $\beta_{\text{tilt}} = 2.5^\circ$. See also next page.

(d)



(e)



(f)

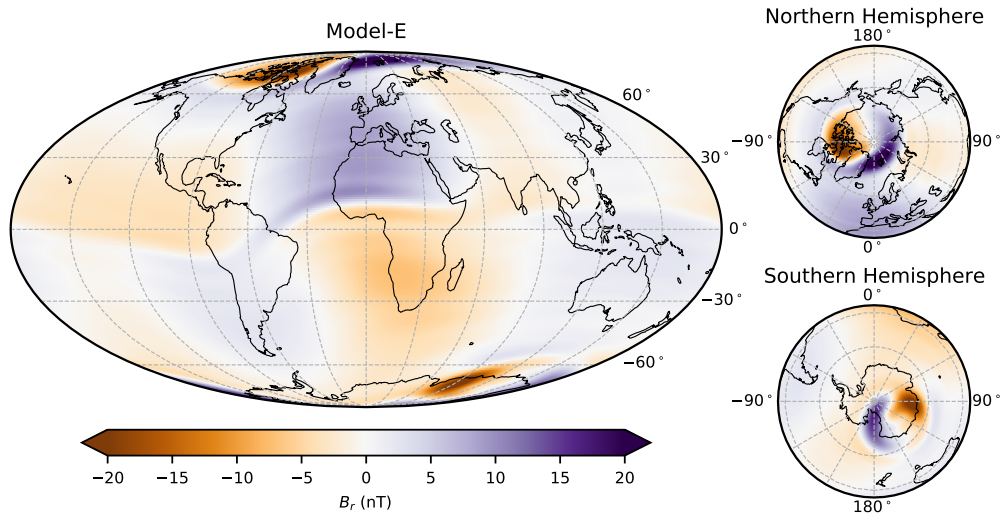


Figure 6.9.: Continued.

The reason the AE indices are usually omitted when attempting to identify quiet conditions in satellite data, as pointed out by *Ritter et al. (2004)*, is that the location of the observatories that contribute to the AE indices are unfortunately located too far south and are, therefore, not useful to monitor auroral activity under quiet conditions. To address this and other similar issues with other indices, the SuperMAG³ initiative (*Newell and Gjerloev, 2011a,b, 2012, 2014*) has released several new indices based on a more extensive network of more than 100 ground variometer and observatory stations, which should, in principle, allow for an improved monitoring of the spatiotemporal behaviour of the current systems around Earth. In particular the SuperMAG version of the *AL* index, called *SML*, provides a new opportunity for diagnosing auroral activity. *SML* is based on 1 min observations of the field parallel to the horizontal component of the IGRF reference field, from all available ground magnetometer stations of the SuperMAG network between 40°–80° dipole latitude. In addition to *SML*, which is a global index, SuperMAG offers a local, MLT-dependent index, *SML_{MLT}*, which consists of 24 indices: *SML-00*, *SML-01*, ..., and *SML-23*. Each of those is derived similar to *SML* but is only based on the subset of stations that fall into a 3 h window in MLT. For example, *SML-01* is produced by data at MLT between 0 h–3 h.

In this section I report on the impact on field models when selecting satellite data with a criterion based on the *SML* and *SML_{MLT}* indices. The selection criterion is very simple, i.e. it only consists of a threshold that is set on the linearly interpolated index values at the times of the satellite data. In contrast to *SML*, the interpolation of the *SML_{MLT}* is more complicated because it depends on two independent variables (observation time and MLT) and is constructed from overlapping 3 h windows in MLT, which give some freedom regarding the choice of the interpolation procedure. For simplicity, I used a bilinear interpolation scheme to find the *SML_{MLT}* index values between the known points in time and the points (0 h, *SML-00*), (1 h, *SML-01*), ..., (23 h, *SML-23*) in MLT. To simplify the presentation of the effects of data selection, I chose 15 s satellite data from Swarm-A between 15 November 2018 and 15 December 2018 as an example dataset. During this month, Swarm-A passed the northern polar region 463 times under mostly dark conditions as defined by the sun having a zenith angle of more than 100° (more than 10° below the horizon). Fig. 6.10 shows scalar residuals ΔF of the Swarm-A data with respect to Model-E along the 463 ascending-descending orbit segments within a 100° interval in QD latitude centered around the magnetic north pole. The residuals presented have not undergone any data selection except for the usual subsampling applied to reduce the original 1 s samples to 15 s samples. The scalar residuals are positively correlated within 70°–80° QD latitude on the ascending part of the orbit and, similarly, on the descending part of the orbit. However, when comparing the residuals on the ascending part with those on the descending part, the correlation is negative. Furthermore, Fig. 6.10 shows that the scalar residuals not only depend on the location in QD latitude but also vary in time. The large residuals in the second half of the considered month after orbit 28220 indicate an increased auroral activity. The structure in these residual patterns provides a clear illustration that the magnetic signal of the polar ionospheric currents is not well captured by Model-E when a broader range of geomagnetic conditions is considered.

Similar to *Ritter et al. (2004)*, to investigate the effect of the data selection, I computed the RMS value of the 15 s scalar residuals for each of the 463 orbit segments, first, without applying any data selection and plotted them against the orbit number in Fig. 6.11 (black lines in both panels). Next,

³<https://supermag.jhuapl.edu/>

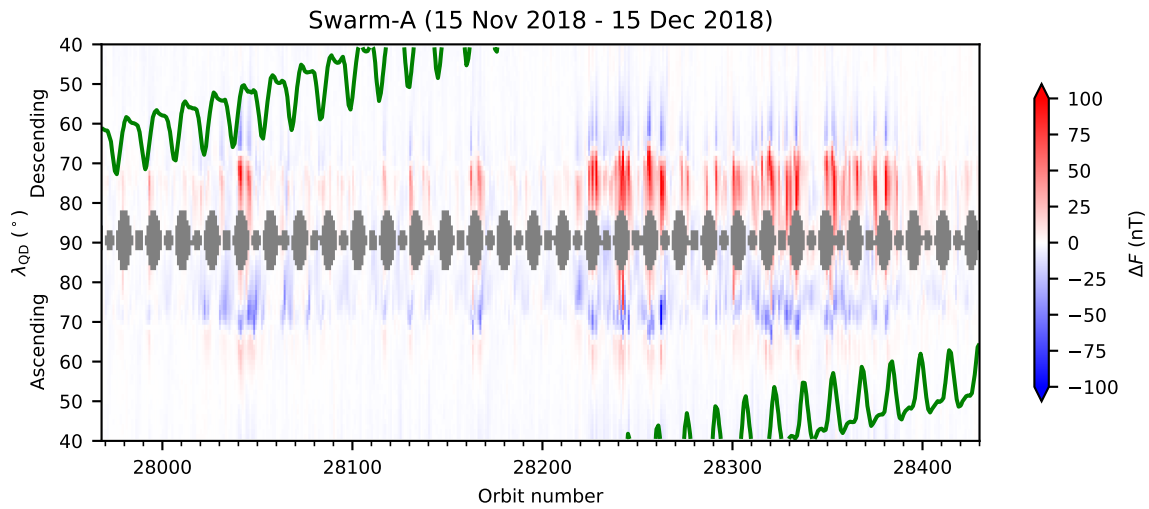


Figure 6.10.: Scalar residuals ΔF of Swarm-A with respect to Model-E along 463 orbit segments centered on the magnetic north pole between 15 November 2018 and 15 December 2018. The grey color indicates locations of missing data and the green line shows the contour of $\chi = 100^\circ$, i.e. the polar region was in darkness.

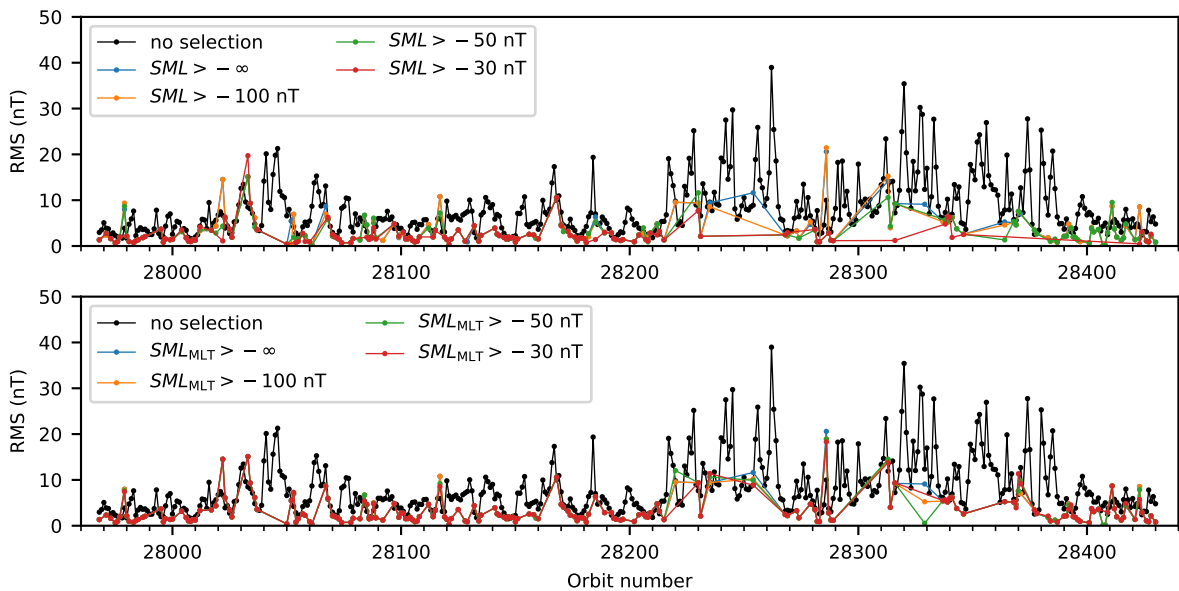


Figure 6.11.: RMS values of the scalar residuals with respect to Model-E for each of the 463 orbit segments with different choices of selection criteria applied. The black lines correspond to the original data without any selection, blue lines to data under geomagnetic quiet-time selection criteria, and the remaining lines show the RMS values for residuals that were selected using quiet-time selection supplemented with a criterion based on either SML -index (upper panel) or SML_{MLT} -index (lower panel) for three different thresholds (-100 nT, -50 nT, -30 nT).

Table 6.6.: Total number of orbit segments with at least one data point, total number of data, and overall RMS values of the scalar residuals shown in Fig. 6.10 for different selection criteria.

<i>SML</i>	No selection	$> -\infty$	> -100 nT	> -50 nT	> -30 nT
No. of orbits	463 (100%)	196 (42%)	192 (41%)	179 (37%)	132 (29%)
No. of data	172800 (100%)	13280 (8%)	12609 (7%)	11222 (6%)	8178 (5%)
RMS (nT)	9.80 (100%)	4.51 (46%)	4.12 (42%)	3.55 (36%)	3.06 (31%)

<i>SML</i> _{MLT}	No selection	$> -\infty$	> -100 nT	> -50 nT	> -30 nT
No. of orbits	463 (100%)	196 (42%)	196 (42%)	196 (42%)	190 (41%)
No. of data	172800 (100%)	13280 (8%)	13258 (8%)	13086 (8%)	12670 (7%)
RMS (nT)	9.80 (100%)	4.51 (46%)	4.41 (45%)	4.33 (44%)	4.22 (43%)

I computed the RMS values with the same scalar residuals but after applying a selection based on the geomagnetic quiet-time criteria including the dark condition criterion as summarized in Sec. 6.2 (blue lines in both panels). Finally, in addition to the previous quiet-time selection, I further removed scalar residuals at the times when *SML* (upper panel) and *SML*_{MLT} (lower panel) were below the chosen thresholds of -100 nT (orange lines), -50 nT (green lines), and -30 nT (red lines). Tab. 6.6 summarizes the number of orbit segments with at least one data point, number of data, and the overall RMS values after data selection. Looking at the quiet-time data selection ($SML > -\infty$ and $SML_{MLT} > -\infty$), Fig. 6.11 and Tab. 6.6 show that the RMS for each orbit segment, as well as the overall RMS, can be significantly reduced, from 9.80 nT to 4.51 nT in the case of the overall RMS. This, of course, is the intended outcome of applying data selection criteria. However, this reduction in RMS is achieved at the cost of removing 92% of the data and 58% of the orbit segments (recall that an orbit is only removed if all its data points are removed). A further reduction is possible by selecting data with a criterion based on either *SML* or *SML*_{MLT}, but *SML* appears to be more efficient. Considering the cases $SML > -100$ nT and $SML_{MLT} > -30$ nT, where the amount of orbit segments and data are approximately the same and the overall RMS values are similar while the threshold values differ considerably, suggests that the *SML*_{MLT} may require stricter threshold values than *SML*. However, increasing the *SML*_{MLT} threshold to, for example, -5 nT reduced the amount of data to 5583 (3%) but only achieved an RMS of 3.91 nT, which is not as low as for the case $SML > -30$ nT. Based on the example dataset and the performed tests, an additional selection based on the *SML*-index appears to be the preferred choice since it strikes the best balance between reducing the RMS and keeping as many data as possible. Therefore, I will focus on the *SML*-index.

As a next step, I built geomagnetic field models similar to the reference model in Sec. 6.6 (Reference) but also used the data selection criterion based on the *SML*-index. To give the data a greater control in determining the model parameters, I reduced the regularization of the time-dependent internal field by a factor of 10, i.e. $\lambda_t = 0.1 \left(\frac{\text{nT}}{\text{yr}^3}\right)^{-2}$, $\lambda_{t_s} = \lambda_{t_e} = 0.001 \left(\frac{\text{nT}}{\text{yr}^2}\right)^{-2}$. Fig. 6.12 shows the normalized histogram of the observed 1 min *SML*-index and the linearly interpolated index for the quiet-time selected satellite data. It indicates that, for example, 95% of the satellite data have an *SML*-index of greater than -100 nT. Therefore, an additional selection using the *SML*-index removes another 5% ($SML > -100$ nT), 20% ($SML > -50$ nT), and 55% ($SML > -30$ nT) from the geomagnetic quiet-time satellite data. The coefficients of the SA can be seen in Fig. 6.13 for

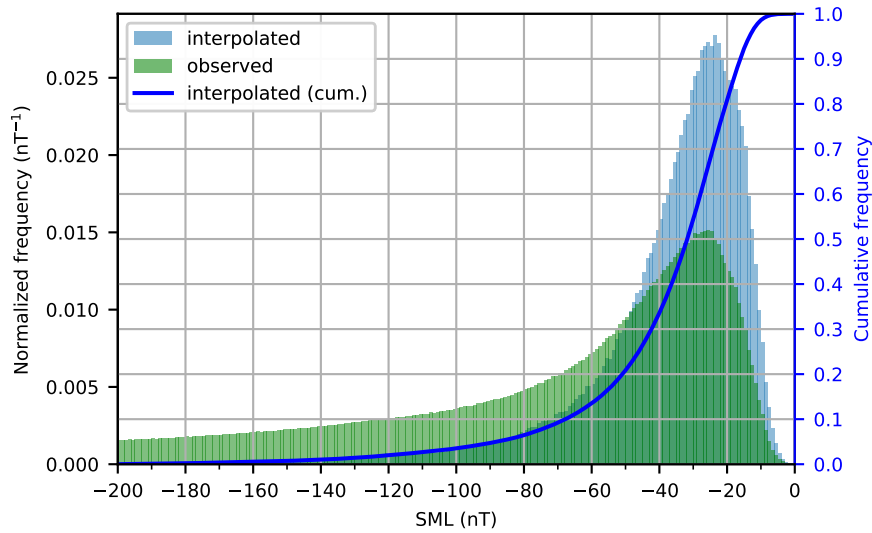


Figure 6.12.: Normalized histograms of the 1 min SML -index (observed) from 2000.0 to 2020.0 and the linearly interpolated index at the times of the satellite data after quiet-time data selection (interpolated). The blue line shows the cumulative histogram of the interpolated index. The histograms are normalized to unit area and the bin size is 1 nT.

Table 6.7.: RMS values of the scalar residuals in the polar region (poleward $\pm 55^\circ$ QD latitude) and the non-polar region (equatorward $\pm 55^\circ$ QD latitude).

	Model-E	Model-E	$SML > -100$ nT	$SML > -50$ nT	$SML > -30$ nT
		(low reg.)	(low reg.)	(low reg.)	(low reg.)
Polar	7.70 nT	7.67 nT	7.25 nT	6.57 nT	5.98 nT
Non-polar	3.49 nT	3.48 nT	3.46 nT	3.43 nT	3.45 nT

the period from 2014.0 to 2019.0, when *Swarm* data is available. The time series demonstrates that a decrease of the temporal regularization of the internal field increases the time variations in the SA coefficients, which appear as oscillations around the stronger regularized reference model (blue). The amplitude of the oscillations reduces again as the threshold of the SML -index criterion is increased, e.g. when looking at \ddot{g}_5^0 in the year 2016. It seems that the additional data selection provides a smoother time series of the SA. However, one should keep in mind that the data selection involves removal of data. Therefore, the impact of the regularization with fixed regularization parameters is slightly increased, which will also smooth temporal variations. This should especially be the case around 2014.0, when the sun was at solar maximum and more data was removed. This complicates the interpretation of the model results, but in all cases I find the SML -index data selection helps reduce the RMS value of the scalar residuals in the polar regions, i.e. poleward of $\pm 55^\circ$ QD latitude, whereas the RMS value remained unchanged in the non-polar region (Tab. 6.7).

The tests above provide evidence that a data selection criterion based on the SML -index can help to further reduce the misfit in the polar region, as measured by the RMS, when applied in addition to the typical quiet-time data selection. They also showed that the threshold needs to be set rather strict, for example, data below -30 nT should be removed. This leads to the rejection of an additional 50% of the quiet-time selected data (Fig. 6.12), which is a rather high percentage of the data. In fact, since the quiet-time data selection criteria are already fairly effective, an additional SML -based

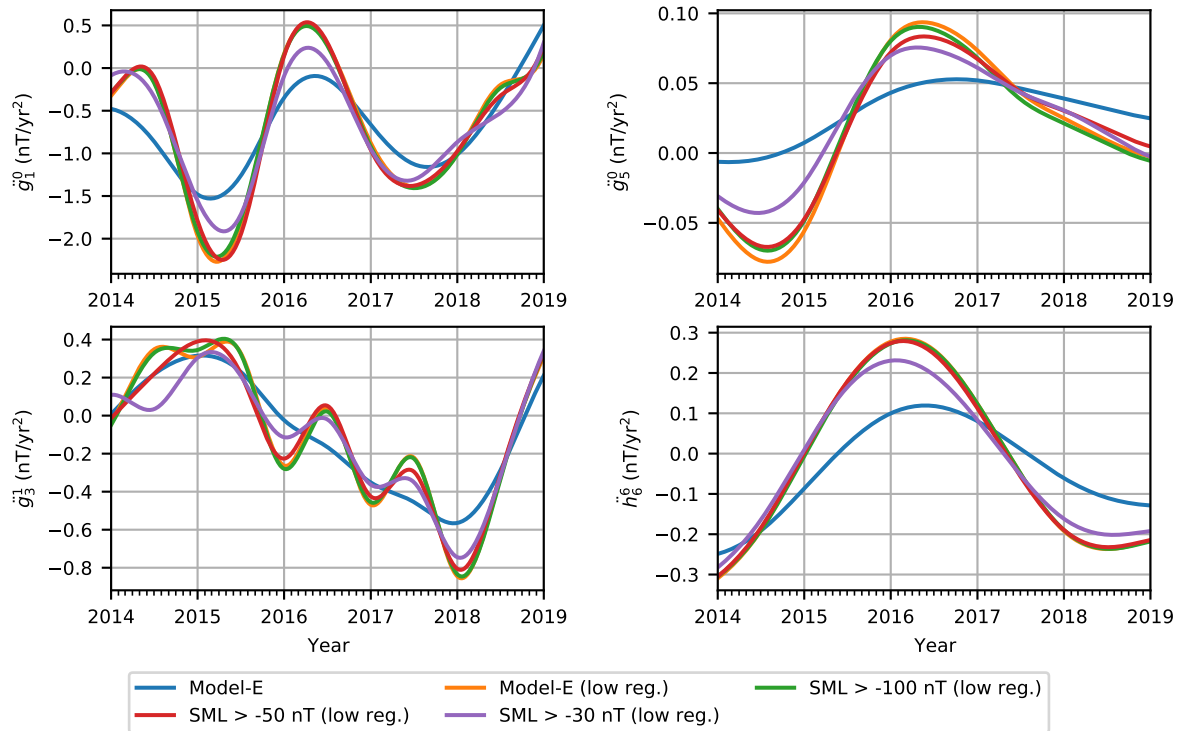


Figure 6.13.: Time series of the SA coefficients between 2013.0 and 2019.0 for the reference model (blue), the reference model with a lowered internal field regularization (orange), and models with a lowered regularization and an additional *SML*-index data selection using a threshold of -100 nT (green), -50 nT (red), and -30 nT (purple).

criterion does not seem to have a crucial impact on models with an AMPS-type ionospheric field. In particular because there is no evidence that the internal field model is significantly changed under a quiet-time selection supplemented with the *SML*-index. However, this can also be a result of the applied temporal regularization, which may not allow for significant changes to happen. In future, it could also be interesting to test a selection criterion based on the time derivative of the *SML*-index.

6.7. Results and discussion

The experiments in Sec. 6.6.2 showed that in the absence of further assumptions regarding the sources (e.g. imposed regularizations) there is a fundamental ambiguity between the ionospheric E-layer zonal field and the static internal field since both are internal sources with respect to the satellites and have the same time-dependence. This resulted in strong patterns organized by QD latitude in the difference maps between reference models and the test models which also accounted for the ionospheric E-layer field. In the results presented below I deal with this issue by adopting the approach of Model-E whereby the constant zonal coefficients in the parameterization of the ionospheric E-layer field are regularized. Model-E produced the most promising results in the tests of Sec. 6.6.2, with considerably reduced zonal artifacts. In this section I present results from Model-E in more detail, focusing on the quality of the co-estimated internal and ionospheric field models.

6.7.1. Spatial and temporal characteristics of quiet-time, nightside polar currents

Having obtained a promising co-estimated model of the ionospheric field during the conditions used in geomagnetic field modelling, it is of interest to ask what can be learned about the ionospheric currents under such geomagnetically quiet and dark conditions. Here I address this question by comparing the ionospheric part of Model-E, which was derived from quiet-time selected data, with AMPS. AMPS assumed linear relations to driving parameters from a wider range of conditions, including all IMF orientations and a strong coupling to the solar wind, and an internal field model (an earlier version of CHAOS) was removed from the data prior to the estimation of the AMPS parameters. Nonetheless, AMPS should reflect the basic features of the ionospheric current system even at quiet conditions and, therefore, help ascertain whether the currents given by Model-E have a realistic morphology and reasonable amplitudes. For simplicity, I focus on the northern hemisphere during winter when the north polar region is in darkness and the activity level of auroral currents was low.

Fig. 6.14 shows the divergence-free currents and the Birkeland currents given by Model-E and AMPS for different clock angles in the north polar region at 110 km altitude during winter. For the solar wind parameters I chose $B_t = 2 \text{ nT}$, $v_x = 350 \text{ km s}^{-1}$ and $F_{10.7} = 70 \text{ sfu}$, which are close to the peaks of the distributions in Fig. 6.1. I set $\beta_{\text{tilt}} = -25^\circ$ to select winter conditions. Each panel shows the currents in QD/MLT coordinates above 60° QD latitude with magnetic noon at the top, midnight at the bottom, dawn on the right and dusk on the left. The contours are the levels of the divergence-free current function ψ^{df} (Eq. 6.6a) drawn every 5 kA. The associated divergence-free part of the horizontal currents flows along the contours in the direction of the local gradient of the current function rotated counter-clockwise by 90° . The dashed and solid contour styles indicate the direction of the gradient and have, otherwise, no significance. The colors represent the Birkeland currents (Eq. 6.9) having a positive (negative) value if the current is directed upward (downward). The chosen clock angles correspond to IMF conditions ranging from purely northward ($\theta_c = 0^\circ$: $B_{\text{IMF},z} > 0 \text{ nT}$, $B_{\text{IMF},y} = 0 \text{ nT}$), eastward ($\theta_c = 90^\circ$: $B_{\text{IMF},z} = 0 \text{ nT}$, $B_{\text{IMF},y} > 0 \text{ nT}$), southward ($\theta_c = 180^\circ$: $B_{\text{IMF},z} < 0 \text{ nT}$, $B_{\text{IMF},y} = 0 \text{ nT}$) to westward ($\theta_c = -90^\circ$: $B_{\text{IMF},z} = 0 \text{ nT}$, $B_{\text{IMF},y} < 0 \text{ nT}$). It is important to stress that the ionospheric currents of Model-E were determined from geomagnetically quiet conditions. Under these conditions, roughly 40% of the satellite data that contributed to Model-E fell into the northward IMF category ($|\theta_c| < 45^\circ$), 30% into eastward IMF ($45^\circ \leq \theta_c \leq 135^\circ$), 29% into westward IMF ($-45^\circ \leq \theta_c \leq -135^\circ$), and 1% into southward IMF ($|\theta_c| > 135^\circ$). Hence, the southward IMF condition is poorly represented in Model-E and results for these conditions should be considered an extrapolation.

The divergence-free and Birkeland currents for Model-E are found to be weak for all shown clock angles. Although weak, there is an appreciable asymmetry in the strength of the divergence-free currents with respect to $B_{\text{IMF},y}$ and $B_{\text{IMF},z}$, causing stronger currents when the IMF turns away from the northward direction and $B_{\text{IMF},y} > 0 \text{ nT}$. This is less the case for the Birkeland currents, which remain mostly unchanged for different clock angles. The two-cell pattern is largely absent for all clock angles. Instead, the divergence-free currents encircle the magnetic north pole and create a single cell pattern, offset towards the night side and towards dawn, which seems to depend only weakly on the clock angle. The divergence-free currents for southward IMF appear more complex and there may be a second cell in the dusk sector.

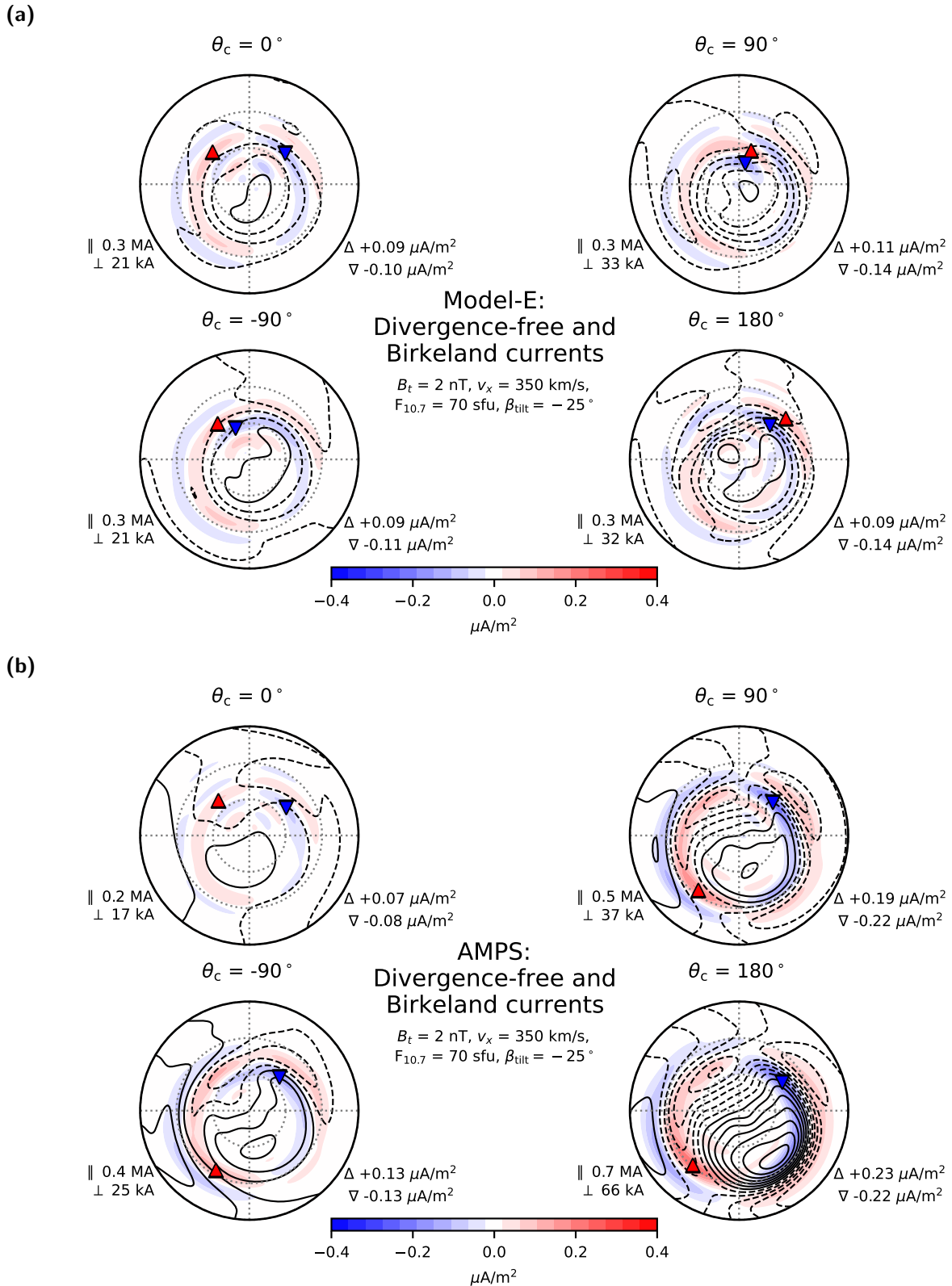


Figure 6.14.: Divergence-free and Birkeland currents given by Model-E (a) and AMPS (b) for different clock angles in the north polar region at 110 km altitude during winter. The currents are given in QD/MLT coordinates above 60° QD latitude with magnetic noon at the top. The contours show the current function of the divergence-free currents every 5 kA (solid lines for positive values and dashed lines for negative) and the colors are the Birkeland currents (positive upward). The location of the largest upward (Δ) and downward (∇) Birkeland currents are marked by the colored triangles and their strength is given in the lower right corner of each panel. The integrated field-aligned (||) and horizontal (\perp) current is given in the lower left corner. These figures are similar in form to those originally presented by [Laundal et al. \(2017\)](#) for AMPS.

Turning to AMPS, the currents are considerably stronger compared to Model-E except for northward IMF, when they are comparable in strength during these dark conditions due to the lack of ionizing radiation from the sun and the weak solar wind-magnetosphere coupling. When the IMF rotates southward, both divergence-free and Birkeland currents increase in strength and the two-cell pattern of the divergence-free currents manifests itself more clearly. Also, the R1 and R2 Birkeland currents become more prominent. The currents are strongest for southward IMF when the dayside reconnection maximizes. In that case, the dawn cell completely dominates and peaks in the post-midnight sector (lower right quadrant). Similar to Model-E, although more pronounced, there is an asymmetry in the current strength with respect to $B_{\text{IMF},z}$ and $B_{\text{IMF},y}$. The equatorward edge of the dawn cell is the westward electrojet.

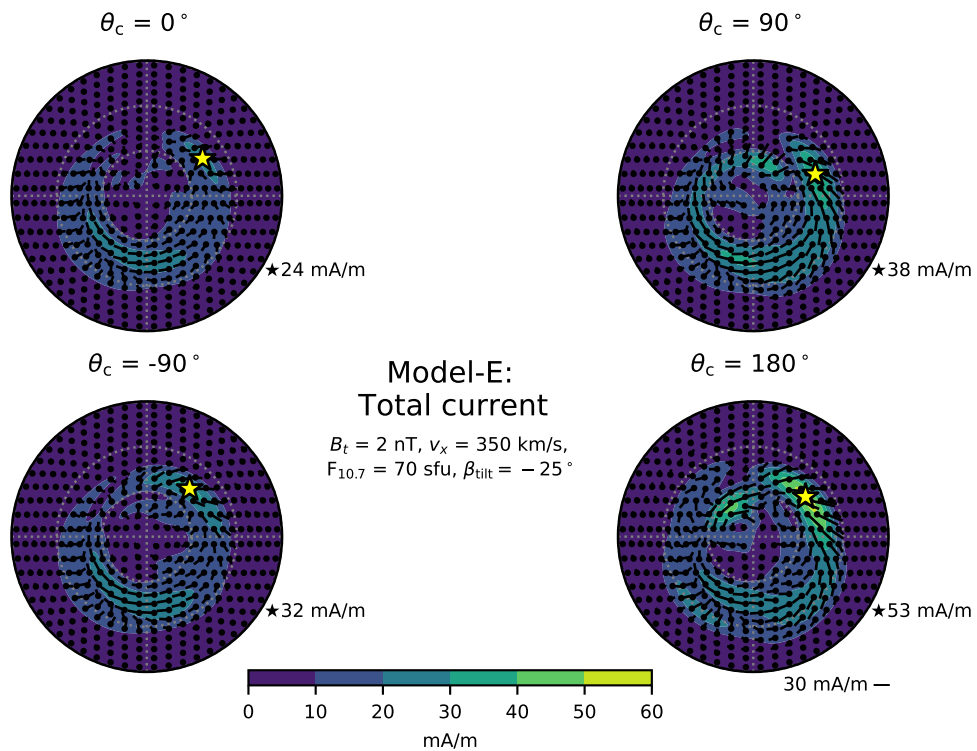
An alternative to looking at the divergence-free and Birkeland currents, is to consider the total horizontal currents (sheet currents), which can be computed directly through Eq. (6.5). Fig. 6.15 shows the total currents given by Model-E and AMPS for different clock angles in the north polar region at 110 km altitude during winter. The direction of the arrows is along the currents and the length is proportional to the current strength. The color scales with the strength of the currents and the location of the maximum is marked by the yellow star, while its value is given in the lower right corner of each panel.

Beginning with Model-E, the total horizontal currents are weak for all the shown clock angles. Note the difference in the color scale between Model-E and AMPS, which amplifies the small amplitude structures in the currents for Model-E. The currents are confined to the auroral oval and are mostly zero in the polar cap (region poleward of the auroral oval) for all clock angles. The maximum of the currents stays on the dayside and increases in strength as the IMF becomes more southward. But as before, the case of southward IMF is more uncertain for Model-E due to the quiet-time data selection. Noteworthy are the strong westward currents in the auroral oval for all clock angles around midnight and even in the dusk sector, where AMPS predicts an eastward current.

Turning to AMPS, the total horizontal currents for northward IMF are close to zero in the entire polar region, which is similar to Model-E. As the IMF turns southward, the currents in the auroral oval increase and are strongest for southward IMF with a peak in the post-midnight sector. In contrast, the polar cap stays largely free of currents, irrespective of the clock angle. As the currents mostly flow along the auroral oval, they form the westward electrojet in the post-midnight sector. They then converge in the pre-midnight sector, which coincides with the location where the upward currents maximize in Fig. 6.14b. Again, the currents are clearly sensitive to $B_{\text{IMF},y}$ as they are stronger for $B_{\text{IMF},y} > 0$ nT than for $B_{\text{IMF},y} < 0$ nT.

To summarize, the currents, i.e. divergence-free and Birkeland currents and total horizontal currents, given by Model-E are similar in strength to the corresponding estimates of AMPS for northward IMF for which Model-E has most contributing data. While for AMPS the currents are very sensitive to a southward turning IMF and increase rapidly in strength, for Model-E they experience only a moderate change, which is a consequence of the quiet-time data selection. This suggests that, at least in terms of the current strength, Model-E gives realistic estimates for the range of conditions covered by its input data. However, in terms of the morphology of the currents, there is a considerable difference between Model-E and AMPS. For Model-E, the divergence-free currents and the total horizontal currents flow predominantly westward along the auroral oval, whereas, for AMPS, the

(a)



(b)

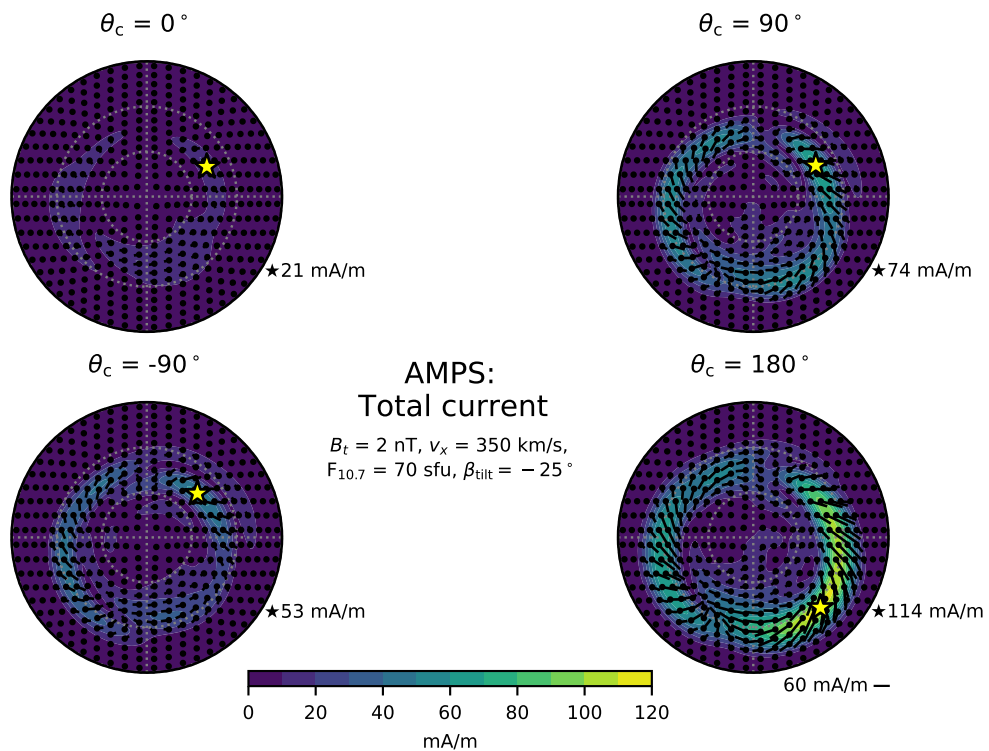


Figure 6.15.: Total horizontal currents given by Model-E (a) and AMPS (b) for different clock angles in the north polar region at 110 km altitude during winter. The currents are given in QD/MLT coordinates above 60° QD latitude with magnetic noon at the top. The arrows point in the direction of the current and the length is proportional to the current strength, which is also shown by the color (note the difference in scale between (a) and (b)). The location of the strongest current is marked by the yellow star and its strength is given in the lower right corner of each panel. These figures are similar in form to those originally presented by [Laundal et al. \(2017\)](#) for AMPS.

divergence-free currents form a two-cell pattern and the total currents have an eastward component on the dusk side of the auroral oval. It is worth considering whether the pattern of strong westward currents might be enhanced for Model-E due to the ambiguity regarding the internal field. Hence, in another experiment (not shown) I increased the regularization parameter of the $g_{n,0}^{0,\text{ion}}$ coefficients in Model-E by a factor of 100 to $\lambda_{\text{df}} = 1 \times 10^6$ but found no discernible difference in the strength and morphology of the currents. I also found the same westward flowing currents but much larger in strength for Model-A and Model-B, where the constant zonal coefficients $g_{n,0}^{0,\text{ion}}$ of the ionospheric E-layer field were treated differently compared to Model-E.

6.7.2. Extending the AMPS model parameterization to include indirectly driven polar currents

The previous section showed that the total horizontal currents for Model-E under geomagnetic quiet and dark conditions have a strong westward component along the auroral oval and that this pattern is essentially unchanged for different IMF orientations. This is due to the applied data selection, which, by design, reduces the impact of direct driving processes associated with magnetic reconnection at the magnetopause on the dayside. However, indirect driving usually associated with nightside reconnection occurring in the equatorial plane of the magnetotail is also an important driver of ionospheric electrodynamics ([Milan et al., 2017](#)). Thanks to nightside reconnection, there are times when the currents in the auroral oval are enhanced and generate magnetic perturbations even though solar wind driving parameters satisfy geomagnetically quiet criteria and the polar ionosphere is in darkness. Such indirectly-driven nightside magnetic variations, if they do not average to zero over time, could then lead to a remaining contamination of the internal field model in the polar regions.

AMPS does not explicitly account for the nightside reconnection because, as [Laundal et al. \(2017\)](#) explains, there is presently no ideal proxy to parameterize it. In principle, a possible choice of a proxy could involve the AE indices since they reflect the magnetic perturbations of the currents in the auroral oval for all conditions. In particular, an *AL*-type index is an interesting candidate since negative excursions of its value are a typical signature of indirectly driven substorms. Given our particular interest in dark and nightside conditions, in this section I test an extension of the AMPS parameterization by incorporating an *AL*-type index as an additional input, along with the other solar wind driving parameters. The aim is to explore whether this may lead to an ionospheric model which takes better account of nightside auroral activity in general and substorms in particular.

Within the AMPS framework of modelling the ionospheric field, I therefore derived a test model, Model-F, which is identical to Model-E but includes the *SML*-index (which is derived from an improved geographical coverage of stations than the original *AL*-index) in the parameterization of the ionospheric E-layer field and the toroidal field, increasing the number of base functions X_i from 18 to 19 with

$$X_{19} = SML, \quad \bar{X}_{19} = -31 \text{ nT}. \quad (6.19)$$

The *SML*-index is therefore used in the same way as $F_{10.7}$, i.e. without an explicit dependency on θ_c because the *SML*-index already changes amplitude with θ_c (also see Fig. 6.2 for the distribution of *SML*-index values used to derive Model-F). The regularization parameters were unchanged.

Fig. 6.16 shows the divergence-free currents, the Birkeland currents and the total horizontal currents from Model-F, for different *SML*-index values instead of the clock angle as in Figs. 6.14 and

6.15, again in the north polar region at 110 km altitude during winter. The currents were computed for purely northward IMF and, therefore, represent conditions when the dayside driving is weak. The SML -index gradually decreases from one panel to the next, down to $SML = -160$ nT, which could be considered an extrapolation since only very few of the selected data had values this low according to Fig. 6.12.

The divergence-free currents are dominated by the dawn cell producing a circumpolar pattern while the total current is weak for SML close to zero. With decreasing SML , the currents become stronger as indicated by the total upward and horizontal currents (2–3 times stronger for $SML = -160$ nT compared to $SML = -40$ nT). The divergence-free currents form a two-cell pattern as the dusk cell becomes visible and gains in strength. But the two-cell pattern remains very asymmetric with a strong dawn cell, while the dusk cell is elongated and crescent-shaped. The total current increases in the auroral oval and reaches a maximum in the post-midnight sector. The total horizontal currents in the polar cap are largely absent.

Two interesting observations can be made in the case of strong negative SML -index values. First, the fact that the total horizontal currents maximize in the post-midnight sector agrees well with the location where the westward electrojet is strongest. This is very encouraging since SML is based on ground observatory data from all local times and does not in itself reflect an MLT-dependence, this must arise due to the newly estimated spherical harmonic terms which do have an MLT dependence. Model-F succeeds in estimating the location of the maximum current where one would expect the westward electrojet to be strong. Second, the sector around midnight does not only exhibit strong horizontal currents but is also where the field-aligned currents are strong and form a pattern that is consistent with a substorm current wedge in darkness. That is, a pair of field-aligned currents, down at dawn and up at dusk, connected in the ionosphere via the auroral oval. A similar pattern of Birkeland and horizontal closure currents was also found by [Laundal et al. \(2017\)](#) in the AMPS model for purely southward IMF, which in their interpretation is the dominant winter current system.

6.7.3. Effect of co-estimating ionospheric currents on the estimated high-latitude time-dependent internal field

Isolating the internal field at polar latitudes is challenging due to the strong and highly dynamic disturbance fields produced by the polar ionospheric currents and the ionospheric-magnetospheric coupling currents. Since those disturbance fields may leak into the estimated internal field, it is of relevance to see in what way, if any, the co-estimation of average ionospheric currents through the AMPS approach affects the internal field at high latitudes. In the following, I compare Model-F with the reference model from Sec. 6.6 giving special attention to the time-dependence of the internal field.

Fig. 6.17 shows the evolution of the spatial power spectra of the internal field, SV and SA over the model time interval computed with Model-F at the CMB. The spatial power spectra reveal that the power of the difference fields between Model-F and the reference model, which reflects the effect on the internal field when co-estimating an ionospheric field model, is consistently lower than the power spectra of the models themselves in all three panels and for all spherical harmonic degrees, except for the high degree SV. The difference fields are generally more pronounced at small spatial scales at the CMB, especially regarding the SV.

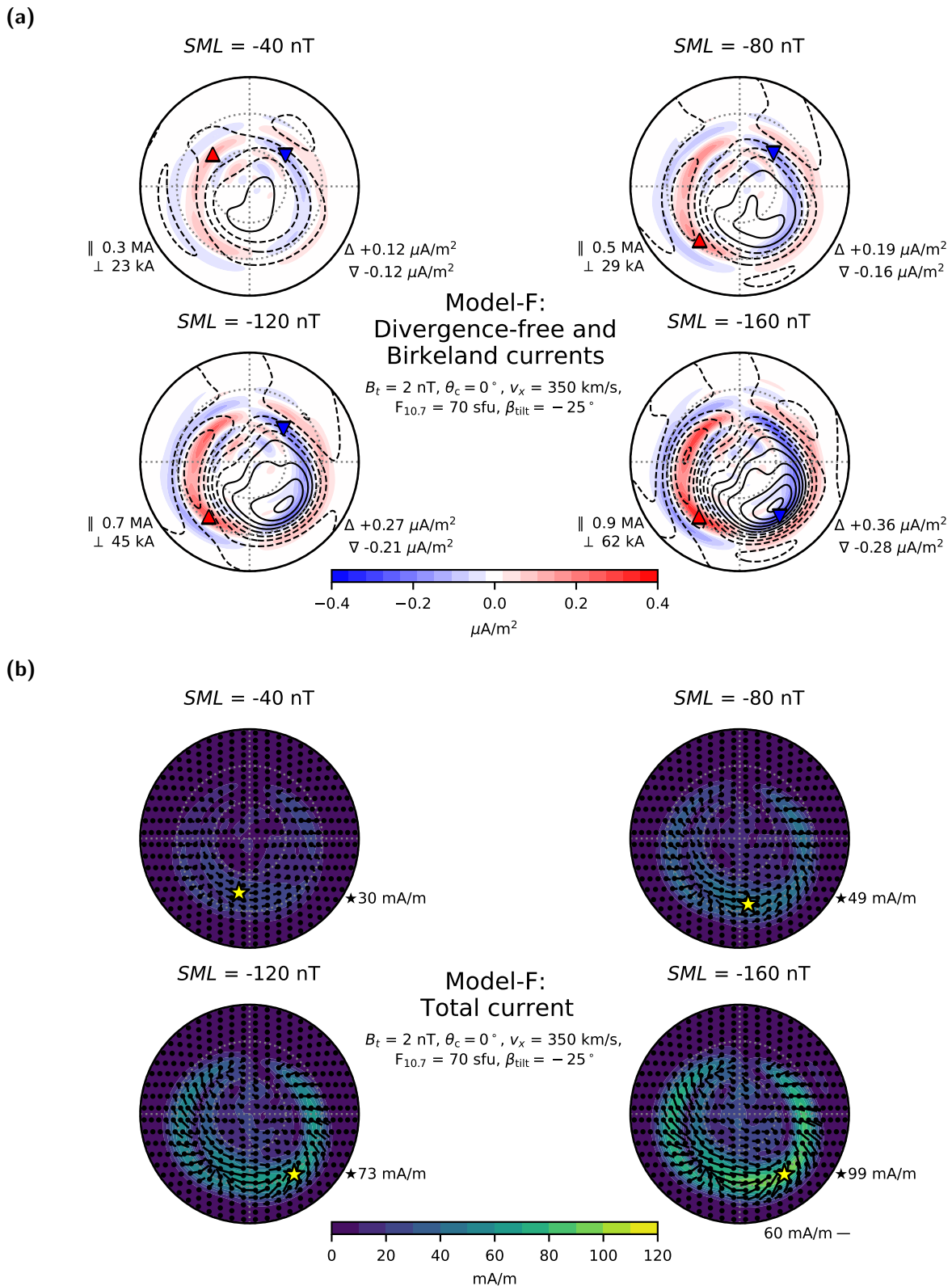


Figure 6.16.: Divergence-free and Birkeland currents (a) and total horizontal currents (b) given by Model-F for different SML -index values in the north polar region above 60° QD latitude at 110 km altitude during winter. The currents were computed with northward IMF but are otherwise identical to Figs. 6.14 and 6.15.

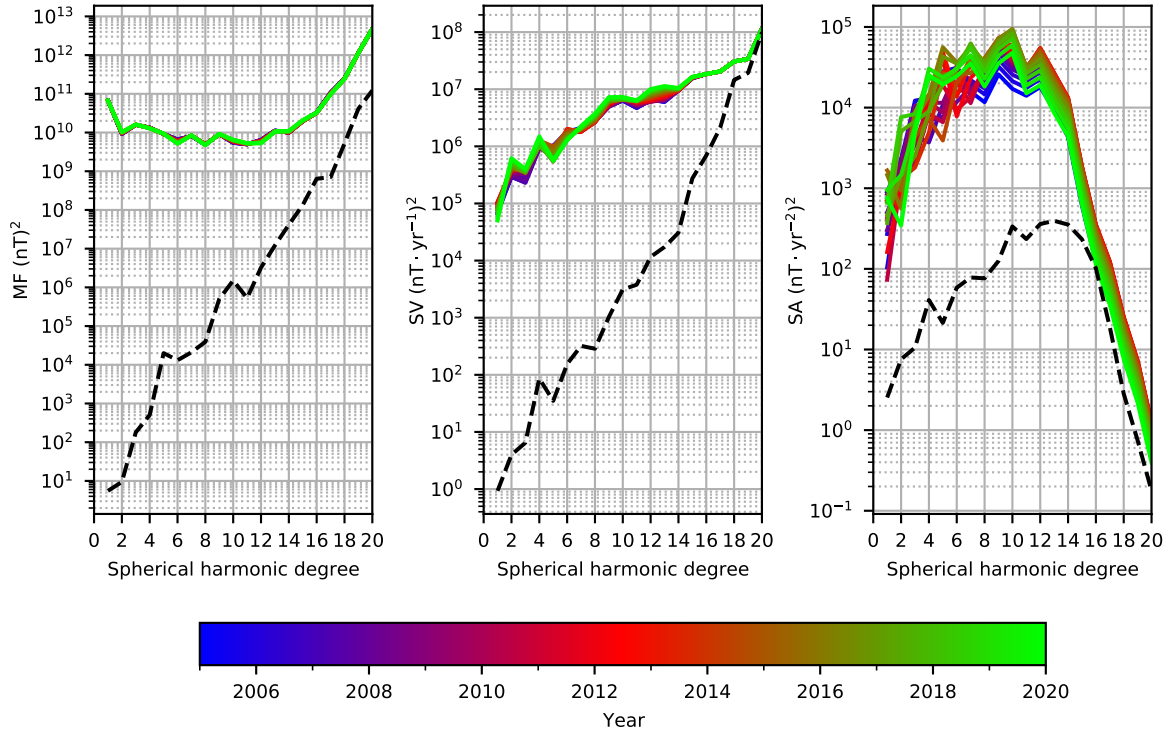


Figure 6.17.: Spatial power spectra of the internal magnetic field (left), SV (center) and SA (right) up to degree 20 given by Model-F at the CMB. The colors indicate different time points equally spaced over the model time interval. Blue roughly corresponds to the CHAMP time period, green to the gap period and red to the *Swarm* time period. The colored lines are computed with Model-F and the black dashed line is the average spectrum of the difference between estimates of Model-F and the reference model.

In Fig. 6.18 I compare the time series of a selection of SV coefficients given by Model-F and the reference model. The coefficients range from spherical harmonic degree $n = 1$ to $n = 20$ and from spherical harmonic order $m = 0$ (zonal terms) to the maximum order of the given degree (sectorial terms). The first row presents the SV coefficients of the internal dipole, which are essentially identical for Model-F and the reference. Going along the panels in each column, i.e. with increasing degree, the time series of both models start to deviate from each other. At the same time, going along each row, i.e. with increasing order, the models show increasingly similar coefficients. Noteworthy are the coefficients shown for $n = 20$, which are constant in time due to the strong temporal regularization at high degree. The arrangement of the coefficients illustrates that the difference in the SV between Model-F and the reference is mostly represented in the high-degree and low-order Gauss coefficients. This agrees with the expected structure of ionospheric field as seen in the geocentric frame when time-averaged over years and longer as is relevant for these internal field models. Although I do find differences between the SV in the reference model and Model-F the amplitude of these differences is fairly small.

The fact that the difference between the reference model and Model-F is relatively small is also apparent when looking at global maps of Model-F and the difference in 2018.0 at the CMB (Fig. 6.19). The maps show the fields truncated at spherical harmonic degrees that are considered least affected by artifacts of the modelling setup. In the case of the internal field, I chose the truncation level $n = 14$, which is approximately where the spatial power spectrum starts to diverge. In the case of the SV and the SA, I used $n = 16$ and $n = 10$ because the temporal regularization of the internal

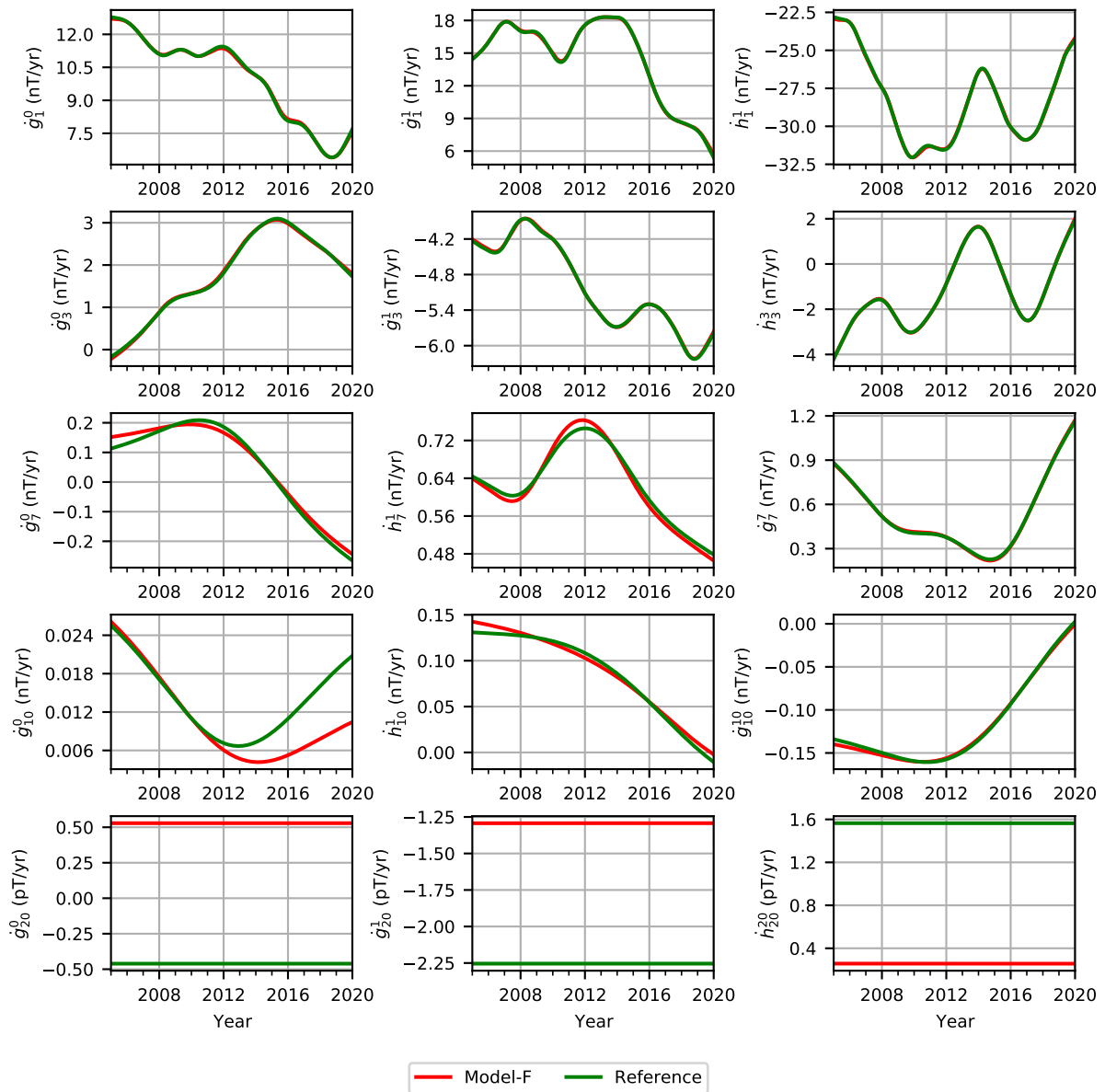


Figure 6.18.: Time series of the SV coefficients given by Model-F (red) and the reference model (green). Coefficients along each row have the same spherical harmonic degree but increase in order, while the coefficients along each column have the same spherical harmonic order but increase in degree. Note the difference in units for the last row.

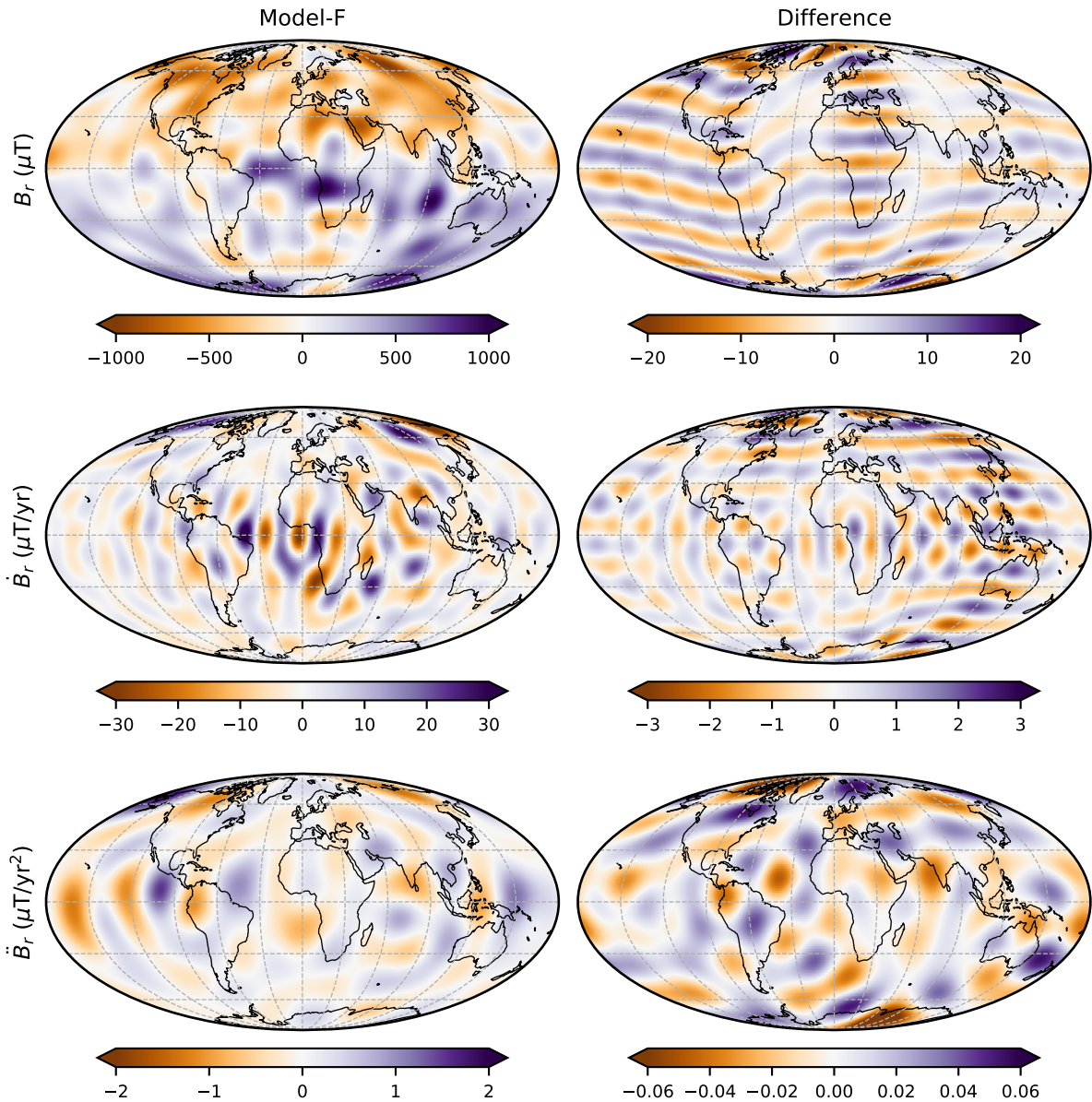


Figure 6.19.: Radial estimates of the internal magnetic field for $n \leq 14$ (top row), SV for $n \leq 16$ (center row) and SA for $n \leq 10$ (bottom row) given by Model-F (left column) and the difference to the reference model (right column) in 2018.0 at the CMB.

field starts to dominate the spectra as can be seen in Fig. 6.17 by the SV becoming constant in time around $n = 16$ and the sharp drop in the SA power beyond $n = 10$. Although there is structure in the difference fields, e.g. the zonal pattern in QD latitude for the radial field and partly the radial SV, the amplitudes are more than 50 times smaller in the field and 10 times smaller in the SV compared to the original signals as given by Model-F. Therefore, the change in the internal field of Model-F with respect to the reference model in terms of interpretable features at these truncation degrees, is rather small. This indicates that standard field models, built using data selection and regularization similar to that of the reference model are probably not badly contaminated by leakage from the ionospheric field at these degrees.

Returning to the spatial power spectrum of the SV in Fig. 6.17, notice that the power in the SV difference field is comparable to Model-F for spherical harmonic degrees above $n = 18$. At $n = 19$

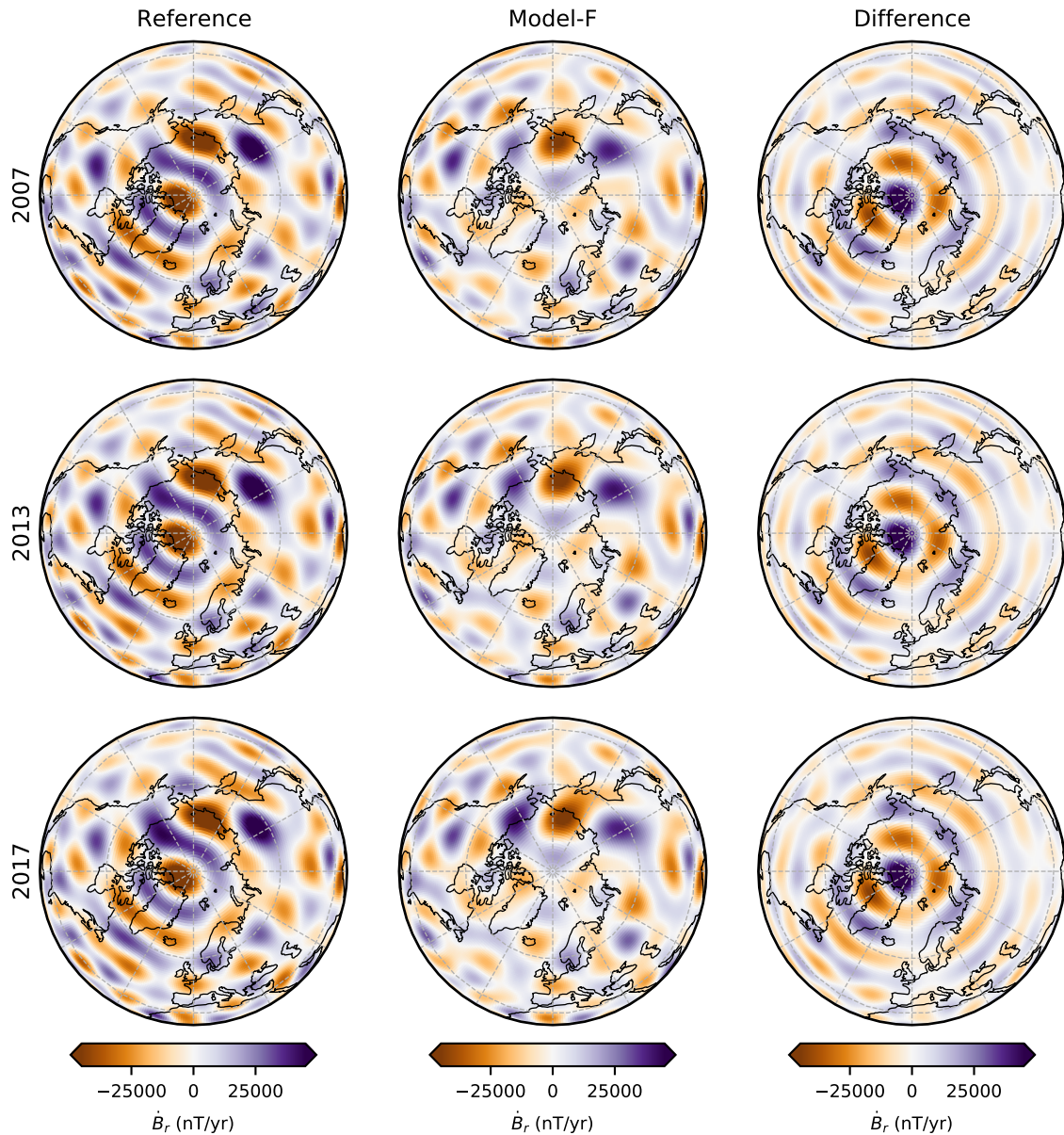


Figure 6.20.: Estimates of the radial SV up to degree $n = 20$ given by the reference model (left column), Model-F (center column) and their difference (right column) in 2007.0 (top row), 2013.0 (center row) and 2017.0 (bottom row) in the north polar region at the CMB.

the power increases slightly, which could indicate that the spectrum is about to become unstable. However, since the power increase is rather small, it may be justified to plot the SV up to $n = 20$ at the CMB. This is a higher truncation level than is usually considered from plotting the SV, precisely because it tends to become unstable at the CMB at this level. In Fig. 6.20 I present the estimates of the radial SV up to $n = 20$ given by Model-F, the reference model and their difference in 2007.0, 2013.0 and 2017.0 evaluated in the north polar region at the CMB. The SV in the maps is dominated by small-scale contributions as can be seen by the large number of positive and negative flux patches. The patches hardly change in time due to the strong temporal regularization of the internal field at high degree, which eliminates most of the SA at such high spherical harmonic degrees. In the case of the reference model, those flux patches tend to be elongated approximately in the longitudinal direction, which creates a faint but noticeable pattern of concentric rings. This is clearly an artifact

of the parameterization of the reference model, which does not take ionospheric sources into account. In contrast, the maps computed with Model-F do not show the pattern of rings but instead display well-focused flux patches in the polar region. This improvement is most noticeable in the high latitude SV flux patches investigated in models truncated at lower spherical harmonic degree by [Livermore et al. \(2017\)](#). It is conceivable that Model-F also improves the resolution of the SV at lower spherical harmonic degrees although this cannot be seen directly. The difference between the reference model and Model-F isolates an obvious leakage of the ionospheric signal into the reference model. Fig. 6.20 thus provides evidence that the co-estimation of the ionospheric field in Model-F improves the high-degree time-dependent internal field at high latitudes.

The overall small difference between Model-F and the reference model raises the question whether or not the temporal regularization of the internal field exerts too much control over the model parameter estimation. After all, the spatial power spectrum of the SA above, say $n = 12$, is essentially eliminated by the temporal regularization, which is conventionally applied to reduce contamination of the core field by magnetospheric, ionospheric and related induced fields. One might wonder whether more interesting differences related to co-estimating the ionospheric field might be seen if the temporal regularization were relaxed. In a final investigation I therefore compare models where the temporal regularization has been relaxed.

Based on Model-F, I derived a low-regularized version, called Model-G, by reducing the temporal regularization parameters by a factor of 10^4 to $\lambda_t = 10^{-4} (\text{nT/yr}^3)^{-2}$, $\lambda_{t_s} = \lambda_{t_e} = 10^{-6} (\text{nT/yr}^2)^{-2}$. Moreover, all internal coefficients were treated the same way, i.e. the zonal terms were not regularized heavier than the non-zonal terms. In a similar way, I derived a low-regularized version of the reference model. Fig. 6.21 shows the time series of some low-degree SV coefficients of the models with relaxed regularization. Reducing the temporal regularization increases the temporal variation of all shown coefficients for both Model-G and the low-regularized reference model, especially in the case of coefficients that are zonal (e.g. \dot{g}_3^0, \dot{g}_4^0) or near zonal (e.g. \dot{g}_2^1, \dot{g}_3^1). I also found similar oscillations at higher spherical harmonic degrees but with decreasing amplitude. Focusing on the zonal coefficients, the oscillations are very distinct during CHAMP and *Swarm* times with an oscillation period close to 1 yr but less so during the gap period where I did not use satellite data in these models (e.g. \dot{g}_4^0). Among the presented zonal terms, only the oscillation in \dot{g}_1^0 appears more erratic. It is interesting to note that co-estimating an AMPS-type ionospheric model leaves these annual oscillations essentially unchanged with the exception of \dot{g}_1^0 during CHAMP and \dot{g}_2^0 during *Swarm*, for which the amplitudes are smaller in Model-G compared to the low-regularized reference model.

In an effort to extract the structure of this annual signal, which obviously pollutes the internal field at low temporal regularization, I computed the SA of Model-G and Model-F, and then took the difference between these low regularized and strongly regularized versions of the SA. This processing acts as a high-pass filter, which highlights the annual variations and removes the slow change of the SA over the model time interval. Figs. 6.22 and 6.23 presents maps of the radial SA difference up to degree $n = 14$ at different times during a 2 yr period from 2016.0 to 2018.0 at the Earth's surface. The presented snapshots of the SA difference are separated by 3 months and each column covers a full year. The maps reveal a distinct structure of the annual oscillation pattern in the radial SA in the form of three patches. There are two patches centered on the Pacific, which are opposite in sign, and a single patch over Antarctica, which is opposite in sign to the patch in the South Pacific. The

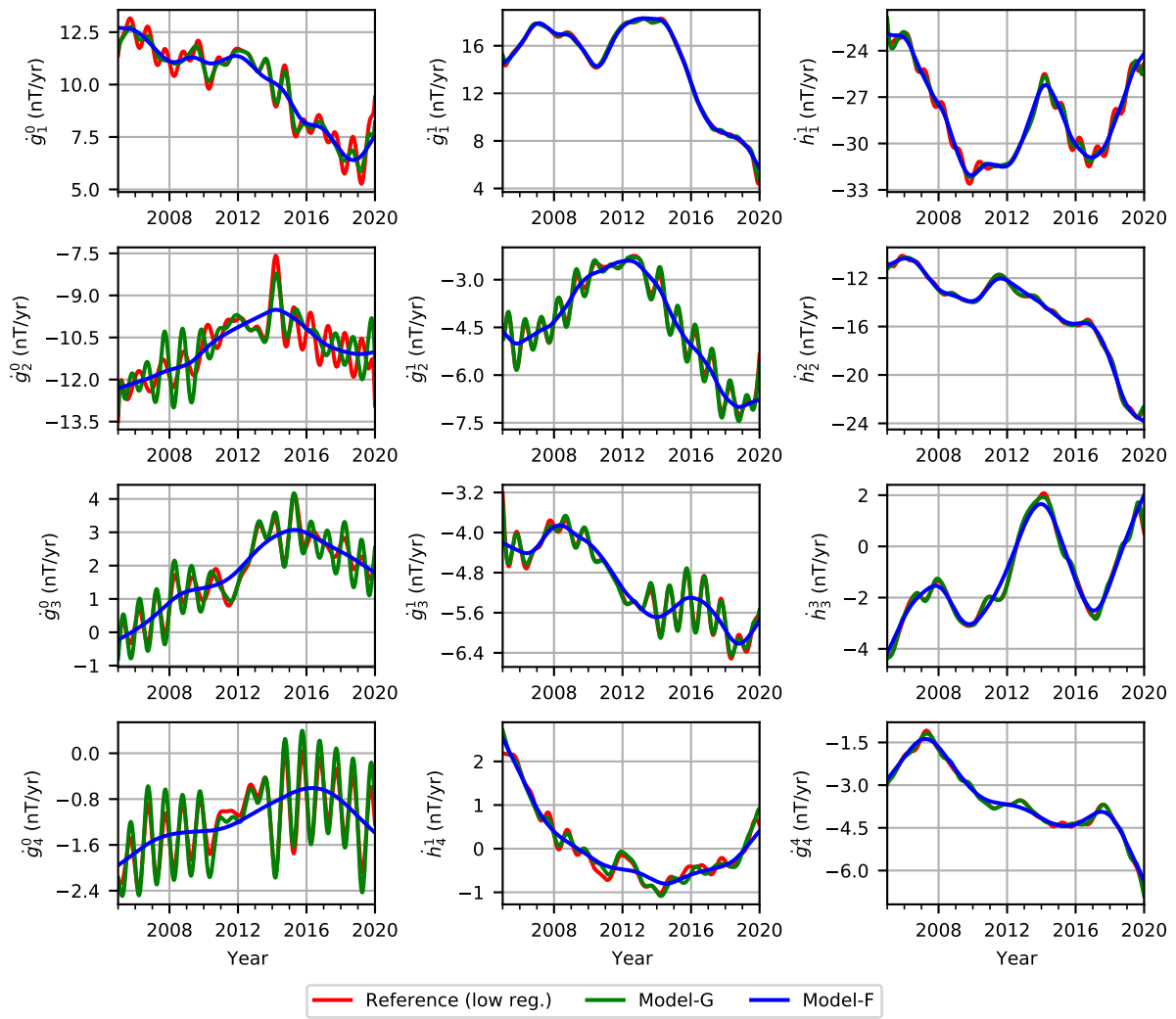


Figure 6.21.: Time series of the SV coefficients given by the low-regularized version of the reference model (red), Model-G (green) and Model-F (blue). Coefficients along each row have the same spherical harmonic degree but increase in order, while the coefficients along each column have the same spherical harmonic order but increase in degree.

radial SA is intense in both summer and winter, but the polarity is reversed. Apparently, the radial SA undergoes a sign change in spring and autumn, when it is relatively weak. It is also striking to see that the radial SA is strong over the oceans such as the Pacific and the Indian Ocean but less so over the continents with the exception of Antarctica. The amplitude of the annual oscillation is approximately 60 nT/yr^2 which is comparable to the amplitude of SA signals for the internal field often interpreted for internal field models (*Finlay et al., 2020*). A similar pattern is also visible in the large-scale SV at the Earth's surface except for a 90° phase shift in the time variation. That is, the maximum is reached in spring and autumn rather than summer and winter. The amplitude of the radial SV is then approximately 10 nT yr^{-1} . Regarding the radial field itself, the amplitude is around 3 nT with maxima in summer and winter similar to the SA.

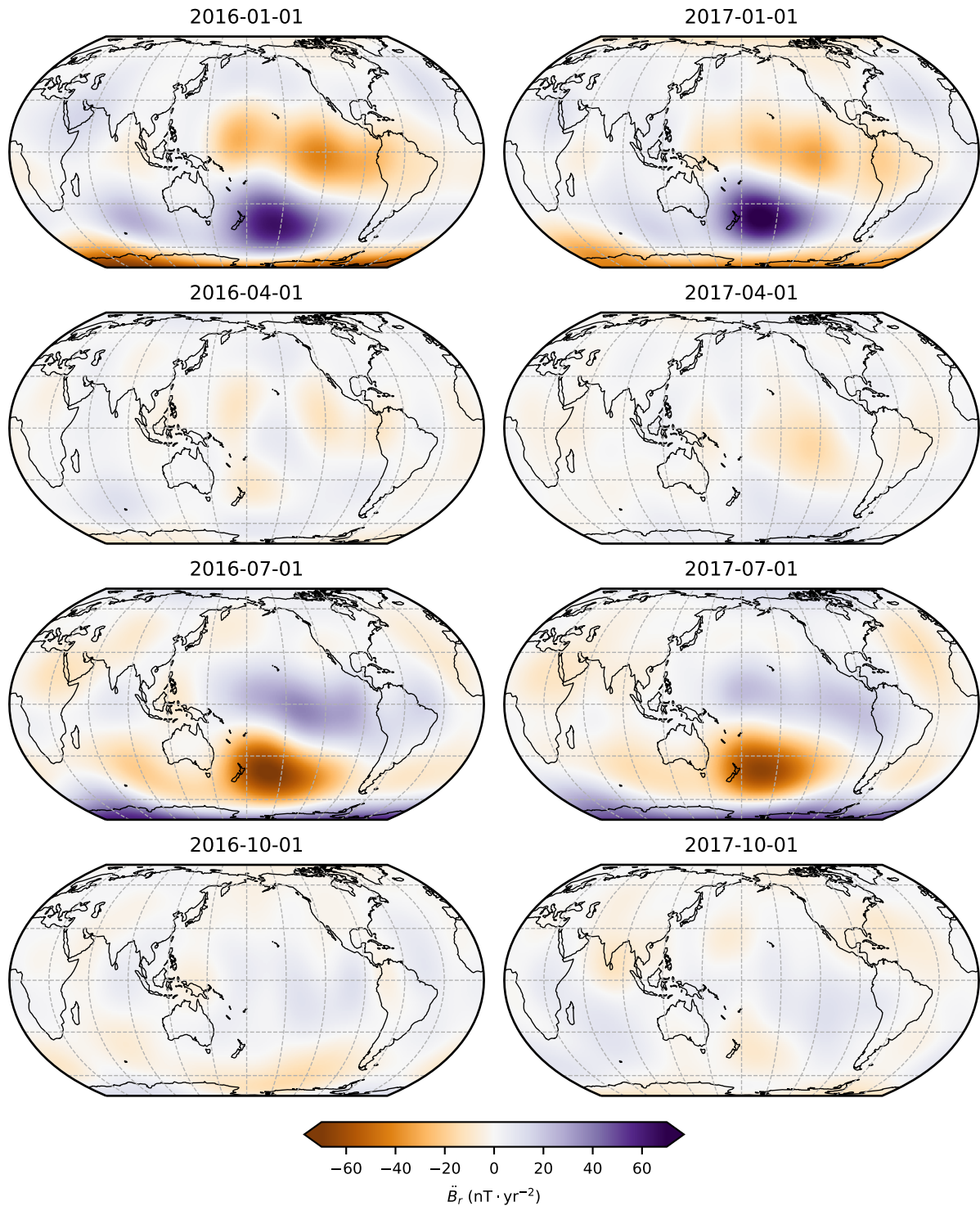


Figure 6.22.: Global maps of the difference between radial estimates of the SA up to degree 14 given by Model-E and Model-G in 2016 (left column) and 2017 (right column) at the Earth's surface. The maps are centered on the Pacific and the map projection is Equal Earth ([Šavrič et al., 2018](#)).

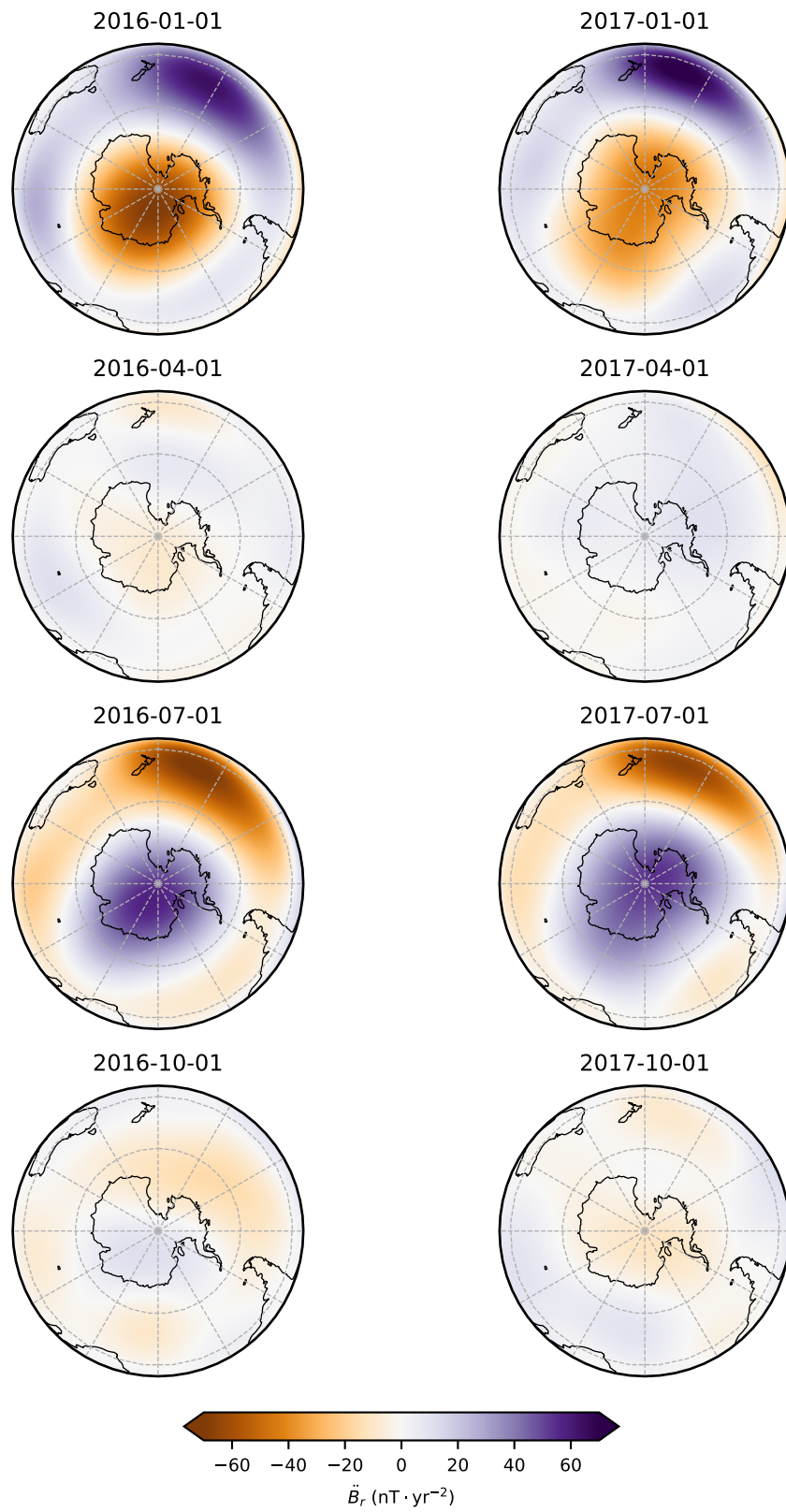


Figure 6.23.: Similar to Fig. 6.22 but as a polar projection of the South pole.

6.8. Concluding remarks

In this chapter, I presented an extension of the CHAOS framework for geomagnetic field modelling using an AMPS-type model of the ionospheric magnetic field. Through experimentation with the parameterization of the ionospheric field, I found Model-F to give the best results concerning the co-estimation of internal and ionospheric fields and the reduction of zonal artifacts due to the internal field ambiguity. Model-F shows a clear improvement of the high-degree SV in the polar regions and the co-estimated ionospheric field model seems to capture well the contributions from indirectly driven currents in the polar ionosphere thanks to the use of the *SML*-index. I also used the *SML*-index as a selection criterion in addition to the typical quiet-time selection and found that it can help reduce the misfit in the polar regions but leads to the removal of a large fraction of the data.

The results of Model-F are encouraging, but a detailed analysis of the structures in the estimated polar current system under quiet conditions depends on how well the ambiguity between the internal and ionospheric fields is resolved. Resolving this ambiguity proved to be a difficult task. For the estimation of Model-F, I designed a regularization based on the AMPS coefficient values to facilitate the separation between the internal field and the ionospheric field. This approach worked relatively well, but it essentially sets the amplitudes of the zonal terms in the co-estimated ionospheric model at a level similar to those in the AMPS model. The fact that the co-estimation was possible in Model-F with this kind of regularization, however, stresses the importance of having sufficient prior knowledge for the co-estimation of the ionospheric field. An alternative approach could be to use ground observatory data since the ionospheric sources are then external and, hence, separable from the internal field. I included ground-based magnetic observations in the form of annual differences of revised monthly means to only provide information on the slowly-varying time-dependent internal field. The use of these ground-based (annual differences of Revised Monthly Mean ([Olsen et al., 2014](#))) SV data assumes that external field contributions are removed to the greatest possible extent from the monthly means using other field models. This is however inconsistent with the use of these data in the context of co-estimating ionospheric fields. In the future it may therefore be preferable to directly include hourly mean ground-based observations of the field as this should, in principle, help resolve the ambiguity between internal and ionospheric fields. A major challenge in this respect will be how to deal correctly with induced fields in the ground data. Another possibility could perhaps be to make use of statistics derived from magnetohydrodynamics simulations of the polar ionosphere in the design of regularization approaches on the AMPS model parameters.

Overall, it seems that co-estimating an ionospheric field model primarily improves the estimation of the high-degree core field. Reducing the strength of the temporal regularization leads to distinct annual oscillations of the low-degree internal field that are not QD-zonal in structure. The AMPS-based parameterization of the ionospheric field does not capture this periodic signal, which raises the question whether it may be related to unaccounted induced or oceanic sources. Better characterizing and modelling this signal will be an important task for the next generation of geomagnetic field models.

7. Summary and conclusions

The main goal of studying the Earth's magnetic field is to achieve an improved understanding of its origin and evolution. The ability of geomagnetic field modelling to provide accurate mathematical models of the field with high spatial and temporal resolution, and resolved into various sources, is a key activity towards achieving this goal. In this thesis, I have aimed to advance two aspects of geomagnetic field modelling within the CHAOS framework. First, to improve the satellite data coverage, I implemented a co-estimation scheme to allow platform magnetometer data to provide additional information on the geomagnetic field. Second, to better account for the ionospheric current sources in field modelling, I explored the possibility of co-estimating AMPS-type models of the ionospheric field.

Co-estimating calibration parameters

The co-estimation of calibration parameters allows crude platform magnetometer data collected onboard many satellites for navigational purposes to supplement the high-quality data from magnetic survey missions. This co-estimation scheme is an alternative to using a-priori geomagnetic field models for the calibration of platform magnetometer data. It offers a more consistent use of these data but also comes with additional challenges.

Taking advantage of this new capability, I derived a geomagnetic field model spanning the period from 2008.0 to 2018.0 using previously uncalibrated magnetic data from the three platform magnetometers on the CryoSat-2 satellite and the platform magnetometer on each of the two GRACE satellites along with high-quality magnetic data from CHAMP and *Swarm* satellite missions. In addition to the satellite data, the model estimation of the time-dependent internal field made use of annual differences of revised monthly means from ground observatories. The inclusion of five platform magnetometer datasets created an uninterrupted time series of satellite data, providing valuable information for the field modelling in particular during the gap period between the CHAMP and *Swarm* missions. The resulting geomagnetic field model was similar to previous CHAOS models but also included calibration parameters for the five platform magnetometer datasets using 30-day bins to allow for a time-dependence.

I performed several experiments to investigate the effect of co-estimating calibration parameters along with the internal and magnetospheric field models. The experiments showed that the co-estimation of calibration parameters significantly affects the axial internal dipole and the *RC*-baseline corrections in the gap period, creating unrealistic detours in the time series of these coefficients. In particular the sensitivities correlated strongly with the axial dipole and the *RC*-baseline corrections. Therefore, I implemented an approach whereby the platform magnetometer data were not used to determine the axial dipole coefficients, which can be well determined from the available ground data, and the time-dependent *RC*-baseline corrections were neglected during the gap period.

In addition, I found that the co-estimated calibration parameters are significantly changed depending on whether only nightside data or data from all local times is used in the calibration. The use of nightside platform magnetometer data generally resulted in a smoother time series of the calibration parameters. In one notable case, the sensitivity was shifted in value by a constant amount, which was probably caused by unmodelled ionospheric current sources on the dayside.

An analysis of the resulting internal field model, derived including platform magnetometer data, showed that the SA is practically unchanged during the periods when high quality data from CHAMP and *Swarm* is available. However, I found larger differences in the SA in the West and South Pacific during the gap period.

Overall, I found that platform magnetometer data can provide useful information on the core field and are in particular valuable when no high-quality satellite data is available. A successful co-estimation of calibration parameters requires that the correlations between the calibration parameters and other field model parameters are sufficiently reduced, which can be achieved through a suitable model parameterization and estimation. Also, the local time coverage of the platform magnetometer data is an important factor in the estimation of the calibration parameters.

Co-estimating models of the polar ionospheric field

Turning to ionospheric field models, I included an AMPS-type parameterization of the ionospheric currents within the CHAOS modelling framework. I investigated the effect of co-estimating the ionospheric field on the recovery of the internal field, with a particular focus on the polar regions, and also studied the form of the polar current system under geomagnetically quiet conditions.

I derived several test geomagnetic field models, which included AMPS-type ionospheric field models that essentially differed in the treatment of the constant zonal terms in the ionospheric E-layer field. For all these models, the misfit to the satellite data was significantly reduced, most notably on the dayside at all latitudes and in the polar regions for all local times. This indicated a successful accounting for the previously unmodelled ionospheric field. On the other hand the estimated internal field, in particular the static part, showed relatively strong zonal patterns in QD coordinates, which suggested an unresolved ambiguity between the internal field and the ionospheric field. Further evidence of this ambiguity was found in a comparison between the ionospheric field estimates of CM6 and the ionospheric fields co-estimated here. The differences in the strength of these zonal artifacts across the various models made it clear that the ambiguity was primarily a result of the constant zonal terms in the ionospheric E-layer field, which are static in time and independent of any external input parameters. It was found to be possible to reduce the zonal artifacts by removing the median values of the external input parameters and regularizing the amplitude of the constant zonal terms.

I went on to test a possible data selection criterion based on the *SML*-index in addition to the typical quiet-time data selection in an effort to reconcile the satellite data and the AMPS model parameterization, which only accounts for the dayside processes that drive the ionospheric currents but not indirect processes such as substorms. Setting a threshold on the *SML*-index reduced the misfit in the polar regions, while it remained unchanged at low latitudes. I found that the threshold had to be set in a relatively strict fashion, which unfortunately resulted in the removal of a large

number of data.

Using the basic AMPS parameterization of the ionospheric field I investigated maps of the divergence-free and Birkeland currents and the total horizontal currents in dependence of the IMF clock angle, similar to those presented by [Laundal et al. \(2017\)](#). I found currents that were weak for all clock angles and with similar amplitude to the original AMPS model under northward IMF conditions, which indeed was the most frequent condition found in the selection of quiet-time data used. The divergence-free part of the horizontal currents in this case were dominated by a single cell irrespective of the clock angle, while the original AMPS model indicated a two-cell structure when the IMF was not strictly northward.

To better account for indirectly driven currents in the polar ionosphere, I therefore included the *SML*-index as an external input parameter in the ionospheric field parameterization. The divergence-free currents of the resulting model changed from a one-cell to a two-cell structure with decreasing *SML*-index, consistent with an intensifying westward polar electrojet. In this case of enhanced westward currents, the Birkeland currents maximized on the nightside and formed a pair of upward and downward currents centred on midnight, similar in structure to a substorm current wedge.

Next, I analyzed the change to the time-dependent internal field. Compared to a model without the co-estimated ionospheric field, the difference was small in amplitude and mostly visible in the high-degree and low-order internal field in the polar regions and I was able to demonstrate that the high-degree SV flux patches were better resolved when co-estimating the ionospheric field. In an effort to further emphasize differences due to the co-estimation of an ionospheric field, I relaxed the temporal regularization of the time-dependent internal field imposed during the modelling. In the resulting low-regularized model, I found annual oscillations in the internal field but most clearly in the SA. By removing the SA for a strongly regularized model, it was possible to isolate the annual oscillations in the form of three SA flux patches in the Pacific and over Antarctica. These patches alternated in sign over a period of one year and were not organized in QD coordinates. Similar patterns but with smaller amplitudes were also found in the field itself and in the SV.

To summarize this part, my investigations showed that it is beneficial to co-estimate an AMPS-type model of the ionospheric field as part of the geomagnetic field model. This approach better isolates the time-dependent internal field at high latitudes and achieves a smaller misfit in the polar regions and on the dayside. Indirectly-driven ionospheric currents can also be at least accounted for by including a dependence on the *SML*-index. The resulting increase in the resolution of the high-degree internal field lends support to the interpretation that non-zonal SV patches found in the northern polar region, on downward continuation to the core surface, are robust and of internal origin, which is an important issue for studies of outer core dynamics ([Livermore et al., 2017](#)). Despite such obvious improvements to the field models, there remains a clear need to more rigorously resolve the ambiguity between the zonal part of the internal field and the ionospheric field. More prior information on the model parameters or additional data (or both) is needed to improve the separation of this specific part of the sources. Also, at the moment, the AMPS-type ionospheric model explored here does not include a parameterization of the internally-induced counterpart.

Outlook

Future work should focus on ways to help with the separation of internal and ionospheric sources. In particular ground observatory data could, in principle, be useful since the ionospheric field is external with respect to these. However, ground observatory data would not help with the separation of the internal field and the internally induced part of the ionospheric field unless the latter can be coupled to the inducing currents in the ionosphere via a Q -response function. This approach is used in the CM models (e.g. [Sabaka et al., 2020](#)), however, only for periodic ionospheric signals of daily and annual frequencies. The CM approach is applicable to the Sq current system but less so to the rapidly time-varying currents in the polar ionosphere, which is one reason why AMPS uses external input parameters for the temporal parameterization. To account for induction in the AMPS parameterization, one possible option may be to follow an approach whereby the external input parameters are decomposed into internal and external parts using a Q -response function in the time-domain, similar to the decomposition of the RC -index in the model of the near-magnetospheric field. However, it will be necessary to account for the fact that the spherical harmonics in an AMPS-type model are given with respect to QD/MA latitude and MLT. Nonetheless, finding better ways of representing the induced field is worthwhile and could perhaps also help with explaining the annual oscillations found in weakly-regularized internal field models, which appear despite including a parameterization of the ionospheric field.

The results of this thesis have shown that geomagnetic field models benefit from platform magnetometer data and from the co-estimation of the ionospheric field. Combining both is an obvious next step. It will also be interesting to increase the truncation order of AMPS-type models to map the ionospheric currents with higher resolution in longitude. In this case, gradient data, which are more sensitive to the small-scale magnetic field, could be useful for the model estimation.

Finally, there is the exciting prospect of improved local time coverage from planned high precision mapping missions that are now on the horizon, such as NanoMagsat and MacaoSat. With better local time coverage, and use of prior information from models such as AMPS, it may become feasible to parameterize the ionospheric currents more directly over shorter time windows and beyond climatological models of the ionospheric field.

Bibliography

- Akasofu, S.-I. (1964), The development of the auroral substorm, *Planetary and Space Science*, 12(4), 273–282, doi: 10.1016/0032-0633(64)90151-5.
- Akasofu, S.-I., and S. Chapman (1961), The ring current, geomagnetic disturbance, and the Van Allen radiation belts, *Journal of Geophysical Research*, 66(5), 1321–1350, doi: 10.1029/jz066i005p01321.
- Alken, P., N. Olsen, and C. C. Finlay (2020), Co-estimation of geomagnetic field and in-orbit fluxgate magnetometer calibration parameters, *Earth, Planets and Space*, 72(1), 1–32, doi: 10.1186/s40623-020-01163-9.
- Alken, P., et al. (2021), International Geomagnetic Reference Field: the thirteenth generation, *Earth, Planets and Space*, 73(1), doi: 10.1186/s40623-020-01288-x.
- Backus, G. (1986), Poloidal and toroidal fields in geomagnetic field modeling, *Reviews of Geophysics*, 24(1), 75–109.
- Backus, G., B. George, R. L. Parker, R. Parker, and C. Constable (1996), *Foundations of Geomagnetism*, Cambridge University Press.
- Backus, G. E. (1970), Non-uniqueness of the external geomagnetic field determined by surface intensity measurements, *Journal of Geophysical Research*, 75(31), 6339–6341, doi: 10.1029/ja075i031p06339.
- Baerenzung, J., M. Holschneider, J. Wicht, V. Lesur, and S. Sanchez (2020), The kalmag model as a candidate for IGRF-13, *Earth, Planets and Space*, 72(1), doi: 10.1186/s40623-020-01295-y.
- Birkeland, K. (1908), *The Norwegian Aurora Polaris Expedition, 1902-1903: Volume I. On the Cause of Magnetic Storms and the Origin of Terrestrial Magnetism*, vol. 1, H. Aschehoug & Company.
- Chapman, S., and V. C. A. Ferraro (1931), A new theory of magnetic storms, *Journal of Geophysical Research*, 36(2), 77, doi: 10.1029/te036i002p00077.
- Chapman, S., and V. C. A. Ferraro (1941), The geomagnetic ring-current: I— its radial stability, *Journal of Geophysical Research*, 46(1), 1, doi: 10.1029/te046i001p00001.
- Chulliat, A., and S. Maus (2014), Geomagnetic secular acceleration, jerks, and a localized standing wave at the core surface from 2000 to 2010, *Journal of Geophysical Research: Solid Earth*, 119(3), 1531–1543, doi: 10.1002/2013jb010604.

- Chulliat, A., E. Thebault, and G. Hulot (2010), Core field acceleration pulse as a common cause of the 2003 and 2007 geomagnetic jerks, *Geophysical Research Letters*, 37(7), doi: 10.1029/2009GL042019.
- Chulliat, A., J. Matzka, A. Masson, and S. E. Milan (2016), Key ground-based and space-based assets to disentangle magnetic field sources in the earth's environment, *Space Science Reviews*, 206(1-4), 123–156, doi: 10.1007/s11214-016-0291-y.
- Constable, C. G. (1988), Parameter estimation in non-gaussian noise, *Geophysical Journal International*, 94(1), 131–142.
- Cowley, S. W. H. (2000), Magnetosphere-ionosphere interactions: A tutorial review, in *Magnetospheric Current Systems*, pp. 91–106, American Geophysical Union, doi: 10.1029/gm118p0091.
- Davis, T. N., and M. Sugiura (1966), Auroral electrojet activity index AE and its universal time variations, *Journal of Geophysical Research*, 71(3), 785–801, doi: 10.1029/jz071i003p00785.
- De Boor, C. (1978), *A practical guide to splines*, vol. 27, Springer-Verlag New York.
- Dungey, J. W. (1961), Interplanetary magnetic field and the auroral zones, *Physical Review Letters*, 6(2), 47.
- Emmert, J. T., A. D. Richmond, and D. P. Drob (2010), A computationally compact representation of magnetic-apex and quasi-dipole coordinates with smooth base vectors, *Journal of Geophysical Research: Space Physics*, 115(A8), doi: 10.1029/2010JA015326.
- Finlay, C. C. (2019), Models of the main geomagnetic field based on multi-satellite magnetic data and gradients—techniques and latest results from the Swarm mission, in *Ionospheric Multi-Spacecraft Analysis Tools*, pp. 255–284, Springer International Publishing, doi: 10.1007/978-3-030-26732-2_12.
- Finlay, C. C., M. Dumberry, A. Chulliat, and M. A. Pais (2010), Short timescale core dynamics: Theory and observations, *Space Science Reviews*, 155(1-4), 177–218, doi: 10.1007/s11214-010-9691-6.
- Finlay, C. C., N. Olsen, and L. Tøffner-Clausen (2015), DTU candidate field models for IGRF-12 and the CHAOS-5 geomagnetic field model, *Earth, Planets and Space*, 67(1), doi: 10.1186/s40623-015-0274-3.
- Finlay, C. C., V. Lesur, E. Thébault, F. Vervelidou, A. Morschhauser, and R. Shore (2016a), Challenges handling magnetospheric and ionospheric signals in internal geomagnetic field modelling, *Space Science Reviews*, 206(1-4), 157–189, doi: 10.1007/s11214-016-0285-9.
- Finlay, C. C., N. Olsen, S. Kotsiaros, N. Gillet, and L. Tøffner-Clausen (2016b), Recent geomagnetic secular variation from Swarm and ground observatories as estimated in the CHAOS-6 geomagnetic field model, *Earth, Planets and Space*, 68(1), doi: 10.1186/s40623-016-0486-1.
- Finlay, C. C., C. Kloss, N. Olsen, M. Hammer, L. Tøffner-Clausen, A. Grayver, and A. Kuvshinov (2020), The CHAOS-7 geomagnetic field model and observed changes in the south atlantic anomaly, *Earth, Planets and Space*, doi: 10.1186/s40623-020-01252-9.

- Fournier, A., G. Hulot, D. Jault, W. Kuang, A. Tangborn, N. Gillet, E. Canet, J. Aubert, and F. Lhuillier (2010), An introduction to data assimilation and predictability in geomagnetism, *Space Science Reviews*, 155(1-4), 247–291, doi: 10.1007/s11214-010-9669-4.
- Friis-Christensen, E., H. Lühr, D. Knudsen, and R. Haegmans (2008), Swarm – an earth observation mission investigating geospace, *Advances in Space Research*, 41(1), 210–216, doi: 10.1016/j.asr.2006.10.008.
- Gillet, N., D. Jault, C. C. Finlay, and N. Olsen (2013), Stochastic modeling of the earth’s magnetic field: Inversion for covariances over the observatory era, *Geochemistry, Geophysics, Geosystems*, 14(4), 766–786, doi: 10.1002/ggge.20041.
- Gillet, N., O. Barrois, and C. C. Finlay (2015), Stochastic forecasting of the geomagnetic field from the COV-OBS.x1 geomagnetic field model, and candidate models for IGRF-12, *Earth, Planets and Space*, 67(1), doi: 10.1186/s40623-015-0225-z.
- Gorski, K. M., E. Hivon, A. J. Banday, B. D. Wandelt, F. K. Hansen, M. Reinecke, and M. Bartelmann (2005), HEALPix: A framework for high-resolution discretization and fast analysis of data distributed on the sphere, *The Astrophysical Journal*, 622(2), 759–771, doi: 10.1086/427976.
- Grayver, A. V., F. D. Munch, A. V. Kuvshinov, A. Khan, T. J. Sabaka, and L. Tøffner-Clausen (2017), Joint inversion of satellite-detected tidal and magnetospheric signals constrains electrical conductivity and water content of the upper mantle and transition zone, *Geophysical Research Letters*, 44(12), 6074–6081.
- Griffiths, D. (2014), *Introduction to electrodynamics*, Pearson Education Limited, Harlow.
- Holme, R. (2000), Modelling of attitude error in vector magnetic data, *Earth, Planets and Space*, 52(12), 1187–1197.
- Holme, R., and J. Bloxham (1996), The treatment of attitude errors in satellite geomagnetic data, *Physics of the Earth and Planetary Interiors*, 98(3-4), 221–233.
- Huber, P. J. (2004), *Robust Statistics*, Wiley Series in Probability and Statistics - Applied Probability and Statistics Section Series, Wiley.
- Huder, L., N. Gillet, C. C. Finlay, M. D. Hammer, and H. Tchoungui (2020), COV-OBS.x2: 180 years of geomagnetic field evolution from ground-based and satellite observations, *Earth, Planets and Space*, 72(1), doi: 10.1186/s40623-020-01194-2.
- Hulot, G., C. C. Finlay, C. G. Constable, N. Olsen, and M. Mandea (2010), The magnetic field of planet Earth, *Space Science Reviews*, 152(1-4), 159–222, doi: 10.1007/s11214-010-9644-0.
- Hulot, G., T. J. Sabaka, N. Olsen, and A. Fournier (2015), The present and future geomagnetic field, *Treatise on Geophysics*.
- Iijima, T., and T. A. Potemra (1976), The amplitude distribution of field-aligned currents at northern high latitudes observed by Triad, *Journal of Geophysical Research*, 81(13), 2165–2174, doi: 10.1029/ja081i013p02165.

- Jackson, A., and C. Finlay (2007), Geomagnetic secular variation and its applications to the core, in *Treatise on Geophysics*, pp. 147–193, Elsevier, doi: 10.1016/b978-044452748-6.00090-0.
- Jackson, A., and C. Finlay (2015), Geomagnetic secular variation and its applications to the core, in *Treatise on Geophysics*, pp. 137–184, Elsevier, doi: 10.1016/b978-0-444-53802-4.00099-3.
- Jackson, J. D. (1999), *Classical electrodynamics*, 3rd ed., John Wiley & Sons, Inc.
- Jørgensen, J., T. Denver, M. Betto, and P. Jorgensen (2003), MicroASC a miniature star tracker, small satellites for earth observations, in *Fourth International Symposium of the IAA, Berlin*.
- Kan, J. R., and L. C. Lee (1979), Energy coupling function and solar wind-magnetosphere dynamo, *Geophysical Research Letters*, 6(7), 577–580, doi: 10.1029/gl006i007p00577.
- Kauristie, K., A. Morschhauser, N. Olsen, C. C. Finlay, R. L. McPherron, J. W. Gjerloev, and H. J. Opengoorth (2017), On the usage of geomagnetic indices for data selection in internal field modelling, *Space Science Reviews*, 206(1-4), 61–90, doi: 10.1007/s11214-016-0301-0.
- Kepko, L., et al. (2015), Substorm current wedge revisited, *Space Science Reviews*, 190(1-4), 1–46.
- King, J. H., and N. E. Papitashvili (2005), Solar wind spatial scales in and comparisons of hourly wind and ACE plasma and magnetic field data, *Journal of Geophysical Research: Space Physics*, 110(A2), doi: <https://doi.org/10.1029/2004JA010649>.
- Kloss, C. (2020), ChaosMagPy v0.5, doi: 10.5281/zenodo.4396315.
- Kloss, C., C. C. Finlay, and N. Olsen (2021), Co-estimating geomagnetic field and calibration parameters: modeling Earth’s magnetic field with platform magnetometer data, *Earth, Planets and Space*, 73(1), doi: 10.1186/s40623-020-01351-7.
- Kuvshinov, A. V. (2008), 3-D global induction in the oceans and solid earth: Recent progress in modeling magnetic and electric fields from sources of magnetospheric, ionospheric and oceanic origin, *Surveys in Geophysics*, 29(2), 139–186, doi: 10.1007/s10712-008-9045-z.
- Laundal, K. M., and A. D. Richmond (2017), Magnetic coordinate systems, *Space Science Reviews*, 206(1-4), 27–59.
- Laundal, K. M., C. C. Finlay, and N. Olsen (2016), Sunlight effects on the 3D polar current system determined from low Earth orbit measurements, *Earth, Planets and Space*, 68(1), 142.
- Laundal, K. M., J. P. Reistad, C. C. Finlay, and N. Olsen (2017), A new model of global ionospheric currents: Solar wind and seasonal influence, *Journal of Geophysical Research: Space Physics*.
- Lesur, V., I. Wardinski, M. Rother, and M. Manda (2008), GRIMM: the GFZ reference internal magnetic model based on vector satellite and observatory data, *Geophysical Journal International*, 173(2), 382–394, doi: 10.1111/j.1365-246x.2008.03724.x.
- Lesur, V., I. Wardinski, M. Hamoudi, and M. Rother (2010), The second generation of the GFZ reference internal magnetic model: GRIMM-2, *Earth, Planets and Space*, 62(10), 765–773, doi: 10.5047/eps.2010.07.007.

- Livermore, P. W., R. Hollerbach, and C. C. Finlay (2017), An accelerating high-latitude jet in earth's core, *Nature Geoscience*, *10*(1), 62.
- Livermore, P. W., C. C. Finlay, and M. Bayliff (2020), Recent north magnetic pole acceleration towards siberia caused by flux lobe elongation, *Nature Geoscience*, *13*(5), 387–391, doi: 10.1038/s41561-020-0570-9.
- Lockwood, M. (2013), Reconstruction and prediction of variations in the open solar magnetic flux and interplanetary conditions, *Living Reviews in Solar Physics*, *10*, doi: 10.12942/lrsp-2013-4.
- Love, J. J. (2008), Magnetic monitoring of earth and space, *Physics Today*, *61*(2), 31–37, doi: 10.1063/1.2883907.
- Macmillan, S., and N. Olsen (2013), Observatory data and the Swarm mission, *Earth, Planets and Space*, *65*(11), 1355–1362, doi: 10.5047/eps.2013.07.011.
- Mandea, M., R. Holme, A. Pais, K. Pinheiro, A. Jackson, and G. Verbanac (2010), Geomagnetic jerks: rapid core field variations and core dynamics, *Space Science Reviews*, *155*(1-4), 147–175.
- Manoj, C., A. Kuvshinov, S. Maus, and H. Lühr (2006), Ocean circulation generated magnetic signals, *Earth, Planets and Space*, *58*(4), 429–437, doi: 10.1186/bf03351939.
- Matsuo, T., D. J. Knipp, A. D. Richmond, L. Kilcommons, and B. J. Anderson (2015), Inverse procedure for high-latitude ionospheric electrodynamics: Analysis of satellite-borne magnetometer data, *Journal of Geophysical Research: Space Physics*, *120*(6), 5241–5251, doi: 10.1002/2014ja020565.
- Matzka, J., A. Chulliat, M. Mandea, C. C. Finlay, and E. Qamili (2010), Geomagnetic observations for main field studies: From ground to space, *Space Science Reviews*, *155*(1-4), 29–64, doi: 10.1007/s11214-010-9693-4.
- Matzka, J., C. Stolle, Y. Yamazaki, O. Bronkalla, and A. Morschhauser (2021), The geomagnetic Kp index and derived indices of geomagnetic activity, *Space Weather*, doi: 10.1029/2020sw002641.
- Maus, S. (2007), Electromagnetic ocean effects, *Encyclopedia of Geomagnetism and Paleomagnetism*, pp. 740–742.
- Maus, S., and H. Lühr (2005), Signature of the quiet-time magnetospheric magnetic field and its electromagnetic induction in the rotating earth, *Geophysical Journal International*, *162*(3), 755–763.
- Maus, S., M. Rother, C. Stolle, W. Mai, S. Choi, H. Lühr, D. Cooke, and C. Roth (2006), Third generation of the Potsdam Magnetic Model of the Earth (POMME), *Geochemistry, Geophysics, Geosystems*, *7*(7), doi: 10.1029/2006gc001269.
- Meeren, C. V. D., A. G. Burrell, and K. M. Laundal (2018), Apexpy: ApexPy version 1.0.3, doi: 10.5281/ZENODO.1214206.
- Merayo, J. M. G., J. L. Jørgensen, E. Friis-Christensen, P. Brauer, F. Primdahl, P. S. Jørgensen, T. H. Allin, and T. Denver (2008), The Swarm magnetometry package, in *Small Satellites for Earth Observation*, pp. 143–151, Springer, Dordrecht, doi: 10.1007/978-1-4020-6943-7_13.

- Milan, S. E., L. B. N. Clausen, and J. C. Coxon (2017), Overview of solar wind-magnetosphere-ionosphere-atmosphere coupling and the generation of magnetospheric currents, *Space Science Reviews*, doi: 10.1007/s11214-017-0333-0.
- Newell, P. T., and J. W. Gjerloev (2011a), Evaluation of SuperMAG auroral electrojet indices as indicators of substorms and auroral power, *Journal of Geophysical Research: Space Physics*, 116(A12), doi: 10.1029/2011ja016779.
- Newell, P. T., and J. W. Gjerloev (2011b), Substorm and magnetosphere characteristic scales inferred from the SuperMAG auroral electrojet indices, *Journal of Geophysical Research: Space Physics*, 116(A12), doi: 10.1029/2011ja016936.
- Newell, P. T., and J. W. Gjerloev (2012), SuperMAG-based partial ring current indices, *Journal of Geophysical Research: Space Physics*, 117(A5), doi: 10.1029/2012ja017586.
- Newell, P. T., and J. W. Gjerloev (2014), Local geomagnetic indices and the prediction of auroral power, *Journal of Geophysical Research: Space Physics*, 119(12), 9790–9803, doi: 10.1002/2014ja020524.
- Newell, P. T., T. Sotirelis, K. Liou, C. I. Meng, and F. J. Rich (2007), A nearly universal solar wind-magnetosphere coupling function inferred from 10 magnetospheric state variables, *Journal of Geophysical Research: Space Physics*, 112(A1), doi: 10.1029/2006JA012015.
- Olsen, N. (1997), Ionospheric F region currents at middle and low latitudes estimated from Magsat data, *Journal of Geophysical Research: Space Physics*, 102(A3), 4563–4576.
- Olsen, N. (1999), Induction studies with satellite data, *Surveys in Geophysics*, 20(3/4), 309–340, doi: 10.1023/a:1006611303582.
- Olsen, N. (2020), Magnetometer data of the GRACE satellite duo, *Earth, Planets and Space*, doi: 10.1186/s40623-021-01373-9.
- Olsen, N., and M. Manda (2007), Investigation of a secular variation impulse using satellite data: The 2003 geomagnetic jerk, *Earth and Planetary Science Letters*, 255(1-2), 94–105, doi: 10.1016/j.epsl.2006.12.008.
- Olsen, N., and C. Stolle (2012), Satellite geomagnetism, *Annual Review of Earth and Planetary Sciences*, 40(1), 441–465, doi: 10.1146/annurev-earth-042711-105540.
- Olsen, N., et al. (2003), Calibration of the Ørsted vector magnetometer, *Earth, Planets and Space*, 55(1), 11–18, doi: 10.1186/BF03352458.
- Olsen, N., F. Lowes, and T. J. Sabaka (2005a), Ionospheric and induced field leakage in geomagnetic field models, and derivation of candidate models for DGRF 1995 and DGRF 2000, *Earth, Planets and Space*, 57(12), 1191–1196, doi: 10.1186/bf03351903.
- Olsen, N., T. J. Sabaka, and F. Lowes (2005b), New parameterization of external and induced fields in geomagnetic field modeling, and a candidate model for IGRF 2005, *Earth, Planets and Space*, 57(12), 1141, doi: 10.1186/BF03351897.

- Olsen, N., H. Lühr, T. J. Sabaka, M. Manda, M. Rother, L. Tøffner-Clausen, and S. Choi (2006a), CHAOS—a model of the Earth's magnetic field derived from CHAMP, Ørsted, and SAC-C magnetic satellite data, *Geophysical Journal International*, 166(1), 67–75.
- Olsen, N., R. Haagmans, T. J. Sabaka, A. Kuvshinov, S. Maus, M. E. Purucker, M. Rother, V. Lesur, and M. Manda (2006b), The Swarm End-to-End mission simulator study: A demonstration of separating the various contributions to Earth's magnetic field using synthetic data, *Earth, Planets and Space*, 58(4), 359–370, doi: 10.1186/bf03351934.
- Olsen, N., J. T. Sabaka, and L. Pique (2007), *Study of an improved comprehensive magnetic field inversion analysis for Swarm*, Danish National Space Center Scientific Report, Copenhagen.
- Olsen, N., M. Manda, T. J. Sabaka, and L. Tøffner-Clausen (2009), CHAOS-2 — a geomagnetic field model derived from one decade of continuous satellite data, *Geophysical Journal International*, 179(3), 1477–1487, doi: 10.1111/j.1365-246x.2009.04386.x.
- Olsen, N., G. Hulot, and T. J. Sabaka (2010a), Measuring the Earth's magnetic field from space: concepts of past, present and future missions, *Space Science Reviews*, 155(1-4), 65–93, doi: 10.1007/s11214-010-9676-5.
- Olsen, N., G. Hulot, and T. J. Sabaka (2010b), Sources of the geomagnetic field and the modern data that enable their investigation, in *Handbook of geomathematics*, pp. 105–124, Springer, doi: 10.1007/978-3-642-27793-1_5-2.
- Olsen, N., M. Manda, T. J. Sabaka, and L. Tøffner-Clausen (2010c), The CHAOS-3 geomagnetic field model and candidates for the 11th generation IGRF, *Earth, Planets and Space*, 62(10), 719–727, doi: 10.5047/eps.2010.07.003.
- Olsen, N., H. Lühr, C. C. Finlay, T. J. Sabaka, I. Michaelis, J. Rauberg, and L. Tøffner-Clausen (2014), The CHAOS-4 geomagnetic field model, *Geophysical Journal International*, 197(2), 815–827.
- Olsen, N., C. C. Finlay, S. Kotsiaros, and L. Tøffner-Clausen (2016), A model of Earth's magnetic field derived from 2 years of Swarm satellite constellation data, *Earth, Planets and Space*, 68(1), 124, doi: 10.1186/s40623-016-0488-z.
- Olsen, N., D. Ravat, C. C. Finlay, and L. K. Kother (2017), LCS-1: a high-resolution global model of the lithospheric magnetic field derived from CHAMP and Swarm satellite observations, *Geophysical Journal International*, 211(3), 1461–1477.
- Olsen, N., G. Alбини, J. Bouffard, T. Parrinello, and L. Tøffner-Clausen (2020), Magnetic observations from CryoSat-2: calibration and processing of satellite platform magnetometer data, *Earth, Planets and Space*, 72, 1–18.
- Olson, P. (2007), Overview, in *Treatise on Geophysics*, pp. 1–30, Elsevier, doi: 10.1016/b978-044452748-6.00125-5.
- Richmond, A. D. (1995), Ionospheric electrodynamics using magnetic apex coordinates, *Journal of geomagnetism and geoelectricity*, 47(2), 191–212, doi: 10.5636/jgg.47.191.

- Ritter, P., H. Lühr, S. Maus, and A. Viljanen (2004), High-latitude ionospheric currents during very quiet times: their characteristics and predictability, *Annales Geophysicae*, 22(6), 2001–2014, doi: 10.5194/angeo-22-2001-2004.
- Ropp, G., V. Lesur, J. Baerenzung, and M. Holschneider (2020), Sequential modelling of the earth's core magnetic field, *Earth, Planets and Space*, 72(1), doi: 10.1186/s40623-020-01230-1.
- Rother, M., and I. Michaelis (2019), CH-ME-3-MAG - CHAMP 1 Hz combined magnetic field time series (level 3), doi: 10.5880/GFZ.2.3.2019.004.
- Sabaka, T. J., N. Olsen, and R. A. Langel (2002), A comprehensive model of the quiet-time, near-earth magnetic field: phase 3, *Geophysical Journal International*, 151(1), 32–68, doi: 10.1046/j.1365-246x.2002.01774.x.
- Sabaka, T. J., N. Olsen, and M. E. Purucker (2004), Extending comprehensive models of the Earth's magnetic field with Ørsted and CHAMP data, *Geophysical Journal International*, 159(2), 521–547, doi: 10.1111/j.1365-246x.2004.02421.x.
- Sabaka, T. J., G. Hulot, and N. Olsen (2010), Mathematical properties relevant to geomagnetic field modeling, in *Handbook of geomathematics*, pp. 503–538, Springer.
- Sabaka, T. J., N. Olsen, R. H. Tyler, and A. Kuvshinov (2015), CM5, a pre-Swarm comprehensive geomagnetic field model derived from over 12 yr of CHAMP, Ørsted, SAC-C and observatory data, *Geophysical Journal International*, 200(3), 1596–1626, doi: 10.1093/gji/ggu493.
- Sabaka, T. J., L. Tøffner-Clausen, N. Olsen, and C. C. Finlay (2018), A comprehensive model of Earth's magnetic field determined from 4 years of Swarm satellite observations, *Earth, Planets and Space*, 70(1), doi: 10.1186/s40623-018-0896-3.
- Sabaka, T. J., L. Tøffner-Clausen, N. Olsen, and C. C. Finlay (2020), CM6: a comprehensive geomagnetic field model derived from both CHAMP and Swarm satellite observations, *Earth, Planets and Space*, 72(1), doi: 10.1186/s40623-020-01210-5.
- Šavrič, B., T. Patterson, and B. Jenny (2018), The equal earth map projection, *International Journal of Geographical Information Science*, 33(3), 454–465, doi: 10.1080/13658816.2018.1504949.
- Schwartz, M. (2012), *Principles of electrodynamics*, Courier Corporation.
- Snekvik, K., N. Østgaard, P. Tenfjord, J. P. Reistad, K. M. Laundal, S. E. Milan, and S. E. Haaland (2017), Dayside and nightside magnetic field responses at 780 km altitude to dayside reconnection, *Journal of Geophysical Research: Space Physics*, 122(2), 1670–1689, doi: 10.1002/2016ja023177.
- Sugiura, M., and T. Kamei (1991), Equatorial Dst index 1957–1986, IAGA Bull., 40, by A. Berthelier and M. Menville (*Int. Serv. Geomagn. Indices Publ. Off., Saint Maur, 1991*).
- Tapping, K. F., and D. P. Charrois (1994), Limits to the accuracy of the 10.7 cm flux, *Solar Physics*, 150(1-2), 305–315, doi: 10.1007/bf00712892.
- Tarantola, A. (2005), *Inverse problem theory and methods for model parameter estimation*, SIAM.

- Thébault, E., K. Hemant, G. Hulot, and N. Olsen (2009), On the geographical distribution of induced time-varying crustal magnetic fields, *Geophysical Research Letters*, *36*(1), doi: 10.1029/2008gl036416.
- Thébault, E., et al. (2015), International geomagnetic reference field: the 12th generation, *Earth, Planets and Space*, *67*(1), 79.
- Tøffner-Clausen, L., V. Lesur, N. Olsen, and C. C. Finlay (2016), In-flight scalar calibration and characterisation of the Swarm magnetometry package, *Earth, Planets and Space*, *68*(1), doi: 10.1186/s40623-016-0501-6.
- Toresen, M., and K. M. Laundal (2018), pyAMPS, doi: 10.5281/zenodo.1435613.
- Treumann, R. A., and W. Baumjohann (1997), *Advanced space plasma physics*, vol. 30, Imperial College Press London.
- VanZandt, T. E., W. L. Clark, and J. M. Warnock (1972), Magnetic apex coordinates: A magnetic coordinate system for the ionospheric F2 layer, *Journal of geophysical research*, *77*(13), 2406–2411.
- Weimer, D. R. (2001), Maps of ionospheric field-aligned currents as a function of the interplanetary magnetic field derived from Dynamics Explorer 2 data, *Journal of Geophysical Research: Space Physics*, *106*(A7), 12,889–12,902, doi: 10.1029/2000ja000295.
- Weimer, D. R. (2013), An empirical model of ground-level geomagnetic perturbations, *Space Weather*, *11*(3), 107–120, doi: 10.1002/swe.20030.
- Winch, D. E., D. J. Ivers, J. P. R. Turner, and R. J. Stening (2005), Geomagnetism and Schmidt quasi-normalization, *Geophysical Journal International*, *160*(2), 487–504, doi: 10.1111/j.1365-246x.2004.02472.x.
- Yamazaki, Y., and A. Maute (2016), Sq and EEJ—a review on the daily variation of the geomagnetic field caused by ionospheric dynamo currents, *Space Science Reviews*, *206*(1-4), 299–405, doi: 10.1007/s11214-016-0282-z.
- Yin, F., and H. Lühr (2011), Recalibration of the CHAMP satellite magnetic field measurements, *Measurement Science and Technology*, *22*(5), 055,101.
- Zonca, A., L. Singer, D. Lenz, M. Reinecke, C. Rosset, E. Hivon, and K. Gorski (2019), healpy: equal area pixelization and spherical harmonics transforms for data on the sphere in Python, *Journal of Open Source Software*, *4*(35), 1298, doi: 10.21105/joss.01298.

A. Publications

The following publication has been made during this PhD study and is included on the next pages.

Kloss, C., C. C. Finlay, and N. Olsen (2021), Co-estimating geomagnetic field and calibration parameters: modeling Earth's magnetic field with platform magnetometer data, *Earth, Planets and Space*, 73(1), doi: 10.1186/s40623-020-01351-7

FULL PAPER

Open Access



Co-estimating geomagnetic field and calibration parameters: modeling Earth's magnetic field with platform magnetometer data

Clemens Kloss* , Christopher C. Finlay and Nils Olsen

Abstract

Models of the geomagnetic field rely on magnetic data of high spatial and temporal resolution to give an accurate picture of the Earth's internal magnetic field and its time-dependence. The magnetic data from low-Earth orbit satellites of dedicated magnetic survey missions such as CHAMP and *Swarm* play a key role in the construction of such models. Unfortunately, there are no magnetic data available from such satellites after the end of the CHAMP mission in 2010 and before the launch of the *Swarm* mission in late 2013. This limits our ability to recover signals on timescales of 3 years and less during this gap period. The magnetic data from platform magnetometers carried by satellites for navigational purposes may help address this data gap provided that they are carefully calibrated. Earlier studies have demonstrated that platform magnetometer data can be calibrated using a fixed geomagnetic field model as reference. However, this approach can lead to biased calibration parameters. An alternative approach has been developed in the form of a co-estimation scheme which consists of simultaneously estimating both the calibration parameters and a model of the internal part of the geomagnetic field. Here, we go further and develop a scheme, based on the CHAOS field modeling framework, that involves co-estimation of both internal and external geomagnetic field models along with calibration parameters of platform magnetometer data. Using our implementation, we are able to derive a geomagnetic field model spanning 2008 to 2018 with satellite magnetic data from CHAMP, *Swarm*, secular variation data from ground observatories, and platform magnetometer data from CryoSat-2 and the GRACE satellite pair. Through a number of experiments, we explore correlations between the estimates of the geomagnetic field and the calibration parameters, and suggest how these may be avoided. We find evidence that platform magnetometer data provide additional information on the secular acceleration, especially in the Pacific during the gap between CHAMP and *Swarm*. This study adds to the evidence that it is beneficial to use platform magnetometer data in geomagnetic field modeling.

Keywords: Geomagnetism, Core field modeling, Inverse theory, Secular acceleration, Secular variation

Introduction

The Earth's magnetic field is a superposition of many sources. By far, the largest contribution comes from within the Earth at a depth of more than 3000 km. There,

in the outer core, a liquid iron alloy is rapidly moving and thus advecting, stretching, and maintaining the ambient magnetic field against dissipation in a process called the Geodynamo. Earth's core dynamics are not fully understood, but can be studied using time-dependent geomagnetic field models. Such models are constructed using measurements of the magnetic field taken at and above Earth's surface.

*Correspondence: ancklo@space.dtu.dk
Division of Geomagnetism, DTU Space, Technical University of Denmark,
Centrifugevej 356, 2800 Kongens Lyngby, Denmark



© The Author(s) 2021. This article is licensed under a Creative Commons Attribution 4.0 International License, which permits use, sharing, adaptation, distribution and reproduction in any medium or format, as long as you give appropriate credit to the original author(s) and the source, provide a link to the Creative Commons licence, and indicate if changes were made. The images or other third party material in this article are included in the article's Creative Commons licence, unless indicated otherwise in a credit line to the material. If material is not included in the article's Creative Commons licence and your intended use is not permitted by statutory regulation or exceeds the permitted use, you will need to obtain permission directly from the copyright holder. To view a copy of this licence, visit <http://creativecommons.org/licenses/by/4.0/>.

The study of core processes on decadal or longer time-scales requires long time-series of magnetic vector data with high spatial and temporal resolution. Along with ground-based magnetic observatories, low-earth orbit satellites from dedicated magnetic survey missions such as CHALLENGING Minisatellite Payload (CHAMP, 2000–2010) and the *Swarm* trio (since 2013) provide such data. However, other than scalar data from Ørsted, no high-quality calibrated magnetic vector data from satellites are available between the end of the CHAMP mission in September 2010 and the launch of the *Swarm* satellites in November 2013. This data gap not only cuts in two an otherwise uninterrupted time-series of high-quality magnetic satellite data since the year 2000, but also limits our ability to derive accurate core field models that resolve temporal changes of the magnetic field on timescales of a few years and less in the gap period. To address the issue, one can utilize the crude magnetometers that are carried by most satellites for navigational purposes, the so-called platform magnetometers. Although not a substitute for dedicated high-quality magnetic survey satellites, platform magnetometers can supplement ground observatory data in gaps between dedicated missions and help improve the local time data coverage of simultaneously flying high-quality magnetic survey satellites.

Satellite-based magnetic vector data need to be calibrated to remove magnetometer biases, scale factors, and non-orthogonalities between the three vector component axes (Olsen et al. 2003). Comparing the vector magnetometer output with a magnetic reference field allows the estimation of these calibration parameters. On dedicated survey mission satellites, the reference is a second, absolute scalar, magnetometer mounted in close proximity to the vector magnetometer and measuring the magnetic field intensity. However, non-dedicated satellites carrying platform magnetometers are typically not equipped with such scalar reference magnetometers. In this case, it is possible to use a-priori geomagnetic field models like CHAOS (Olsen et al. 2006; Finlay et al. 2020) or the IGRF (Thébault et al. 2015) as reference. Such an approach has been successfully used, e.g., by Olsen et al. (2020) for calibrating data from the CryoSat-2 magnetometer, but use of a fixed reference field model is not without risks and could lead to biased calibration parameters.

An alternative venue has been explored by Alken et al. (2020), who combined high-quality magnetic data from CHAMP and *Swarm* with platform magnetometer data from CryoSat-2 and several satellites of the Defense Meteorological Satellite Program (DMSP) to estimate a model of the internal field and the required calibration parameters for each satellite simultaneously. Ideally, such a co-estimation scheme eliminates the

need for a-priori geomagnetic field models, but Alken et al. (2020) fall short by co-estimating only the internal field while still relying on a fixed model of the external field. Nevertheless, their study convincingly demonstrated that platform magnetometer data provide valuable information about the time-dependence of Earth's magnetic field.

In this study, we followed Alken et al. (2020) and developed a co-estimation strategy but within the framework of the CHAOS field model series. Our implementation differs in three important aspects. First, we estimated both the internal (core and crust) and external (magnetospheric) geomagnetic field contributions in contrast to only the internal field. This way, we avoided having to remove a fixed external field model from the satellite data prior to the model parameter estimation. Following the methodology of the CHAOS model, we did use a prior external field model for processing the ground observatory data which we used in addition to the satellite data. Second, we used the platform magnetometer data from CryoSat-2 and, instead of DMSP, data from the Gravity Recovery and Climate Experiment (GRACE) satellite pair. Finally, to reduce the significant correlation between the internal axial dipole and the calibration parameters during periods of poor coverage of high-quality magnetic data, we excluded platform magnetometer data from determining the internal axial dipole (its time variation is well resolved with ground observatory data during the gap period, while its absolute value is constrained by *Swarm* and CHAMP data on both sides of the gap) rather than controlling the temporal variability of the internal axial dipole through an additional regularization as done by Alken et al. (2020).

The paper is organized as follows. In the first part, we present the datasets and the data processing. Next, we describe the model parameterization and define the calibration parameters, which are similar to those used for the Ørsted satellite (Olsen et al. 2003). We go on by presenting a geomagnetic field model derived from high-quality calibrated data from the CHAMP and the *Swarm* satellites as well as ground observatory secular variation data and supplemented this with previously uncalibrated platform magnetometer data from CryoSat-2 and GRACE, spanning a 10 year period from 2008 to 2018. Finally, we explore in a series of experiments the effect of co-estimating an external field, the trade-off between the internal dipole and the calibration parameters, and the importance of including dayside platform magnetometer data when estimating calibration parameters. We conclude the paper by looking at the secular acceleration of our model, paying particular attention to the data gap between 2010 and 2013.

Data and data processing

We used calibrated magnetic data from the *Swarm* satellites Alpha (*Swarm-A*) and Bravo (*Swarm-B*), and from the CHAMP satellite from January 2008 to the end of December 2017, supplemented with five datasets of uncalibrated magnetic data from the three platform fluxgate magnetometers (FGM) on-board the CryoSat-2 satellite (CryoSat-2 FGM1, CryoSat-2 FGM2 and CryoSat-2 FGM3), the one on-board the first GRACE satellite (GRACE-A), and the other one on-board the second GRACE satellite (GRACE-B). In addition to the satellite data, we included revised monthly mean values of the SV from ground observatories to contribute to the Earth's internal time-dependent field. Details of the datasets are given in the following.

Absolute satellite data from scientific magnetometers

The satellite data from scientific magnetometers are in general of high quality in terms of accuracy, precision, and magnetic cleanliness. The high standard of the data is achieved by low-noise instruments that are mounted together with star cameras on an optical bench further away from the spacecraft body at the center of a several meter long boom. The data are regularly calibrated in-flight with a second absolute scalar magnetometer placed at the end of the boom and carefully cleaned from magnetic disturbance fields originating from the spacecraft body.

From the CHAMP mission, we used the Level 3 1 Hz magnetic data, version CH-ME-3-MAG (Rother and Michaelis 2019), between January 2008 and August 2010, downsampled to 15 s, and only when attitude information from both star cameras was available. From the *Swarm* mission, we used the Level 1b 1 Hz magnetic data product, baseline 0505/0506, from the *Swarm-A* and *Swarm-B* satellites between November 2013 and December 2018, also downsampled to 15 s. Here, we worked with vector data from CHAMP and *Swarm* in the magnetometer frame.

Relative satellite data from platform magnetometers

Relative satellite data refer to the raw sensor output from platform magnetometers. The data have to be corrected and calibrated before they can be used in geomagnetic field modeling. The correction of the data accounts for temperature effects, magnetic disturbances due to solar array and battery currents, magnetorquer activity, as well as non-linear sensor effects, whereas the calibration removes magnetometer biases, scale differences, and non-orthogonalities between the three vector component axes.

From CryoSat-2, we took magnetic data, baseline 0103, from the three platform magnetometers as described in

Olsen et al. (2020) from August 2010 to December 2018 and only when the attitude uncertainty q_{error} was below $40''$. Since the purpose of this paper is the co-estimation of calibration parameters for the platform magnetometers, we processed the dataset using the original calibration parameters to undo the calibration step that has been performed by Olsen et al. (2020) but keeping the applied correction for magnetic disturbances from the spacecraft and its payload. This way, we obtained essentially uncalibrated data while still retaining the corrections for magnetic disturbances, temperature effects and non-linearities. In a pre-whitening and data reduction step, we computed residuals to the CHAOS-6-x9 model in the uncalibrated magnetometer frame, removed those larger than 1000 eu (quasi nanoTesla, in the following referred to as engineering units) in absolute value to discard gross outliers, computed component-wise robust mean values of the residuals in 1 min bins to reduce the original 4 s sampled data to 1 min values, and added the CHAOS-6-x9 model values back. Figure 1 shows an example of the raw vector residuals ΔE of CryoSat-2 FGM1 in the uncalibrated magnetometer frame over 3 h on March 24, 2016.

In a similar way, we processed the 1 Hz data from the GRACE satellites, baseline 0101, to obtain 1 min uncalibrated but corrected vector data between January 2008 and October 2017 (GRACE-A) and August 2017 (GRACE-B) (Olsen 2020).

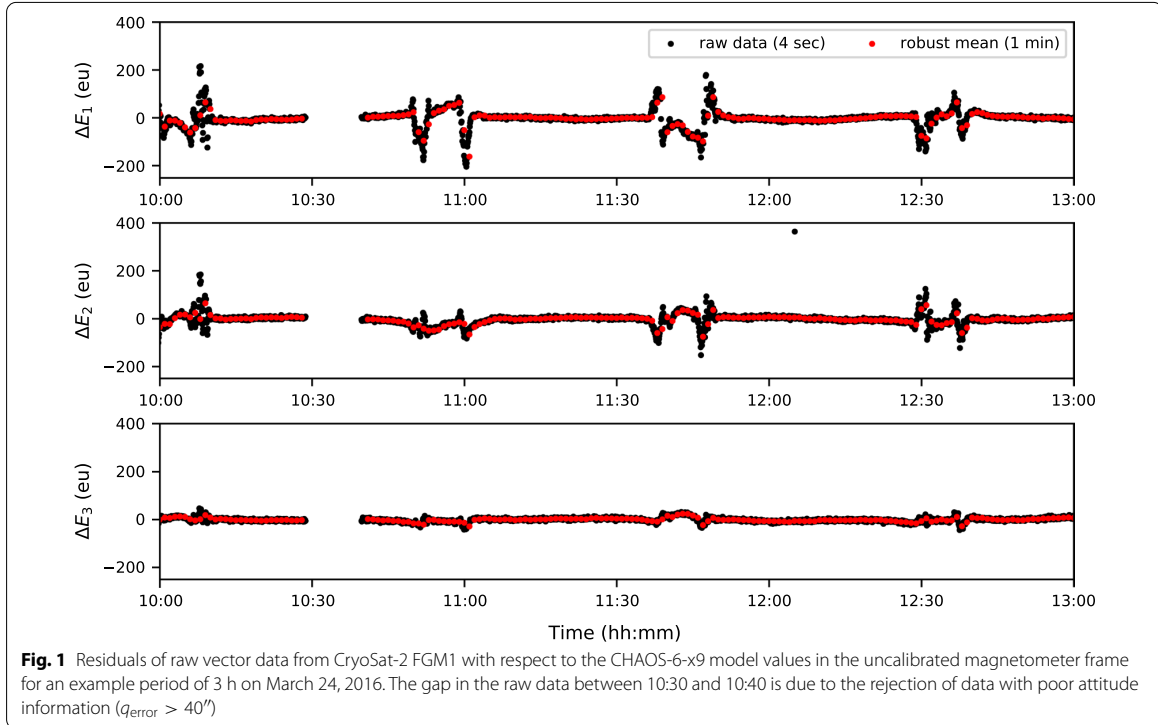
The computation of 1 min values served two purposes. First, to reduce the random noise of the magnetometers by taking the average of successive values and, second, to decrease the number of platform magnetometer data, so that a fair amount of absolute satellite data was able to guide the co-estimation of the calibration parameters.

Ground observatory data

In addition to satellite data, we added annual differences of monthly mean values from 162 ground observatories to help determine the time changes of the core field (secular variation). Following Olsen et al. (2014), we computed revised monthly means as Huber-weighted averages of the hourly observatory mean values from the AUX OBS database (Macmillan and Olsen 2013) at all local times after removing estimates of the ionospheric field of the CM4 model (Sabaka et al. 2004) and the large-scale magnetospheric field of CHAOS-6-x9, including their internally induced parts.

Satellite data selection

We organized the satellite data according to quasi-dipole (QD) latitude (Richmond 1995) into a non-polar (equal to and equatorward of $\pm 55^\circ$) and a polar (poleward of $\pm 55^\circ$) data subset. From each subset, we selected data



under quiet geomagnetic conditions. Specifically, we selected data from the non-polar subset that satisfied the following criteria:

- Low geomagnetic activity as indicated by the planetary activity index Kp smaller than or equal to 2^0 ;
- Dark condition as indicated by a solar zenith angle greater than 100° for the *Swarm* and CHAMP satellites (i.e., sun at least 10° below the horizon). From CryoSat-2 and GRACE, we used data from dark and sunlit regions, since we found that this leads to better determined calibration parameters;
- Slow change of the magnetospheric ring current as indicated by the RC-index (Olsen et al. 2014) rate of change in absolute terms being smaller than 2 nTh^{-1} .

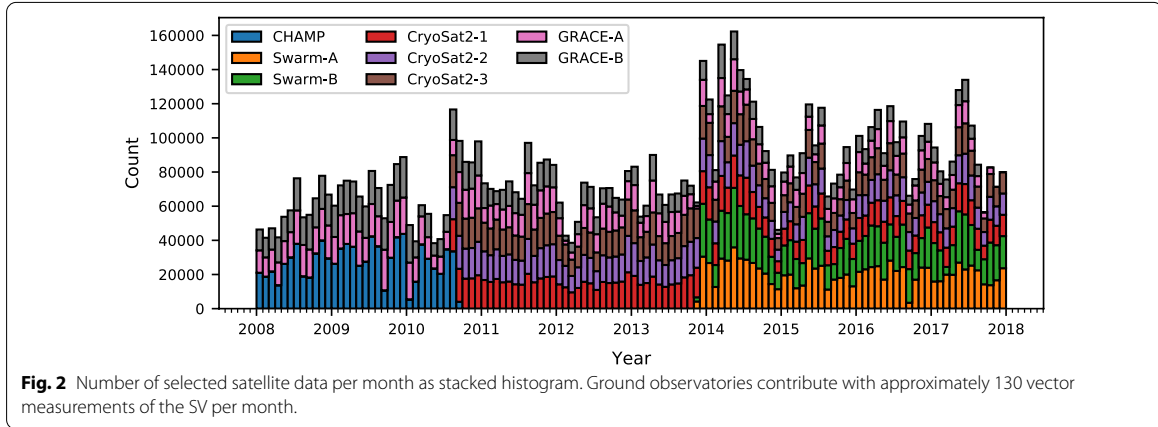
From the polar subset, we kept data according to the following criteria:

- Dark condition except in the case of platform magnetometers on-board CryoSat-2 and GRACE, where we also used sunlit data;
- RC-index rate of change in absolute terms smaller than or equal to 2 nTh^{-1} ;

- The merging electric field at the magnetopause $E_m = v^{4/3} B_T^{2/3} \sin |\Theta|/2$, where v is the solar wind speed, $B_T = \sqrt{B_y^2 + B_z^2}$ is the interplanetary magnetic field in the y - z -plane of the Geocentric Solar Magnetic (GSM) coordinates, and $\Theta = \arctan(B_y/B_z)$, was on average smaller than 2.4 mVm^{-1} over the previous 2 h;
- The interplanetary magnetic field component B_z in GSM coordinates was on average positive over the previous 2 h.

Figure 2 shows a stacked histogram of the number of data for each satellite after the data selection.

It can be clearly seen that platform magnetometer data are the main contributor to the number of data in the gap period, whereas it is comparable to the number of data from CHAMP and the *Swarm* satellites in the time before and after the gap. The ground observatories contribute approximately 130 monthly mean values of the SV each month throughout the entire model time span, which is much less than the monthly average number of satellite data.



Model parameterization and estimation

We are interested in the magnetic field vector \mathbf{B} on length scales smaller than Earth's circumference and time scales that are much longer than the time it takes light to traverse these distances (Backus et al. 1996; Sabaka et al. 2010). On these scales, the displacement current can be neglected and the magnetic field is governed by Ampere's law. We assume that the measurements of Earth's magnetic field are taken in a region free of electrical currents and magnetized material, such that the field is irrotational, which allows us to introduce a scalar potential V to represent the magnetic field as the gradient of the potential $\mathbf{B} = -\nabla V$. The potential consists of two terms $V = V_{\text{int}} + V_{\text{ext}}$ that describe internal sources such as the time-dependent core-generated field and the assumed static lithospheric field, and external sources that we assume are mainly magnetospheric in origin for our chosen data selection criteria and have an internally induced counterpart associated with them (by selecting data from dark regions, we minimize ionospheric field contributions).

To describe the geomagnetic field, we use an Earth-fixed frame of reference whose point of origin coincides with the Earth's center and in which the position vector \mathbf{r} is given in spherical polar coordinates by the radial distance r as measured from the origin (radius), the angular distance θ (co-latitude) as measured from the north polar axis, and the azimuthal angular distance ϕ (longitude) as measured from the Greenwich meridian. In the following, we refer to that system as the Radius-Theta-Phi (RTP) reference frame.

In spherical coordinates, the scalar potential can be expressed as a weighted sum of solid harmonics, which are harmonic functions of the spatial coordinates. Our modeling approach follows that of earlier models of the

CHAOS model series (Olsen et al. 2006, 2014; Finlay et al. 2016, 2020) and consists of describing the geomagnetic field with the help of a scalar potential whose exact form depends on a set of coefficients that multiply the solid harmonics. The coefficients are estimated by minimizing a quadratic cost function in the residuals, which are the difference between the magnetic observations and the magnetic data calculated with the model. We used two kinds of residuals: the components of vector differences in the RTP frame (vector residuals) and the difference of vector magnitudes (scalar residuals). More specifically, we computed vector residuals of the non-polar satellite data, scalar residuals of the polar satellite data, and vector residuals of the ground observatory SV data at all QD latitudes.

Internal field parameters

The scalar potential of the internal sources is given by:

$$V_{\text{int}}(\mathbf{r}, t) = a \sum_{n=1}^{N_{\text{int}}} \sum_{m=0}^n (g_n^m(t) \cos m\phi + h_n^m(t) \sin m\phi) \left(\frac{a}{r}\right)^{n+1} P_n^m(\cos \theta), \quad (1)$$

where $a = 6371.2$ km is the chosen spherical reference radius of the Earth, n and m are, respectively, the spherical harmonic degree and order, N_{int} is the truncation degree, $g_n^m(t)$ and $h_n^m(t)$ are the Gauss coefficients in nanoTesla (nT) for a given n and m , and $P_n^m(\cos \theta)$ are the Schmidt quasi-normalized associated Legendre functions. We truncated the formally infinite sum of solid harmonics at $N_{\text{int}} = 50$ and expanded the Gauss coefficients of degree $n \leq 15$ in time using sixth-order B-splines (De Boor 1978), while we kept the higher degree coefficients ($n > 15$) constant in time:

$$g_n^m(t) = \begin{cases} \sum_j g_{n,j}^m B_{6,j}(t), & n \leq 15 \\ g_n^m, & n > 15, \end{cases} \quad (2)$$

where $g_{n,j}^m$ (similarly for $h_{n,j}^m$) is the coefficient of $B_{6,j}(t)$ — the j th function of the B-spline basis that has knots at 6-month intervals and six-fold multiplicity at the model endpoints in $t_s = 2008.0$ and $t_e = 2018.0$ in years. For the purposes of testing the co-estimation of calibration parameters here, a truncation of the time-dependent internal field at degree $N_{\text{int}} = 15$ was deemed sufficient.

External field parameters

The scalar potential of the external sources consists of two terms $V_{\text{ext}} = V_{\text{SM}} + V_{\text{GSM}}$ that are designed to account for near and remote magnetospheric sources. We use the Solar Magnetic (SM) coordinate system to parameterize near magnetospheric sources:

$$\begin{aligned} V_{\text{SM}} = & a \sum_{m=0}^1 (q_{1,\text{SM}}^m(r,t) \cos m\phi_{\text{SM}} + s_{1,\text{SM}}^m(r,t) \sin m\phi_{\text{SM}}) P_1^m(\cos \theta_{\text{SM}}) \\ & + a \sum_{m=0}^1 (\Delta q_{1,\text{SM}}^m(t) R_{1,\text{SM}}^{m,c}(\mathbf{r},t) + \Delta s_{1,\text{SM}}^m(t) R_{1,\text{SM}}^{m,s}(\mathbf{r},t)) \\ & + a \sum_{m=0}^2 (q_{2,\text{SM}}^{m,c} R_{2,\text{SM}}^{m,c}(\mathbf{r},t) + s_{2,\text{SM}}^m R_{2,\text{SM}}^{m,s}(\mathbf{r},t)), \end{aligned} \quad (3)$$

where θ_{SM} and ϕ_{SM} are, respectively, the SM co-latitude and longitude, $q_{n,\text{SM}}^m$ and $s_{n,\text{SM}}^m$ are the Gauss coefficients with respect to the SM coordinate system, $\Delta q_{1,\text{SM}}^m(t)$ and $\Delta s_{1,\text{SM}}^m(t)$ are the RC-baseline corrections, and $R_{n,\text{SM}}^{m,c}$ and $R_{n,\text{SM}}^{m,s}$ are modification of the solid harmonics that account for the time-dependent transformation from the SM to the geographic coordinate system and include internally induced contributions based on the diagonal part of the Q-response matrix that has been derived from a 3D conductivity model of Earth (Finlay et al. 2020). The external Gauss coefficients with $n = 1$ have a specific time-dependence in the form of:

$$\begin{aligned} q_{1,\text{SM}}^0(r,t) &= \hat{q}_1^0 \left[\epsilon(t) \left(\frac{r}{a} \right) + \iota(t) \left(\frac{a}{r} \right)^2 \right] \\ q_{1,\text{SM}}^1(r,t) &= \hat{q}_1^1 \left[\epsilon(t) \left(\frac{r}{a} \right) + \iota(t) \left(\frac{a}{r} \right)^2 \right] \\ s_{1,\text{SM}}^1(r,t) &= \hat{s}_1^1 \left[\epsilon(t) \left(\frac{r}{a} \right) + \iota(t) \left(\frac{a}{r} \right)^2 \right], \end{aligned} \quad (4)$$

where $\epsilon(t)$ and $\iota(t)$ are the respective internal and external part of the RC-index linearly interpolated from hourly values. The RC-baseline corrections were estimated in

bins of 30 days except in the gap period, where we used a single bin from August 2010 to January 2014 to reduce the strong co-linearity between the calibration parameters and the baseline corrections that earlier tests had revealed.

The remote magnetospheric sources, and the currents at the magnetopause and in the magnetotail, are taken into account by a purely zonal potential in the GSM coordinate system up to degree 2:

$$V_{\text{GSM}}(\mathbf{r},t) = a \sum_{n=1}^2 q_{n,\text{GSM}}^0 R_{n,\text{GSM}}^{0,c}(\mathbf{r},t), \quad (5)$$

where $q_{n,\text{GSM}}^m$ and $s_{n,\text{GSM}}^m$ are Gauss coefficients that are constant in time with respect to the GSM coordinate system, and $R_{n,\text{GSM}}^{m,c}$ are modifications of the solid harmonics similar to corresponding terms in Eq. (3) but for the GSM coordinates.

Alignment parameters

Using satellite data in the vector field magnetometer frame (VFM) requires an additional step, called data alignment, which involves determining alignment parameters that describe the rotation of the magnetic field vector \mathbf{B}_{VFM} in the VFM frame to \mathbf{B}_{CRF} in the common reference frame (CRF) of the satellite. Once in the CRF, the vector components can be combined with the attitude information from the star camera and rotated into the RTP frame for computing the vector residuals. We performed the data alignment for CHAMP, *Swarm*, *CryoSat-2*, and *GRACE*.

The alignment parameters are usually parameterized in the form of Euler angles α , β , and γ . We adopted the 1-2-3 convention of the Euler angles to align the magnetic field:

$$\begin{aligned} \mathbf{B}_{\text{CRF}} &= \mathbf{R}_{\text{CRF}}^{\text{VFM}}(\alpha, \beta, \gamma) \mathbf{B}_{\text{VFM}} \\ &= \mathbf{R}_3(\gamma) \mathbf{R}_2(\beta) \mathbf{R}_1(\alpha) \mathbf{B}_{\text{VFM}}, \end{aligned} \quad (6)$$

where the rotation matrix is a combination of the three rotations:

$$\begin{aligned}
 \underline{\underline{\mathbf{R}}}_1 &= \begin{pmatrix} 1 & 0 & 0 \\ 0 & \cos \alpha & -\sin \alpha \\ 0 & \sin \alpha & \cos \alpha \end{pmatrix} \\
 \underline{\underline{\mathbf{R}}}_2 &= \begin{pmatrix} \cos \beta & 0 & \sin \beta \\ 0 & 1 & 0 \\ -\sin \beta & 0 & \cos \beta \end{pmatrix} \\
 \underline{\underline{\mathbf{R}}}_3 &= \begin{pmatrix} \cos \gamma & -\sin \gamma & 0 \\ \sin \gamma & \cos \gamma & 0 \\ 0 & 0 & 1 \end{pmatrix}.
 \end{aligned} \tag{7}$$

Following the alignment, we applied another rotation matrix $\underline{\underline{\mathbf{R}}}_{\text{RTP}}^{\text{CRF}}$ to rotate the field components from the CRF to the RTP reference frame:

$$\mathbf{B}_{\text{RTP}} = \underline{\underline{\mathbf{R}}}_{\text{RTP}}^{\text{CRF}}(\mathbf{r}, t) \mathbf{B}_{\text{CRF}}, \tag{8}$$

which depends on position and time. That rotation matrix was computed by combining the quaternions that express the rotation from the CRF to the Earth-fixed Earth-centered North-East-Center (NEC) frame with quaternions that describe the change from the NEC to the RTP reference frame. For each satellite dataset, we parameterized the Euler angles in time as a piecewise constant function using a sequence of 30 day bins.

Calibration parameters

The calibration can be viewed as an extension of the data alignment which makes it possible to use platform magnetometer data in geomagnetic field modeling. We performed the calibration for CryoSat-2 and the GRACE satellites.

We assume that the platform magnetometer is a linear vector field magnetometer, which provides information about the desired local magnetic field vector \mathbf{B}_{VFM} (units of nT) in the form of the sensor output $\mathbf{E} = (E_1, E_2, E_3)^T$ (units of eu), which typically consists of components that are measured relative to three biased and non-orthogonal axes employing different scale factors (Olsen et al. 2003). More specifically, the sensor output in the magnetometer frame is related to the local magnetic field through:

$$\mathbf{B}_{\text{VFM}} = \underline{\underline{\mathbf{P}}}^{-1} \underline{\underline{\mathbf{S}}}^{-1} (\mathbf{E} - \mathbf{b}), \tag{9}$$

where

$$\underline{\underline{\mathbf{S}}}(\mathbf{s}) = \begin{pmatrix} s_1 & 0 & 0 \\ 0 & s_2 & 0 \\ 0 & 0 & s_3 \end{pmatrix} \tag{10}$$

is the diagonal matrix of sensitivities or scale factors $\mathbf{s} = (s_1, s_2, s_3)^T$ (units of eu/nT):

$$\underline{\underline{\mathbf{P}}}(\mathbf{u}) = \begin{pmatrix} 1 & 0 & 0 \\ -\sin u_1 & \cos u_1 & 0 \\ \sin u_2 & \sin u_3 & \sqrt{1 - \sin^2 u_2 - \sin^2 u_3} \end{pmatrix} \tag{11}$$

is the matrix that projects the orthogonal components of magnetic field vector \mathbf{B}_{VFM} onto three non-orthogonal directions defined by the non-orthogonality angles $\mathbf{u} = (u_1, u_2, u_3)^T$ (units of radians), and:

$$\mathbf{b} = \begin{pmatrix} b_1 \\ b_2 \\ b_3 \end{pmatrix} \tag{12}$$

is the offset or bias vector (units of eu). Combining the calibration step in Eq. (9), the alignment step involving the Euler angles in Eq. (6) and the change of frame in Eq. (8), yields an equation that transforms the uncalibrated sensor output \mathbf{E} into calibrated, aligned field components in the RTP frame:

$$\mathbf{B}_{\text{RTP}} = \underline{\underline{\mathbf{R}}}_{\text{RTP}}^{\text{CRF}}(r, \theta, \phi) \underline{\underline{\mathbf{R}}}_{\text{CRF}}^{\text{VFM}}(\alpha, \beta, \gamma) \underline{\underline{\mathbf{P}}}^{-1} \underline{\underline{\mathbf{S}}}^{-1} (\mathbf{E} - \mathbf{b}). \tag{13}$$

We estimated the nine basic calibration parameters and the three Euler angles in bins of 30 days. For data equatorward of $\pm 55^\circ$ QD latitude, we performed a vector calibration using the component residuals of \mathbf{B}_{RTP} for estimating the model parameters (see "Model parameter estimation" section). In contrast, for data poleward of $\pm 55^\circ$ QD latitude, we performed a scalar calibration using the residuals of the vector magnitude, in which case the rotation matrices from the VFM to the RTP frame including the Euler angles disappear:

$$\begin{aligned}
 F &= |\mathbf{B}_{\text{RTP}}| = \sqrt{\mathbf{B}_{\text{RTP}}^T \mathbf{B}_{\text{RTP}}} \\
 &= \sqrt{(\mathbf{E} - \mathbf{b})^T \underline{\underline{\mathbf{S}}}^{-1} (\underline{\underline{\mathbf{P}}}^{-1})^T \underline{\underline{\mathbf{P}}}^{-1} \underline{\underline{\mathbf{S}}}^{-1} (\mathbf{E} - \mathbf{b})}
 \end{aligned} \tag{14}$$

at the expense of losing the ability to estimate the Euler angles.

Table 1 summarizes the different parts of the model and the corresponding number of parameters.

Model parameter estimation

The geomagnetic field model parameters \mathbf{p} , the Euler angles \mathbf{q} , and the calibration parameters \mathbf{e} were derived by solving the least-squares problem:

Table 1 Details on the parameterization of the individual model parts. Here, the number of basic parameters refers to the number of parameters irrespective of an explicit time-dependence

Description of the model parameters		Number of basic parameters	Temporal parameterization	Number of parameters
Internal field	Time-dependent ($n \leq 15$)	255	order-6 B-spline	6375
	Static ($16 \leq n \leq 50$)	2345	None	2345
External field	SM degree-1	3	RC-index	3
	SM degree-2	5	None	5
	RC-baseline corrections	3	80 bins (30 days)	240
	GSM	2	None	2
Euler angles	CHAMP	3	33 bins (30 days)	99
	Swarm-A	3	50 bins (30 days)	150
	Swarm-B	3	50 bins (30 days)	150
Euler/Calibration	CryoSat-2 FGM1	12	91 bins (30 days)	1092
	CryoSat-2 FGM2	12	91 bins (30 days)	1092
	CryoSat-2 FGM3	12	91 bins (30 days)	1092
	GRACE-A	12	120 bins (30 days)	1440
	GRACE-B	12	118 bins (30 days)	1416
Total number of parameters (no platform magnetometer data)				9369
Total number of parameters				15501

$$\mathbf{m}^* = \underset{\mathbf{m}}{\operatorname{argmin}} \Phi(\mathbf{m}), \quad (15)$$

where $\mathbf{m} = (\mathbf{p}^T, \mathbf{q}^T, \mathbf{e}^T)^T$ is the entire model parameter vector, and Φ is the cost function:

$$\Phi(\mathbf{m}) = (\mathbf{g}(\mathbf{p}) - \mathbf{d}(\mathbf{q}, \mathbf{e}))^T \underline{\underline{\mathbf{C}_d}}^{-1} (\mathbf{g}(\mathbf{p}) - \mathbf{d}(\mathbf{q}, \mathbf{e})) + \mathbf{m}^T \underline{\underline{\mathbf{A}}} \mathbf{m}, \quad (16)$$

which penalizes a quadratic form in the residuals—the difference between the computed geomagnetic field model values $\mathbf{g}(\mathbf{p})$ and the calibrated, aligned magnetic data $\mathbf{d}(\mathbf{q}, \mathbf{e})$ —using the inverse of the data covariance matrix $\underline{\underline{\mathbf{C}_d}}$, and a quadratic form in the model parameter vector using the regularization matrix $\underline{\underline{\mathbf{A}}}$. For the definition of the matrices $\underline{\underline{\mathbf{C}_d}}$ and $\underline{\underline{\mathbf{A}}}$, see, respectively, "Data weighting" and "Model regularization" sections.

The least-squares solution \mathbf{m}^* in Eq. (15) is found through an iterative quasi-Newton method, which consists of updating the model parameter vector \mathbf{m}_k at iteration k using $\mathbf{m}_{k+1} = \mathbf{m}_k + \Delta \mathbf{m}$ together with:

$$\Delta \mathbf{m} = ((\underline{\underline{\mathbf{G}_k}})^T \underline{\underline{\mathbf{C}_d}}^{-1} \underline{\underline{\mathbf{G}_k}} + \underline{\underline{\mathbf{A}}})^{-1} \cdot ((\underline{\underline{\mathbf{G}_k}})^T \underline{\underline{\mathbf{C}_d}}^{-1} (\mathbf{d}_k - \mathbf{g}_k) - \underline{\underline{\mathbf{A}}} \mathbf{m}_k), \quad (17)$$

where $\mathbf{d}_k = \mathbf{d}(\mathbf{q}_k, \mathbf{e}_k)$, $\mathbf{g}_k = \mathbf{g}(\mathbf{p}_k)$, and $\underline{\underline{\mathbf{G}_k}}$ is a matrix with entries corresponding to the partial derivative of the i th residual with respect to the j th model parameter:

$$(\underline{\underline{\mathbf{G}_k}})_{ij} = \left. \frac{\partial (\mathbf{g}(\mathbf{p}) - \mathbf{d}(\mathbf{q}, \mathbf{e}))_i}{\partial (\mathbf{m})_j} \right|_{\mathbf{m}=\mathbf{m}_k} \quad (18)$$

evaluated at iteration k (Tarantola 2005, p. 69). Some entries of $\underline{\underline{\mathbf{G}_k}}$ are zero owing to data subsets that do not provide information on parts of the model. For example, scalar data do not constrain the Euler angles and vector data from one magnetometer do not constrain the Euler angles associated with another magnetometer. With the same idea in mind, we modified entries of $\underline{\underline{\mathbf{G}_k}}$ to prevent some data subsets from constraining certain parts of the internal field model. In particular, we set entries to zero for the following criteria:

- 1 The row index of the matrix entry corresponded to dayside data from a platform magnetometer, on-board CryoSat-2, or GRACE, and the column index corresponded to model parameters that describe the internal and external magnetic field. Therefore, the dayside data were only used to constrain the Euler angles and calibration parameters of the respective platform magnetometer.
- 2 The row index of the matrix entry corresponded to data from a platform magnetometer, on-board CryoSat-2 or GRACE, and the column index corresponded to the B-spline parameters that param-

Table 2 Overview of which data subset constrained which part of the model. The cross refers to non-zero entries in the matrix of partial derivatives, whereas the circle refers to zeros. The SV data refer to the annual difference of the revised monthly means

Description of the model parameters		Non-polar satellite data		Polar satellite data		SV data
		Day	Night	Day	Night	
Internal field	Time-dependent ($n \leq 15$)	○	X ¹	○	X ¹	X
	Static ($16 \leq n \leq 50$)	○	X	○	X	○
External field	SM	○	X	○	X	○
	GSM	○	X	○	X	○
Euler angles	CHAMP	○	X	○	○	○
	Swarm-A	○	X	○	○	○
	Swarm-B	○	X	○	○	○
	CryoSat-2 FGM1	X	X	○	○	○
	CryoSat-2 FGM2	X	X	○	○	○
	CryoSat-2 FGM3	X	X	○	○	○
	GRACE-A	X	X	○	○	○
	GRACE-B	X	X	○	○	○
	GRACE-B	X	X	○	○	○
Calibration	CryoSat-2 FGM1	X	X	X	X	○
	CryoSat-2 FGM2	X	X	X	X	○
	CryoSat-2 FGM3	X	X	X	X	○
	GRACE-A	X	X	X	X	○
	GRACE-B	X	X	X	X	○

¹ Entries related to g_1^0 B-spline coefficients and platform magnetometer data are zero

eterize the g_1^0 Gauss coefficient of the internal field in time. Therefore, no platform magnetometer data were used to constrain the B-spline coefficients of the axial dipole which we believe are well determined using ground observatory data.

Table 2 gives an overview of whether or not certain datasets constrained specific parts of the model.

Nevertheless, we used the full model description in the forward evaluation to compute the residuals.

The iterative procedure described in Eq. (17) requires a starting model \mathbf{m}_0 to initialize the model parameter estimation. We initialized the internal field model parameters using the corresponding part of CHAOS-6-x9, while we set the external field model parameters to zero. To initialize the Euler angles, we used the values from CHAOS-6-x9 in case of *Swarm* and CHAMP satellites, or set the angles to zero in case of CryoSat-2 and the GRACE satellite duo. For the calibration parameters, we simply set the offsets and non-orthogonalities to zero and the sensitivities to one over the whole time span. The parameter estimation usually converged after 10–15 iterations. We also tested other starting models, e.g., random calibration parameters, but found that our choice had little impact on the converged model parameters other than increasing the number of necessary iterations.

Table 3 Chosen values of σ and ψ for the different satellites. The values under *Swarm* apply to the data from the two *Swarm* satellites in this study (*Swarm-A* and *Swarm-B*), the values under *CryoSat-2* to the data of the three magnetometers (FGM1, FGM2 and FGM3), and the values under *GRACE* to the data from both *GRACE* satellites (*GRACE-A* and *GRACE-B*)

	CHAMP	Swarm	CryoSat-2	GRACE
σ (nT)	2.5	2.2	6	10
ψ (arcsec)	10	5	30	100

Data weighting

For the vector components of the non-polar satellite data, we used a covariance matrix that accounts for the attitude uncertainty of the star cameras:

$$\underline{\mathbf{C}}_{\mathbf{B}23} = \text{diag}(\sigma^2, \sigma^2 + B^2\psi^2, \sigma^2 + B^2\psi^2) \quad (19)$$

with respect to the B23 reference frame defined by unit vectors in the direction of \mathbf{B} , $\mathbf{n} \times \mathbf{B}$, and $\mathbf{n} \times (\mathbf{n} \times \mathbf{B})$, where \mathbf{n} is an arbitrary unit vector not parallel to \mathbf{B} that we chose to be the third CRF base vector, σ^2 is the variance of an isotropic instrument error and ψ^2 is the variance associated with random rotations around the three

reference axes (Holme and Bloxham 1996). Table 3 summarizes the values of σ and ψ for the different satellite datasets.

We scaled the diagonal entries of the covariance matrix with Huber weights (Constable 1988; Sabaka et al. 2004) that we calculated for each component in the B23 reference frame to downweight data points that greatly deviated from the model evaluated at the previous iteration. After inverting and rotating the Huber-weighted covariance matrix of the individual data point into the RTP frame, we arranged them into a block-diagonal matrix completing the desired inverse data covariance matrix \underline{C}_d^{-1} . In case of the vector magnitude of the polar satellite data, we simply used σ^2 scaled with Huber weights as variance. The covariance of the ground observatory SV vector data was derived from detrended residuals to the CHAOS-6-x9 model, including the covariance between vector components at a given location.

Model regularization

The regularization in the form of the matrix $\underline{\Lambda}$ in Eq. (15) is designed to ensure the convergence of the model parameter estimation by limiting the flexibility of the model. The regularization matrix is block diagonal and consists of the blocks $\underline{\Lambda}_{\text{int}}$, $\underline{\Lambda}_{\text{ext}}$, and $\underline{\Lambda}_{\text{cal}}$, which regularized the internal, external, and the calibration parameters, respectively. We did not regularize the Euler angles, such that corresponding blocks in the regularization matrix are zero.

Turning to the internal part of the model, following the example of earlier models in the CHAOS series, we designed a regularization based on the square of the third time-derivative of the radial field component B_r integrated over the core mantle boundary (CMB) and averaged over the entire model time span:

$$\langle \ddot{B}_r^2 \rangle = \frac{1}{4\pi(t_e - t_s)} \int_{t_s}^{t_e} \int_{\Omega(c)} \left(\frac{\partial^3 B_r}{\partial t^3} \right)^2 d\Omega dt, \quad (20)$$

where $c = 3485.0$ km is the chosen spherical reference radius of the CMB, $\Omega(c)$ denotes the CMB given as the spherical surface of radius c , and $d\Omega = \sin\theta d\theta d\phi$ is the surface element for the integration. Furthermore, we set up a regularization of the internal field based on the square of the second time-derivative of the radial component integrated over the CMB at the model start time t_s :

$$\langle \ddot{B}_r^2(t_s) \rangle = \frac{1}{4\pi} \int_{\Omega(c)} \left(\frac{\partial^2 B_r}{\partial t^2} \Big|_{t=t_s} \right)^2 d\Omega, \quad (21)$$

and similarly for the end time by replacing t_s with t_e . Returning to Eq. (20), thanks to the orthogonality of

spherical harmonics on the surface of the sphere, carrying out the spatial integration leads to:

$$\langle \ddot{B}_r^2 \rangle = \sum_{n=1}^{N_{\text{int}}} \left(w_{\Omega}(n) \sum_{m=0}^n \left(\langle \ddot{g}_n^m(t)^2 \rangle_t + \langle \ddot{i}_n^m(t)^2 \rangle_t \right) \right), \quad (22)$$

where $w_{\Omega} = \frac{(n+1)^2}{2n+1} \left(\frac{a}{c} \right)^{2n+4}$ is a spatial factor that follows from the surface integration and $\langle \cdot \rangle_t = \frac{1}{t_e - t_s} \int_{t_s}^{t_e} dt$ denotes the time average. Utilizing the fact that the time-dependence of the Gauss coefficients is given by sixth-order B-splines, terms such as:

$$\begin{aligned} \langle \ddot{g}_n^m(t)^2 \rangle_t &= \sum_{j,j'} g_{n,j}^m g_{n,j'}^m \langle \ddot{B}_{6,j}(t) \ddot{B}_{6,j'}(t) \rangle_t \\ &= \sum_{j,j'} g_{n,j}^m g_{n,j'}^m A_{jj'} \\ &= (\underline{g}_n^m)^T \underline{A}_t \underline{g}_n^m \end{aligned} \quad (23)$$

can be written as a quadratic form in $\underline{g}_n^m = (g_{n,1}^m, g_{n,2}^m, \dots)^T$, the vector of the spline coefficients of g_n^m , using the matrix \underline{A}_t that has entries corresponding to the time averages of products of the third time-derivative of the B-splines. While the time-derivatives of the B-splines are known analytically, we approximated the time average numerically by a Riemann sum of rectangles. A similar computation of Eq. (21), now evaluating the derivatives only at the endpoints instead of averaging in time, yields matrices $(\underline{A}_{t_s})_{jj'} = \ddot{B}_{6,j}(t_s) \ddot{B}_{6,j'}(t_s)$ and $(\underline{A}_{t_e})_{jj'} = \ddot{B}_{6,j}(t_e) \ddot{B}_{6,j'}(t_e)$. Finally, based on the physical quantities in Eqs. (20) and (21), we devised a block-diagonal regularization matrix for the internal magnetic field model:

$$\underline{\Lambda}_{\text{int}} = \text{diag}_{n,m} \left(w_{\Omega}(n) w_m(m) w_{\text{tp}}(n) \cdot \left(\lambda_t \underline{A}_t + \lambda_{t_s} \underline{A}_{t_s} + \lambda_{t_e} \underline{A}_{t_e} \right) \right), \quad (24)$$

where n and m run over the degree and order in the spherical harmonic expansion of the internal field in Eq. (1); $w_m(m)$ and $w_{\text{tp}}(n)$ are functions which control the regularization strength based on the degree and order of the internal Gauss coefficients; λ_t , λ_{t_s} , and λ_{t_e} are parameters that, respectively, set the regularization strength over the entire model time span, at the model start time and end time. Following Finlay et al. (2020), to relax the regularization at higher spherical harmonic degree, we defined $w_{\text{tp}}(n)$ as a tapered window which gradually reduces from one to 0.005:

$$w_{\text{tp}}(n) = \begin{cases} 1, & n < n_{\min} \\ \tau(n), & n_{\min} \leq n \leq n_{\max} \\ 0.005, & n > n_{\max}, \end{cases} \quad (25)$$

where $n_{\min} = 3$ and $n_{\max} = 6$ are the chosen limits of a half-cosine taper:

$$\tau(n) = \frac{0.995}{2} \left[1 + \cos \left(\pi \frac{n - n_{\min}}{n_{\max} - n_{\min}} \right) \right] + 0.005. \quad (26)$$

In contrast to Finlay et al. (2020), who used $n_{\max} = 11$ to achieve stable power spectra with more power in the time-dependence of the high-degree coefficients without causing instabilities, we were able to further decrease the upper limit of the taper. The magnetospheric and ionospheric field and their induced counterparts may also cause the estimation of the internal field parameters to become unstable. Our experience shows that it is typically the zonal harmonics that become unstable first if the regularization is not sufficiently strong. Therefore, in addition to the degree-dependent temporal regularization, there is a special treatment of zonal and non-zonal spherical harmonics based on:

$$w_m(m) = \begin{cases} \lambda_0, & m = 0 \\ \lambda_m, & m \neq 0. \end{cases} \quad (27)$$

Note that the regularization of the internal field model only constrains the time-derivatives of the field but not the field itself.

Turning to the external part of the model, we regularized only the bin-to-bin variability of the three RC-baseline corrections $\Delta q_{1,SM}^0$, $\Delta q_{1,SM}^1$, and $\Delta s_{1,SM}^1$ in Eq. (3) using a quadratic form in the first forward difference of neighboring bins. The forward difference was calculated with the matrix:

$$\underline{\underline{\mathbf{D}}} = \frac{1}{t_e - t_s} \begin{pmatrix} -1 & 1 & & \\ & \ddots & \ddots & \\ & & \ddots & \ddots \\ & & & -1 & 1 \end{pmatrix}, \quad (28)$$

whose number of columns is equal to the number of bins that comprise each RC-baseline correction. Taken together, the regularization matrix for all parameters related to the external field model reads:

$$\underline{\underline{\Lambda}}_{\text{ext}} = \text{diag}(0, \dots, 0, \lambda_{\text{ext}} \underline{\underline{\mathbf{I}}}_3 \otimes \underline{\underline{\mathbf{D}}}_2, 0, \dots, 0), \quad (29)$$

where \otimes is the Kronecker product, $\underline{\underline{\mathbf{I}}}_3$ is the unit matrix of size three corresponding to the three RC-baseline corrections, $\underline{\underline{\mathbf{D}}}_2 = \underline{\underline{\mathbf{D}}}^T \underline{\underline{\mathbf{D}}}$ is the coefficient matrix that determines the quadratic form, additional zeros on the diagonal indicate the other unregularized model

parameters of the external field, and λ_{ext} is the chosen regularization parameter.

Turning to the calibration parameters, we regularized a quadratic form in the bin-to-bin variability of each calibration parameter for the five platform magnetometers (three on CryoSat-2 and one on each of the two GRACE satellites). The regularization matrix $\underline{\underline{\Lambda}}_{\text{cal}}$ is block-diagonal with each block $\underline{\underline{\Lambda}}_{\text{cal},i}$, $i = 1, \dots, 5$, corresponding to the calibration parameters for each of the five platform magnetometers. The regularization matrix can be written as:

$$\begin{aligned} \underline{\underline{\Lambda}}_{\text{cal}} &= \text{diag}(\underline{\underline{\Lambda}}_{\text{cal},1}, \dots, \underline{\underline{\Lambda}}_{\text{cal},5}) \\ \underline{\underline{\Lambda}}_{\text{cal},i} &= \text{diag}(\lambda_{b,i}, \lambda_{s,i}, \lambda_{u,i}) \otimes \underline{\underline{\mathbf{I}}}_3 \otimes \underline{\underline{\mathbf{D}}}_2, \end{aligned} \quad (30)$$

where we define the regularization parameters $\lambda_{b,i}$, $\lambda_{s,i}$ and $\lambda_{u,i}$ to control the temporal smoothness of the offsets, sensitivities, and non-orthogonalities, respectively.

Results and discussion

We built two geomagnetic field models which span 10 years from the 1st of January 2008 to the 31st of December 2018, but differ in the use of platform magnetometer data to constrain the field model parameters.

The first model, Model-A, was derived with data from the Swarm-A, Swarm-B, and CHAMP satellites, and the monthly SV data from ground observatories. It served as a reference model, which allowed us to identify differences to models which were derived using platform magnetometer data in addition. Considering the model parameterization, regularization, and estimation, Model-A is very similar to the CHAOS model series. In fact, the parameterization of the geomagnetic field and the alignment parameters of the satellite data are identical, except for the lower truncation degree of the internal field and the longer bins of the alignment parameters and RC-baseline corrections in Model-A. A notable difference is the use of gradient data in the CHAOS model. The strong temporal regularization of the high-degree Gauss coefficients of the time-dependent internal field has been relaxed in the newly released CHAOS-7 model through a taper, which we also used here. For Model-A, we tuned the regularization, such that the model parameters matched the ones of the CHAOS-6-x9 model as close as possible. Table 4 shows the numerical values of the regularization parameters.

The second model, Model-B, is our preferred model and was derived with data from Swarm-A, Swarm-B, CHAMP, monthly ground observatory SV data, and, as opposed to Model-A, platform magnetometer data from CryoSat-2 FGM1, CryoSat-2 FGM2, CryoSat-2 FGM3, GRACE-A, and GRACE-B. In addition to Model-A and

Table 4 Chosen numerical values of the regularization parameters. The values are valid for all the models built in this paper insofar as the regularization terms are applicable to the specific model

Description of the model parameters	Regularization parameter
Internal field	Time-dependent $\lambda_t = 1.0 \left(\frac{\text{nT}}{\text{yr}^3}\right)^{-2}$, $\lambda_{t_s} = 0.03 \left(\frac{\text{nT}}{\text{yr}^2}\right)^{-2}$, $\lambda_{t_e} = 0.03 \left(\frac{\text{nT}}{\text{yr}^2}\right)^{-2}$, $\lambda_0 = 60$, $\lambda_m = 0.65$
External field	RC-baseline corrections $\lambda_{\text{ext}} = 4 \times 10^5 \left(\frac{\text{nT}}{\text{yr}}\right)^{-2}$
Calibration ¹	CryoSat-2 FGM1 $\lambda_b = 9.1 \times 10^2 \left(\frac{\text{eU}}{\text{yr}}\right)^{-2}$, $\lambda_s = 9.1 \times 10^{10} \left(\frac{\text{eU}}{\text{nT yr}}\right)^{-2}$, $\lambda_u = 2.8 \times 10^2 \left(\frac{1^\circ}{\text{yr}}\right)^{-2}$
	CryoSat-2 FGM2 $\lambda_b = 9.1 \times 10^2 \left(\frac{\text{eU}}{\text{yr}}\right)^{-2}$, $\lambda_s = 9.1 \times 10^{10} \left(\frac{\text{eU}}{\text{nT yr}}\right)^{-2}$, $\lambda_u = 2.8 \times 10^2 \left(\frac{1^\circ}{\text{yr}}\right)^{-2}$
	CryoSat-2 FGM3 $\lambda_b = 9.1 \times 10^2 \left(\frac{\text{eU}}{\text{yr}}\right)^{-2}$, $\lambda_s = 9.1 \times 10^{10} \left(\frac{\text{eU}}{\text{nT yr}}\right)^{-2}$, $\lambda_u = 2.8 \times 10^2 \left(\frac{1^\circ}{\text{yr}}\right)^{-2}$
	GRACE-A $\lambda_b = 1.2 \times 10^3 \left(\frac{\text{eU}}{\text{yr}}\right)^{-2}$, $\lambda_s = 1.2 \times 10^{13} \left(\frac{\text{eU}}{\text{nT yr}}\right)^{-2}$, $\lambda_u = 3.7 \times 10^8 \left(\frac{1^\circ}{\text{yr}}\right)^{-2}$
	GRACE-B $\lambda_b = 1.2 \times 10^3 \left(\frac{\text{eU}}{\text{yr}}\right)^{-2}$, $\lambda_s = 1.2 \times 10^{13} \left(\frac{\text{eU}}{\text{nT yr}}\right)^{-2}$, $\lambda_u = 3.6 \times 10^8 \left(\frac{1^\circ}{\text{yr}}\right)^{-2}$

¹ Not applicable to Model-A, which was not derived from platform magnetometer data

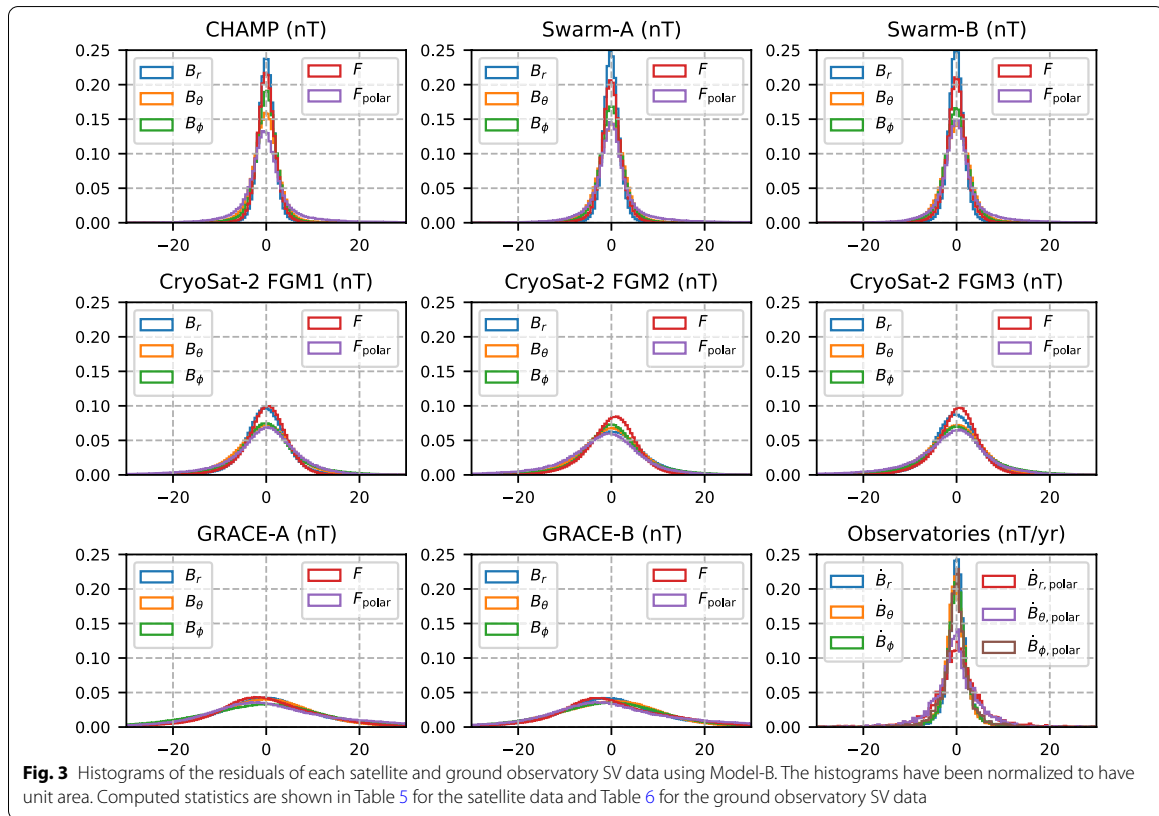


Fig. 3 Histograms of the residuals of each satellite and ground observatory SV data using Model-B. The histograms have been normalized to have unit area. Computed statistics are shown in Table 5 for the satellite data and Table 6 for the ground observatory SV data

Model-B, we built test models in a series of experiments to investigate the effect of platform magnetometer data on the estimation of the geomagnetic field model. Details

of the test models are given below. The regularization parameters are the same for all the presented models, i.e., Model-A, Model-B, and the test models.

Fit to satellite data and ground observatory SV data

We begin with reporting on the fit of Model-B to the satellite data and ground observatory SV data. The histograms of the scalar and vector residuals for each dataset are shown in Fig. 3.

The residuals of Swarm-A, Swarm-B, CHAMP, and the ground observatories show narrow and near-zero centered peaks, which demonstrate the high-quality and low-noise level of these datasets. In contrast, the peaks are broader for CryoSat-2 and even more in the case of

Table 5 Number N , Huber-weighted mean, and standard deviation σ computed from the residuals of the satellite data for each vector component and split into polar (poleward $\pm 55^\circ$) and non-polar (equatorward $\pm 55^\circ$) QD latitudes. Note that non-polar scalar data were not used in the model parameter estimation—statistics are only shown for completeness

Dataset	Quasi-dipole latitude	Component	N	mean (nT)	σ (nT)
CHAMP	Non-polar	B_r	707131	0.02	1.93
		B_θ	707131	-0.11	2.84
		B_ϕ	707131	0.03	2.32
		F	707131	0.01	1.93
CryoSat-2 FGM1	Non-polar	B_r	958362	-0.06	4.39
		B_θ	958362	-0.31	5.76
		B_ϕ	958362	0.06	6.49
		F	958362	0.06	4.18
CryoSat-2 FGM2	Non-polar	B_r	958362	-0.03	6.42
		B_θ	958362	-0.29	6.01
		B_ϕ	958362	0.07	6.55
		F	958362	0.18	4.86
CryoSat-2 FGM3	Non-polar	B_r	958362	-0.07	4.76
		B_θ	958362	-0.23	5.71
		B_ϕ	958362	0.04	6.80
		F	958362	0.12	4.35
GRACE-A	Non-polar	B_r	1082071	-0.12	11.40
		B_θ	1082071	-0.24	10.48
		B_ϕ	1082071	-0.79	13.57
		F	1082071	-0.16	10.59
GRACE-B	Non-polar	B_r	997802	-0.30	11.77
		B_θ	997802	-0.69	11.09
		B_ϕ	997802	-0.68	12.35
		F	997802	0.02	11.53
Swarm-A	Non-polar	B_r	817400	-0.03	1.65
		B_θ	817400	-0.06	2.97
		B_ϕ	817400	-0.02	2.59
		F	817400	-0.03	2.06
Swarm-B	Non-polar	B_r	809720	-0.09	1.63
		B_θ	809720	-0.05	3.02
		B_ϕ	809720	-0.04	2.61
		F	809720	-0.01	2.03
	Polar	F	218106	0.30	4.29

Table 6 Number N , Huber-weighted mean, and standard deviation σ computed from the residuals of the monthly ground observatory SV data for each component and split into polar (poleward $\pm 55^\circ$) and non-polar (equatorward $\pm 55^\circ$) QD latitudes

Dataset	Quasi-dipole latitude	Component	N	Mean (nT/yr)	σ (nT/yr)
Observatories	Non-polar	\dot{B}_r	11348	0.20	2.09
		\dot{B}_θ	11348	-0.18	2.26
		\dot{B}_ϕ	11348	0.06	2.43
	Polar	\dot{B}_r	3609	0.22	4.43
		\dot{B}_θ	3609	-0.19	4.21
		\dot{B}_ϕ	3609	-0.08	2.85

GRACE, which is, as expected, due to the higher data noise level. By separating the residuals poleward of $\pm 55^\circ$ QD latitude from the ones equatorward, we find that peaks are broader at polar QD latitudes for all datasets, which is a result of unmodeled magnetic signal of the polar ionospheric current system. Also, the histograms of the GRACE residuals are biased toward negative values. Upon further investigation, we found a local time-dependence especially visible in the scalar residuals, which could indicate that signals from solar array and battery currents have not been fully removed from the GRACE datasets used here. The residual statistics are summarized in Table 5 for the satellite data and Table 6 for the ground observatory SV data.

Figure 4 shows the time-series of the SV components at six chosen ground observatories together with the computed values from Model-A and Model-B.

Overall, the fit of Model-A and Model-B to the ground observatory SV data is good, as expected, for the first five observatory SV shown, since these data were used in the model parameter estimation. The computed values of Model-A and Model-B differ especially during the gap from 2010 to 2014, where Model-B can make use of platform magnetometer data in addition to the ground observatory SV data, while Model-A only relies on the ground observatories. That shows that platform magnetometer data contribute to the internal field model especially when there is a lack of calibrated satellite data from CHAMP and *Swarm*. Perhaps even more convincing is the performance of both models when compared to a dataset not used in the inversion. With the SV data from Saint Helena, we show such an independent dataset in the last row of Fig. 4. Although both models fit Saint Helena well, Model-B performs slightly better in the radial SV in 2013 and the azimuthal SV at least in the first half of the gap period, until 2012.

To summarize, with Model-B, we built a model that fits both the satellite and ground observatory SV data to a satisfactory level, which shows that platform

magnetometer data can be successfully used in geomagnetic field modeling.

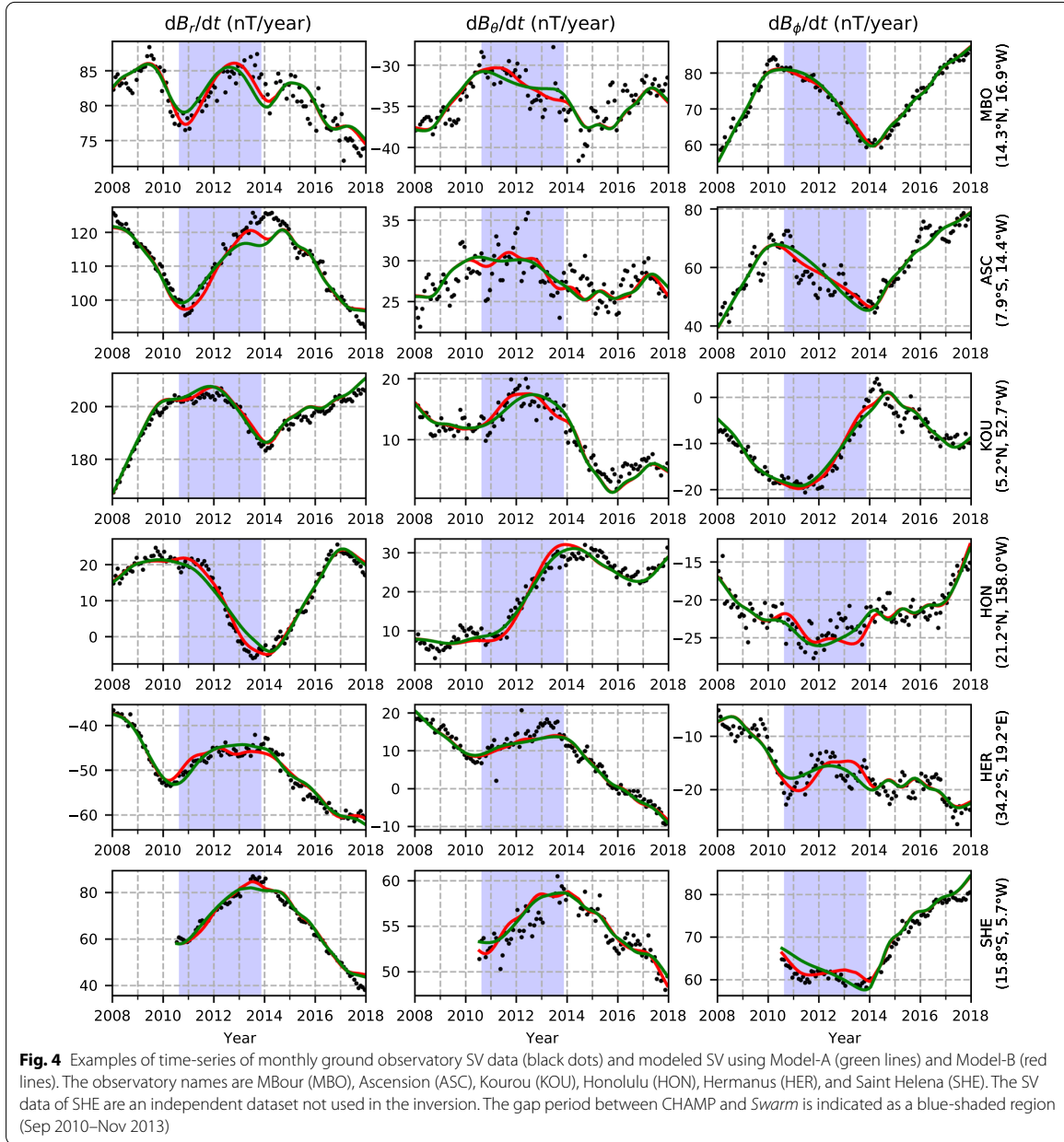
Calibration parameters

We document the estimated calibration parameters of each platform magnetometer dataset by showing the time-series in Fig. 5 and the respective mean values in Table 7.

In Fig. 5, the rows of panels correspond to the CryoSat-2 (top three) and GRACE (bottom two) platform magnetometer datasets, and the columns of panels show the offsets (left), sensitivities (middle), and non-orthogonality angles (right). Since Alken et al. (2020) also used magnetic data from the three platform magnetometers on-board CryoSat-2, it is possible to compare the estimated calibration parameters. First, comparing the time-averaged values of the calibration parameters (Table 7 here and Table 4 in Alken et al. (2020)), we find that the non-orthogonalities are equal to within 0.01° and the offsets to within 1 eu. The averaged values of sensitivities are equal to within 1×10^{-4} eu/nT (notice that Alken et al. (2020) use the reciprocal of the sensitivity). In terms of the temporal variability, we find that our estimated calibration parameters have amplitudes that are smaller, or equal in case of the offsets, which is likely due to a difference in the regularization strength. In Fig. 5, we also show the CryoSat-2 calibration parameters of Olsen et al. (2020) for comparison. Again, the calibration parameters are very similar and differ only in the time variations (e.g., s_1) due to the choice of the regularization parameters of this study and Olsen et al. (2020). Given the acceptable fit to the platform magnetometer data and the reasonable temporal variability of the calibration parameters, we conclude that the calibration of the CryoSat-2 and GRACE platform magnetometers was successful.

Results of the experiments

We conducted a series of experiments in which we changed the model estimation, parameterization, and



data selection with the goal to investigate and document difficulties when dealing with platform magnetometer data in a co-estimation scheme. This section also justifies the modeling strategies that went into the construction of our preferred geomagnetic field model, Model-B.

In a first experiment, we allowed the nightside platform magnetometer data to participate in the estimation of the axial dipole coefficient of the time-dependent

internal field. That is, we derived a test model, Model-C, identical to Model-B but left the matrix of partial derivatives $\underline{\mathbf{G}}$ unchanged, so that the entries corresponding to the B-spline coefficients $g_{1,j}^0$ were non-zero, and thus, the satellite data contributed to the estimation of the internal dipole coefficients. On the left of Fig. 6, we show the time-derivative of g_1^0 as a function of time computed with

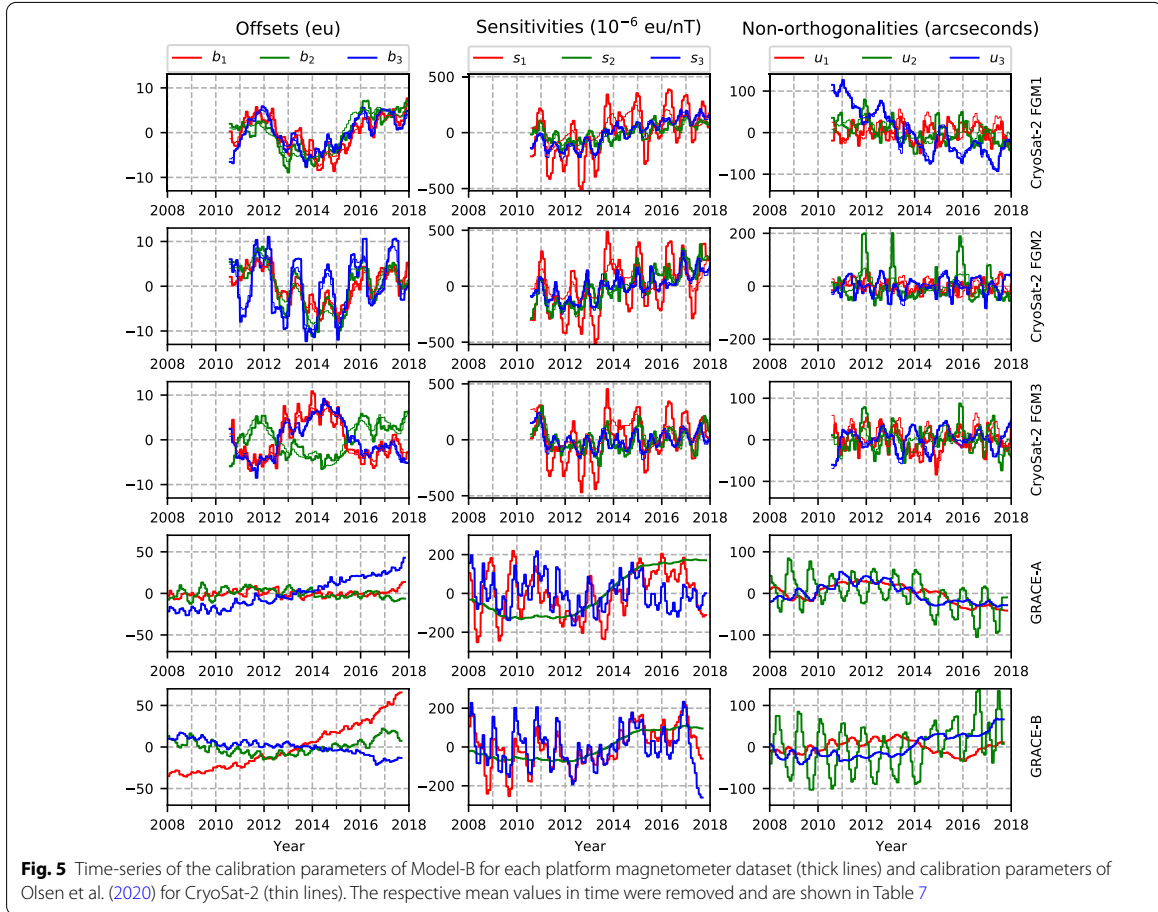


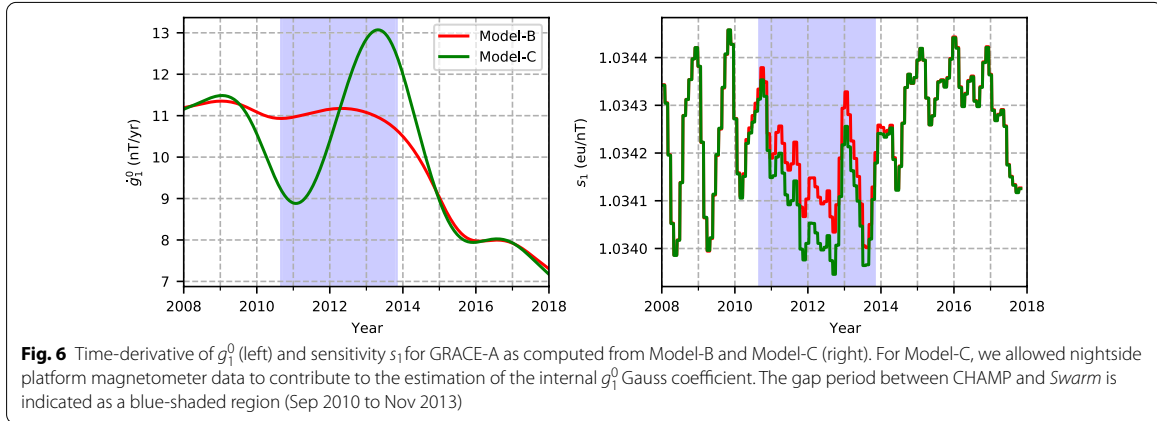
Table 7 Mean values of the calibration parameters for each platform magnetometer dataset. The time-series are shown in Fig. 5

Dataset	b_1 (eu)	b_2 (eu)	b_3 (eu)	s_1 (eu/nT)	s_2 (eu/nT)	s_3 (eu/nT)	u_1 (°)	u_2 (°)	u_3 (°)
CryoSat-2 FGM1	5.0	165.6	-10.7	1.005178	1.004851	1.004479	0.453	0.191	-0.336
CryoSat-2 FGM2	77.6	-16.6	61.8	1.004697	1.003993	1.003427	-0.288	0.050	0.502
CryoSat-2 FGM3	-115.2	-29.4	-44.6	1.000863	1.005424	1.002168	0.745	-0.045	-0.000
GRACE-A	746.4	-2632.1	-2310.0	1.034238	1.032041	1.018168	-0.251	-0.161	0.048
GRACE-B	406.0	-2622.0	-2005.6	1.029785	1.026781	1.017845	-0.056	-0.209	0.106

Model-B and Model-C, while, on the right, we show s_1 of GRACE-A as an example of the calibration parameters.

In contrast to Model-B, Model-C features a conspicuous detour of the time-derivative of the g_1^0 coefficient in the gap between CHAMP and *Swarm* data (blue-shaded region). Although we only show s_1 of GRACE-A in Fig. 6,

we find that all three sensitivities of each platform magnetometer differ in the gap period between Model-C and Model-B. The other internal Gauss coefficients also deviate but to a lesser extent. Interestingly, other model parameters such as the offsets, non-orthogonality angles, Euler angles, and external field parameters seem

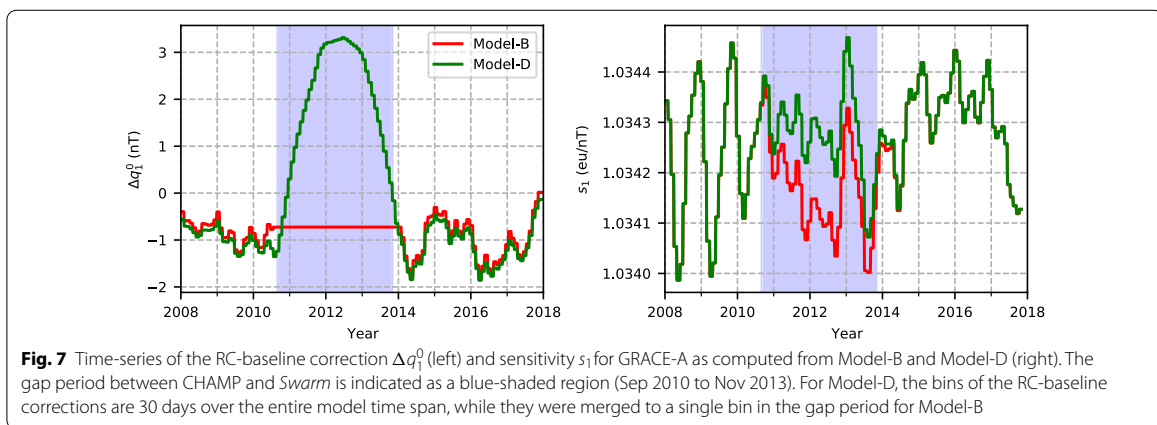


qualitatively unaffected. The same correlation between the internal axial dipole coefficient and the sensitivities has been reported by Alken et al. (2020) who show that this effect can be mitigated either by including large amounts of previously calibrated data or through the use of a regularization that favors a linear time-dependence of the internal dipole during the gap period. Due to the lack of additional calibrated data and our interest in the high-degree SA during the gap that such a regularization affects by redistributing power to higher degrees, we chose to set the dependence of g_1^0 , the most affected internal Gauss coefficient, on the satellite platform magnetometer data to zero. In other words, we completely relied on the ground observatory SV data and the temporal regularization to estimate the time-dependence of g_1^0 in the gap period.

In a second experiment, we built a test model, Model-D, which uses 30 day bins of the RC-baseline corrections consistently over the whole model time span in contrast to Model-A and Model-B, which use a single bin

spanning the entire gap period. As an example, Fig. 7 shows the RC-baseline correction Δq_1^0 on the left and the calibration parameter s_1 of GRACE-A on the right, computed with Model-D and Model-B.

In Model-D, Δq_1^0 has a noticeable peak during the gap period that is much larger in value than the variation during CHAMP or *Swarm* times, while the sensitivity is slightly offset to higher values. We find the same behavior for all RC-baseline corrections and calibration parameters, although most prominently for the sensitivities. Again, other model parameters seem unchanged, which indicates that there is a significant correlation between the RC-baseline corrections and the calibration parameters of the platform magnetometers. Using a single bin for the RC-baseline corrections in the gap period helps to reduce that effect. As a final comment regarding Model-C and Model-D, we performed a simulation combining both experiments; that is, we determined g_1^0 with the platform magnetometer data and estimated the RC-baseline corrections in 30 day bin over the entire model time



span. In this case, we observed deviations from Model-B which were identical to those shown in Figs. 6 and 7, but, now, affected the internal axial dipole, the RC-baseline corrections, and the sensitivities all at the same time.

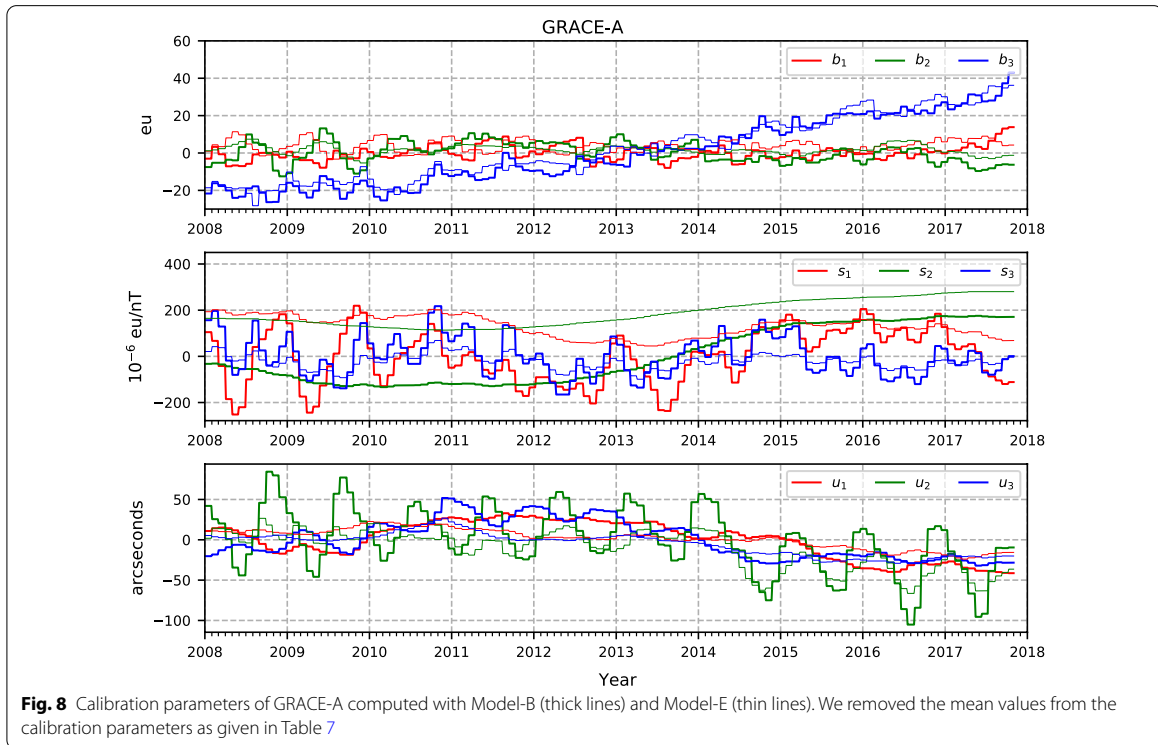
In an effort to analyze the relationship between the calibration and the other model parameters in a quantitative manner, we also investigated the model correlations $\rho_{ij} = C_{ij} / \sqrt{C_{ii}C_{jj}}$ based on the entries of the model covariance matrix:

$$\underline{\mathbf{C}} = (\underline{\mathbf{G}}^T \underline{\mathbf{C}}_d^{-1} \underline{\mathbf{G}} + \underline{\mathbf{\Lambda}})^{-1}, \quad (31)$$

evaluated with the converged model parameters (Taran-tola 2005, p. 71). Unfortunately, the analysis revealed a large number of small correlations, which are difficult to interpret. Therefore, we did not make significant use of it in the modeling and preferred to rely on experiments to guide our modeling strategy.

In a final experiment, we derived a test model, Model-E, by only using nightside platform magnetometer data as opposed to Model-B, where the calibration parameters were determined from dayside and nightside platform magnetometer data. Figure 8 shows the calibration parameters for GRACE-A computed with Model-B (thick lines) and Model-E (thin lines).

In the case of GRACE-A, using dayside data to determine the calibration parameters considerably changes the sensitivities and non-orthogonalities as can be seen, for example, when looking at s_1 , s_2 or u_3 . In particular for s_2 , there is a vertical shift of approximately $200 \times 10^{-6} \text{eu/nT}$, which translates to 10 nT in a magnetic field of 50000 nT. Irrespective of the platform magnetometer, the experiment shows that the local time coverage of the data plays an important role in determining the calibration parameters. The importance of using both day and nightside data becomes clear when appreciating that the orbital plane of the satellites is slowly drifting in local time. Under a possible nightside data selection criteria, the drift leads to the selection of data from either the ascending part or descending part of the orbit at a time. For example, if the ascending node of the orbit is on the nightside, then the platform magnetometer collects data of the magnetic field that mostly points along the direction of flight, in agreement with the predominant dipolar field configuration, until the ascending node crosses over to the dayside placing the descending part of the orbit on the nightside. Now, the observed magnetic field mostly points against the direction of flight. In the case of CryoSat-2, it takes the ascending node 8 months and GRACE around 11 months to



traverse the nightside, which is longer than the monthly bins used for estimating the calibration parameters. Hence, the data of each bin will be collected either from the ascending or descending nodes with the respective bias of the field direction. Instead, using both nightside and dayside, we ensured that the data within each bin covered a broad range of local times to excite the platform magnetometer from various directions, which we believe improves the estimation of the calibration parameters. Nevertheless, we did not use any dayside data to constrain the geomagnetic field model, since we do not account for the strong ionospheric sources on the dayside. Those ionospheric sources, however, may contaminate the calibration parameters.

Secular acceleration

One motivation for using platform magnetometer data has been the growing interest in SA pulses, and enhancements of the SA that occur on sub-decadal time scales and are seen most prominently at low latitudes. These pulses have been reported by several studies (Olsen and Mandaia 2007; Chulliat et al. 2010; Chulliat and Maus 2014) and are thought to reflect the dynamical processes in the Earth’s outer core. To further study SA pulses and the SA in general, accurate internal field models are needed, which rely on long and continuous time-series of satellite data to give a global picture. When supplemented with high-quality satellite data, platform magnetometer data may play an important role in providing those models.

To investigate the effect of platform magnetometer data on the recovered SA, we show in Fig. 9 time-longitude

maps of the radial SA on the Equator at the CMB computed with Model-B (left) and Model-A (center) alongside the difference map (right).

Recall that Model-B is partly based on platform magnetometer data in contrast to Model-A, so that the difference of the two reflects the use of these data. Both models show the SA pulses in 2009, 2013, and most recently in 2017 as enhancement of the radial SA on the Equator. Of special interest is the pulse in 2013, right in between periods of high-quality magnetic data from the CHAMP and *Swarm* missions. In the difference map, the SA during CHAMP and *Swarm* period is largely unchanged, which suggests that the effect of the CryoSat-2 and GRACE data is rather minimal during these times. In contrast, the SA in the gap period is distinctly different for the two models. Differences that are large in absolute value seem to be concentrated around 0° and 180° longitude on the Equator which coincides with the Pacific and the region in the South Atlantic close to Central Africa. The geographical location of the differences is more clearly seen in Fig. 10, which shows global maps of the radial SA at the CMB during the SA pulses in 2009, 2013, and 2017.

Again, the difference between Model-B and Model-A is small in 2009 and 2017, i.e., during CHAMP and *Swarm* times, but large in 2013 in the middle of the gap period. The regions with the largest differences are located in the Southern hemisphere and the Equatorial region with prominent examples in the West and South Pacific Ocean, and Central Africa. Our findings seem to indicate that the platform magnetometers have the desired effect of balancing the uneven spatial distribution of the ground observatory network in the gap period.

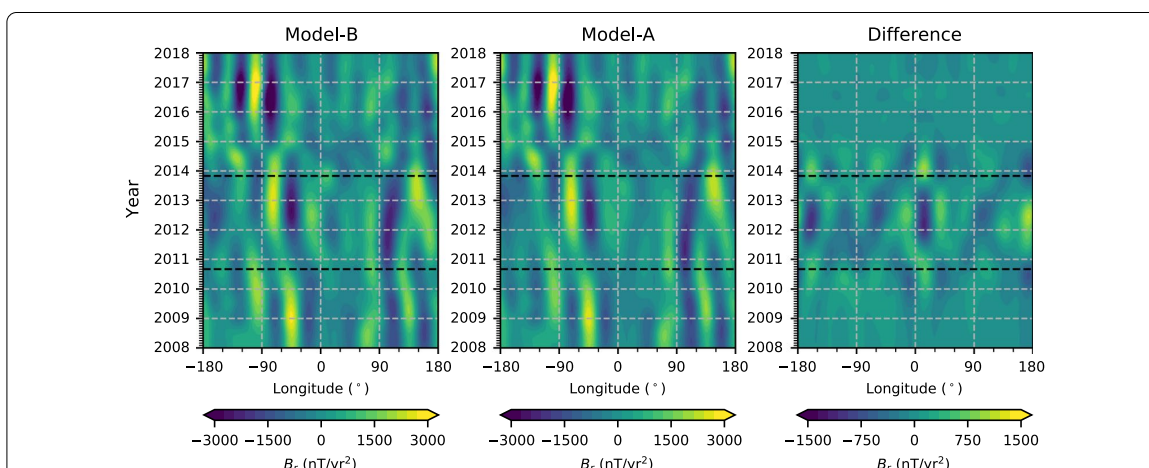
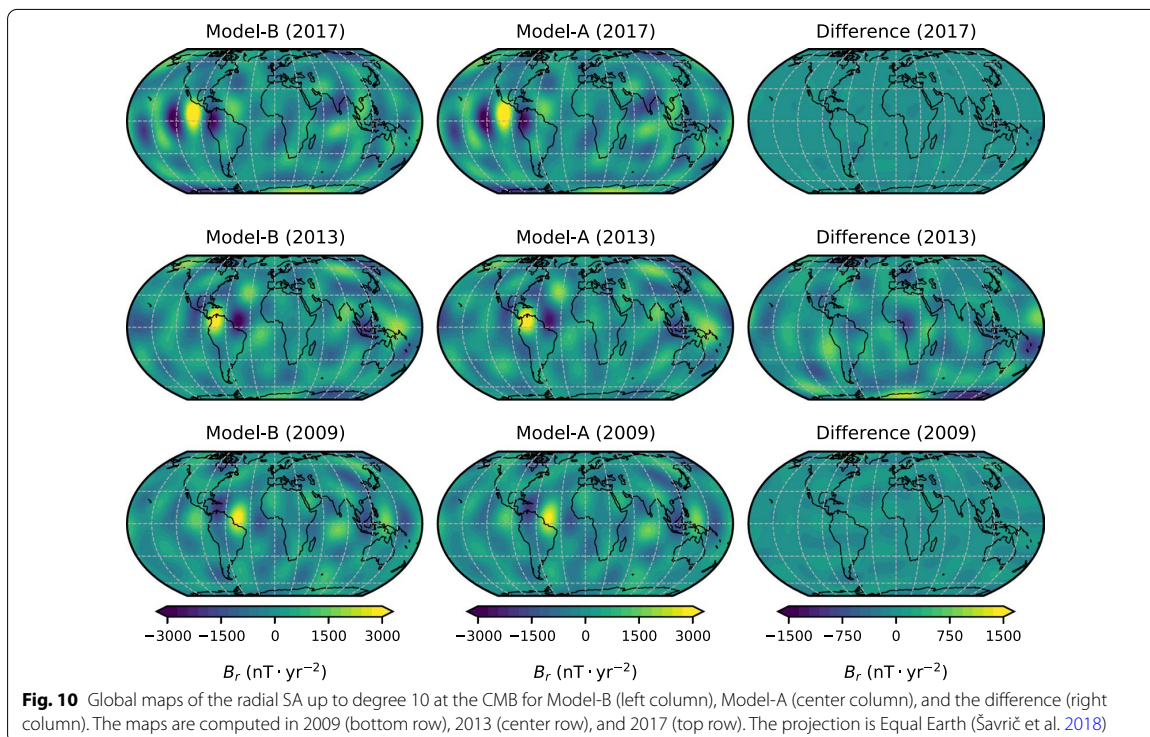


Fig. 9 Time-longitude maps of the radial SA up to degree 10 on the Equator at the CMB as computed with Model-B (left), Model-A (center) and their difference, Model-B minus Model-A (right). The gap period between CHAMP and *Swarm* is in between the black dashed lines (Sep 2010–Nov 2013)



Conclusions

In this study, we present a co-estimation scheme within the framework of the CHAOS field model series that is capable of estimating both a geomagnetic field model and, at the same time, calibration parameters for platform magnetometers. This approach enables us to use platform magnetometer data to supplement high-quality magnetic data from magnetic survey satellites and removes the requirement for utilizing a-priori geomagnetic field models to calibrate platform magnetometer data.

We followed Alken et al. (2020), but went further in that we co-estimated a model of not only the internal field but also the external field. The co-estimation scheme relies on absolute magnetic data which we took from CHAMP, Swarm-A, Swarm-B, and the monthly SV data from ground observatories between 2008 and 2018. Magnetic data from five platform magnetometers were used: three on-board CryoSat-2 and one on-board each of the two GRACE satellites. This allowed us to considerably improve the geographical and temporal coverage of satellite data after CHAMP and before the launch of the *Swarm* satellites.

We successfully co-estimated a geomagnetic field model along with the calibration parameters of the five platform magnetometers. The misfit to the high-quality satellite data and ground observatory SV data was similar to that for

models derived without including platform magnetometer data, and the good fit to an independent ground observatory dataset from Saint Helena provides evidence that our modeling approach performs well.

In a series of experiments, we investigated the trade-offs when co-estimating calibration and geomagnetic field model parameters. We found that the calibration parameters strongly correlate with the internal axial dipole and the RC-baseline corrections of the external field during the gap period, when there is less high-quality data available. By preventing platform magnetometer data from contributing to the internal axial dipole and using constant RC-baseline corrections throughout the entire gap period, we successfully avoided those complications.

Our experiments showed that including platform magnetometer data leaves the SA signal practically unchanged during the CHAMP and *Swarm* period, but leads to differences in the gap period. The difference in the recovered SA signal is stronger in the West and South Pacific, where only a few observatories are located, which suggests that platform magnetometer data help to improve the global picture of the SA. Based on our investigations, we find that it is worthwhile to include platform magnetometer data in internal field modeling, in particular from CryoSat-2 given the relative low noise level.

Abbreviations

CHAMP: CHALLENGING Minisatellite Payload; CMB: Core mantle boundary; CRF: Common reference frame; DMSP: Defense Meteorological Satellite Program; FGM: Fluxgate magnetometer; GRACE: Gravity Recovery and Climate Experiment; GSM: Geocentric solar magnetic; NEC: North-east-center; nT: NanoTesla; QD: Quasi-dipole; RTP: Radius-theta-phi; SM: Solar magnetic; VFM: Vector field magnetometer.

Acknowledgements

The European Space Agency (ESA) is gratefully acknowledged for providing access to the *Swarm* L1b data, CryoSat-2, and GRACE platform magnetometer data and related engineering information. We wish to thank the German Aerospace Center (DLR) and the Federal Ministry of Education and Research for supporting the CHAMP mission. Furthermore, we would like to thank the staff of the geomagnetic observatories and INTERMAGNET for supplying high-quality observatory data. Susan Macmillan (BGS) is gratefully acknowledged for collating checked and corrected observatory hourly mean values in the AUX OBS database.

Open Access

This article is distributed under the terms of the Creative Commons Attribution 4.0 International License (<http://creativecommons.org/licenses/by/4.0/>), which permits unrestricted use, distribution, and reproduction in any medium, provided you give appropriate credit to the original author(s) and the source, provide a link to the Creative Commons license, and indicate if changes were made.

Authors' contributions

CK developed the modeling software for the co-estimation of calibration parameters, derived the presented models, and led the writing of the manuscript. CCF participated in the design of the study. NiO pre-processed the CryoSat-2 and GRACE platform magnetometer data, developed the CHAOS modeling approach, and participated in the design of the study. All authors read and approved the final manuscript.

Funding

CK and CCF were funded by the European Research Council (ERC) under the European Union's Horizon 2020 research and innovation programme (grant agreement No. 772561). The study has been partly supported as part of *Swarm* DISC activities, funded by ESA contract no. 4000109587.

Availability of data and materials

The datasets supporting the conclusions of this article are available in the following repositories: *Swarm* and CryoSat-2 data are available from <https://earth.esa.int/web/guest/swarm/data-access>; The GRACE data are available from <ftp://ftp.spacecenter.dk/data/magnetic-satellites/GRACE/>; CHAMP data are available from <https://isdc.gfz-potsdam.de/champ-isdc>; Ground observatory data are available from ftp://ftp.nerc-murchison.ac.uk/geomag/Swarm/AUX_OBS/hour/; The RC-index is available from <http://www.spacecenter.dk/files/magnetic-models/RC/>; The CHAOS-6 model and its updates are available from <http://www.spacecenter.dk/files/magnetic-models/CHAOS-6/>; and Solar wind speed, interplanetary magnetic field, and Kp-index are available from <https://omniweb.gsfc.nasa.gov/ow.html>.

Competing interests

The authors declare that they have no competing interests.

Received: 30 September 2020 Accepted: 26 December 2020

Published online: 20 January 2021

References

- Alken P, Olsen N, Finlay CC (2020) Co-estimation of geomagnetic field and in-orbit fluxgate magnetometer calibration parameters. *Earth Planets Space* 72(1):1–32. <https://doi.org/10.1186/s40623-020-01163-9>
- Backus G, George B, Parker RL, Parker R, Constable C (1996) *Foundations of Geomagnetism*. Cambridge University Press, Cambridge

- Chulliat A, Maus S (2014) Geomagnetic secular acceleration, jerks, and a localized standing wave at the core surface from 2000 to 2010. *J Geophys Res* 119(3):1531–1543. <https://doi.org/10.1002/2013jb010604>
- Chulliat A, Thebaud E, Hulot G (2010) Core field acceleration pulse as a common cause of the 2003 and 2007 geomagnetic jerks. *Geophys Res Lett* 37:7. <https://doi.org/10.1029/2009gl042019>
- Constable CG (1988) Parameter estimation in non-gaussian noise. *Geophys J Int* 94(1):131–142
- De Boor C (1978) *A practical guide to splines*, vol 27. Springer, New York
- Finlay CC, Olsen N, Kotsiaros S, Gillet N, Tøffner-Clausen L (2016) Recent geomagnetic secular variation from Swarm and ground observatories as estimated in the CHAOS-6 geomagnetic field model. *Earth Planets Space* 68:1. <https://doi.org/10.1186/s40623-016-0486-1>
- Finlay CC, Kloss C, Olsen N, Hammer M, Tøffner-Clausen L, Grayver A, Kuvshinov A (2020) The CHAOS-7 geomagnetic field model and observed changes in the south atlantic anomaly. *Earth Planets Space*. <https://doi.org/10.1186/s40623-020-01252-9>
- Holme R, Bloxham J (1996) The treatment of attitude errors in satellite geomagnetic data. *Phys Earth Planet Inter* 98(3–4):221–233
- Macmillan S, Olsen N (2013) Observatory data and the Swarm mission. *Earth Planets Space* 65(11):1355–1362. <https://doi.org/10.5047/eps.2013.07.011>
- Olsen N (2020) Magnetometer data of the GRACE satellites duo. *Earth Planets Space* (in review)
- Olsen N, Manda M (2007) Investigation of a secular variation impulse using satellite data: The 2003 geomagnetic jerk. *Earth Planet Sci Lett* 255(1–2):94–105. <https://doi.org/10.1016/j.epsl.2006.12.008>
- Olsen N et al (2003) Calibration of the Ørsted vector magnetometer. *Earth Planets Space* 55(1):11–18. <https://doi.org/10.1186/BF03352458>
- Olsen N, Lühr H, Sabaka TJ, Manda M, Rother M, Tøffner-Clausen L, Choi S (2006) CHAOS-a model of the Earth's magnetic field derived from CHAMP, Ørsted, and SAC-C magnetic satellite data. *Geophys J Int* 166(1):67–75. <https://doi.org/10.1111/j.1365-246x.2006.02959.x>
- Olsen N, Lühr H, Finlay CC, Sabaka TJ, Michaelis I, Rauberg J, Tøffner-Clausen L (2014) The CHAOS-4 geomagnetic field model. *Geophys J Int* 197(2):815–827
- Olsen N, Albini G, Bouffard J, Parrinello T, Tøffner-Clausen L (2020) Magnetic observations from CryoSat-2: calibration and processing of satellite platform magnetometer data. *Earth Planets Space* 72:1–18
- Richmond AD (1995) Ionospheric electrodynamics using magnetic apex coordinates. *J Geomagn Geoelectr* 47(2):191–212. <https://doi.org/10.5636/jgg.47.191>
- Rother M, and I. Michaelis (2019), CH-ME-3-MAG - CHAMP 1 Hz combined magnetic field time series (level 3), <https://doi.org/10.5880/GFZ.2.3.2019.004>
- Sabaka TJ, Olsen N, Purucker ME (2004) Extending comprehensive models of the earth's magnetic field with Ørsted and CHAMP data. *Geophys J Int* 159(2):521–547
- Sabaka, T. J., G. Hulot, and N. Olsen (2010), *Mathematical properties relevant to geomagnetic field modeling*. In: *Handbook of geomathematics*. Springer: New York. pp. 503–538
- Šavrič B, Patterson T, Jenny B (2018) The equal earth map projection. *Int J Geogr Inform Sci* 33(3):454–465. <https://doi.org/10.1080/1365816.2018.1504949>
- Tarantola A (2005), *Inverse problem theory and methods for model parameter estimation*, SIAM
- Thebaud E et al (2015) International geomagnetic reference field: the 12th generation. *Earth Planets Space* 67(1):79

Publisher's Note

Springer Nature remains neutral with regard to jurisdictional claims in published maps and institutional affiliations.

ISBN: 978-87-91694-50-9

DTU Space
National Space Institute

Centrifugevej 356
DK-2800 Kongens Lyngby

www.space.dtu.dk